Challenging systems for quantum chemistry: inorganic excited states and intermolecular aggregates

Nuno Miguel da Silva Almeida

Submitted for the degree of Doctor of Philosophy
(Chemistry)

Heriot-Watt University

School of Engineering and Physical Sciences

September 2016

Abstract

This thesis focuses on challenging systems for computational chemistry: inorganic excited states and intermolecular aggregates. Excited states of inorganic systems can be extremely challenging for conventional methods of quantum chemistry, mostly due to strong correlation, degeneracy and near-degeneracy problems, in addition to a large density of states. A calibration study of the electronic excited states of a range of complexes has been carried out in a number of chapters using a wide range of methods. A range of all-electron and ECP basis sets were used. These calculations reveal the effect of improving the treatment of electron correlation systematically. A CASSCF/RASSCF study was performed for the most complex systems to be able to capture and analyse the multireference nature of the complexes. Later in the thesis the photochemistry arising from the photodissociaton of $Mn_2(CO)_{10}$ and $Cr(CO)_6$ is described using CASPT2 to recover the dynamic correlation of the system and compare with previous CASSCF results. The last part focuses on intermolecular aggregates. Supramolecular structures have grown in importance in recent years due to their potential applications as advanced functional materials. The fine-tuning of these structures allows to build up higher hierarchical superstructures with very diverse and interesting properties. A bottom-up approach for this kind of systems is used to characterize the multichromophoric self-assembly of gels and detail their responses to light.

Acknowledgments

Firstly, I would like to express my sincere gratitude to everyone that has helped me develop this thesis for about four years, especially those who helped me solve problems that I myself could not do alone. All the meetings I had with my group and chemistry department were of the utmost importance to help me improve as a scientist.

I would like to thank my supervisor, Professor Martin J. Paterson in particular, for the help, support and patience to complete this thesis and not forgetting all the long hours we have spent debating topics and discussing new ideas for my research. Without his support finishing this thesis would not be possible.

Another special thank you note for Dr. Russell G. McKinlay for all the assistance and work performed for the research papers for this thesis, especially on Chapter 4 and 6 for his big contributions. Another thank you note for Dr. Jeremy Coe on performing calculations helping me solve important questions on Chapter 5 and 6. The last note goes for all the researchers involved in the experimental work performed on Chapter 8.

In memory of Laura Anne Cox, thank you for the all the support and enthusiasm. You have helped me finish this step of my life and I wish you were here to finish it with me. I would also like to thank my family for always being there encouraging me all the time.

The ERC is thanked for funding under the European Union's Seventh Framework Programme (FP7/2007-2013)/ERC Grant No. 258990.

Contents

Publications

[1] Almeida, N. M. S.; McKinlay, R. G.; Paterson, M. J., *Structure and Bonding; Theoretical Insights into Organometallic Mechanisms* (Computation of excited states of transition metal complexes); Springer Berlin Heidelberg; **2014**, 1-32.

[2] Almeida, N. M. S.; McKinlay, R. G.; Paterson, M. J., *Chemical Physics* (Excited electronic states of MnO_4^-: challenges for wavefunction and density functional response theories); **2015**, *446*, 86-91.

[3] McKinlay, R. G.; Almeida, N. M. S.; Coe, J. P.; Paterson, M. J., *The Journal of Physical Chemistry A* (Excited states of the nickel carbonyls Ni(CO) and Ni(CO)4: Challenging molecules for electronic structure theory); **2015**, *119*(39), 10076-10083.

[4] Foster, J. S.; Żurek, J. M.; Almeida, N. M. S.; Hendriksen, W. E.; le Sage, V. A. A.; Lakshminarayanan, V.; Thompson, A. L.; Banerjee, R.; Eelkema, R.; Mulvana, H.; Paterson, M. J.; van Esch, J. H.; Lloyd, G. O., *Journal of the American Chemical Society* (Gelation landscape engineering using a multi-reaction supramolecular hydrogelator system); **2015**, *137*(45), 14236-14239.

[5] Coe, J.; Almeida, N. M. S.; Repiščák, P.; Paterson, M. J., (Investigating Monte-Carlo configuration interaction for open-shell systems); *in prep.*

List of Abbreviations

5Z - Quintuple-Zeta
BD - Brueckner doubles
BTA - Benzene-1,3,5-tricarboxamide
CASPT2 - Complete active space second order perturbation theory
CASSCF - Complete active space self-consistent field
CC - Coupled-cluster
CC2 - Second-order approximate coupled cluster singles and doubles model
CC3 - Third-order approximate coupled cluster singles and doubles and triples model
CCR(3) - Non iterative triples corrections in linear response coupled-cluster methods
CCS - Coupled-cluster singles
CCSD(T) - Coupled-cluster singles doubles and perturbative correction triples
CCSD - Coupled-cluster singles and doubles
CI - Configuration interaction
CIS - Configuration interaction singles
CISD - Configuration interaction singles and doubles
DFT - Density functional theory
DZ - Double-zeta
EOM-CC - Equation of motion coupled-cluster
GTO - Gaussian type orbitals
HF - Hartree-Fock
LMCT - Ligand-to-metal charge transfer
LMWG - Low molecular weight gelators
LF - Ligand field
MCCI - Monte-Carlo configuration interaction
MLCT - Metal-to-ligand charge transfer
MP2 - MøllerPlesset second order perturbation theory

MP3 - Møller Plesset third order perturbation theory

MS SCF - Multi-configurational self-consistent field method

NBO - Natural bond orbitals

QCISD - Quadratic configuration interaction singles and doubles

QZ - Quadruplet-Zeta

RHF - Restricted Hartree-Fock

ROHF - Restricted Open-Shell Hartree-Fock

SBLCT - σ bond-to-ligand charge transfer

SCF - Self-consistent field

SEM - Scanning electronic microscope

STO - Slater type orbitals

TD-DFT - Time density functional theory

TM - Transition metals

TS - Transition state

TZ - Triple-zeta

UHF - Unrestricted Hartree-Fock

XLCT - Halide-to-ligand charge transfer

Chapters review

- **Chapter 1** introduces concepts that are used in this thesis and reviews previous studies performed on the excited states of transition metal complexes.

- **Chapter 2** details an extensive review of the range of methods and basis sets used in this thesis to perform all the computational studies.

- **Chapter 3** describes well known inorganic transition metal complexes and transition metal oxides using highly accurate methods.

- **Chapter 4** details ground and excited states analysis of the permanganate ion.

- **Chapter 5** provides a detailed description of the ground spin state of first-row transition metal monocarbonyls.

- **Chapter 6** investigates the ground and low-lying excited states of $NiCO_4$ and NiCO.

- **Chapter 7** details the photochemistry of $Cr(CO)_5$ and $Mn(CO)_5$ showing the pathway these molecules undergo after their parent molecules undergo photodissociation.

- **Chapter 8** focuses on the formulation of intermolecular aggregates that have an increasing importance in the field of chemistry for their multiple applications in supramolecular chemistry.

Chapter 1

Introduction

1.1 Introduction to transition metal complexes

In this introduction the current state-of-the-art for the computation of transition metal chemistry will be discussed. The use of different levels of theory is fundamental in this field of chemistry to capture the behaviour of small transition metal complexes, to extrapolate to larger, more complex systems. By using these techniques, it is possible to benchmark and gather what is possible, or not, from modern computational techniques applied to transition metal systems and supramolecular chemistry. The application of computational and theoretical methods to organometallic chemistry in ground electronic states has been the subject of several reviews during the past few years [1] [2] [3]. The focus of this thesis is on an area that has seen less activity: the computation of inorganic excited states. The work includes aspects of both theoretical spectroscopy and reactive photochemistry. Nowadays, due to the current evolution of computer hardware and software, as well as advanced theories of computational chemistry, scientists can gain further understanding of such systems to improve fundamental knowledge.

Before discussing previous studies in the literature, basic inorganic nomenclature is given. Ligands can be classed as either x-type or l-type. X-type ligands can coordinate to the metal with a covalent bond via an electron being donated to the metal and one received from the metal. These electronic donations usually complete the octet rule (18 electron

rule [4]) and fill the valence shell. An l-type ligand normally has a complete octet, so the way it coordinates to the metal is different: through a σ, π-bond or a lone pair of electrons. L-type ligands usually donate two electrons to the metal centre. A complex has the form of ML_n and the number of electrons (N_e) around the centre is counted using the following equation:

$$N_e = N_m + 2N_l + N_x - q \tag{1.1}$$

- N_m - metal electron count
- N_l - number of l-type ligands
- N_x - number of x-type ligands
- q - overall charge of the complex

It is worth mentioning that if a complex has an electron count that is inferior to 18 electrons, then it is very reactive, and some of such complexes are discussed in this thesis, for example in Chapter 5. Scientists have always tried to predict the formation of these complexes in a consistent and rational way, so several theories have been developed. Two of the most important ones are: crystal field theory and ligand field theory. The former, describes the interaction between d orbitals and how the arrangement depends on the geometry, and stabilizes the energetic levels. It is a simple model and it is based on the ligands around the metal treated as point charges that will generate an electrical field which will affect the stabilization of the central d orbitals. So, depending on the geometry, a splitting arises (Δ) causing the energetical difference on d orbitals for different inorganic complexes.

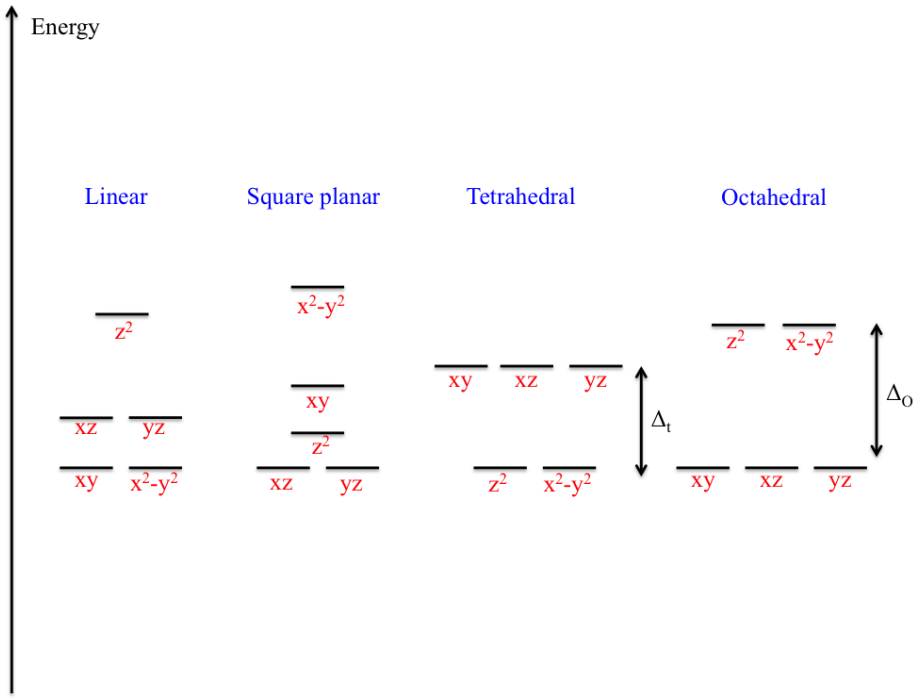

Figure 1.1: Splitting energies for different geometries in a complex.

In Figure 1.1 the Δ for the tetrahedral case (Δt) is smaller than the octahedral (Δo) one, $\Delta t = 4/9\Delta o$. The destabilization on the octahedral complex is more severe, giving a larger energetic gap. Ligand field theory was developed after crystal field theory and is more advanced when describing the bonding in d-block metal complexes. This can include orbital mixing and is able to describe the chemical bonding more in more depth, e.g. the Dewar-Chatt-Duncanson model [5] [6].

Transition metals usually have 9 valence atomic orbitals, consisting of five d (d_{xy}, d_{xz}, d_{yz}, d_{z^2} and $d_{x^2-y^2}$), three p (p_x, p_y and p_z) and one s. The interactions are very rich and depend on the geometry of the complex. There are different kinds of transitions possible, for example among d orbitals, these are called ligand field (LF) transitions. Other types are: metal-to-ligand charge transfer (MLCT), or the opposite ligand-to-metal charge transfer (LMCT). Metal complexes usually absorb light in the visible regions of the spectrum which leads to coloured complexes. The intensity of charge transfer is usually much higher compared to ligand field transitions. Some of these aspects will be described in the following chapters, for example in Chapter 4, where

MnO_4^- is rich in LMCT transitions for the low-lying excited states.

Computational methods such as density functional theory (DFT), Møller Plesset theory (MP), coupled-cluster (CC), multireference complete active space self consistent field (CASSCF), complete active space with perturbation theory (CASPT2), or Monte-Carlo configuration interaction (MCCI) will be discussed in detail in the next chapter. Some of these will be mentioned briefly in the introduction section but any detail and the theory behind them will be more extensively described in Chapter 2.

As a computational chemist, when a problem is formulated one has to think about choosing a method, which comes down to a balance between levels of accuracy required versus computational expense. For difficult cases, as discussed in Chapter 4 or Chapter 6 black-box methods (system that can be viewed as input/output, without knowledge of internal workings) sometimes are not the best choice. These kind of problems are much more predominant when transition metals are involved, compared to most organic systems. As mentioned before, inorganic excited states have not been widely researched in the past and only a few groups have applied the complex machinery required to decipher inorganic spectroscopy, and even less have looked at the reactive photochemistry. Some of the previous studies are discussed in the next subsection.

1.1.1 Previous studies on the excited states of transition metal complexes

Binary transition metal complexes, so called for containing a single metal and ligand type, are probably one of the most studied class of complexes. These can serve as model complexes for metal-ligand bonding and have a lower computational cost in comparison to larger systems.

The first study mentioned is from Beach and Gray from 1963 [7] who provided insight on the electronic spectra of group 6 hexacarbonyls. Initially they discussed their spectroscopic results in terms of basic molecular orbitals. This was the foundation for attempting to describe general features of several isoelectronic complexes. Such topics as the competition between electronic states of very different chemical character (LF vs. MLCT) were covered, and the authors assigned correctly most of the experimental bands. However, they assigned a low energy shoulder on the MLCT band to be of ligand field character, which resulted in CO loss. It is now considered that MLCT states are initially excited and undergo vibronic couplings with LF states to cause ultimate dissociation [8] [9].

Baerends *et al* researched on the excited states as well as the photochemistry of $Cr(CO)_5CNCN$ and $MnCl(CO)_5$ [10] [11].

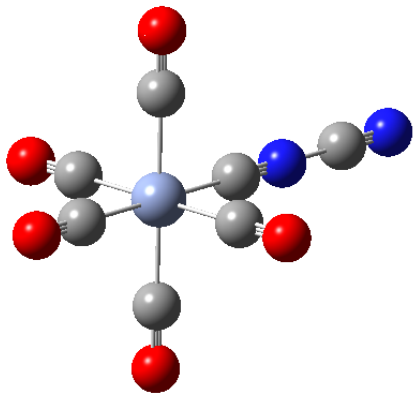

Figure 1.2: $Cr(CO)_5CNCN$, discussed in [10].

For $Cr(CO)_5CNCN$ the manner by which the CNCN ligand coordinates to the metal centre was investigated by both experiment and using DFT/TD-DFT. It was found that spectroscopic results compared well with experimental (UV-vis, UV photoelectron and IR) results and further confirmed that the way in which CNCN bonds to the metal centre is similar to the carbonyl ligand. The σ donor abilities of the two ligands were found to be quite similar, while the CNCN ligand was a stronger

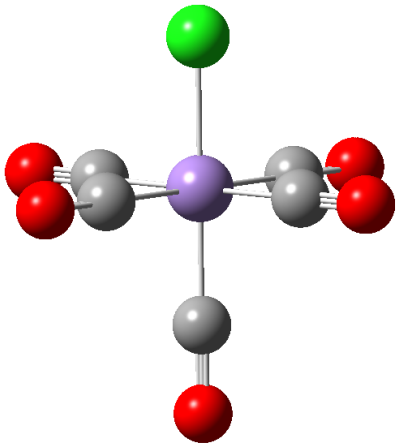

Figure 1.3: $MnCl(CO)_5$, discussed in [11].

π acceptor ligand than CO; the authors concluded that the CNCN $3\pi^*$ ligand had a lower amplitude than the $2\pi^*$ orbital on the carbon of the carbonyl ligand.

Baerends *et al* also applied DFT and TD-DFT to a wide range of transition metal systems to study their ground and excited states, as well as their photochemistry. One such system was $Mn_2(CO)_{10}$ [12].

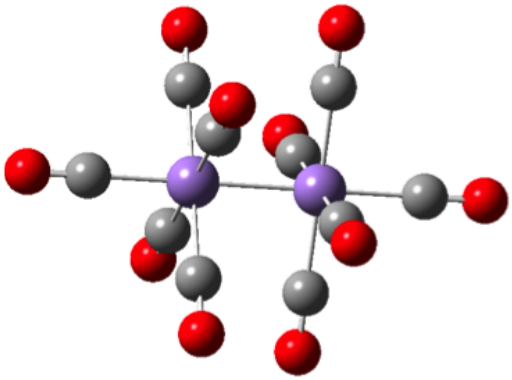

Figure 1.4: $Mn_2(CO)_{10}$ discussed in [12].

The aim was to understand better the photochemistry that results from both Mn-Mn and Mn-CO bond dissociation channels. The group decided to start with the local density approximation (LDA) exchange potential together with a mixture of double and triple zeta STO basis sets. They concluded that the low energy excitations were due to $\sigma \rightarrow \sigma^*$ and $d\pi \rightarrow \sigma^*$ with ligand field (LF) d $\rightarrow$ d transitions occurring at higher energy. The metal p orbitals were found to mix with the metal 3d.

Mn-Mn dissociation was thought to occur from the $\sigma \rightarrow \sigma^*$ transition and Mn-CO dissociation occurring from the ligand field d $\rightarrow$ d transitions. Another study was performed by the same group later, where they present potential energy curves for Mn-Mn and Mn-CO bond dissociation channels. They concluded that Mn-Mn bond dissociation occurred from the low energy $\sigma \rightarrow \sigma^*$ transition. There is still a debate concerning the CO lost, that can be axial or equatorial. The energy of the d $\rightarrow$ d state then decreases below that of the $\sigma \rightarrow \sigma^*$ state with the lengthening of Mn-CO bond. The dominant process upon photoexcitation above 266 nm was believed to be the ejection of a single carbonyl ligand.

In 1999 the authors looked into this complex once again, performing the first TD-DFT on a variety of molecules containing transition metals [13]. The final part of their article compared their results to experimental ones, which proved to be in close agreement. Apart from $Mn_2(CO)_{10}$, the excited states of other binary carbonyls and substituted carbonyls were also researched by Baerends and co-workers. Another group of complexes that raised interest were group 6 hexacarbonyls $M(CO)_6$ of chromium, molybdenum and tungnsten [12] as well as the involvement of ligand field excited states in the M-CO bond dissociation photochemistry of $Cr(CO)_6$ [14]. The main finding of these two studies was that the lowest energy excited states were not of ligand field character but in fact of charge transfer character.

$Mn_2(CO)_{10}$ lowest excited states were researched further by Daniel *et al.* CASSCF and CASPT2 were chosen to capture the static and dynamic correlation of the system [15]. They found two bands centred at 3.31 eV and 3.68 eV and assigned these to MLCT and LF transitions respectively. A lot of work has been done by the groups of Daniel and Baerends on $Mn_2(CO)_{10}$, applying different DFT and wavefunction-based methods to study the chemical character, excitation energies and transition moments of this system to test the performance of these methods. The

exact order of these states and how they interact vibronically with each other is not entirely settled.

Daniel *et al* also studied the near-UV-vis electronic spectroscopy of [Ru(X) (Me)$(CO)_2$(Me-DAB)] (X=Cl or I, DAB=1,4-Diaza-1,3-butadiene).

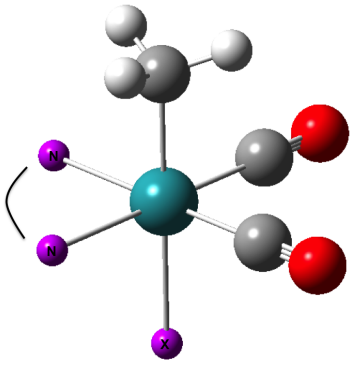

Figure 1.5: Ru(X)(Me)$(CO)_2$(Me-DAB), discussed in [16].

This complex served as model for the more commercially "interesting" complex [Ru(X)(Me)$(CO)_2$ (iPr-DAB)] [16]. These complexes were very interesting due to their photochemical, photophysical, and electronic properties and were believed to have applications as photosensitizers. It was found that the experimental spectral and UV-vis bands could be assigned with CASSCF and CASPT2, however, the accuracy of results was found to be sensitive to the functionals used with TD-DFT, with non-hybrid functionals producing unreasonable results. There are many different types of transitions in the electronic spectra of this molecule, for example MLCT, halide-to-ligand charge transfer (XLCT) and σ bond-to-ligand charge transfer (SBLCT).

$MnCl(CO)_5$ photodissociation was investigated using DFT to produce potential energy curves in order to probe the initial processes in the dissociative photochemistry. It was found that the initial excited states included the population of Mn-Cl σ^* orbital at the equilibrium geome-

try and the potential energy curves of these states were dissociative for either equatorial or axial CO loss. The loss of the Cl ligand did not occur from the lowest excited state which was surprising considering that the initial transition was to its σ^* orbital. This mechanism for the loss of a CO ligand was also found to be the case for other similar complexes like $Mn_2(CO)_{10}$ or $MnH(CO)_5$. However the mechanism by which the σ bond was broken was found to be different for each complex, for example the lowest strongly absorbing state was a $\sigma \rightarrow \sigma^*$ transition that leads to the homolytic cleavage in $Mn_2(CO)_{10}$ and its group 7 mixed metal cousins [17].

The same group performed studies on $Cr(CO)_5PH_3$ and *ax*-$Fe(CO)_4PH_3$, with respect to their photodissociation mechanisms compared to their binary counterparts ($Cr(CO)_6$ and $Fe(CO)_5$) [18].

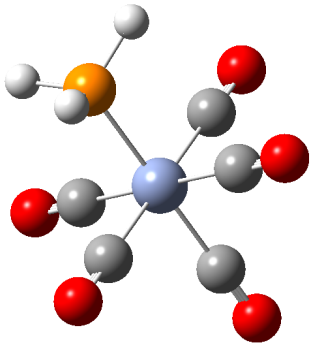

Figure 1.6: $Cr(CO)_5PH_3$, discussed in [18].

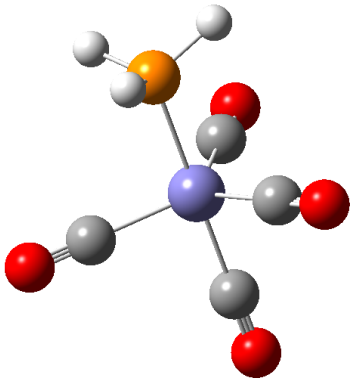

Figure 1.7: *ax*-$Fe(CO)_4PH_3$, discussed in [18].

Since the mechanism of smaller binary complexes was understood, the

photodissociation of larger phosphine ligands took place. It was found that both species favour dissociation of their phosphine ligands over their carbonyl ligands, while the lowest excited state of *ax*-$Fe(CO)_4PH_3$ was repulsive for both phosphine and carbonyl ligands. Excited state quantum dynamics simulations were performed along the potential energy curve of this state and showed that ejection of the phosphine ligand was heavily favoured over the carbonyl ligand by a branching ratio of 99 to 1. The theoretical results showed a preference for PH_3 over CO dissociation from both these excited complexes, as the phosphine group is a weaker π-acceptor ligand than CO.

Another complex studied and its photophysics analysed was octabutoxy phthalocyaninato-Nickel (II), that was researched in a joint theoretical/experimental study [19]. This particular complex was studied due to its possible use in new cancer therapies. It could efficiently absorb photon energy, and then rapidly deactivate it, creating thermal energy that is highly localized that can result in cell death. The researchers followed the excitation to the S_1 (π,π^*) state. The authors' DFT results showed that the preferred structure included a D_{2d} saddle-like coordination sphere around the nickel that had an equivalent structure separated from the other by a D_{4d} planar structure, and it could readily 'flip' between the two saddle structures. The proposed deactivation mechanism applies to both configurations around the nickel atom. Following excitation to the S_1 state a transformation occurred to a vibrationally hot ^{3}(d,d) state, which then cooled to the lowest vibrational state approximately 8 ps later. There was then a population transfer to a ^{3}LMCT state, that eventually decayed to the ground state after 640 ps.

Another heavily researched inorganic complex was $W(CO)_5$. Two systems studied comprised of W(CO)5 bonded to either 4-[(E)-2-carbomethoxy-2-cyanovinyl]pyridine or 4-(2,2-dicyanovinyl)pyridine. The excited states of these π acceptor complexes were investigated using TD-DFT and CASPT2 methods [20].

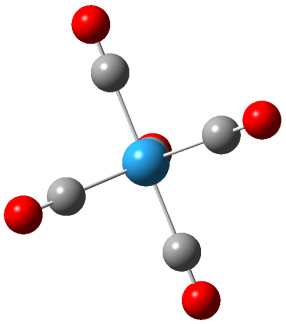

Figure 1.8: $W(CO)_5$, discussed in [20].

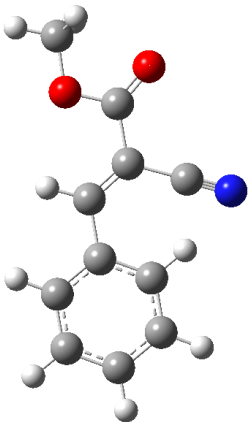

Figure 1.9: 4-[(E)-2-carbomethoxy-2-cyanovinyl]pyridine, discussed in [20].

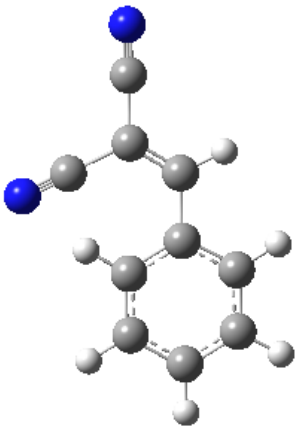

Figure 1.10: 4-(2,2-dicyanovinyl)pyridine, discussed in [20].

The low-lying excited states needed to be investigated to make a comparison of the complexes with weaker acceptor ligands, as well as looking into the dynamics of these systems. The experimental set-up involved time-resolved laser flash spectroscopy. The ground state was optimised using B3LYP and the excited states using TD-DFT, CASSCF and CASPT2. It was found that the lowest two excited states of both complexes did in fact correspond to MLCT from a tungsten 5d orbital

to a π^* orbital on the ethylenic bridge of the acceptor ligand. The scientists believed that the photoreactivity is due to the irradiation to these MLCT states.

The study of the MLCT in $HRe(CO)_3$(H-dab) (H-dab=1,4-diaza-1,3-butadiene) was performed using: CASSCF, CASPT2 and MRCI [21]. This system was treated as a model complex for a range of different α-diimine transition metal carbonyls. The potential energy curves for the Re-H bond elongation were reproduced for the ground state, low-lying MLCT states and a ^{3}SBLCT state that was also believed to play a meaningful part in the photochemistry of this system through a ^{1}MLCT to ^{3}SBLCT intersystem crossing that promotes the homolysis of the Re-H bond. Wavepacket propagation dynamics were applied to the system to obtain the 1D emission spectra. The researchers were able to describe adequately the features of the spectra that represented these two photo-activated processes, even though higher accuracy calculations are needed to describe the competition between the photoproducts.

Vallet *et al* investigated the electronic spectroscopy of two other complexes $H_2M(CO)_4$ (M=Fe,Os) [22].

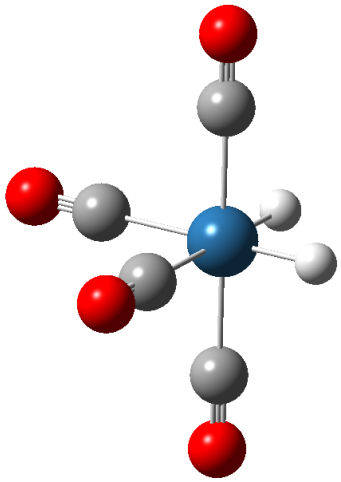

Figure 1.11: $H_2M(CO)_4$, discussed in [22].

They looked into both singlet and triplet low-lying excited states of both complexes using a two-step approach. Firstly, they used state-averaged

CASSCF and CASPT2 calculations to get the spin-free energies of the first eight electronic excited states of singlet and triplet spin of A_1, B_1 and B_2 symmetry in C_{2v}. The next step involved using SO-CI (uncontracted spin-orbit configuration interaction) and the researchers looked into the spin-orbit interactions between the various spin states. It was concluded that the absorption wavelength was not widely influenced by SO-CI, although osmium absorption spectrum was more affected than iron.

Higher hierarchy methods like CASSCF and CASPT2 were also chosen to investigate the spectra of two cobalt-based complexes $RCo(CO)_4$ (R=H,CH_3) [23]. State-of-the-art methods were chosen to study the electronic spectra of these hydrides and compared with femtosecond laser control spectroscopy. The authors found that both complexes absorbed at around 4.33 eV and both had a strong band centred at 4.95 eV. It was found out that SBLCT and MLCT states contributed to these bands in agreement with the experimental assignment. They also concluded that due to their similarities in the spectra, their photoreactivity would also be quite similar. Daniel *et al* studied the MLCT states for the trans-cis photoisomerization of the styrylpyridine ligand in $[Re(CO)_3$(2,20-bipyridine) (t-4-styrylpyridine)$]^+$ [24]. For the ground state they used DFT methods to optimize the possible trans and cis isomers, with a barrier of 113 kJ/mol. CASSCF, CASPT2 and TD-DFT were used to calculate the electronic spectra of these isomers. The low-lying states correspond to a MLCT transition with a singlet intraligand state nearby. Another part of the study included calculations using CASSCF as a function of the C-C bond torsion angle on the styrylpyridine ligand. It was found that the states that were important for the photoisomerization of the styrylpyridine ligand were different between the free ligand and the complex form. For the free ligand the singlet intraligand state determined the mechanism. In the complex this happened through a triplet intraligand state. The same kind of methods were also used to compute the photochemistry of $CH_3Mn(CO)_5$.

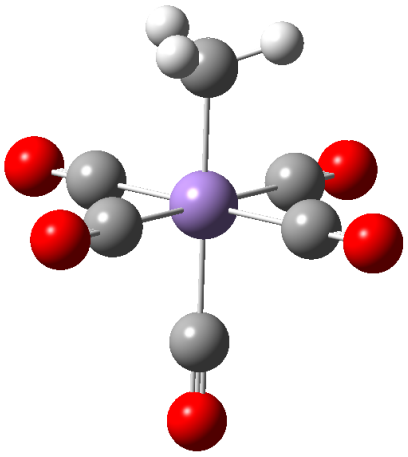

Figure 1.12: $CH_3Mn(CO)_5$.

The authors tried to characterize the electronic excited states calculated with experiments (in solvent). The results showed that the carbonyl ligand was lost preferentially to the methyl ligand following excitation above 4.02 eV. The character of the excited states showed a MLCT trend (metal 3d to π^*) and a large density of these states was present between 4.69 eV and 6.01 eV. This complex was considered very demanding since there were several minor channels for the dissociation.

Similar complexes to $RCo(CO)_4$ were also studied by this group [25]. Both the singlet and triplet states were discussed and time-dependent wavepacket propagation was used as a function of both Co-CO (axial) and Co-R bond cleavages. There were two major peaks found for the absorption spectrum of each complex and were assigned to MLCT (metal 3d to ligand π^*) states as before. In both complexes a photoactive metal to σ bond charge transfer (MSBCT) and metal charged transfer states resulted in either Co-CO (axial) or Co-R bonds.

Villaume *et al* applied EOM-CCSD to smaller transition metal complexes ($NiCH_2^+$), as well as the rhenium-based complex, CH_3ReO_3 [26]. They used a similar approach to their previous work and performed 1D wavepacket propagation studies for the lowest singlet and triplet states. The authors found that TD-DFT results with the PW91 func-

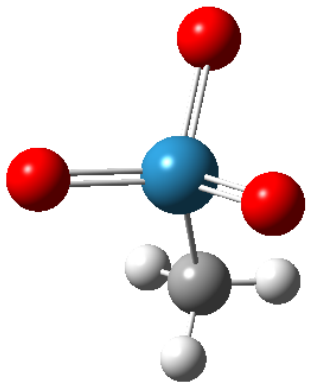

Figure 1.13: CH_3ReO_3, discussed in [26].

tional provided an excellent agreement with experimental spectra, while CASSCF and CASPT2 were unable to improve on this. Experimentally the lowest observed transition was associated to a LMCT state from an oxygen p orbital to a d orbital on the rhenium atom. The second and third transitions were also LMCT states. The wavepacket propagation for the low-lying singlet and triplet states found that the lowest state was the initial absorbing state that was of $^1A_1$ symmetry. This state was coupled non-adiabatically to the lowest bright state of ^1E symmetry with the state responsible for the homolysis of the Re-CH_3 bonding, $^3A_1$. Following population of the initial absorbing state the two latter states were found to be populated within a few tens of femtoseconds, with an intersystem crossing controlling the photodissociation. Recent studies have looked at the photoisomerization mechanisms of rhenium(I) complexes with ligands larger than the ones discussed above e.g., diimine complexes [27, 28, 29, 30]. For these, spin-orbit coupling is a big contributor to the photoisomerization mechanism and interplays between the singlet and triplet states.

Tom Ziegler and co-workers have performed extensive studies on the photochemistry of transition metal complexes. They have developed a method for studying accurately the UV-vis spectra of molecules with spatially degenerate ground states, applied to d^1 and d^2 transition metal complexes with either tetrahedral or octahedral symmetry [31]. This

method is called TRICKSTDDFT ('transforms reference via an intermediate configuration Kohn-Sham TD-DFT'). It was implemented to remove the difficulties when dealing with multireference ground sates. This method replaced the ground state with a non-degenerate excited state with similar properties to the calculated system. After benchmarking it, they found that the agreement with experimental results was very good. One issue raised by the authors was that in some cases the calculated transition densities were made for states that were not spin eigenfunctions. A way to counteract this problem was to use a SCF sum method.

An example of those type of systems reported by Ziegler and co-workers in which they performed a TD-DFT study of the platinum (II) complexes $[PtCl_4^{2-}]$, $[PtBr_4^{2-}]$ and $[Pt(CN)_4^{2-}]$. They were all reported to have square planar geometry [32].

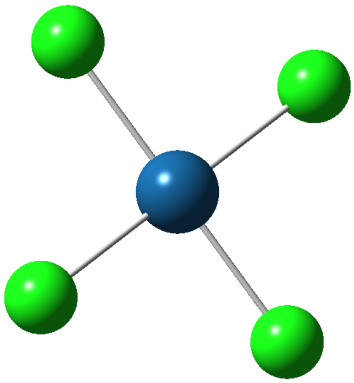

Figure 1.14: $Pt(Cl)_4^{2-}$, discussed in [32].

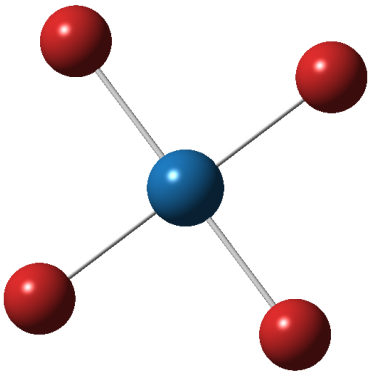

Figure 1.15: $Pt(Br)_4^{2-}$, discussed in [32].

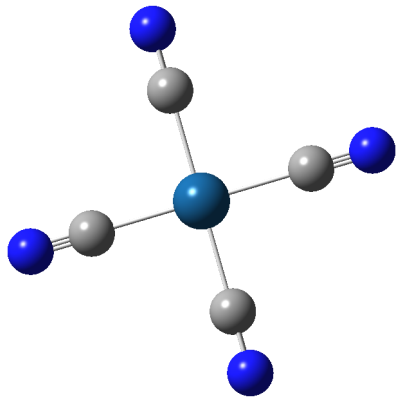

Figure 1.16: $Pt(CN)_4^{2-}$, discussed in [32].

The systems evaluated were all Pt $5d^8$ closed-shell and the transitions studied originated out of the 5d orbitals of the platinum. The authors noticed that these transitions are susceptible to spin-orbit coupling effects. Once again good agreement with experimental results was obtained.

Another paper that used TD-DFT looks at the ligand field states of $[Co(en)_3]^{3+}$ and $[Rh(en)_3]^{3+}$ and the lowest energy states of $[Fe(phen)_3]^{2+}$ (en=ethylenediamine and phe=1,10-phenanthroline) [33]. The authors studied the circular dichroism of these states and focused on the impact of charge transfer corrections in 3d transition metal complexes. A range of different density functionals was tried for each complex and it was noted that the excitation energies were very sensitive to the choice of functional, whereas it was the opposite for spectral intensities. It was also found that the iron complex studied here had a dense spectrum that made it difficult to assess the accuracy of the theoretical spectrum due to a complicated interplay between the ability of a functional to optimize not only the ground state geometry of the complex accurately, but also the different types of excitations present in the spectrum.

The amount of data and information gathered for this field of study over the years is extensive with a lot of new and important systems being researched and analysed in depth in recent years. In this introduction the systems discussed are illustrative of the rich results that can be ob-

tained by computational studies of inorganic excited states.

The last part of this thesis (Chapter 8) consists of a bottom-up approach to intermolecular aggregates. This area has been considered very important lately due to its multichromophoric self-assembly and pH dependency. The interest in these kind of structures grew a lot in the past, due to the capability of these systems to be used as sensing or selective binding agents, some examples are [34, 35, 36, 37, 38, 39, 40]. Although the electronic structure of these structures is not as demanding, their size sometimes makes theoretical investigations challenging.

Bibliography

[1] Schreiber, M.; Silva-Junior, M. R.; Sauer, S. P. A.; Thiel, W. *J. Chem. Phys.* **2008**, *128*(13), 134110.

[2] Silva-Junior, M. R.; Sauer, S. P.; Schreiber, M.; Thiel, W. *Mol. Phys.* **2010**, *108*(3-4), 453–465.

[3] Paterson, M. J.; Christiansen, O.; Pawłowski, F.; Jørgensen, P.; Hättig, C.; Helgaker, T.; Sałek, P. *J. Chem. Phys.* **2006**, *124*(5), 054322.

[4] Langmuir, I. *Science* **1921**, *54*(1386), 59–67.

[5] Dewar, M. *Bull. Soc. Chim. Fr.* **1951**, *18*, C79.

[6] Chatt, J.; Duncanson, L. A. *J. Chem. Soc.* **1953**, pages 2939–2947.

[7] Gray, H. B.; Beach, N. A. *J. Am. Chem. Soc.* **1963**, *85*(19), 2922–2927.

[8] McKinlay, R.; Paterson, M. In *The Jahn-Teller Effect*; Köppel, H., Yarkony, D. R., Barentzen, H., Eds., Vol. 97 of *Springer Series in Chemical Physics;* Springer Berlin Heidelberg, 2009; pages 311–344.

[9] Mckinlay, R. G.; Żurek, J. M.; Paterson, M. J. In *Theor. Comp. Inorg. Chem.*; van Eldik, R., Harvey, J., Eds., Vol. 62 of *Advances in Inorganic Chemistry;* Academic Press, 2010; pages 351–390.

[10] Aarnts, M. P.; Stufkens, D. J.; Solá, M.; Baerends, E. J. *Organometallics* **1997**, *16*(11), 2254–2262.

[11] Wilms, M. P.; Baerends, E. J.; Rosa, A.; Stufkens, D. J. *Inorg. Chem.* **1997**, *36*(8), 1541–1551.

[12] Rosa, A.; Ricciardi, G.; Baerends, E. J.; Stufkens, D. J. *Inorg. Chem.* **1995**, *34*(13), 3425–3432.

[13] van Gisbergen, S. J. A.; Groeneveld, J. A.; Rosa, A.; Snijders, J. G.; Baerends, E. J. *J. Phys. Chem. A* **1999**, *103*(34), 6835–6844.

[14] Pollak, C.; Rosa, A.; Baerends, E. J. *J. Am. Chem. Soc.* **1997**, *119*(31), 7324–7329.

[15] Kühn, O.; Hachey, M.; Rohmer, M.; Daniel, C. *Chem. Phys. Lett.* **2000**, *322*(3–4), 199–206.

[16] Zalliš, S.; Ben Amor, N.; Daniel, C. *Inorg. Chem.* **2004**, *43*(25), 7978–7985.

[17] McKinlay, R. G.; Paterson, M. J. *J. Phys. Chem. A* **2012**, *116*(37), 9295–9304.

[18] Goumans, T. P. M.; Ehlers, A. W.; van Hemert, M. C.; Rosa, A.; Baerends, E.-J.; Lammertsma, K. *J. Am. Chem. Soc.* **2003**, *125*(12), 3558–3567.

[19] Gunaratne, T. C.; Gusev, A. V.; Peng, X.; Rosa, A.; Ricciardi, G.; Baerends, E. J.; Rizzoli, C.; Kenney, M. E.; Rodgers, M. A. J. *J. Phys. Chem. A* **2005**, *109*(10), 2078–2089.

[20] Zakrzewski, J.; Delaire, J. A.; Daniel, C.; Cote-Bruand, I. *New J. Chem.* **2004**, *28*, 1514–1519.

[21] Villaume, S.; Daniel, C. *Cr. Acad. Sci. II. C. Cr.* **2005**, *8*(9–10), 1453–1460.

[22] Vallet, V.; Strich, A.; Daniel, C. *Chem. Phys.* **2005**, *311*(1–2), 13–18.

[23] Ambrosek, D.; Villaume, S.; González, L.; Daniel, C. *Chem. Phys. Lett.* **2006**, *417*(4–6), 545–549.

[24] Bossert, J.; Daniel, C. *Chem-Eur J.* **2006**, *12*, 4835–4843.

[25] Ambrosek, D.; Villaume, S.; Daniel, C.; González, L. *J. Phys. Chem. A* **2007**, *111*(22), 4737–4742.

[26] Villaume, S.; Daniel, C.; Strich, A.; Perera, S. A.; Bartlett, R. J. *J. Chem. Phys.* **2005**, *122*(4), 44313.

[27] Kayanuma, M.; Gindensperger, E.; Daniel, C. *Dalton Trans.* **2012**, *41*(42), 13191–13203.

[28] Kayanuma, M.; Daniel, C.; Köppel, H.; Gindensperger, E. *Coord. Chem. Rev.* **2011**, *255*(21-22), 2693–2703.

[29] Gindensperger, E.; Köppel, H.; Daniel, C. *Chem. Comm.* **2010**, *46*(43), 8225–8227.

[30] Baková, R.; Chergui, M.; Daniel, C.; Jr., A. V.; Záliš, S. *Coord. Chem. Rev.* **2011**, *255*(7-8), 975–989.

[31] Seth, M.; Ziegler, T. *J. Chem. Phys.* **2005**, *123*(14), 144105.

[32] Wang, F.; Ziegler, T. *J. Chem. Phys.* **2005**, *123*(19), 194102.

[33] Rudolph, M.; Ziegler, T.; Autschbach, J. *Chem. Phys.* **2011**, *391*(1), 92–100.

[34] Swinburne, A.; Paterson, M.; Fischer, K.; Dickson, S.; Wallace, E.; Belcher, W.; Beeby, A.; Steed, J. *Chem-Eur J.* **2010**, *16*(5), 1480–1492.

[35] Swinburne, A.; Paterson, M.; Beeby, A.; Steed, J. *Chem-Eur J.* **2010**, *16*(9), 2714–2718.

[36] Swinburne, A. N.; Paterson, M. J.; Beeby, A.; Steed, J. W. *Org. Biomol. Chem.* **2010**, *8*(5), 1010–1016.

[37] Barnard, A.; Dickson, S. J.; Paterson, M. J.; Todd, A. M.; Steed, J. W. *Org. Biomol. Chem.* **2009**, *7*(8), 1554–1561.

[38] Filby, M. H.; Dickson, S. J.; Zaccheroni, N.; Prodi, L.; Bonacchi, S.; Montalti, M.; Paterson, M. J.; Humphries, T. D.; Chiorboli, C.; Steed, J. W. *J. Am. Chem. Soc.* **2008**, *130*(12), 4105–4113.

[39] Dickson, S. J.; Wallace, E. V.; Swinburne, A. N.; Paterson, M. J.; Lloyd, G. O.; Beeby, A.; Belcher, W. J.; Steed, J. W. *New J. Chem.* **2008**, *32*(5), 786–789.

[40] Dickson, S.; Paterson, M.; Willans, C.; Anderson, K.; Steed, J. *Chem-Eur J.* **2008**, *14*(24), 7296–7305.

Chapter 2

Methods

(Note that all the citations of functionals or basis sets will only be used once.)

Computational chemistry is a rapidly developing subfield of theoretical chemistry. The main goal is to describe chemically related problems using high performance calculations. Note that computers do not solve problems but people do, so some care must be taken when analysing any kind of results obtained. Calculations that ten years ago would take years to complete, now can be done in ten or twenty minutes. The real strength of computational chemistry is the ability of generating data that the scientist can then evaluate and process.

Before the development of quantum chemistry everything was solved in a classical way (classical mechanics), with the laws of motion introduced by Isaac Newton. They were able to predict the movements of objects such as planets. However, in the end of the nineteenth century, experimental evidence showed that classical mechanics failed on small systems like electrons. At the beginning of the 20^{th} century scientists started noticing a lot of effects that could not been described by classical physics, for example black-body radiation and electron diffraction.

In 1926, Erwin Schrödinger proposed an equation for finding the absolute energy of any molecular system. It allowed us to solve a one

electron system analytically, for example the case of the hydrogen atom. For other cases, numerical approximations have to be implemented to solve it. The non-relativistic time-independent Schrödinger equation is:

$$\hat{H}\Psi_i = E\Psi_i \tag{2.1}$$

where E is the absolute energy of the system and Ψ_i the wavefunction. $\hat{H}$ is an operator (Hamiltonian), relating to the absolute energy of a molecular system of N electrons and M nuclei:

$$\hat{H} = -\sum_{i=1,N} \frac{\hbar^2}{2m_e} \bigtriangledown_i^2 - \sum_{i=1,M} \frac{\hbar^2}{2m_{nuc}} \bigtriangledown_i^2 - \sum_{i=1,M} \sum_{j=1,N} \frac{Z_i e^2}{4\pi\epsilon_0 |\vec{r}_j - \vec{R}_i|} + \sum_{i<j=1,M} \frac{Z_i Z_j e^2}{4\pi\epsilon_0 |\vec{R}_j - \vec{R}_i|} + \sum_{i<j=1,N} \frac{e^2}{4\pi\epsilon_0 |\vec{r}_i - \vec{r}_j|} \tag{2.2}$$

$\hbar$ is equal to:

$$\hbar = \frac{h}{2\pi} = 1.05457 * 10^{-34}\text{J.s} \tag{2.3}$$

In equation 2.2, m corresponds to the mass (electrons or nuclei), e is the elementary charge, $\vec{r}$ and $\vec{R}$ are the electronic and nuclear positions, and Z is the nuclear charge. The first and second terms correspond to the kinetic energy of the system for electrons and nuclei, the third describes the nuclear-electron attraction. The fourth and fifth terms are repulsive and portray the nuclear-nuclear and electron repulsion.

A wavefunction has to be continuous, have a continuous first derivative, is single-valued, and is square-integrable. The interpretation of the wavefunction in terms of location of a single particle is based on a suggestion made by Max Born, a German-English physicist. He found that if the wavefunction of a particle has the value Ψ at some point r, then the probability of finding the particle in an infinitesimal volume $d\tau = dxdydz$ at that point is proportional to $|\Psi|^2 d\tau$.

$$|\Psi|^2 = \Psi^* \Psi \tag{2.4}$$

The value of $|\Psi|^2$ is proportional to the probability of finding the particle in a region around that point. This way it is possible to say that $|\Psi|^2$ is the probability density.

2.1 Born-Oppenheimer approximation

The movement of electrons is much faster than nuclei due to their mass discrepancy, the lightest of these (the proton) is around 1836 heavier than the electron. The nuclei experience an averaged electronic motion, since they are not fast enough to respond to electron movement instantaneously. Due to this, the kinetic energy of the nuclei can be left out and evaluated after the electronic motion. The electronic Hamiltonian can be described as:

$$\hat{H}_{el}(\vec{r};\vec{R}) = -\sum_{i=1,N} \frac{\hbar^2}{2m_e} \bigtriangledown_i^2 - \sum_{i=1,M} \sum_{j=1,N} \frac{Z_i e^2}{|\vec{r}_j - \vec{R}_i|} + \sum_{i<j=1,M} \frac{Z_i Z_j e^2}{|\vec{R}_j - \vec{R}_i|} + \sum_{i<j=1,N} \frac{e^2}{|\vec{r}_i - \vec{r}_j|} \tag{2.5}$$

The full Hamiltonian can be described as kinetic energy and potential energy acting on nuclear coordinates:

$$\hat{H}_T(\vec{r},\vec{R}) = \hat{T}_N(\vec{R}) + \hat{H}_e(\vec{r};\vec{R}) \tag{2.6}$$

Equation 2.6 is composed of two different parts, the nuclear kinetic energy $\hat{T}_N$ that acts on nuclear coordinates $\vec{R}$ and the electronic Hamiltonian that is defined above. The latter acts on the electronic coordinates, resulting from the clamping of the nuclei to fixed positions. The components still depend on position of the fixed position of the nuclei, but it has been reduced to a second-order differential equation in *3N* electron coordinates. So, considering the nuclei static, the electronic Hamilto-

nian can then be solved resulting in an eigenvalue problem:

$$\hat{H}_e \Psi_i^e(\vec{r};\vec{R}) = V_i(\vec{R})\Psi_i^e(\vec{r};\vec{R}) \tag{2.7}$$

where Ψ_i^e is the so called adiabatic electronic wavefunction. Each eigenvalue $V_i(\vec{R})$, is dependent on the fixed nuclear coordinates. This is called the adiabatic potential energy surface for any given state. The total molecular wavefunction is shown in Equation 2.8.

$$\Psi_T(\vec{r},\vec{R}) = \sum_{i=1}^{\infty} \Psi_i^n(\vec{R})\Psi_i^e(\vec{r};\vec{R}) \tag{2.8}$$

The Born-Oppenheimer approximation is of particular importance in molecular quantum mechanics, allowing scientists to calculate energies of molecules. The Born-Oppenheimer approximation can be obtained by neglecting the off-diagonal terms ($i \neq j$) that couple the nuclei and electrons and the diagonal term ($\langle \chi_i^e | \bigtriangledown_n^2 | \Psi_i^e \rangle$) and Equation 2.9 to obtain,

$$\hat{T}_N(\vec{R})\Psi_i^n + V_i(\vec{R})\Psi_i^n = E_{tot}\Psi_i^n \tag{2.9}$$

This approximation breaks down when there is coupling of nuclei and electronic motion, for example in the case of conical intersections (see Chapter 7). For these the non-diagonal terms cannot be neglected. These terms are called the first and second order non-adiabatic coupling. They are the coupling between different electronic states through the motion of the nuclei. The first-order term is the fundamental one since it deals with non-adiabatic problems, and the second-order term can be written in terms of it. In equation 2.10 the first-order non-adiabatic coupling is shown:

$$\langle \Psi_j^e | \bigtriangledown_N | \Psi_i^e \rangle = \frac{\langle \Psi_j^e | \frac{\partial \hat{H}_e}{\partial R} | \Psi_i^e \rangle}{V_j - V_i} \tag{2.10}$$

This coupling is dependent on the inverse difference between the electronic eigenvalues (E_i and E_j). So, when these two points become de-

generate the coupling has a singularity. Calculating this coupling is fundamental for the calculation of conical intersections, and to obtain the magnitude of Jahn-Teller couplings as discussed in the next section.

2.2 Conical Intersections

In 1929 John von Neumann and Wigner performed mathematical calculations and came to the conclusion that any electronic degeneracy could originate a conical intersection [1]. When applied to diatomic molecules, it was found that two electronic states could not cross if they had the same symmetry. Later Teller started studying this curious effect and realized that for polyatomic molecules there was a space in which they could intersect with a dimension of *n-2*, where n represented the number of vibrational degrees of freedom [2]. The two remaining degrees of freedom compose the gradient difference vector ($\vec{x}_1$) and the derivative coupling vector ($\vec{x}_2$), see Equations 2.11 and 2.12.

$$\vec{x}_1 = \frac{\partial(E_1 - E_2)}{\partial \vec{R}} \tag{2.11}$$

$$\vec{x}_2 = \langle \vec{C}_2^t | \left(\frac{\partial \hat{H}_e}{\partial \vec{R}} \right) | \vec{C}_1 \rangle \tag{2.12}$$

In equation 2.11 E_1 and E_2 are the energy of two electronic states and $\vec{R}$ is the vector that varies with the nuclear cartesian displacements. In equation 2.12 $\vec{C}_1$ and $\vec{C}_2$ are the eigenvectors of the Schrödinger equation. The degeneracy of any system can be lifted by the any infinitesimal movement of these vectors that compose the branching space [3]. These vectors are fundamental to show how the system goes from the upper to the lower surface and shows the typical photochemical funnel (see photochemistry section).

There are different types of cones that can arise from conical intersections and two examples are shown in Figure 2.1. When studying chemical systems one can come across these phenomena by studying

any molecular system with degenerate energetic levels. Two of the most typical conical intersection arrangements are: the tilted one, where gradient vectors on the upper and lower surfaces point in the same direction, and the circular one. The last one is the most typical for inorganic cases, some of these will be discussed further in Chapter 7.

The intersection space represents the orthogonal space relative to the branching space, the dimension of which is $3N$-8, where N is the number of nuclei. A few articles describing this phenomenon have emerged over the past few years [4] [5] [6].

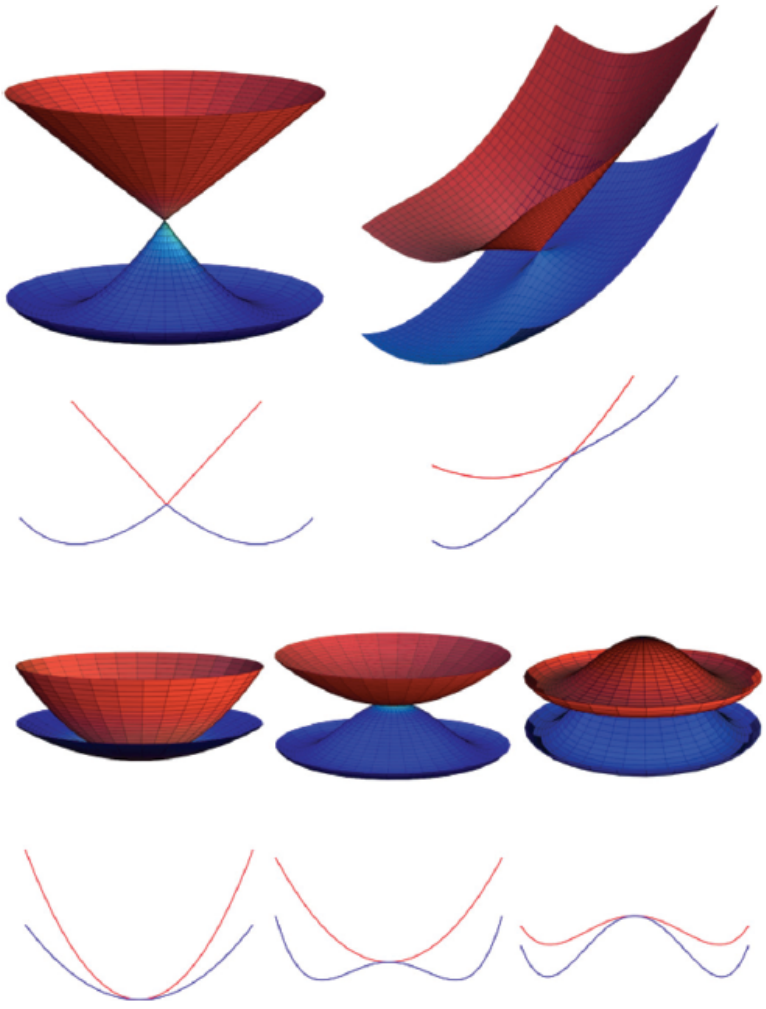

Figure 2.1: Different types of a) conical intersections (top) and b) Renner-Teller (bottom). Adapted from: Mckinlay, R.G.; Żurek J. M.;Paterson, M. J., Theoretical and Computational Inorganic Chemistry **2010**, 62 351-390.

2.2.1 The Jahn-Teller effect

The Jahn-Teller effect has been subject of study for at least eighty years and a lot of new applications and data have been found for this effect more recently [7] [8]. The Jahn-Teller effect has wide ranging implications that include molecular physics, theoretical/computational chemistry and solid state physics. In their original paper, Jahn and Teller proved that orbitally degenerate states are energetically unstable. Such degenerate states are necessarily conical intersections between the components of the state.

The vibrations that lift the degeneracy can be identified having the symmetry of the square of the degenerate electronic state irreducible representation with itself [9]. It was found that there is always one vibrational mode (non-totally symmetric) that lifts the degeneracy of the electronic state and lowers the symmetry of the molecule. Typical nomenclature for this phenomena is for example $T_2 \otimes e$, which means that the triply degenerate T_2 state breaks the degeneracy via an e vibration. Since the beginning, the Jahn-Teller effect has been used to predict symmetry problems and has helped figuring out molecular properties of transition metal complexes. More recently it has been applied to the field of photochemistry using time-resolved spectroscopy. It is possible to drive an excited-state to the ground through a conical intersection, for example a photodissociaton case, some examples follow [10, 11, 12, 13, 14].

2.3 Electronic structure methods

When describing the electron distribution quantum mechanics is a necessity. As it was mentioned before, classical physics fails to describe most of the important effects that take place at the electronic level. The motion of any many-electron chemical system is very complex. The number of interactions among the particles are very difficult to account for. Independent particle models are the simplest description of a system. The Schrödinger equation gets simplified, because the interaction among the

particles is either non-existent or is averaged some way.

The Hartree–Fock (HF) method is a method of approximation for the determination of the ground-state wavefunction and ground-state energy of a quantum many-body system. The origin of the Hartree–Fock method dates back to the end of the 1920s, soon after the derivation of the Schrödinger equation in 1926. The Hartree-Fock (HF) equations, were developed as non-linear differential-integral equations, that could be solved using numerical methods. Before computers appeared, it had been impossible to solve the Hartree-Fock equations for more than few electron systems.

When considering electrons it is possible to think of them to have a spin quantum number of $\frac{1}{2}$ and when submitted to the presence of a magnetic field it can align along or opposite to the same (α or β spin). In the Hartree-Fock model the total wavefunction is described by a product of orbitals. The electrons are described by a spin-orbital (a product of a spatial and a spin function), that generates an eigenvalue problem in the form of:

$$f|\chi_a\rangle = \epsilon_a|\chi_a\rangle \tag{2.13}$$

In equation 2.13, f is the Fock operator and consists of:

$$f(1) = h(1) + \sum_i (J_i(1) - K_i(1)) \tag{2.14}$$

this corresponds to the sum of the core-Hamiltonian operator h(1) and as well as an effective electron potential operator called the Hartree-Fock potential $\nu^{HF}(1)$.

$$\nu^{HF}(1) = \sum_i (J_i(1) - K_i(1)) \tag{2.15}$$

This term is equal to $\sum_i^{N/2} 2\, J_i$-K_i for closed-shell systems. J_i and K_i are the Coulomb and exchange operators. Electrons are fermions since

their spin is $\frac{1}{2}$, so their overall wavefunction must be antisymmetric to particle interchange (including spin). χ_i and χ_j in Equation 2.16 are spin-orbitals. Adding one electron to χ_i and χ_j both are occupied and can be arranged these two ways. A wavefunction can be built with no distinction between electrons, using an appropriate linear combination between the two products and adding a normalization constant:

$$\Psi(x_1, x_2) = 2^{-1/2}(\chi_i(x_1)\chi_j(x_2) - \chi_j(x_1)\chi_i(x_2)) \tag{2.16}$$

In Equation 2.16 the minus sign makes sure that $\Psi(x_1, x_2)$ is antisymmetric considering the interchange of coordinates, so:

$$\Psi(x_1, x_2) = -\Psi(x_2, x_1) \tag{2.17}$$

this can be written as a determinant, the Slater determinant:

$$\Psi(x_1, x_2) = 2^{-1/2} \begin{vmatrix} \chi_i(x_1) & \chi_j(x_1) \\ \chi_i(x_2) & \chi_j(x_2) \end{vmatrix}$$

which for an N-electron system can be generalized as:

$$\Psi(x_1, x_2, ..., x_N) = (N!)^{-1/2} \begin{vmatrix} \chi_i(x_1) & \chi_j(x_1) & ... & \chi_k(x_1) \\ \chi_i(x_2) & \chi_j(x_2) & ... & \chi_k(x_2) \\ \vdots & \vdots & & \vdots \\ \chi_i(x_N) & \chi_j(x_N) & ... & \chi_k(x_N) \end{vmatrix}$$

This Slater determinant has N-electrons that are distributed in n spin-orbitals without specifying which electron is in which orbital. This principle also implies that interchanging the coordinates of two electrons, changes the sign of the determinant. No more than one electron can occupy any given orbital since it would violate Pauli's principle. This antisymmetrizing property generates an exchange effect. This way it can be inferred that the Slater determinant incorporates exchange-correlation, which allows two electrons with the same spin to correlate to each other. In this method electrons with opposite spin are not correlated to each other so they are considered to have an uncorrelated wavefunction.

Figure 2.2 represents the evolution of Hartree-Fock and some of the methods available nowadays in increasing order of computational cost. Multireference methods have to be used carefully because a wrong choice of basis set or active space can lead to very costly calculations and sometimes not the best outcome. All of these will be discussed in the following sections.

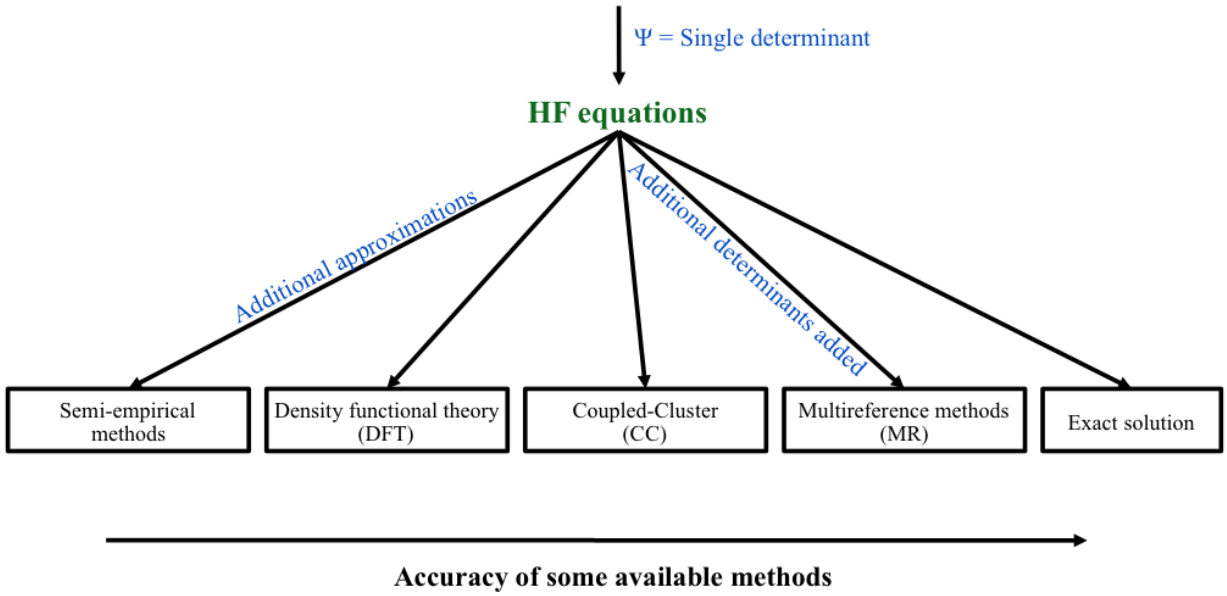

Figure 2.2: Evolution since Hartree-Fock.

2.3.1 The self-consistent field (SCF) procedure

In 1927, D.R. Hartree introduced a procedure, which he called the self-consistent field method, to calculate approximate wavefunctions and energies for atoms and ions. Hartree was guided by some earlier, semi-empirical methods of the early 1920s (by *E. Fues, R. B. Lindsay, and himself*) set in the old quantum theory of Bohr. The Hartree-Fock equations generated a set of pseudo-eigenvalue equations as the Fock operator depended on all the occupied MOs, using the Coulomb and exchange operators. A specific Fock orbital could only be determined if all the other occupied orbitals were known, and iterative methods must therefore be

employed for solving the problem. A set of functions that are a solution to $F\psi = \epsilon\psi$ are called self-consistent field (SCF) orbitals. The canonical MOs may be considered as a convenient set of orbitals for carrying out the variational calculation. The total energy, however, depends only on the total wavefunction, which is a Slater determinant written in terms of the occupied molecular orbitals.

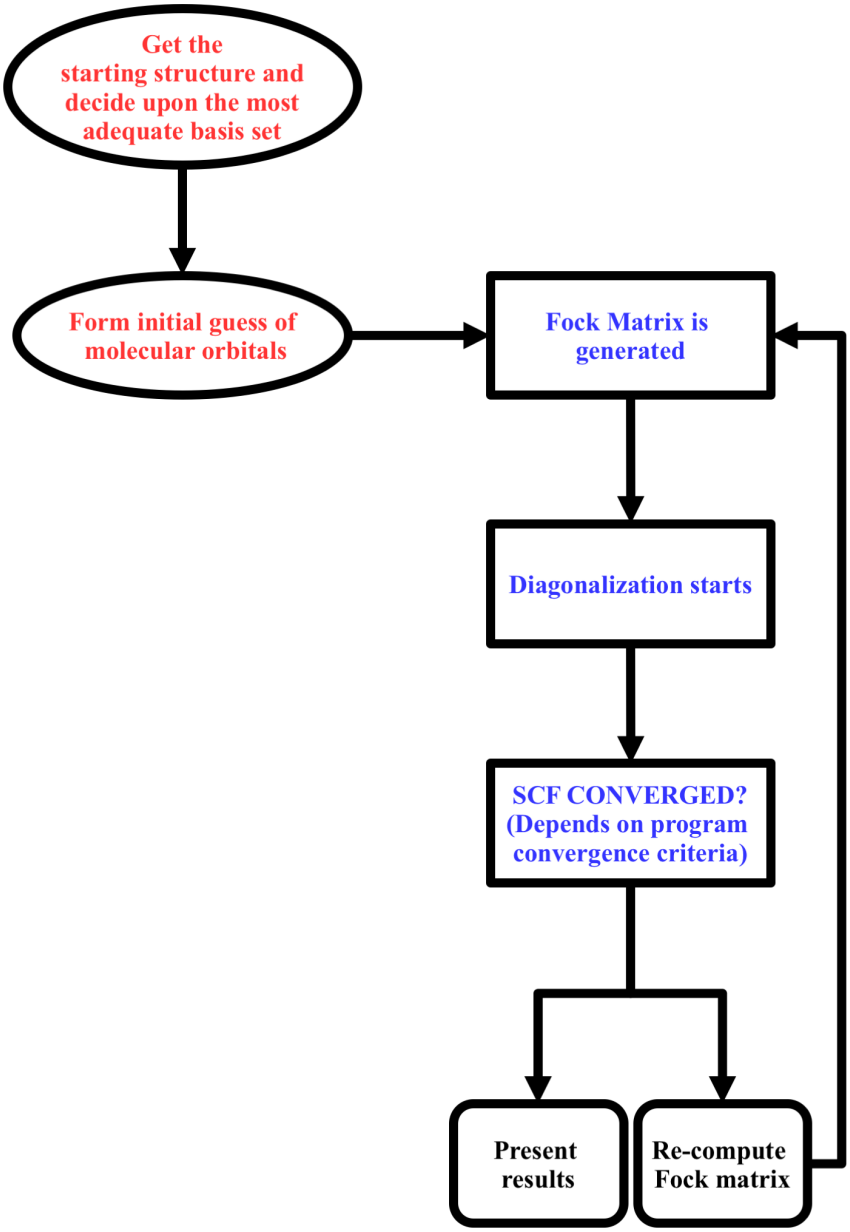

Figure 2.3: Self-consistent field procedure.

Figure 2.3 shows the standard procedure of a self-consistent field in Hartree-Fock theory. Starting with a geometry, an initial guess of molecular orbitals is formed. After this step a Fock matrix is generated and diagonalized. This cycle keeps going until it reaches a solution for the variational problem, i.e the energy is stationary and the molecular orbitals do not change.

2.3.2 Koopmans' theorem

Given a system with N-electrons, a single determinant ($|^N\Psi_0\rangle$) is constructed using Hartree-Fock theory, with occupied and virtual (unoccupied) spin-orbital energies (ϵ_a and ϵ_r). Koopmans' theorem equates the energy of the HOMO (highest occupied molecular orbital) with the negative of the ionization potential. This procedure removes an electron from χ_a and equates the electron affinity for $(N+1)$ electron single determinant $|^{N+1}\Psi^r\rangle$, that has identical spin-orbitals, by adding an electron to a spin-orbital χ_r. This theorem provides insight into approximate ionization potentials and electron affinities. There is a small error associated for not allowing the orbitals to relax for $|^{N-1}\Psi^r\rangle$ or $|^{N+1}\Psi^r\rangle$. Generally Koopmans' theorem provides reasonable results for ionization potentials, although the affinities calculated are not usually accurate.

2.3.3 Slater-Condon rules

The Slater-Condon rules were developed to represent one and two body operators that span over the wavefunctions when using Slater determinants and orthonormal orbitals. These rules are used in deriving any methods that solve the Schrödinger's equation using Slater determinants.

In the end of 1929 John Slater derived expressions for diagonal matrix elements of approximate Hamiltionians and in 1930, Condon used these expressions and extended them to non-diagonal terms. Since the Hamiltonian operator consists of a sum of the one and two-electron operators,

if two determinants differ by more than two molecular orbitals, there is always at least one overlap that is zero. This important finding means that when analysing a CI (described later) matrix, the terms will only be non-zero if two determinants differ by zero, one or two molecular orbitals.

2.3.4 Restricted and unrestricted Hartree-Fock

So far, there are no restrictions to the construction of the molecular orbitals used to build a wavefunction. The restricted Hartree-Fock (RHF) wavefunction, restricts the spatial part of the orbitals to be the same for each spin, where the system corresponds to a closed-shell system with all orbitals doubly occupied.

UHF allows different spatial orbitals for each electron of either spin type. The restricted approach applies constraints on the variation parameters, so the final energy calculated by each method is usually different. UHF has always the same or lower energy than ROHF approach, for example the case where an unpaired electron has α spin and it will interact differently with other α and β spins, so the optimum α and β orbitals will be different. One disadvantage of the UHF approach is the fact that it is not an eigenfunction of the S^2 operator, so it has contributions from higher lying spins (quartet, sextet, octet). These contributions are considered non-physical and affect the result, so this spin contamination is always a key factor to take into account when performing calculations on open-shell systems using UHF. Figure 2.4 summarizes what has been discussed.

2.4 Basis sets

2.4.1 Slater basis set

Basis sets are fundamentally important for computational chemistry. They will influence any result of a computational calculation. The HF

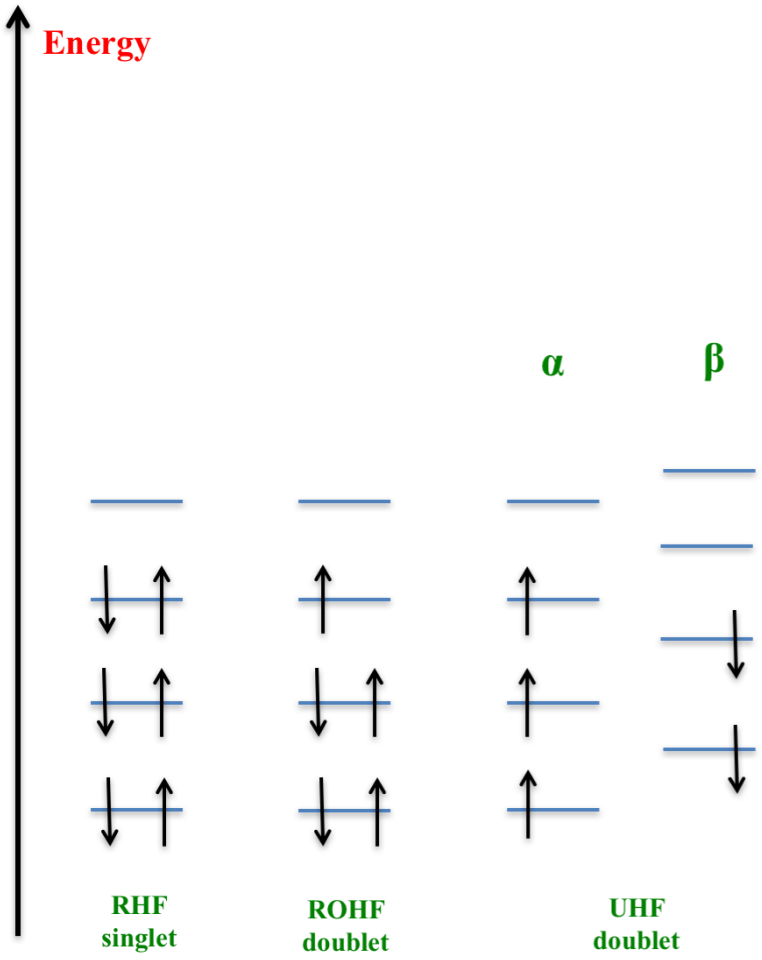

Figure 2.4: Differences between RHF, ROHF and UHF.

molecular orbitals are expanded in a basis (i.e. as a linear combination of atomic orbitals (LCAOs)). A basis expansion of each molecular orbital can be written as,

$$\Phi_i = \sum_{\mu=1}^{n} C_{\mu i}\chi_\mu \tag{2.18}$$

In Equation 2.18, Φ_i corresponds to the i-th molecular orbital and $C_{\mu i}$ to the coefficient of the linear combination that is determined by the SCF procedure explained in the previous section. χ_μ is the μ-th atomic orbital and n the number of atomic orbitals (basis functions). A selection of basis sets is based on different factors. One of the first choices for basis sets, was to use Slater orbitals. Unfortunately, the Slater functions are not very easy to implement in molecular orbital calculations,

Equation 2.19. This is due to some mathematical difficulties, particularly when the atomic orbitals are centred on different atoms. Slater basis functions have a lot of advantages, for example they are able to describe radial behaviour more accurately as shown in Figure 2.5.

$$\Phi^{Slater} = x^a y^b z^c e^{(-\alpha r)} \tag{2.19}$$

2.4.2 Gaussian type orbitals (GTO)

It is common in *ab initio* calculations to substitute Slater orbitals for Gaussians. GTOs were introduced to overcome the intractability of Slater basis sets. A Gaussian function is shown in Equation 2.20.

$$\Phi^{Gaussian} = x^a y^b z^c e^{(-\alpha r^2)} \tag{2.20}$$

The most flexible way to use Gaussian functions in molecular orbital calculations is to allow the coefficients and exponents to vary during the calculation. GTOs can be combined to resemble a Slater orbital; therefore more GTOs are needed to describe molecular properties than STOs.

The following example (Equations 2.21 and 2.22) compare the 1s Slater type orbital with a 1s Gaussian type orbital for hydrogen.

$$\Phi_{1s}^{STO} = \left(\frac{\zeta^3}{\pi}\right)^{1/2} e^{-\zeta r} \tag{2.21}$$

$$\Phi_{1s}^{GTO} = \left(\frac{2\alpha}{\pi}\right)^{3/4} e^{-\alpha r^2} \tag{2.22}$$

Contracted basis sets use their coefficients in a smart way, making them larger for the outer-shell electrons that are more chemically important. The coefficients of the inner-shell electrons do not vary a lot, when considering the chemical bonding, these are not very important. This concept is explained in Figure 2.5.

Two different 1s Gaussian type orbital can combine and form linear

combinations of Gaussian orbitals (Figure 2.5).

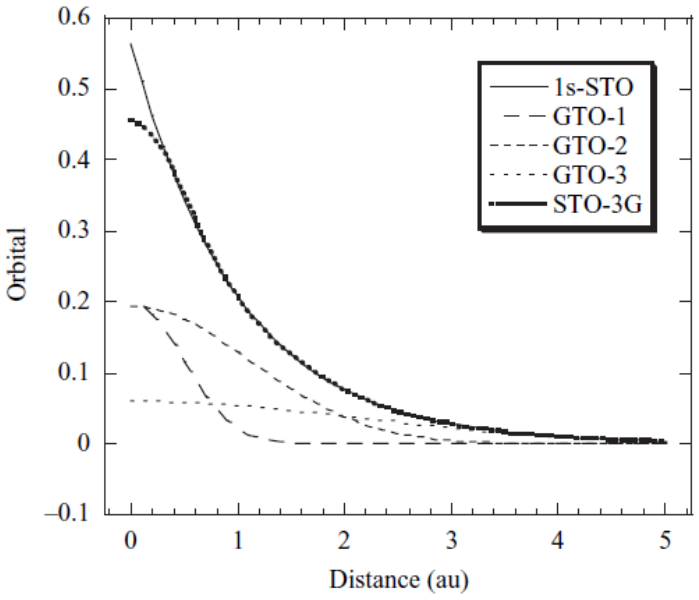

Figure 2.5: Comparison of 1s Slater type orbital and Gaussian expansions. The abscissa shows the distance from the nucleus. Adapted from: "Introduction to Computational Chemistry", Jensen, 2^{nd} edition 2007, Pag. 194.

As the number of Gaussians increases, the end of convergent series are closer and closer to Slater type orbitals.

2.4.3 Minimal basis set

A minimal basis set refers to a representation that contains the minimum number of basis functions to describe a given system. This kind of basis set results from all the inner shell and the valence orbitals in the corresponding atoms. When analysing a molecule like water there are the following orbitals: one 1s of oxygen, two 1s for hydrogen, 2s of oxygen and three 2p. These summed up are 7AOs, the minimal basis set for this molecule would be seven functions. It was found that at least three Gaussians are required to represent each Slater orbital and thus the basic functions of STO-3G are the minimum that should be used in a calculation of an *ab initio* method. A wrong choice of basis set can lead to results that are too far away from the "real answer" as shown in Figure 2.6.

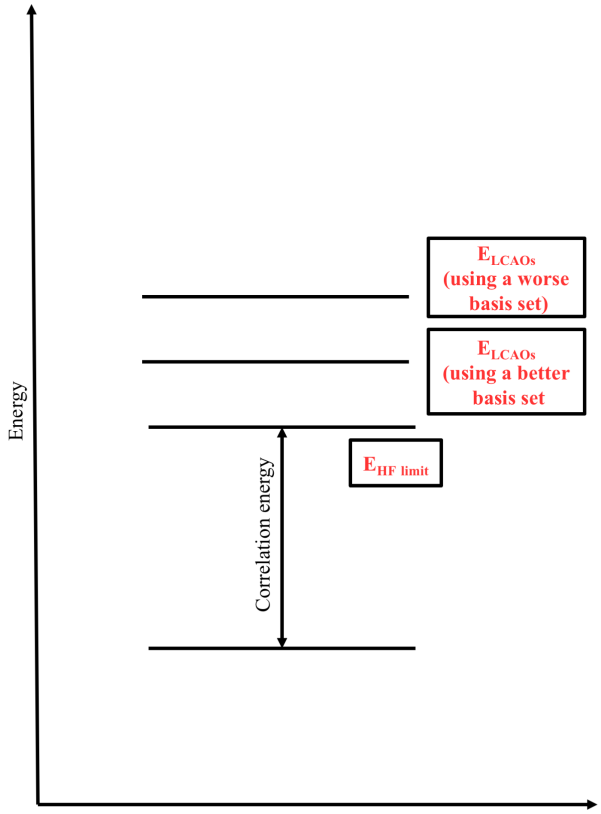

Figure 2.6: Hartree-Fock using different basis sets.

2.4.4 Beyond the minimal basis set

The problems that rise from using minimal basis set can be solved if more than one function is used for each electron. A basis set that doubles the number of functions in the minimal basis set can be described as a double zeta basis. An alternative approach to the double zeta basis is to double the number of functions used to describe just the valence electrons, keeping only one function to describe the inner layers of atoms (atoms of the core). The notation used for this type of method (split valence double zeta basis set) is expressed for example by: 3-21G [15, 16, 17, 18, 19, 20]. This is the first basis set in a series that starts from three contracted core functions. The valence electrons are also represented by three Gaussians: two of them are contracted, combined with fixed coefficients. This method may be applied in the following examples: 3-21G, 4-31G [21, 22, 23, 24] and 6-31G [21, 22, 23, 24, 25, 26, 27, 28, 29, 30]. When comparing a carbon atom using a 3-21G basis set and 6-31G the first basis set would have primitive functions of 6s3p which contract to 3s2p,

while using 6-31G it has 10s4p which contracts to 3s2p. This is the most important property of this kind of basis set and is called the degree of contraction.

Another type of basis set that is used extensively throughout this thesis is Dunning and co workers [31] cc-pVDZ, cc-pVTZ, cc-pVQZ, etc. The cc in the acronym means correlation consistent. The p stands for polarization which is a subject that is going to be discussed in the following subsection. The "real chemistry" or the chemical changes in any studied system are due to changes in the outer shell (valence electrons). Correlation consistent basis sets are very accurate dealing with the behaviour of outer electrons. They offer a different contraction compared to Pople since any given atom has a specific set of CGTOs but uses different coefficients. Combining a full set of basis functions, known as PGTOs (primitive GTOs), into CGTOs can be performed differently depending on the basis set chosen (Equation 2.23).

$$\Phi(CGTO) = \sum_{i}^{k} a_i \Phi_i(PGTO) \tag{2.23}$$

Pople bases use segmented contraction, which means one basis function is not used in another function.

Another commonly used basis sets across this thesis are atomic natural orbitals (ANO). Natural orbitals are very important in computational chemistry since they diagonalize the density matrix of the system and determine the occupation of each orbital, so these are used in CASSCF calculations discussed later. Natural orbitals are formed from initial correlated calculations of the free atoms. The idea is that when correlated methods are used the occupation varies from zero (empty orbital), to two (fully occupied orbital). Metals can sometimes be problematic due to the high number of electrons and difficulty establishing adequate electron correlation. Even though most of these are core electrons, the computational cost is very demanding if one decides to use Pople or Dun-

ning basis sets. Core correlation is not defined by default in every basis set, neither are relativistic effects. In Chapter 5, cc-pwCVTZ (polarised weighted core correlation) [32] [33] is used to perform calculations on transition metal monocarbonyls and the effects of having core correlation are compared to calculate ground state properties.

2.4.5 Effective core potentials (ECPs)

A solution to deal with the very high computational cost of all-electron basis sets are effective core potentials. Two examples of ECP basis sets are LANL2DZ [34] and SDD [35]. These were fundamental for my thesis, especially in Chapter 7 where it was used for transition metal complexes like $Cr(CO)_5$ and $Mn(CO)_5$. The name effective core potential comes from the fact that the core electrons are replaced by a potential and only the valence electrons are treated explicitly in the calculations. For example $Cr(CO)_5$ and $Mn(CO)_5$ on Chapter 7, the $1s^2 2s^2 2p^6$ inner orbitals have a potential describing them. The computational cost is decreased and there is as well an efficient treatment of relativistic effects of core electrons. The treatment of *ab initio* effective core potentials derives from all-electron relativistic calculations and are usually calibrated against them for comparison. In this thesis only transition metals are treated with ECPs. The problem of dealing with these is how to evaluate the number of core electrons that should be considered in the calculation, so "small-core" and "large-core" ECPs are available for a variety of elements.

2.4.6 Polarization and diffuse functions

Increasing the number of radial basis functions (triple zeta, quadruple zeta, etc..), does not necessarily improve the model. It is advisable also to include polarization functions. This can be highlighted for example in the case of hydrogen. This single atom is spherical, but the presence of an external electrical field causes a distortion. This can add some additional flexibility, considering the basis set, effectively allowing molecular

orbitals involving the hydrogen atoms to be more asymmetric about the hydrogen nucleus.

Polarization functions have a higher angular momentum, corresponding to p orbitals for hydrogen, d orbitals for the elements of the first and second row and f for transition metals for example. The use of polarization functions is indicated by an (*) in Pople sets.

The deficiency in the basis functions described so far corresponds to their inability to describe species such as anions and molecules that contain pairs of unshared electrons, which have a significant amount of electronic density away from the nuclei. This failure is due to the amplitudes of the Gaussian basis functions and do not represent an area quite distant from the core. To solve this deficiency of small exponents for the GTOs, diffuse functions can be added to the basis set . These basis set are defined by a "+", so 3-21+G(*) contains an addition of orbital s and p diffuse Gaussian functions. The symbol "++" indicates that the diffuse functions are included in the hydrogen and heavy atoms. An example of such basis set is: 6-311G++G (3df, 3dp). For Dunning basis sets, as it has been mentioned before, the presence of a lower capital p represents the presence of polarization in the fundamental definition of the basis.

2.5 Electron correlation

So far, through this chapter electron correlation has not been discussed and it is an important part of describing any chemical system. Electron correlation can be divided into dynamic correlation and static correlation: dynamic correlation is the instantaneous correlation of movement of electrons, while static correlation is more permanent, it manifests when more than one determinant is needed to describe the same state, (for example an open-shell system that needs to be described by two different determinants). When this happens, Hartree-Fock is qualitatively

wrong, because it only uses a single determinant. Electron correlation is defined as (E_{corr}=E_{total}-E_{HF}).

2.6 Configuration interaction theory (CI)

Configuration interaction was one of the first theories that started using more than one determinant to define a state of a system. As it was mentioned before, Hartree-Fock has limitations and while it is successful in some areas, it can be remarkably wrong in others, so robust methods like configuration interaction were formulated afterwards. In CI theory, the trial wavefunction used is formulated as a linear combination of determinants with the expansion coefficients determined by the minimal of energy of the system. The wavefunction is constructed by the summation of coefficients multiplied by Slater determinants (constructed from spin-orbitals, Equation 2.24):

$$\Psi_{CI} = \sum_{I} c_I \Phi_I \tag{2.24}$$

This method is one of the oldest and straightforward concepts and like Hartree-Fock it is based on the variational principle. In most cases CI theory is used for ground state calculations but there are also approximations to the excited states, obtaining different values for the c_I coefficients. The Slater determinants Ψ_I are obtained by the replacement of occupied spin-orbitals with virtual. When calculating excited states, two approaches are followed: wavefunction and response methods. These are going to be discussed in more detail in the following sections. For example, CIS (configuration interaction singles) is the simplest wavefunction method. It describes and represents the excited states that are mainly dominated by single excitations from the ground state. The big problem with this method is that it neglects the effects of dynamic correlation so it is not always a very accurate one. This is due to Brillouin's theorem, that states that singly excited states do not interact with the ground state, so the corresponding matrix element of

the Hamiltonian is zero, (Equation 2.25).

$$\hat{H}_{GE} = \langle \Psi_{HF} | \hat{H} | \Psi_S \rangle = 0 \tag{2.25}$$

In Equation 2.26, the subscripts S,D,T, etc, show determinants that are singly, doubly, triply, etc, excited relative to the Hartree-Fock configuration.

$$\Psi_{CI} = a_0 \Psi_{HF} + \sum_S a_S \Psi_S + \sum_D a_D \Psi_D + \sum_T a_T \Psi_T + ... = \sum_{i=0} a_i \Psi_i \tag{2.26}$$

This is an example of a constrained optimization. The energy should be minimized under the constraint that the total CI wavefunction is normalized:

$$L = \left\langle \Psi_{CI} | \hat{H} | \Psi_{CI} \right\rangle - \lambda \left(\langle \Psi_{CI} | \Psi_{CI} \rangle - 1 \right) \tag{2.27}$$

λ is the Lagrange multiplier. The configuration interaction equation is solved variationally, so it can be transformed into a set of CI secular equations.

The terms included in the CI expansion may include specific CSFs or Slater determinants. CSFs (configuration state functions) refer to a linear combination of determinants that are an eigenfunction of two operators: $\hat{S}^2$ and $\hat{S}^z$. CSFs, also belong to an irreducible representation of the symmetry point group of the Hamiltonian. In theory using either approach should lead to the same results, even though using CSFs could be more efficient for a wavefunction that transforms itself according to the irreducible representations. Figure 2.7 describes the formation of singlet and triplet CSFs. As it can be seen both determinants have an S_z value equal to zero. The difference (left diagram) and the sum (right diagram) of these two determinants describe a singlet state and the S_z=*0* component of a triplet state.

Since the CI equations are solved variationally adding new functions

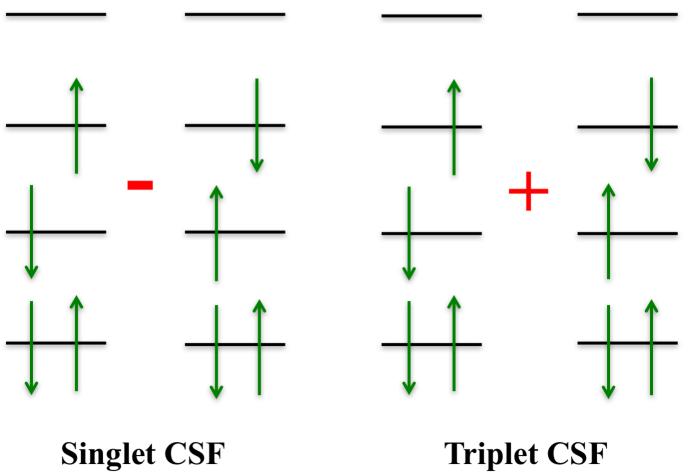

Figure 2.7: Using Slater determinants to construct CSFs.

will either maintain or lower the energy of the system. The configuration interaction approach can be problematic, because the convergence of the CI expansion is very slow, so the number of determinants to include should be very well-balanced before the start of any calculation. The general opinion in computational chemistry seems to think that multiple excitations tend to be less and less important. Using up to quadruple excitations, in the case of H_2O with a minimal basis set, the number of determinants will be very large (25000) and will obtain around 99% of the correlation. If only single and double excitations are used (CISD), 94% of the correlation can be obtained which is usually enough to describe accurately the system and uses only 360 determinants, so the computational cost is much smaller. This is one example, for a very simple molecule but shows why CISD is one of the most popular approaches when using CI theory, because it provides a balanced approach of correlation energy and system accuracy. The problem sometimes arises from the fact that not all excitations are equally important. Lower excitations usually dominate the ground state. When performing calculations and including all excitations would represent a exact full CI calculation, which is not possible for practical applications.

2.6.1 Natural Orbitals (NO)

Using CI theory, the optimal convergence is achieved when using a basis set of natural orbitals (NO). The spin-orbitals are formed from these and form Slater determinants. The density matrix ρ can be described as follows:

$$\rho(1,1^{'}) = \int \Psi^{*}(1^{'},2,3,...,N)\Psi(1,2,3,...,N)d\tau_2 d\tau_3 ... d\tau_N$$
$$= \sum_{ij} D_{ji}\Phi_i^{*}(1^{'})\Phi_j(1), \quad D_{ij} = D_{ji}^{*} \quad (2.28)$$

The summation on Equation 2.28 runs over all the spin-orbitals and the diagonalization of the matrix D, formulates the density matrix expressed in the natural spin-orbitals. When using a unitary transformation:

$$\rho(1,1^{'}) = \sum_{i} (D_{diag})_{ii}\Phi_i^{'*}(1)\Phi_i^{'}(1^{'}) \quad (2.29)$$

This way the inclusion of only the most important contributions of the Φ_i creates a computationally compact wavefunction.

2.6.2 Size consistency

Size consistency refers to the extrapolation of properties with increasing size of the system, for example energy. The increasing number of atoms in a system will be proportional to the energy, otherwise the system is said not to be size consistent. Size consistency is a problem that affects CI theory and may have an important effect on the applicability of the method. One example of this effect can be explained by comparing two H_2 molecules, one calculation where the two H_2 are separated (by a few Å) and another where they are far apart (non-interacting). Considering configuration interaction doubles (CID) and states described by Ψ_1 and Ψ_2, Equation 2.30 follows:

$$\Psi_{CID}(2H_2)_{closetogether} = (\Psi_{HF} + t\Psi_{1\bar{1}}^{2\bar{2}}) * (\Psi_{HF} + t\Psi_{1\bar{1}}^{2\bar{2}}) \quad (2.30)$$

$$\Psi_{CID}(2H_2)_{non-interacting} = \Psi^2_{HF} + t_A\Psi^{2\bar{2}}_{1\bar{1}} + t_B\Psi^{2\bar{2}}_{1\bar{1}} \tag{2.31}$$

For both equations t represents the amplitudes and $\Psi^{2\bar{2}}_{1\bar{1}}$ the excited electrons from bonding to antibonding orbitals. In the Equation 2.30, the molecules close together, quadruple excitations are included for calculating the wavefunction, while the molecules that are far apart (Equation 2.31), the quadruple excitations are not included. Since CI is not size consistent some care must be taken when performing calculations on a large scale and thought must be put in the extrapolation of the properties of the system.

2.7 Monte-Carlo configuration interaction (MCCI)

Monte-Carlo methods are computational techniques that use intelligent algorithms for sampling and obtaining numerical results. They are used across a variety of fields that range from chemistry, physics to mathematics. These are used in numerical integration and optimisation using a probability of distribution.

Monte-Carlo theory is used in physics, for example for simulation purposes in areas such as fluids, interacting particles systems or any phenomena with a probability or uncertainty associated with it. Monte-Carlo methods can vary but they usually follow the same particular trend:

- Define a particular set of possible inputs.
- These inputs are generated randomly using probabilities over a certain domain.
- After having been selected, a deterministic computation is performed.

In chemistry Monte-Carlo theory has been applied to many-body problems and has been optimised for parallel computing which makes it

very fast to use for performing calculations [36]. MCCI is a stochastic method that aims to approximate a full CI wavefunction using a complicated algorithm to discard and keep randomly generated configurations, obtaining very compact variational CI wavefunctions. Configuration interaction is the basis of this Monte-Carlo approach that tries to obtain an optimised wavefunction, using independent samples of the expansion space. The threshold is set up by the researcher, that has to use his/her chemical intuition to know how much the wavefunction can/needs to be improved and to know how to balance the computational resources by choosing an adequate basis set. The Monte-Carlo CI method relies on two different observations. The first one is based on the fact that from all the many configurations generated in a full CI calculation only a few are relevant to lower the total energy or to improve the wavefunction for the lowest eigenstates. After the CI vector is generated, it will only interact with the configurations that come from single and double substitutions. These configurations are relative to the components of the generated trial wavefunction when using orthogonal orbitals (see Figure 2.8).

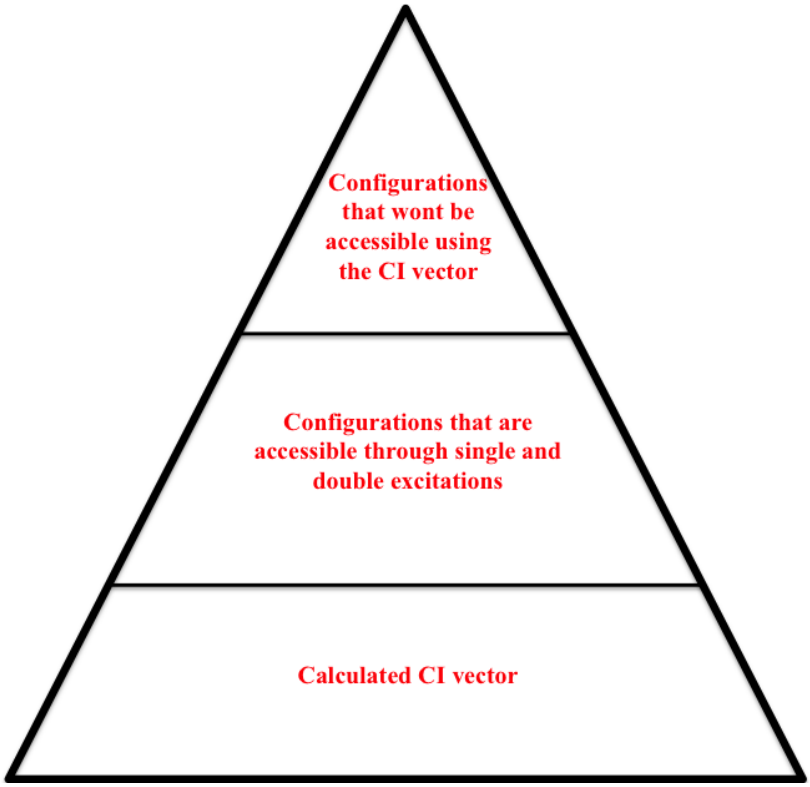

Figure 2.8: The Full CI space partitioned into the different spaces.

MCCI uses a diagonalization step that is the core of all CI calculations. It starts by randomly generating single and double excitation for the reference trial vector. After this step, it is an eigenvector/eigenstate problem, that can be solved. The components of the generated vector need to be analysed by the program and decide wether they should be discarded or not. This procedure is repeated until the threshold set up for the energy and the length of the CI vector is satisfied. The use of MCCI is simplified by the fact the initial guest can be for example a Hartree-Fock wavefunction. Higher spins can be used as well and so the method and the application is very robust and can be used in a large variety of systems. The applications of MCCI have been increasing the past few years with a range of studies that go from dissociative potentials, to electric multipole moments, or arbitrary excited electronic states [37, 38, 39, 40, 41, 42, 43, 44]. More of these properties will be discussed in Chapter 5 and 6.

2.8 Coupled-cluster theory (CC)

One alternative to CI wavefunctions is coupled-cluster theory. It is size extensive and uses a different multiplicative behaviour compared to CI. The wavefunction can be written as,

$$\Psi_{CC} = e^{\hat{T}}\Psi_{HF} \tag{2.32}$$

Equation 2.32 is challenging to solve since one needs to find an operator $\hat{T}$ in such a way that the operator $e^{\hat{T}}$, needs to be the ideal solution for Schrödinger's equation. This operator is considered an *ansatz*, which means is an "educated guess" to solve Schrödinger's equation. The cluster operator is defined as:

$$\hat{T} = \hat{T}_1 + \hat{T}_2 + \hat{T}_3 + ... + \hat{T}_n \tag{2.33}$$

In Equation 2.33, n is the total number of electrons and the different $\hat{T}$ operators generate all possible combinations of determinants as in CI.

$\hat{T}_1$ acting on a wavefunction Ψ_{HF} for takes the form of:

$$\hat{T}_1\Psi_{HF} = \sum_{i}^{occ}\sum_{a}^{virt} t_i^a \Psi_i^a \tag{2.34}$$

This operator takes care of single excitations while $\hat{T}_2$ takes care of double:

$$\hat{T}_2\Psi_{HF} = \sum_{i<j}^{occ}\sum_{a<b}^{virt} t_{ij}^{ab} \Psi_{ij}^{ab} \tag{2.35}$$

The symbols *a,b,...,* are spin-orbitals from the reference state while *p,q,r,s,...,* correspond to virtual spinorbitals. t represents the amplitudes and this is the main goal for any coupled-cluster calculation.

Another important property of coupled-cluster methods is the fact that the method is size consistent: meaning that for an infinite distance between molecules A and B, both Ψ_A and Ψ_B can be expressed in the form of the product of the wavefunctions for A and B.

2.8.1 Connections in CI theory and CC theory

There is an obvious relationship between CI theory and coupled-cluster as shown in Equation 2.36.

$$\begin{aligned} e^{\hat{T}}\Psi_{HF} &= [1 + (\hat{T}_1 + \hat{T}_2 + \hat{T}_3 + ...) + \frac{1}{2}(\hat{T}_1 + \hat{T}_2 + \hat{T}_3 + ...)^2 + ...]\Psi_{HF} \\ &= (1 + \hat{C}_1 + \hat{C}_2 + \hat{C}_3 + ...)\Psi_{HF} \end{aligned} \tag{2.36}$$

$\hat{C}$ are related to the cluster operators as follows:

$\hat{C}_1$=$\hat{T}_1$,
$\hat{C}_2$=$\hat{T}_2$+$\frac{1}{2!}\hat{T}_1^2$,
$\hat{C}_3$=$\hat{T}_3$+$\frac{1}{3!}\hat{T}_1^3$+$\hat{T}_1\hat{T}_2$,
$\hat{C}_4$=$\hat{T}_4$+$\frac{1}{4!}\hat{T}_1^4$+$\frac{1}{2!}\hat{T}_2^2$+$\hat{T}_3\hat{T}_1$+$\frac{1}{2!}\hat{T}_1^2\hat{T}_2$

Considering for example $\hat{C}_4$, the $\frac{1}{2!}\hat{T}_2^2$ contains very important determinants to describe the wavefunction accurately.

For configuration interaction, considering all the possible excited configurations that are generated using the HF determinant, a full configuration is formed (FCI). A calculation like this would usually be too demanding computationally, so certain truncations to the method are performed as shown in Equation 2.33. When expanding Equation 2.33 if it was truncated to $(1 + \hat{T}_2)$ would be defined as CID, configuration interaction of double excitations. If $\hat{T}_1^2$ and $\hat{T}_2$ operators were chosen it is possible to generate all the doubly excited determinants. Considering Equation 2.37:

$$e^{\hat{T}} = 1+\hat{T}_1+(\hat{T}_2+\frac{1}{2}\hat{T}_1^2)+(\hat{T}_3+\hat{T}_2\hat{T}_1+\frac{1}{6}\hat{T}_1^3)+(\hat{T}_4+T_3\hat{T}_1+\frac{1}{2}\hat{T}_2^2+\frac{1}{2}\hat{T}_2\hat{T}_1^2 + \frac{1}{24}\hat{T}_1^4)+... \quad (2.37)$$

it is possible to generate all the determinants that are needed in CISDTQ. A Taylor expansion can be used as a way to divide the contributions of each excitation type. One of the main problems of using for example CISD is the lack of the term $\hat{T}_2^2$, so this is the main reason why this method is not size extensive. As the system size increases this term becomes more important. CCSD has not only the same connected terms as CISD, but also has disconnected terms allowing it to be size extensive. A connected term is for example $\hat{T}_4$, that corresponds to four electrons interacting simultaneously, while a disconnected term, for example $\hat{T}_2^2$, corresponds to non-interacting pairs of interacting electrons. When trying to solve coupled-cluster equation analogously to CI theory:

$$E_{CC}^{var} = \frac{\langle\Psi_{CC}|\hat{H}|\Psi_{CC}\rangle}{\langle\Psi_{CC}|\Psi_{CC}\rangle} = \frac{\langle e^{\hat{T}}\Psi_{HF}|\hat{H}|e^{\hat{T}}\Psi_{HF}\rangle}{\langle e^{\hat{T}}\Psi_{HF}|e^{\hat{T}}\Psi_{HF}\rangle} \quad (2.38)$$

$$E_{CC}^{var} = \frac{\langle(1+\hat{T}+\frac{1}{2}\hat{T}^2...\frac{1}{N!}\hat{T}^N)\Psi_{HF}|\hat{H}|(1+\hat{T}+\frac{1}{2}\hat{T}^2...\frac{1}{N!}\hat{T}^N)\Psi_{HF}\rangle}{\langle(1+\hat{T}+\frac{1}{2}\hat{T}^2...\frac{1}{N!}\hat{T}^N)\Psi_{HF}|(1+\hat{T}+\frac{1}{2}\hat{T}^2...\frac{1}{N!}\hat{T}^N)\Psi_{HF}\rangle} \tag{2.39}$$

when expanding the numerator and denominator leads to terms that do not vanish and create a very computationally demanding set of equations that can only be solved for small systems. Trying to solve the coupled-cluster equations the same way as CI theory is not feasible. Projecting the coupled-cluster Schrödinger equation in the reference function Ψ_{HF} and integrating:

$$\langle\Psi_{HF}|\hat{H}e^{\hat{T}}|\Psi_0\rangle = E_{CC}\langle\Psi_{HF}|e^{\hat{T}}\Psi_0\rangle = E_{CC}\langle(1+\hat{T}_1+\hat{T}_2+...)\Psi_{HF}\rangle \tag{2.40}$$

Leads to:

$$E_{CC} = \langle\Psi_{HF}|\hat{H}e^{\hat{T}}|\Psi_{HF}\rangle \tag{2.41}$$

Equation 2.41 represents the standard formulation of the coupled-cluster equation which can be solved.

2.8.2 Truncation of coupled-cluster methods

Until now the description of coupled-cluster has been towards the exact solution, meaning using all the cluster operators until $\hat{T}_N$. Using this approach, all the possible determinants are generated and this wave-function is exactly the same as a full CI. As mentioned before, a full CI calculation is too demanding and can only be performed for small systems, and therefore the cluster operator must be truncated at some designated excitation level. When truncating the operator $\hat{T}$, some of the amplitudes in the equations will become zero, so the final calculated amplitudes will not be exact anymore. A very widely used method when thinking of coupled-cluster is CCSD. It offers a balanced way to describe electronic correlation and computational cost. The CCSD truncation

looks like:

$$e^{\hat{T}_1+\hat{T}_2} = 1+\hat{T}_1+(\hat{T}_2+\frac{1}{2}\hat{T}_1^2)+(\hat{T}_2\hat{T}_1+\frac{1}{6}\hat{T}_1^3)+(\frac{1}{2}\hat{T}_2^2+\frac{1}{2}\hat{T}_2\hat{T}_1^2+\frac{1}{24}\hat{T}_1^4)+... \tag{2.42}$$

2.8.3 Møller Plesset perturbation theory

In Møller Plesset perturbation theory $\hat{H}^{(0)}$ is the sum of the Hartree-Fock operators and $\Psi_0^0 = \Psi_{HF}$:

$$\hat{H}^{(0)}\Psi_{HF} = E_0^{(0)}\Psi_{HF} \tag{2.43}$$

$$E_0^{(0)} = \sum_i \epsilon_i \tag{2.44}$$

Equation 2.44 shows the summation over the occupied spin-orbitals in the Hartree-Fock wavefunction. The sum of Fock operators counts the electron-electron repulsion twice and the operator associated with this difference is called fluctuation potential (Equation 2.45).

$$\hat{H}^{(1)} = \hat{H} - \hat{H}^{(0)} = \sum_{i=1}^{N_{elec}}\sum_{j>i}^{N_{elec}} g_{ij} - \sum_{i=1}^{N_{elec}}\sum_{j=1}^{N_{elec}}\langle g_{ij}\rangle = \hat{V}_{ee} - 2\langle\hat{V}_{ee}\rangle \tag{2.45}$$

When calculating the mean value of the Hamiltonian, using Hartree-Fock, the sum of zeroth order energies is: $\sum_i \epsilon_i$ and the first-order correction is: $\langle\Psi_{HF}|\hat{H}^{(1)}|\Psi_{HF}\rangle$:

$$E_{HF} = \langle\Psi_{HF}|\hat{H}|\Psi_{HF}\rangle = \langle\Psi_{HF}|(\hat{H}^{(0)}+\hat{H}^{(1)})|\Psi_{HF}\rangle = (\sum_i \epsilon_i) + \langle\Psi_{HF}|\hat{H}^{(1)}|\Psi_{HF}\rangle \tag{2.46}$$

Note that Equation 2.46 is first-order corrected. Hartree-Fock is first order corrected due to Brillouin's theorem, electron correlation is calculated starting at second order corrections.

Different truncations to the energy can be made and the second order is the most used, it is known as MP2, but higher orders exist (MP3, MP4, etc). The second-order Møller-Plesset correction (MP2) is given by:

$$E(MP2) = \sum_{i<j}^{occ} \sum_{a<b}^{vir} \frac{(\langle \Phi_i \Phi_j | \Phi_k \Phi_l \rangle - \langle \Phi_i \Phi_j | \Phi_l \Phi_k \rangle)}{\epsilon_i + \epsilon_j - \epsilon_k - \epsilon_l} \tag{2.47}$$

2.9 Multiconfigurational self-consistent field method (MC SCF)

When using configuration interaction, sometimes it is clear that one needs to use more than one determinant to describe the system accurately. More contributions to the wavefunction are necessary, so the CI expansion needs to be balanced adequately. One example where this kind of approach plays a role is for example, on open-shell systems when different states are important for the ground state. Other systems where these kind of methods are important are: when a bond is being broken, or the opposite, a bond is being formed, several determinants have to be considered for constructing the wavefunction. The determinants for the construction of the wavefunction also have similar weights and should all be included. This part is tricky since it is up to the researcher to use his/her chemical intuition to decide what determinants to include in order not to make the calculation too demanding. Each of the determinants is built from molecular spin-orbitals which cannot be fixed. The classical MC SCF approach is:

$$\Psi = \sum_{I} d_I \Phi_I \tag{2.48}$$

Equation 2.48 differs from the previous CI equation where the d represents variational coefficients and Φ_I individual Slater determinants or CSFs. In the classical MC SCF approach:

1. The CI expansion needs to be finite, the Slater determinants and

orbitals are calculated using an initial guess.

2. Optimisation of coefficients in CI expansion.

3. Then, LCAO coefficients are varied in the orbitals and this way obtain the optimum molecular orbitals for that CI expansion.

4. If convergence is not reached you have to return to step 1.

2.9.1 Complete active space self-consistent field (CASSCF)

A widely used case of the MC SCF method is CASSCF [45] [46] [47]. For CASSCF the orbitals are divided in *virtual*, *inactive* and *active*. The active space always depends on the system studied. CASSCF is the main MC SCF wavefunction method used for geometry optimisations, because it allows the gradient and second derivatives to be computed analytically. The procedure to do a CAS calculation can be very tricky so one has to use chemical intuition to build an active space successfully. For the active space all the possible excitations and occupancies (0 to 2 electrons) are considered. This way all the determinants from the MC SCF expansion are considered with all excitations within the active space and size consistency is achieved. Since the results do not depend on any linear transformation of the molecular spin orbitals, it makes the result invariant regarding the localization of the molecular orbitals. The only limitation is the basis set, that depends on the size of the system.
Figure 2.9 summarizes what has been being discussed.
CASSCF has numerous advantages over other methods:

- All the regions on the potential energy surface are treated in a balanced way.

- Any number of electronic states can be treated.

- It is a multiconfigurational method, meaning that it can treat all the possible electronic configurations of the orbitals of the system.

- It is one of the best methods to describe conical intersections.

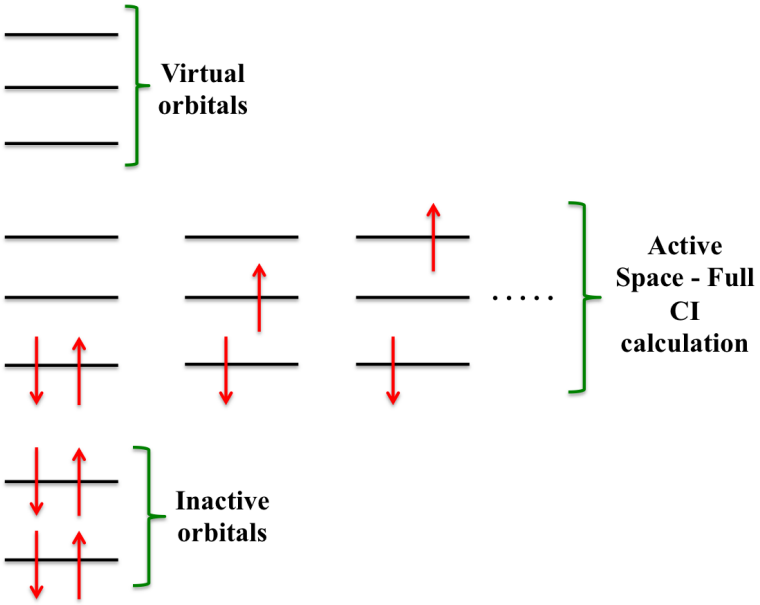

Figure 2.9: CASSCF - Scheme how orbitals are divided for a calculation.

Although this multiconfigurational method has numerous advantages, it also has a few disadvantages:

- It is not a black-box.
- It cannot include all the orbitals in the active space, except for very small molecules.
- It is very expensive for large active spaces.

CASSCF has been widely used due to its robustness to describe a lot of system properties even though it can be very difficult to set up and the region of full CI is limited due to computational resources.

CASSCF can be used to calculate conical intersections. As it was mentioned in the beginning of this chapter, rich photochemical reactions are very important to research, because they can help the scientists to understand phenomena that happen when molecules are irradiated with light.

2.9.2 Restricted active space self-consistent field (RASSCF)

An extension of the complete active space self-consistent field is the restricted active space self-consistent field (RASSCF). In this method the active orbitals are partitioned into three different sub-spaces: RAS1, RAS2 and RAS3. RAS2 is equivalent to CASSCF where a full CI calculation is performed. RAS1 and RAS3 have restrictions, RAS1 has a maximum number of holes allowed and in RAS3 a maximum number of electrons. As it happens for CASSCF there is a core of inactive orbitals that make up the wavefunction. The large number of coupling coefficients present in these calculations create problems in terms of computational time. This method can be very helpful as it is described for example is Chapter 4. The limitation of a CASSCF calculation is around 16 orbitals and 16 electrons, which already produces a very large number of configurations. RASSCF performs calculations that include more orbitals and electrons and allows a large space to be chosen with specific restrictions.

2.9.3 Perturbation approaches to multireference methods

CASSCF is able to recover the static correlation successfully, although is usually lacking dynamic correlation. One can use perturbation theory to solve this problem. One of the most popular methods nowadays is CASPT2. This method was proposed by Andersson *et al* initially [48].

In CASPT2 a multiconfigurational wavefunction generated from a CASSCF calculation is used as the zeroth-order wavefunction, which has a perturbation approach on top of that. The configuration space can be divided into four subspaces: V_0, V_K, V_{SD} and $V_{TQ...}$. V_0 is the one-dimensional space composed by the CAS reference function. V_K is the space spanned by the orthogonal complement to the CAS reference function. V_{SD} is the space spanned by the single and double replacement states usually in reference to V_0 and $V_{TQ...}$ gathers the higher excitations not included in the previous ones. This way it allows the inclusion

of the necessary dynamic correlation that many systems need. Nowadays, most of the multireference methods have been limited to second order perturbation. Analytical gradients are not available yet and geometry optimisation steps are too demanding so, numerical gradients have to be used instead. Another variant of perturbation theory used on this thesis (Chapter 5 and 6) is NEVPT2. This variant of multireference perturbation theory is very powerful and uses different approximations to the system. Depending on the computational cost different approaches to this method can be used (totally uncontracted, strongly contracted and partially contracted). Another advantage is the fact that it avoids intruder states in perturbation series i.e avoids large denominators in the perturbation expansion.

2.10 Density functional theory

Nowadays, methods based on density functional theory that use the Kohn-Sham formalism are considered a valuable alternative to the traditional *ab initio* methods of quantum mechanics. Kohn and Sham tried to find solutions from first principles of SCF and treat electronic correlation differently from wavefunction techniques. DFT methods can be applied to large systems, like coordination compounds, inorganic or biological systems. DFT has been established as a valuable research tool because it can serve either to validate the conclusions that have been reached from experiments or to distinguish between possibilities that are left open. Density functional theory using the Kohn-Sham approach is considered an improvement over Hartree-Fock theory. The system can be modelled as a function of the electronic density. The biggest disadvantage of DFT is the non-systematic approach to improve the results towards an exact solution.

2.11 Hohenberg-Kohn theorem

Hohenberg and Kohn showed that the ground state energy of a multi-electron, non-degenerate system is determined by its electronic density, although the functional dependency on the density is not known. Density functional theory also satisfies the variational principle; the energy associated for the true electronic density of the system is minimal.

When thinking of a wavefunction for an N-electron system, it depends on $4N$ variables, three spatial and one spin dependent for each electron. The electron density has the same number of variables whatever the size of the system is 3, while in wavefunction methods the complexity of the system increases exponentially with the number of electrons. The main goal of DFT is to find a way to connect a calculated electron density to an energy.

2.12 Kohn-Sham formalism

The formalism developed by Kohn and Sham for a N-electron system is given by:

$$E_{[\rho]} = -\frac{1}{2}\sum_{i=1}\int_{-\infty}^{+\infty} \Psi_i(\vec{r}_1) \bigtriangledown_i^2 \Psi_i(r_1)dr_1 - \frac{e^2}{4\pi\epsilon_0}\sum_{A}^{n}\int_{-\infty}^{+\infty}\frac{Z_A}{|\vec{r}_1 - \vec{R}_A|}\rho(r_1)dr_1 + \frac{1}{2}\int_{-\infty}^{+\infty}\int_{-\infty}^{+\infty}\frac{\rho(r_1)\rho(r_2)}{|\vec{r}_1 - \vec{r}_2|}dr_1dr_2 + E_{xc}[\rho] \quad (2.49)$$

1. The first term corresponds to the kinetic energy of the system, with the same total electronic density as the actual real system. Ψ_i are the spinorbitals.

2. The second term represents the potential energy that comes from the interaction between electrons and nuclei. The sum are the charges Z_A located at $\vec{R}_A$.

3. The third term shows the classic Coulomb energy of repulsion of

the electrons with $\rho(r)$ density.

4. The fourth term, the E_{xc} : the exchange-correlation energy of interactions, the effects of correlation and the difference between the exact kinetic energy and the reference system of the electrons that do not interact.

The first three terms in this equation are identical to the conventional *ab initio* methodologies, although the fourth term, the exchange and correlation energy needs more attention. The biggest problem in DFT concerns this term, because there is no analytical formula to solve it. So in a N-electron system it is necessary to use approximations to solve this problem.

2.13 Approximate functionals

2.13.1 Local Density Functionals approximation - (LDA)

In practice it is necessary to use approximate expressions of the ε_{xc} term and the search for appropriate functionals for this term is the biggest challenge of DFT theory. The simplest model proposed that if the system defined by the electronic density has only small changes, the LDA approximation (local density approximation) can be used. In Equation 2.50, ε_{xc} is the exchange-correlation of energy per particle of a uniform electronic cloud. E_{xc} can be deduced by this approximate expression of ε_{xc}. It is assumed that the density of this system can be seen as a uniform cloud, or as the density being a slowly varying function.

$$E_{xc} = \int_{-\infty}^{+\infty} \rho(r)\varepsilon_{xc}\rho(r)dr \tag{2.50}$$

2.13.2 Generalized Gradient approximation - (GGA)

Typical molecular systems are generally very different from a uniform electronic cloud. In fact any real system is spatially non-uniform, so there is a spatial variation of $\rho(r)$. The GGA methods (generalized gradient approximation) incorporate this idea, promoting that the energy

of exchange and correlation terms are not only dependent on the density, but also on the gradient of their density.

The vast majority GGA methods tend to show a significant improvement compared with the LDA methods. GGA methods provided more precise calculations of atomization and activation energies or energy barriers. Still, such methods have some shortcomings including Van der Waals interactions. Yet, GGA returns good values for ionic, covalent, metallic and also hydrogen bonds.

A functional used in Chapter 8 is a recent approach to the generalized gradient approximation, B97D [49]. GGA functionals usually have difficulties when describing long-range electron-correlations, which are responsible for Van der Waals dispersive forces that are fundamental to describe interactions between atoms and molecules. The difference in these functionals relies on the way it is parameterized. It includes damped atom-pairwise dispersion corrections, $C_6 \cdot R^{-6}$. This method is very good at describing medium to large interatomic distances as shown in Chapter 8 when comparing B3LYP and B97D geometry optimizations. This way pairwise dispersions are described allows for a more real description of large chemical systems.

2.13.3 Meta Generalized Gradient approximation - (M-GGA)

More recently, a new class of functionals based on GGA methods was developed including additional semi-local information. These methods are named meta-GGA (M-GGA), depending explicitly on higher orders of the gradient of density or typically in the kinetic energy, which involves doubled occupied orbitals derived from Kohn-Sham. These methods represent a significant improvement in the determination of properties such as atomization energies [50]. However, they are technically more challenging with many difficulties in terms of numerical stability. Some M-GGA methods are: BRC[51], VSXC[52] and TPSS[50].

2.13.4 Hybrid Generalized Gradient approximation - (H-GGA)

Hybrid methods brought several improvements to quantum mechanics, matching the terms of exchange and correlation of a GGA method and mixing with a percentage of Hartree-Fock exchange. The hybrid functionals allowed a significant advance for GGA for various molecular properties. They became a very popular choice in quantum mechanics and are widely used. Some examples of these type of functionals are: B971 [53], B972 [54], M06 [55] and B3LYP [56, 57, 58, 59].

2.13.5 Hybrid Meta Generalized Gradient approximation - (HM-GGA)

The last class of DFT functionals are HM-GGA (hybrid meta-GGA). These represent a new class of density functional, based on a concept similar to the H-GGA and still developing. The difference is based on the fact that its development began with M-GGA and GGA. Thus, these methods depend on the Hartree-Fock exchange, its gradient and the kinetic energy density. The functionals are constructed using empirical fittings of their parameters. One example of such functional is: TPSSh [60]. These methods represent an improvement from the previous formalisms, particularly in the determination of energy barriers and atomization energies.

2.14 Photochemistry - Excited States

In this section particular aspects that need to be considered when studying electronic excited states are discussed. An understanding of a reaction pathway in electronic excited states allows the researchers to increase and develop their ability to design and control photochemical reactions.

The study of photochemical mechanisms is a considerable challenge in computational chemistry. The objective is to get a complete descrip-

tion of the reaction from the Franck-Condon region to the ground state product. The dynamic electron correlation (correction for the incorrect instantaneous repulsion of electrons in occupied orbitals) is fundamental to obtain precise energies. Figure 2.10 illustrates the electronic states of a molecule and the transitions between them. The states are arranged vertically by energy and grouped horizontally by spin multiplicity. Non-radiative transitions are indicated by squiggly arrows (which some of them decay to the ground state) and radiative transitions by straight arrows. The vibrational ground states of each electronic state are indicated with thick lines, the higher vibrational states with thinner lines. In Table 2.1 the time scales of these phenomena are shown.

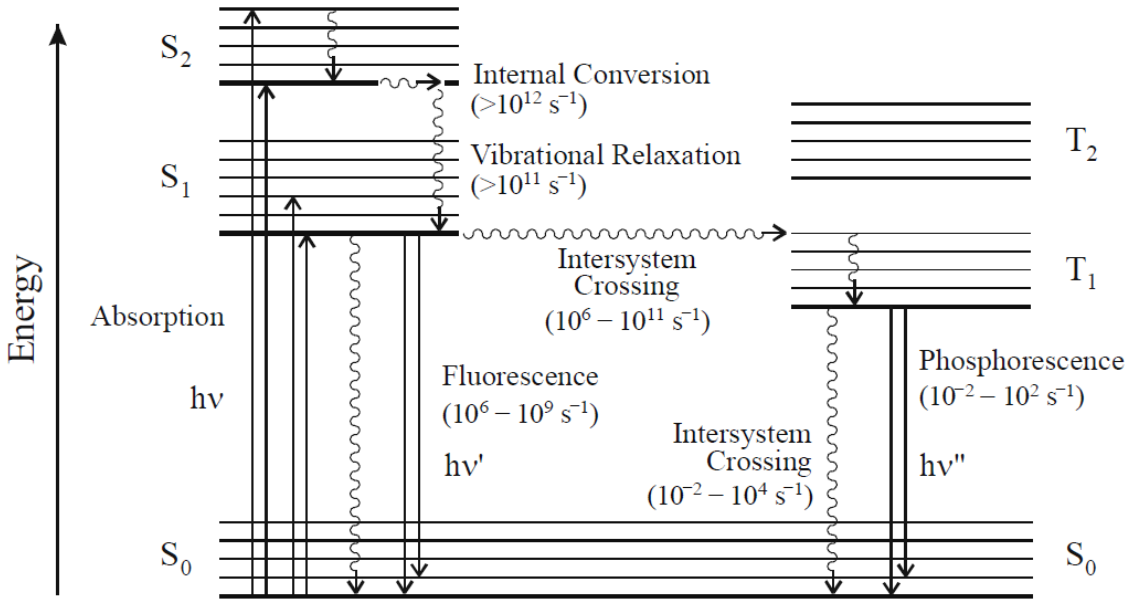

Figure 2.10: The Jablonski diagram. Adapted from: "The Handbook of Photochemistry", Montalti M.; Credi A.; Prodi.; Gandolfi M. T., 3^{rd} edition 2006, pag 200.

Transition	Time Scale (seconds)	Radiative Process
Absorption	10^{-15}	YES
Internal conversion	10^{-14} - 10^{-11}	NO
Vibrational Relaxation	10^{-14} - 10^{-11}	NO
Fluorescence	10^{-9} - 10^{-7}	YES
Intersystem Crossing	10^{-8} - 10^{-3}	NO
Phosporescence	10^{-4} - 10^{-1}	YES

Table 2.1: Time scale for the Jablonski diagram.

In Figure 2.11 a photochemical funnel is portrayed. There are two differ-

ent adiabatic surfaces (ground state and electronic excited state). The molecule is excited from the ground state, first to the Franck-Condon region. The Franck-Condon principle states that a molecule can be promoted to an excited state, keeping the same nuclear configuration, since the electronic excitation is so fast, that the nuclei do not have time to rearrange. After this excitation, the molecule flows down to M*, which is a minimum and it might have enough energy to go through the energetical barrier (activation energy) and reach the transition state (TS). After this step the system relaxes to the ground state through a conical intersection (point C) and reaches it with almost 100% efficiency. The final product is point P or P', which are stable minima.

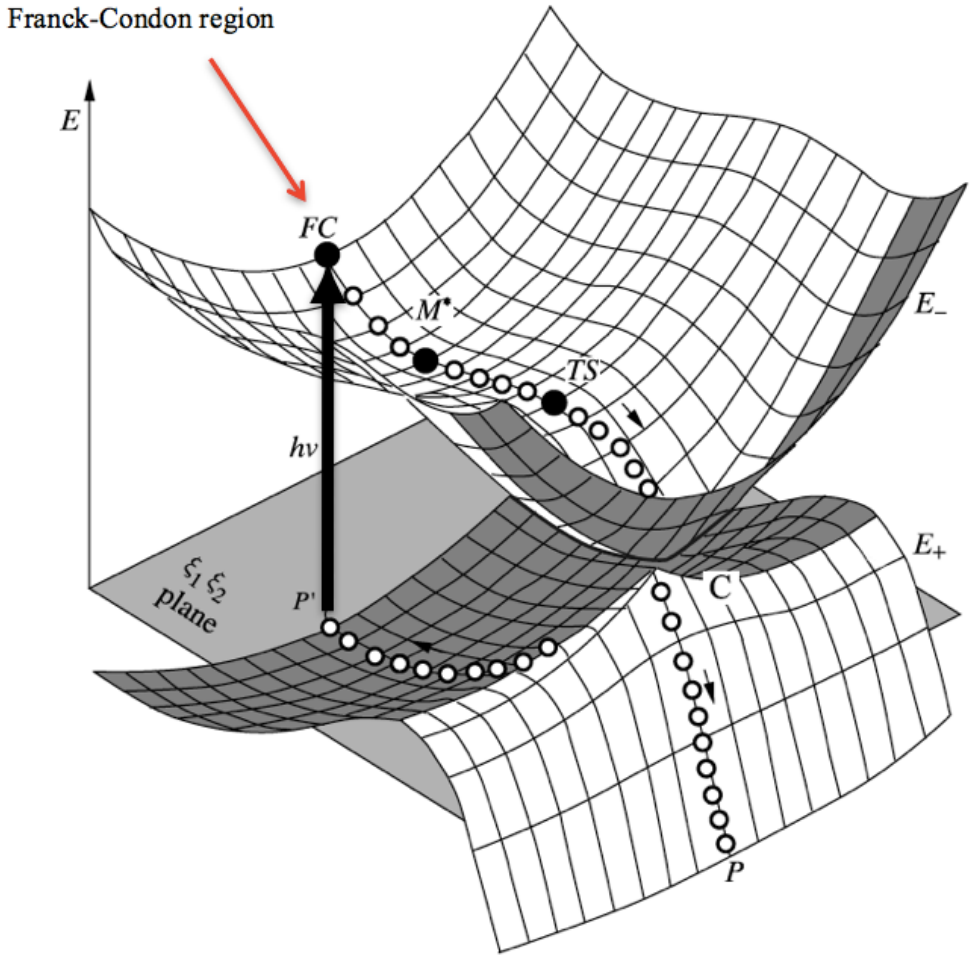

Figure 2.11: Illustration of the photochemical funnel effect. Adapted from: "Ideas of Quantum Chemistry", Lucjan Piela, 1^{st} edition 2007, Pag. 266.

2.15 Spectroscopy of electronically excited states

Many of the following chapters involve electronic transitions that happen in transition metal complexes. The electronic spectroscopy of these can become very complex, depending on what phenomena researchers want to analyse. When studying electronic excited states, one looks for ways to measure or describe the population of these states. Doing a complete analysis of the nature of excited states of any complex can be a very demanding task, since it involves not only electronic transitions, but also vibration and rotation.

This thesis is primarily concerned with electronic transitions. A molecule can absorb a photon or photons of some frequency if this corresponds to an excitation energy of the system. Specific selection rules command the way quantum numbers are allowed to change in transitions, while gross selection rules describe possible transitions based on geometrical properties of any given molecule, depending on the point group symmetry. Regarding specific selection rules, the overall spin state must not change in molecules that have an inversion centre (i), the transition must involve a change in parity, which is also known as the Laporte rule. One important conclusion of this rule is that transitions between orbitals with the same angular momentum are not allowed. The electronic spectra of transition metals can be very demanding to resolve due to the high number of electronic states available. Gross selection rules show that depending on the symmetry of the molecules d-d transitions may not be entirely forbidden, although they are usually very weak. Regarding different type of transitions discussed previously, the most common ones for metals are: ligand-to-metal charge transfer (LMCT), metal-to-ligand charge transfer (MLCT) and ligand field transitions (d-d) (LF).

Another important property to be described is the polarizability of a molecule (α), that measures that response of a molecule to an applied

electric field.

$$\alpha_{xx} = -2 \sum_{i}^{'} \frac{\langle 0|\mu_x|i\rangle\langle i|\mu_x|0\rangle}{E_0^{(0)} - E_i^{(0)}} \tag{2.51}$$

$$\alpha_{yy} = -2 \sum_{i}^{'} \frac{\langle 0|\mu_y|i\rangle\langle i|\mu_y|0\rangle}{E_0^{(0)} - E_i^{(0)}} \tag{2.52}$$

$$\alpha_{zz} = -2 \sum_{i}^{'} \frac{\langle 0|\mu_z|i\rangle\langle i|\mu_z|0\rangle}{E_0^{(0)} - E_i^{(0)}} \tag{2.53}$$

The isotropic polarizability of a molecule is the averaged sum of these three contributions on the different axes. $E_0^{(0)}$ - $E_i^{(0)}$ measures the difference in every electronic states of the system. The further away electrons are from nuclei the higher value of polarizability they will generally have. As it was shown before, in the basis set section, large molecules should be studied with polarization functions to help describe these effects. The oscillator strength, f as shown in Equation 2.54, reflects the probability of a transition from state ($i \rightarrow f$).

$$f_{if} = \left(\frac{4\pi m_e}{3e^2\hbar}\right) \nu_{if} |\vec{\mu}_{if}|^2 \tag{2.54}$$

ν_{if} is the frequency associated to this transition and the oscillator strength can be related to the polarizability as:

$$\alpha = \frac{\hbar^2 e^2}{m_e} \sum_{i}^{'} \frac{f_{if}}{\Delta E_{if}^2} \tag{2.55}$$

The Kuhn-Thomas rule states that the sum over the oscillator strengths is equal to the number of valence electrons.

2.16 Response and propagator methods

The $\hat{H}$ (Hamiltonian) can be time-dependent (if the energy changes with time for the interacting system) or time-independent (the energy is conserved, an isolated system). Equation 2.56 is the time-dependent

Schrödinger equation, for example for a molecule in a time-dependent field. The time-evolution of the wavefunction Ψ is given by the equation:

$$i\hbar\frac{\partial\Psi(x,t)}{\partial t} = \hat{H}\Psi(x,t) \tag{2.56}$$

Depending on the nature of this field, different properties can be calculated. More aspects about this technique will be discussed in one of the next subsections (coupled-cluster response) and its applications to molecular systems. The focus here is on excited electronic states, where a time-dependent electric field is the perturbation. The effect of an electromagnetic field allows spectroscopic transitions to occur between quantized energy levels.

$$\Psi(x,t_0)$$
$$\downarrow$$
$$\hat{H}\Psi(x,t_0)$$
$$\downarrow$$
$$i\hbar(\tfrac{\partial\Psi}{\partial t})_{t=t_0}$$
$$\downarrow$$
$$\Psi(x,t_0+d\tau) = \Psi(x,t_0) - \tfrac{i}{\hbar}\hat{H}\Psi d\tau$$

In the above flow chart by knowing the value of a wavefunction Ψ at a given time, it allows us to compute $\hat{H}\Psi$ *(x,*t_0*)*. After this step, using the equation written before, it is possible to advance to the next step. So, if the wavefunction at a certain time (t_0) is known, the calculation of the function at an infinitesimal time later is possible (t=t_0+$d\tau$). Normally, for a molecule to interact with an electromagnetic field it needs to absorb or emit a photon and must possess, at least transiently, a dipole oscillating at that frequency. The Hamiltonian in a perturbed system can be divided in:

$$\hat{H} = \hat{H}^{(0)} + \hat{H}^{(1)} \tag{2.57}$$

$\hat{H}^{(0)}$ represents the time-independent Hamiltonian. $\hat{H}^{(1)}$ shows the in-

crement represented by the time-dependent perturbation. The perturbation is generated from the effect of an oscillating electric field with an electrical dipole (for example the z-direction), so:

$$\hat{H}^{(1)} = -\mu_z \epsilon cos(\omega t) \tag{2.58}$$

ω is the frequency of the field and ϵ corresponds to its amplitude.
The rate of change of population of the state Ψ_f considering the transitions from state Ψ_i $(w_{i \leftarrow f})$ is equal to:

$$w_{i \leftarrow f} \propto |\hat{H}^{(1)}_{fi}|^2 \tag{2.59}$$

$$w_{i \leftarrow f} \propto |\vec{\mu}_{fi}|^2 \epsilon^2 \tag{2.60}$$

It is now possible to get to the definition of transition dipole moment:

$$\vec{\mu}_{fi} = \int \Psi^*_f \vec{\mu} \Psi_i d\tau \tag{2.61}$$

The transition dipole moment is defined by a transition between an initial state i, and a final state f, and corresponds to the electric dipole moment associated with this transition. This usually includes the phase factors associated with the two states, but these are not observable.

Propagator methods are used throughout this thesis to calculate electronic excited states. A propagator defines the probability amplitude that a particle at some point $(\vec{r}_1)$, at some time (t_1), will move to a different point $(\vec{r}_2)$ at a time (t_2) later. A propagator $\langle\langle \vec{r}; \vec{r} \rangle\rangle_\omega$ corresponds to the polarizability (α_{if}) and when acting on two states i and f has the following form:

$$\langle\langle \vec{r}; \vec{r} \rangle\rangle_\omega = \sum_{f \neq 0} \frac{|\langle \Psi_i | \vec{r} | \Psi_f \rangle|^2}{\omega - E_f + E_i} - \frac{|\langle \Psi_i | \vec{r} | \Psi_f \rangle|^2}{\omega + E_f - E_i} \tag{2.62}$$

In Equation 2.62, when the frequency ω is equal to the energy difference between states i and f, then a pole will be present. The propagator

relates this to excitation energies E_i and E_f. In the numerator (residue), transition moments between state i and f are determined.

2.16.1 Time-dependent density functional theory (TD-DFT)

Density functional theory is not a wavefunction method, making the description of excited states with the same symmetry as the ground state problematic. Excited state properties, however, can be calculated by time-dependent DFT (linear response) methods, since the excited state is never explicitly needed. These type of methods allow for example the calculation of excitation energies and transition moments, as well as gradients of the excited surface, allowing the excited states to be optimised. The most important theorem for time-dependent DFT, Runge-Gross, states that there is a one-to-one correspondence between the external (time-dependent) potential, $\nu_{\text{ext}}(\vec{r},t)$, and the electronic one-body density, $\rho(\vec{r},t)$, for many-body systems evolving from a fixed initial state Ψ_0. The density $\rho(\vec{r},t)$ is the probability (normalized to the particle number N) of finding any one electron, of any spin σ, at position $\vec{r}$ is:

$$\rho(\vec{r},t) = N \sum_{\sigma,\sigma_2..\sigma_N} \int d^3\vec{r}_2 ... \int d^3\vec{R}_N |\Psi(\vec{r}\sigma, \vec{r}_2\sigma_2 ... \vec{r}_N\sigma_{N,t})|^2 \qquad (2.63)$$

The density of an interacting system is given by:

$$\rho(\vec{r},t) = \sum_{j=1}^{N} |\psi_j(\vec{r},t)|^2 \qquad (2.64)$$

with orbitals $\phi_j(\vec{r},t)$ satisfying the time-dependent Kohn-Sham equation (Equation 2.65).

$$i\frac{\partial}{\partial t}\psi_t(\vec{r},t) = \left[-\frac{\nabla^2}{2} + \nu_{KS}[n;\phi_0(\vec{r},t)\right] \psi_j(\vec{r},t) \qquad (2.65)$$

ν_{KS} is decomposed into three terms:

$$\nu_{KS}[n;\phi_0](r,\vec{r}) = \nu_{\text{ext}}\left[n;\Psi_0\right](\vec{r},t) + \int d^3\vec{r}\,' \frac{n(\vec{r}\,',t)}{|\vec{r}-\vec{r}\,'|} + \nu_{XC}\left[n;\Psi_0,\phi_0\right](\vec{r},t) \tag{2.66}$$

$\nu_{\text{ext}}[n;\Psi_0](\vec{r},t)$ corresponds to the external time-dependent field. The second term on the right-hand side of the equation is the time-dependent Hartree potential, describing the interaction of classical electronic charge distributions. The last term refers to the exchange-correlation potential. Considering time-dependent DFT for a system with initial state (i), then the external potential that produced this density can be identified. The electronic density is a function of three spatial variables and time. It determines all the properties of the interacting many-electron system. Time-dependent DFT is usually more successful for low-energy excitations.

TD-B3LYP and TD-CAM-B3LYP are used throughout this thesis for electronic excited state calculations. CAM-B3LYP uses the coulomb-attenuation method and has advantages over the hybrid method because it accounts for long-range corrections [61] [62]. CAM-B3LYP is more suited to describe charge transfers than TD-B3LYP due to these corrections. It has the same ground state properties of B3LYP, but changes the ratio of Hartree-Fock and B88 exchange. More B88 exchange is used for short distances and Hartree-Fock exchange for longer distances.

2.16.2 Coupled-Cluster response

Coupled-cluster response theory assumes that there is a weak perturbation to the Hamiltonian (e.g an electrical field), meaning that the solution can be written in terms of the eigenstates of the unperturbed system. Coupled-cluster response has many similarities to Møller Plesset theory, although it is a true many-body method.

Recently, two response methods were developed and have been implemented widely in the next chapters: CC2 [63] and CC3 [64]. CC2 was

derived from CCSD by using the doubles contribution arising from the lowest (non-zero) order in perturbation theory. This perturbation is defined the same as in Møller-Plesset theory (true electron-electron potential minus twice the average repulsion). By using this idea it is possible to consider CC2 very similar to MP2 with the feature of orbital relaxation arising from the singles. Although, an approximation to the doubles has been done for CC2 it is not a complete solution for the singles and doubles space as CCSD is, and does not include all terms to infinite order. CC2 is as accurate as the MP2 energy for ground state energies. CC3 can be directly compared to the CCSDT (full coupled-cluster singles, doubles and triples), where the triples contribution is approximated by the expression resulting from the lowest order in perturbation theory. CC2 and CC3 result from the same philosophy in the way they approximate the CCSD and CCSDT models. CC3 is as accurate as CCSD(T) for the ground state. CCSD(T) differs from the full CCSDT as it consists of a perturbative (non-iterative) correction to the CCSD energy. Dynamic molecular properties, energies and transition moments can be obtained by these methods. Crucially CC2 and CC3 response allow the calculation of excited states. By using these models among the hierarchy of coupled-cluster there is a relation as follows for the general accuracy of excited states:

$$\text{HF}<<\text{CC2}<\text{CCSD}<\text{CC3}<\text{CCSDT}$$

CCS(N^4), CC2(N^5), CCSD(N^6), CC3(N^7), CCSDT(N^8), etc. The computational scaling increases with each step. In Figure 2.12 a graphical description of the computational cost/accuracy is provided, more accurate solutions further to the top right.

2.17 Equation of motion Coupled-cluster (EOM-CC)

Coupled-cluster is usually added to calculate ground state energies, but it is also possible to use it for excited states using EOM-CC (equation of motion coupled-cluster) [65]. While a fundamental different theoretical

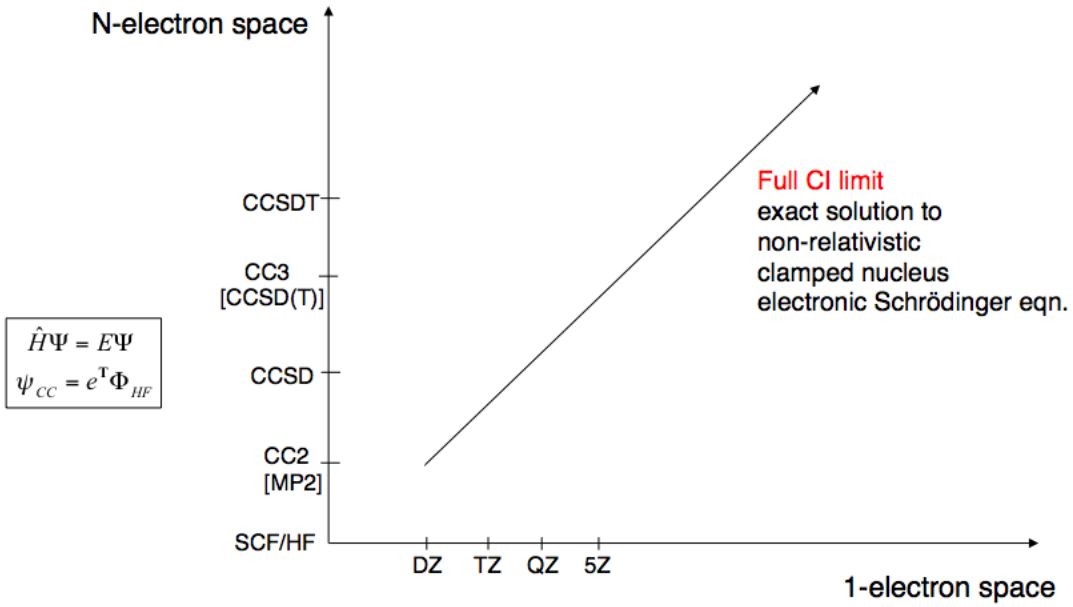

Figure 2.12: Methods and basis set accuracy, and computational cost.

approach to LR-CC, EOM-CC has been shown to give the same excitation energies as LR-CC.

Before writing the EOM-CC equations a sequence of transformations are performed on the wave operator $e^{\hat{T}}$:

$$e^{-T}\hat{H}\Psi = Ee^{-\hat{T}}\Psi \tag{2.67}$$

$$e^{-\hat{T}}\hat{H}e^{\hat{T}}e^{-\hat{T}}\Psi = Ee^{-\hat{T}}\Psi \tag{2.68}$$

doing a similarity transformation on the Hamiltonian:

$$\hat{H}_{mod}\Psi_{mod} = E\Psi_{mod} \tag{2.69}$$

there is no change in energy and: $\hat{H}_{mod}{=}e^{-\hat{T}}\hat{H}\,e^{\hat{T}}$ and $\Psi_{mod}{=}e^{-\hat{T}}\Psi$.

EOM-CC is formulated by using the ground state equation used for coupled-cluster and adding an operator ($\hat{U}_k$) to excite the system to an upper level. $\hat{U}_k$ in Equation 2.70 is defined as "EOM-CC *Ansatz*" meaning that it is an educated guess that will be confirmed later.

$$\Psi_k = \hat{U}_k \Psi_{HF} \tag{2.70}$$

This operator will change the coefficients in front of the configurations. These type of operators are not linear with respect to excitations. For the case of single and double excitations (EOM-CCSD) there is a $\hat{T}$ for the sum of single and double excitations:

$$\hat{T} = \hat{T}_1 + \hat{T}_2 \tag{2.71}$$

and

$$\hat{U_k} = \hat{U}_{k,0} + \hat{U}_{k,1} + \hat{U}_{k,2} \tag{2.72}$$

To exemplify the task of $\hat{U}_{k,0}$ is to make a change on the coefficient in front of the function Ψ_0 to the one appropriate for $|K\rangle$. In this case the operators are different from coupled-cluster:

$$\hat{U}_{k,0} = T_0(k), \tag{2.73}$$

$$\hat{U}_{k,1} = \sum_{a,p} t_a^p(k) \hat{p}^\dagger \hat{a}, \tag{2.74}$$

$$\hat{U}_{k,2} = \sum_{a,b,p,q} t_{ab}^{pq}(k) \hat{q}^\dagger \hat{p}^\dagger \hat{a} \hat{b}, \tag{2.75}$$

this method excites the operators with t amplitudes (different from coupled-cluster t amplitudes). These amplitudes are the main focus of the EOM-CC method.

Once again, it is worth noting that the calculated excitation energies from CC-LR and EOM-CC should be identical. Properties can be different between the two methods e.g. transition moments and oscillator strengths, with the LR-CC properties being theoretically more accurate. EOM-CC methods do not scale correctly with system size for these properties, but the differences are usually small [66] [67]. In Chapter 4 and

6 there are a few comparisons between the excitation energies of EOM-CCSD and LR-CCSD. The values vary slightly due to the use of different basis sets. More details will be added in the respective chapters.

2.18 Thermodynamic properties and models

In this thesis, especially in Chapter 8, thermodynamic properties were calculated. Properties such as enthalpy and entropy were calculated using the Gaussian program [68]. The program assumes an ideal gas system, with non-interacting particles. Another approximation details that the first and higher excited states are considered inaccessible when concerning electronic contributions. The enthalpy, entropy and heat capacity can be calculated from the extrapolation of translational, electronic, rotational and vibrational motion. Using partition function expressions one can calculate the entropy of a system as follows:

$$S = Nk_B + Nk_B ln\left(\frac{q(V,T)}{N}\right) + Nk_B T\left(\frac{\partial lnq}{\partial T}\right)_V \tag{2.76}$$

Where K_B is Boltzmann's constant, N number of particles and $q(V,T)$ the partition function. Likewise, the enthalpy can be calculated consequently obtaining Gibbs' energy. In Gaussian [68], the expressions used to calculate the reaction enthalpy and reaction Gibbs energy are described in Equation 2.77 and Equation 2.78:

$$\Delta_r H^\circ(T) = \sum(\epsilon_0 + H_{corr})_{products} - \sum(\epsilon_0 + H_{corr})_{reactants} \tag{2.77}$$

$$\Delta_r G^\circ(T) = \sum(\epsilon_0 + G_{corr})_{products} - \sum(\epsilon_0 + G_{corr})_{reactants} \tag{2.78}$$

ϵ_0 is the absolute energy, H_{corr} and G_{corr} the corrections for the enthalpy and free energy values respectively. These are fundamental for reaction mechanisms and to analyse reaction profiles.

Bibliography

[1] von Neumann, J.; Wigner, E. *Phys. Z* **1929**, *30*, 467–470.

[2] Teller, E. *Israel J. Chem.* **1969**, *7*(2), 227–235.

[3] Paterson, M. J.; Bearpark, M. J.; Robb, M. A.; Blancafort, L.; Worth, G. A. *Phys. Chem. Chem. Phys.* **2005**, *7*, 2100–2115.

[4] Paterson, M. J.; Blancafort, L.; Wilsey, S.; Robb, M. A. *J. Phys. Chem. A* **2002**, *106*(47), 11431–11439.

[5] Paterson, M. J.; Robb, M. A.; Blancafort, L.; DeBellis, A. D. *J. Phys. Chem. A* **2005**, *109*(33), 7527–7537.

[6] Sicilia, F.; Blancafort, L.; Bearpark, M. J.; Robb, M. A. *Journal of Chemical Theory and Computation* **2008**, *4*(2), 257–266.

[7] Bersuker, I. B. *Chem. Rev.* **2001**, *101*(4), 1067–1114.

[8] Bersuker, I. *The Jahn-Teller Effect;* Cambridge University Press, 2006.

[9] Jahn, H. A.; Teller, E. In *Stability of polyatomic molecules in degenerate electronic states. I. Orbital degeneracy*, Vol. 161, pages 220–235. The Royal Society, 1937.

[10] Fuß, W.; Trushin, S.; Schmid, W. *Res. Chem. Intermed.* **2001**, *27*(4-5), 447–457.

[11] Trushin, S.; Fuß, W.; Schmid, W. *Chem. Phys.* **2000**, *259*(2-3), 313–330.

[12] Trushin, S. A.; Fuß, W.; Kompa, K. L.; Schmid, W. E. *J. Phys. Chem. A* **2000**, *104*(10), 1997–2006.

[13] Trushin, S. A.; Fuß, W.; Schmid, W. E.; Kompa, K. L. *J. Phys. Chem. A* **1998**, *102*(23), 4129–4137.

[14] Trushin, S.; Kosma, K.; Fuß, W.; Schmid, W. *Chem. Phys.* **2008**, *347*(1-3), 309–323.

[15] Binkley, J. S.; Pople, J. A.; Hehre, W. J. *J. Am. Chem. Soc.* **1980**, *102*(3), 939–947.

[16] Gordon, M. S.; Binkley, J. S.; Pople, J. A.; Pietro, W. J.; Hehre, W. J. *J. Am. Chem. Soc.* **1982**, *104*(10), 2797–2803.

[17] Pietro, W. J.; Francl, M. M.; Hehre, W. J.; DeFrees, D. J.; Pople, J. A.; Binkley, J. S. *J. Am. Chem. Soc.* **1982**, *104*(19), 5039–5048.

[18] Dobbs, K. D.; Hehre, W. J. *J. Comp. Chem.* **1986**, *7*(3), 359–378.

[19] Dobbs, K. D.; Hehre, W. J. *J. Comp. Chem.* **1987**, *8*(6), 861–879.

[20] Dobbs, K.; Hehre, W. *J. Comp. Chem.* **1987**, *8*(6), 880–893.

[21] Gordon, M. S. *Chem. Phys. Lett.* **1980**, *76*(1), 163–168.

[22] Hehre, W. J.; Ditchfield, R.; Pople, J. A. *J. Chem. Phys.* **1972**, *56*(5), 2257–2261.

[23] Dill, J. D.; Pople, J. A. *J. Chem. Phys.* **1975**, *62*(7), 2921–2923.

[24] Hariharan, P.; Pople, J. *Mol. Phys.* **1974**, *27*(1), 209–214.

[25] Binning, R. C.; Curtiss, L. A. *J. Comp. Chem.* **1990**, *11*(10), 1206–1216.

[26] Rassolov, V. A.; Ratner, M. A.; Pople, J. A.; Redfern, P. C.; Curtiss, L. A. *J. Comp. Chem.* **2001**, *22*(9), 976–984.

[27] Francl, M. M.; Pietro, W. J.; Hehre, W. J.; Binkley, J. S.; Gordon, M. S.; DeFrees, D. J.; Pople, J. A. *J. Chem. Phys.* **1982**, *77*(7), 3654–3665.

[28] Blaudeau, J.-P.; McGrath, M. P.; Curtiss, L. A.; Radom, L. *J. Chem. Phys.* **1997**, *107*(13), 5016–5021.

[29] Rassolov, V. A.; Pople, J. A.; Ratner, M. A.; Windus, T. L. *J. Chem. Phys.* **1998**, *109*(4), 1223–1229.

[30] Hariharan, P. C.; Pople, J. A. *Theor. Chim. Acta. 28*(3), 213–222.

[31] Dunning, T. H. *J. Chem. Phys.* **1989**, *90*(2), 1007–1023.

[32] Balabanov, N. B.; Peterson, K. A. *J. Chem. Phys.* **2005**, *123*(6), 064107.

[33] Balabanov, N. B.; Peterson, K. A. *J. Chem. Phys.* **2006**, *125*(7), 074110.

[34] Hay, P. J.; Wadt, W. R. *J. Chem. Phys.* **1985**, *82*(1), 299–310.

[35] Dolg, M.; Wedig, U.; Stoll, H.; Preuss, H. *J. Chem. Phys.* **1987**, *86*(2), 866–872.

[36] Greer, J. *J. Comput. Phys.* **1998**, *146*(1), 181–202.

[37] Coe, J. P.; Taylor, D. J.; Paterson, M. J. *J. Chem. Phys.* **2012**, *137*(19), 194111.

[38] Kelly, T. P.; Perera, A.; Bartlett, R. J.; Greer, J. C. *J. Chem. Phys.* **2014**, *140*(8), 084114.

[39] Gyorffy, W.; Bartlett, R.; Greer, J. *J. Chem. Phys.* **2008**, *129*(6), 064103.

[40] Coe, J. P.; Paterson, M. J. *J. Chem. Phys.* **2013**, *139*(15), 154103.

[41] Coe, J. P.; Taylor, D. J.; Paterson, M. J. *J. Comp. Chem.* **2013**, *34*(13), 1083–1093.

[42] Coe, J. P.; Paterson, M. J. *J. Chem. Phys.* **2014**, *141*(12), 124118.

[43] Coe, J.; Murphy, P.; Paterson, M. *Chem. Phys. Lett.* **2014**, *604*(0), 46–52.

[44] Coe, J.; Paterson, M. *Theor. Chem. Acc.* **2015**, *134*(5), 58.

[45] Roos, B.O.; Siegbahn, P. *Modern Theoretical Chemistry*, Vol. III; H.F. Schaefer, Plenum Press, New york, 1977.

[46] Roos, B. O.; Taylor, P. R.; Siegbahn, P. E. *Chem. Phys.* **1980**, *48*(2), 157–173.

[47] Siegbahn, P. E. M. *J. Chem. Phys.* **1979**, *70*(12), 5391–5397.

[48] Andersson, K.; Malmqvist, P.; Roos, B. O. *J. Chem. Phys.* **1992**, *96*(2), 1218–1226.

[49] Grimme, S. *J. Comp. Chem.* **2006**, *27*(15), 1787–1799.

[50] Tao, J.; Perdew, J. P.; Staroverov, V. N.; Scuseria, G. E. *Phys. Rev. Lett.* **2003**, *91*, 146401.

[51] Becke, A. D.; Roussel, M. R. *Phys. Rev. A* **1989**, *39*, 3761–3767.

[52] Van Voorhis, T.; Scuseria, G. E. *J. Chem. Phys.* **1998**, *109*(2), 400–410.

[53] Hamprecht, F. A.; Cohen, A. J.; Tozer, D. J.; Handy, N. C. *J. Chem. Phys.* **1998**, *109*(15), 6264–6271.

[54] Wilson, P. J.; Bradley, T. J.; Tozer, D. J. *J. Chem. Phys.* **2001**, *115*(20), 9233–9242.

[55] Zhao, Y.; Truhlar, D. *Theor. Chem. Acc.* **2008**, *120*(1-3), 215–241.

[56] Becke, A. D. *J. Chem. Phys.* **1993**, *98*(7), 5648–5652.

[57] Lee, C. Y.; Parr, W. *Phys. Rev. A* **1988**, *38*, 3098–3100.

[58] Vosko, S. H.; Wilk, L.; Nusair, M. *Can. J. Phys.* **1980**, *58*(8), 1200–1211.

[59] Vosko, S.; Wilk, L.; Nusair, M. *Can. J. Phys.* **1980**, *58*(8), 1200–1211.

[60] Tao, J.; Perdew, J. P.; Staroverov, V. N.; Scuseria, G. E. *Phys. Rev. Lett.* **2003**, *91*, 146401.

[61] Yanai, T.; Tew, D. P.; Handy, N. C. *Chem. Phys. Lett.* **2004**, *393*(1–3), 51–57.

[62] Tawada, Y.; Tsuneda, T.; Yanagisawa, S.; Yanai, T.; Hirao, K. *J. Chem. Phys.* **2004**, *120*(18), 8425–8433.

[63] Christiansen, O.; Koch, H.; Jørgensen, P. *Chem. Phys. Lett.* **1995**, *243*(5-6), 409–418.

[64] Christiansen, O.; Koch, H.; Jørgensen, P. *J. Chem. Phys.* **1995**, *103*(17), 7429–7441.

[65] Geertsen, J.; Rittby, M.; Bartlett, R. J. *Chem. Phys. Lett.* **1989**, *164*(1), 57–62.

[66] Kobayashi, R.; Koch, H.; Jørgensen, P. *Chem. Phys. Lett.* **1994**, *219*(1-2), 30–35.

[67] Koch, H.; Kobayashi, R.; Sanchez de Merás, A.; Jørgensen, P. *J. Chem. Phys.* **1994**, *100*(6), 4393–4400.

[68] Gaussian 09 Revision A.02. Frisch, M. J.; Trucks, G. W.; Schlegel, H. B.; Scuseria, G. E.; Robb, M. A.; Cheeseman, J. R.; Scalmani, G.; Barone, V.; Mennucci, B.; Petersson, G. A.; Nakatsuji, H.; Caricato, M.; Li, X.; Hratchian, H. P.; Izmaylov, A. F.; Bloino, J.; Zheng, G.; Sonnenberg, J. L.; Hada, M.; Ehara, M.; Toyota, K.; Fukuda, R.; Hasegawa, J.; Ishida, M.; Nakajima, T.; Honda, Y.; Kitao, O.; Nakai, H.; Vreven, T.; Montgomery, Jr., J. A.; Peralta, J. E.; Ogliaro, F.; Bearpark, M.; Heyd, J. J.; Brothers, E.; Kudin, K. N.; Staroverov, V. N.; Kobayashi, R.; Normand, J.; Raghavachari, K.; Rendell, A.; Burant, J. C.; Iyengar, S. S.; Tomasi, J.; Cossi, M.; Rega, N.; Millam, J. M.; Klene, M.; Knox, J. E.; Cross, J. B.; Bakken, V.; Adamo, C.; Jaramillo, J.; Gomperts, R.; Stratmann, R. E.; Yazyev, O.; Austin, A. J.; Cammi, R.; Pomelli, C.; Ochterski, J. W.; Martin, R. L.; Morokuma, K.; Zakrzewski, V. G.; Voth, G. A.; Salvador, P.; Dannenberg, J. J.; Dapprich, S.; Daniels, A. D.; Farkas, .; Foresman, J. B.; Ortiz, J. V.; Cioslowski, J.; Fox, D. J.

Chapter 3

Computational study of the electronic excited states of some common first-row transition metal complexes: a coupled-cluster and density functional theory analysis

3.1 Introduction

The first part of this chapter focuses on excited states of inorganic complexes that have never undergone a rational computational study before. This kind of investigation can be used in order to evaluate excited states of well-known molecules, and whenever possible, to compare to experimental results. The aim of this chapter is to develop an original computational study for inorganic systems, which are small and not too computationally demanding with interesting properties. In Chapters 4, 5 and 6, the electronic structure of the complexes is more challenging.

In the second part of this study, computational models were chosen to evaluate the different ground state properties of first-row transition metals (from scandium to copper) monoxides and try to understand the interactions between metals and oxygen atoms using density functional theory. These unsaturated complexes are important to investigate, because they can be used as models for larger complexes that are more

demanding to study. Transition metal oxides are very important in different fields like microelectronics or catalysis.

Performing a computational study on first-row transition metal complexes can provide relevant information on properties of the most diverse systems and analyse the performance of various computational methodologies. Essential information can be gathered that ranges from thermodynamic to geometric parameters. In the past, benchmarks of organic molecules have been performed [1] [2] [3], but not for inorganic systems. There are some newer studies that discuss the thermochemical properties of a large number of transition metal complexes [4].

Electronic excited states are an area of intense theoretical research for a wide range of systems and different methods. With increasing computational power, various methods like EOM-CCSD, CC2 or CC3 can be assessed. New DFT methods, such as CAM-B3LYP have been developed in order to improve weaknesses found when using TD-DFT to calculate electronic excited states.

Coupled-cluster methods were used to benchmark the electronic excited states of widely used organic molecules [5] [6] [7]. These performed really well for organic systems, providing a low error compared to experimental results. Other properties like electronic spectra for other important organic systems have also been studied [8] [9] [10]. So far it was discussed how these methods perform for organic systems only. A study of this nature for inorganic systems presents a more difficult challenge. Electron correlation is much more important in these type of systems than in their organic counterparts. When using methods such as EOM-CCSD or CC3 the computational expense is very high, it scales to N^6 for EOM-CCSD and N^7 for CC3. The electronic spectra of transition metal systems has been mentioned to often be broad and featureless due to the high density of states and many electronic transitions of different chemical character, making the spectral assignment very difficult [11]

[12].

3.1.1 The inorganic complexes

The choice of molecules was diverse. It ranged from widely used complexes, found in any chemistry laboratory to less common ones, that can be used to mimic the behaviour of saturated complexes and provide insight about their electronic properties. The chosen inorganic complexes have different properties: they range from closed-shell and open-shell, singlet, doublet and triplet spin complexes, all including first-row transition metals. The complexes studied are $TiCl_4$, $[VO_4]^{3-}$, $[Cu(NH_3)_2]^{2+}$, $[MnCl_5]^{2-}$, $Mn(CO)_4NO$, $H_2Fe(CO)_4$, $[Ni(CN)_5]^{3-}$ and $[TiF_6]^{2-}$.

Titanium tetrachloride has been well-described theoretically in the literature by Nakatsuji *et al* [13]. The group performed calculations not only in the electronic excited states but also on the ionized states. The importance of this inorganic complex comes from the fact that it is an important Lewis acid, for both organic and inorganic chemistry. It has an important role for catalysis in the Ziegler-Natta process. Using two robust methods (SAC-CI, MRD-CI) the researchers managed to reproduce a large region of the spectral data for $TiCl_4$ and compare their results with experimental ones. The results obtained by Nakatsuji *et al* were compared to the computational calculations performed in this chapter.

Vanadium oxide complexes have been subjected to several studies in the past [14] [15] [16]. The metal-oxygen bond description is not only fundamental for properties like chemisorption but also for catalytic properties of metal oxides. Wu *et al* performed an extensive investigation on different oxygen/vanadium complexes. Potential energy surfaces (PES) for a series of monovanadium species (1-4 oxygens) were investigated and characterized. In 1974 Petit *el al* investigated the magnetic cir-

cular dichroism and absorption spectra of d^0 tetrahedral oxyanions and thioanions, which included $[VO_4]^{3-}$ [17]. The two bands described in the absorption spectra correspond to 36900 cm^{-1} and 45000 cm^{-1}. These are due to the brightest states described in the literature.

$[Cu(NH_3)_2]^{2+}$ was synthesized by Wu *et al* [18] in recent years. Copper complexes are widely used either in inorganic or in organic chemistry and they are often associated with biological processes. In 1999, Wu *et al* explored the properties of Cu(0), due to its potential applicability in catalysis. A year later the formation of charged copper(II) complexes were reported [19]. The difficulties generated by these kind of complexes are related to the apparent difference between the second ionization potential of the metal and the first of the solvent. This contact created straight away a charge transfer from the complex to the solvent [20]. The barrier heights for the formation of di-ligated Cu^{2+} complexes are around 167 kJ/mol which provided evidence that these species can be detected in the gas phase. A detailed theoretical investigation has been performed for $[Cu(NH_3)_2]^{2+}$ [21] as well as other complexes bound to copper (II). Although a lot of properties have been calculated, such as equilibrium structures or transition state geometries, the excited states have never been characterized. Although this complex has been synthetized, it is not widely studied yet, so there are no experimental spectra. The computational study provides some insight on how the low-lying excited states perform with diverse levels of theory.

$[MnCl_5]^{2-}$ has been described in the literature in 1971 by Bellitto *et al* [22]. The molecular configuration of the anion $[MnCl_5]^{2-}$ was also described in the same year by Bernal *et al* [23]. Manganese is fundamental for binding and activation processes or to water oxidation catalysis in plants. This molecule is used in biological related complexes and is involved in heme enzymes [24] [25]. Although this compound has been extensively used in the literature as a reactant for different biological processes, there is no electronic spectra analysis yet.

The first studies for $Mn(CO)_4NO$ were carried out in 1961 [26]. More recently, Crichton *et al* performed a detailed study of the photochemistry of this complex [27]. There have been only a few studies done on thermal, or substitution reactions [28]. It can undergo as well photolysis in argon or methane matrices. In 1987, the first theoretical study was performed on $Mn(CO)_4NO$ [29]. The researchers used Xα-SW and configuration interaction, using Koopmans' theorem to analyse the valence ionization potentials. The second theoretical study carried out for this complex is an analysis of the infrared spectrum [30]. The results of the experimental data by Polletti *et al* provide evidence for symmetry of the molecule being C_{2v}. The researchers analysed the 27 fundamental modes of this complex for two different symmetries C_{3v} and C_{2v}, the latter is considered the most stable geometry. Unfortunately, the low-lying excited states have not been investigated yet, so it is not possible to compare the experimental results with theoretical ones calculated in this chapter.

$H_2Fe(CO)_4$ is an important complex that has been subject of study due to its ability of being photoreduced, losing its hydrogens, generating intermediates, that are very important in the activation of carbon-hydrogen bonds [31, 32, 33, 34, 35, 36]. A few theoretical studies have been performed for $H_2Fe(CO)_4$ [37] [38] [39]. There is no experimental data, for the low-lying excited states of this complex, since the spectra are very poorly resolved. Heitz *et al* performed an extensive study using CASSCF and CASPT2 for the low-lying excited states and characterized them. Different active spaces were used to be able to capture the static and dynamic correlation necessary for these difficult inorganic complexes. The results of the excited states calculated with CASPT2 and CASSCF/CCI were compared with the computational calculations performed here.

$[Ni(CN)_5]^{3-}$ is one of the few nickel complexes that has five non-chelated

ligands. The first X-ray crystallographic evidence for $[Ni(CN)_5]^{3-}$ was found in 1970 [40]. It is curious to analyse this inorganic complex since nickel behaves as Ni(II), which is not common for this transition metal. Unfortunately, it was not found in the literature any evidence of absorption spectra performed in this complex, which does not yet allow any comparison between the computational data and the experimental one.

The first article describing the X-ray absorption spectra of $[TiF_6]^{2-}$ dates back to 1982 [41]. Further properties of $[TiF_6]^{2-}$ were not studied until twenty years later when Tyagi *et al* wrote about the preparation, crystal structure, and magnetic properties properties of titanium hexafluoride. More recent studies show that $[TiF_6]^{2-}$ can be formed from TiO_2 :

$$TiO_2 + 6F^- + 4H \rightarrow [TiF6]^{2-} + 2H_2O \tag{3.1}$$

Titanium hexafluoride is used for generating nanotubes of titanium oxide, the formation/dissolution of $[TiF_6]^{2-}$ leads to the growth of titanium nanotubes [42]. Titanium hexafluoride is ejected using an electric field. The Ti^{4+} ions are believed to play an important role in the formation of these tubes. Even though a lot of research has been performed for $[TiF_6]^{2-}$, the low-lying excited states have not been calculated experimentally yet.

When describing the low-lying excited states of any of the mentioned transition metal complexes, different chemical characters are shown: metal-to-ligand charge transfers, ligand-to-metal charge transfers or ligand-to-ligand charge transfers. When it is possible, the oscillator strengths are calculated and an attempt to compare these values with experimental or previous computational ones. In Figures 3.1, 3.2, 3.3, 3.4, 3.5, 3.6, 3.7 and 3.8, the mentioned complexes are depicted, showing their optimised structures and respective symmetry point group.

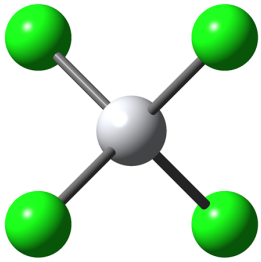

Figure 3.1: $TiCl_4$ - T_d

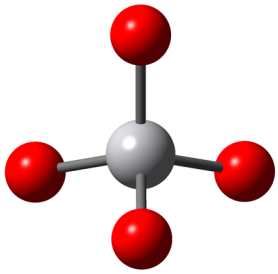

Figure 3.2: $[VO_4]^{3-}$ - T_d

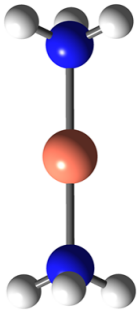

Figure 3.3: $[Cu(NH_3)_2]^{2+}$ - D_{3d}

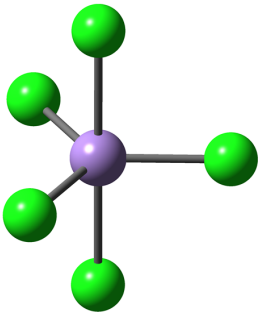

Figure 3.4: $[Mn(Cl)_5]^{2-}$ - D_{3h}

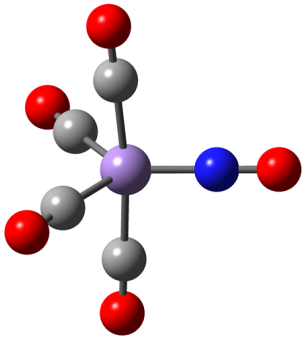

Figure 3.5: $Mn(CO)_4NO$ - C_{2v}

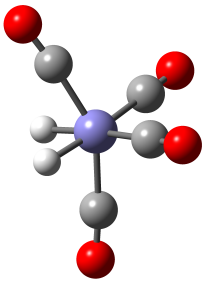

Figure 3.6: $H_2Fe(CO)_4$ - C_{2v}

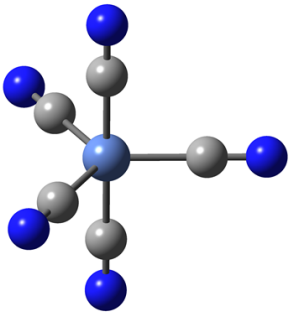

Figure 3.7: $[Ni(CN)_5]^{3-}$ - D_{3h}

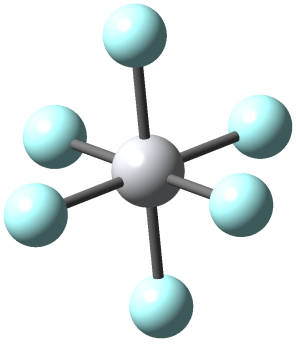

Figure 3.8: TiF_6^{2-} - O_h

3.1.2 First-row transition metal monoxides

The second part of this chapter focuses on the study of the most stable spin state for first-row transition metal monoxides and their bonding properties. When it is possible compare it to other literature and experimental data. Transition metal oxides are very important in many fields (microelectronics, material sciences, catalysis, etc) so a lot of research has been carried out throughout the years. Including transition metal monoxides in this chapter was fundamental, since it represents the chance to study the ability of these highly correlated methods to model excited states in the single M-O. These unsaturated model complexes can also be used to extrapolate properties to larger systems.

In the literature there are a few theoretical studies in first-row transition metal monoxides, describing different properties [43, 44, 45, 46, 47, 48, 49, 50]. Dolg *et al* performed a study using *ab initio* pseudopotential methods to study some first-row transition metal monoxides and iron monohydride [51]. Although this article presents some properties for first-row transition metal monoxides, the properties calculated are more related to technical problems such as testing different pseudopotentials or evaluating different basis sets. There are a few researchers that focused on the energy bands and adsorbing properties of first-row transition metal monoxides. One of the most recent studies was performed by Xu *et al*. The researchers tried to establish a relationship between the reactivity and the electronic structure to be able to connect the oxide surface with the first-row transition metal. The metals used were copper, nickel, manganese, vanadium and titanium [52].

Other previous studies debated the use of first-row transition metal monoxides either as being insulators or not and how the energy bands are described [53] [54] [55]. One of the most up-to-date articles was performed by Dai *et al* that calculated excited states of 3d transition metal monoxides [56]. They calculated many of the important proper-

ties as well as the low-lying excited states of the first-row transition metal monoxides.

3.2 Computational details

For the first part of this chapter all the ground state transition metal complexes were optimised using B3LYP density functional with the cc-pVTZ all electron basis set by Peterson and co-workers [57]. For the transition metal monoxides, B3LYP proved in previous studies to be a good compromise, so these complexes were optimised using this DFT functional along with cc-pVTZ all electron basis set. Frequency calculations were performed to make sure they were a minimum on the potential energy surface.

For the inorganic complexes all excited state calculations were performed with cc-pVTZ, except for $H_2Fe(CO)_4$, where cc-pVDZ was applied, due to difficulties in converging the calculations, especially for EOM-CCSD. Excited states were calculated for each complex using CIS, CIS(D), EOM-CCSD, TD-B3LYP and TD-CAM-B3LYP density functionals. For the excited states of transition metal monoxides TD-B3LYP was used along with cc-pVTZ. The calculations were performed using the Gaussian 09 program [58].

The relative accuracy and computational cost of each coupled-cluster response model along with EOM-CCSD is presented in Table 3.1. EOM-CCSD is considered the most robust method and was chosen to analyse the character of the transitions in the result section. This method is well-known for providing accurate results, usually, in close agreement to experimental ones [59] [60]. The computational cost increases by an order of magnitude from N^4 (CIS, TD-DFT), where N is the number of electrons to CCSDT, that has a computational cost of N^8, and is not practicably used for transition metal complexes.

To provide the reader an idea of the degree of multireference character, the T_1 diagnostic [61] was evaluated. The basis set used for this calculations was the correlation consistent, cc-pVTZ.

Methods	**Computational cost/ N^x**	**Transition moments**	**Singly excited states**
TD-DFT	N^4	-	-
CIS	N^4	0	1
CIS(D)	N^5	0	1
CC2	N^5	1	2
EOM-CCSD	N^6	2	2
CC3	N^7	3	3
CCSDT	N^8	3	3

Table 3.1: Relative computational cost and accuracy of each coupled-cluster method used, N is the number of electrons in the system.

3.3 Results and discussion

3.3.1 First-row transition metal complexes

The lowest singlet excited states and corresponding oscillator strengths for a series of complexes are shown in Tables 3.2, 3.3, 3.4, 3.5, 3.6, 3.7, 3.8 and 3.9.

The first complex to be considered was $TiCl_4$ and the first T_1 and T_2 states are shown in Table 3.2. CIS overestimates the excitation energy for the three considered states and CIS(D) underestimates it compared to experiment. The perturbation on the doubles has a considerable effect on the excitation energy. EOM-CCSD overestimates the vertical excitation energy, around 0.8 eV for both comparable states (1^1T_1 and 1^1T_2). TD-B3LYP has an almost spot on result for the 1^1T_1 state, being only 0.050 eV higher in energy than the experimental result. TD-CAM-B3LYP gets a slightly higher value for the excitation energy, around 0.34 eV for the first state and 0.15 eV for the second state. The character of the transitions was analysed looking at EOM-CCSD molecular orbital coefficients and all the transitions reflect a LMCT.

For $[VO_4]^{3-}$ the results are presented in Table 3.2. CIS overestimates the excitation energies for all given states. CIS(D) with perturbation theory applied to the doubles has considerable discrepancies, having very low excitation energies. For the 5^1T_2, TD-CAM-B3LYP calculated a result closer to experiment (4.220 eV), than EOM-CCSD (4.185 eV). For TD-CAM-B3LYP the long range correction proves to be very important to describe this state. TD-B3LYP is almost 1.0 eV wrong. CIS and CIS(D) give spurious results for all the states.

$[Cu(NH_3)_2]^{2+}$ as it was shown in the introduction, has been synthesized, and these results demonstrate how hard it can be to describe transition metals with theoretical methods (Table 3.3). The most robust method EOM-CCSD calculates the first two excited states as having negative excitation energies, so does TD-B3LYP. There are no calculated vertical excitation energies experimentally, but it is clear that methods are breaking down in this case. Being an unsaturated, open-shell system $[Cu(NH_3)_2]^{2+}$ is a very difficult complex to describe due to strong correlation effects. TD-CAM-B3LYP, using long range correction does not calculate the vertical excitation energies as being negative, but for the first two states it calculates them as having the same energy. The character of the transitions was attributed as MLCT.

Looking at $[Mn(Cl)_5]^{2-}$, the range of methods chosen did not fluctuate much when calculating the low-lying excited states (Table 3.4). On the contrary to what happened for the previous complexes, CIS was only 0.331 eV different for the first state compared to EOM-CCSD. For the next states the difference was larger, around 1.5 eV. The difference in energies between CIS and CIS(D) is not very large for the first two states, but for 3^5B_2 the difference is around 1.0 eV. TD-DFT provided close results to EOM-CCSD with small differences in the excitation energies. The character of the states was a mixture between $\pi \rightarrow \pi^*$ and LMCT.

The next analysed managanse complex, $Mn(CO)_4NO$ has a mixed character for the first three excited states (Table 3.5). CIS underestimates the vertical excitation energies compared to EOM-CCSD for the three states. CIS(D) has very different excitation energies compared to CIS. TD-B3LYP and TD-CAMB3LYP have similar results to EOM-CCSD, although TD-B3LYP has closer results to EOM-CCSD.

When looking at $H_2Fe(CO)_4$, again, CIS underestimates the electronic excited states when compared to CASPT2 and CASSCF/CCI [62] and CIS(D) overestimates it (Table 3.6). As already seen in most of the previous complexes TD-DFT methods have close energetic results to CASPT2 and CASSCF/CCI with no more than 0.20 eV differences for the first two considered and 0.40 eV for 1^1A_1. EOM-CCSD is surprisingly around 0.40 eV higher than the values calculated by Heitz *et al.* The transitions for this complex are of MLCT character.

The second to last studied complex was $[Ni(CN)_5]^{3-}$ (Table 3.7). For CIS, the first excited state energy is about 1.1 eV different when compared to EOM-CCSD for the $1^1E^{'}$ state, but for the second and third state is 2.2 eV higher. When looking at CIS(D) the excitation energy for the first excited state is very close to EOM-CCSD, but for the third is already 3.3 eV higher. As happened before, TD-DFT calculations have close values to EOM-CCSD. The largest difference being 0.4 eV. The character of the states is highly mixed.

The last studied complex was $[TiF_6]^{2-}$. The excitation energies of the first three excited states are very high and CIS overestimates for the first two states, around 3 eV for the first one and 2.5 eV for the second one compared to EOM-CCSD. CIS(D) underestimates it by almost the same amount as CIS did for the first two states. This is the only case where TD-B3LYP and TD-CAM-B3LYP do not have close results to EOM-CCSD, with differences around 1.0 eV to 1.5 eV.

State	Character	CIS	CIS(D)	EOM-CCSD	B3LYP	CAM-B3LYP	SAC-CI [13]	MRD-CI [13]	Exp[63]
1^1T_1	LMCT	6.552	2.254	4.614	4.050	4.343	4.19	4.97	4.00
		(0.000)		(0.000)	(0.000)	(0.000)	(0.000)	(0.000)	-
1^1T_2	LMCT	6.775	2.675	4.821	4.248	4.571	4.42	5.08	4.43
		(0.0242)		(0.0424)	(0.0165)	(0.0197)	(0.00560)	(0.00510)	
2^1T_1	LMCT	6.697	4.062	5.202	4.730	4.964	4.98	6.02	-
		(0.000)		(0.000)	(0.000)	(0.000)	(0.000)	(0.000)	

Table 3.2: Singlet excited states (eV) and corresponding oscillator strengths for $TiCl_4$.

State	Character	CIS	CIS(D)	EOM-CCSD	B3LYP	CAM-B3LYP	Expt.	[17]
1^1T_1	LMCT	3.029	0.197	1.372	1.092	1.559	-	
		(0.000)		(0.000)	(0.000)	(0.000)		
2^1T_1	LMCT	3.743	0.801	2.088	1.831	2.277	-	
		(0.0137)		(0.0025)	(0.000)	(0.0053)		
3^1T_1	LMCT	3.845	0.927	2.168	1.864	2.327	-	
		(0.000)		(0.000)	(0.000)	(0.000)		
5^1T_2	LMCT	5.342	1.926	4.185	3.602	4.220	4.57	
		(0.1452)		(0.1526)	(0.1752)	(0.1586)	(0.15)	

Table 3.3: Singlet excited states (eV) and corresponding oscillator strengths for $[VO_4]^{3-}$.

State	Character	CIS	CIS(D)	EOM-CCSD	B3LYP	CAM-B3LYP
1^2A_g	MLCT	-0.486	-0.664	-0.863	-1.310	1.148
		(0.000)		(0.000)	(0.000)	(0.000)
2^2A_g	MLCT	0.091	0.0240	-0.0116	-0.120	1.148
		(0.000)		(0.000)	(0.000)	(0.000)
3^2A_g	MLCT	0.372	0.357	0.326	0.251	1.224
		(0.000)		(0.000)	(0.000)	(0.000)

Table 3.4: Singlet excited states (eV) and corresponding oscillator strengths for $[Cu(NH_3)_2]^{2+}$.

State	Character	CIS	CIS(D)	EOM-CCSD	B3LYP	CAM-B3LYP
1^5B_1	Mixed character	2.000	1.910	1.669	1.333	1.420
		(0.0164)		(0.0198)	(0.0101)	(0.0120)
1^5B_2	Mixed character	2.501	2.514	2.016	1.663	1.871
		(0.000)		(0.000)	(0.000)	(0.000)
3^5B_2	Mixed character	3.364	2.352	2.519	2.074	2.335
		(01868)		(0.0681)	(0.0137)	(0.0320)

Table 3.5: Singlet excited states (eV) and corresponding oscillator strengths for $[MnCl_5]^{2-}$.

State	Character	CIS	CIS(D)	EOM-CCSD	B3LYP	CAM-B3LYP
1^1A_2	Mixed character	1.511	2.861	2.710	2.414	2.143
		(0.000)		(0.000)	(0.000)	(0.000)
1^1B_2	Mixed character	2.594	4.498	3.514	3.116	3.151
		(0.0023)		(0.0196)	(0.0028)	(0.0025)
1^1B_1	Mixed character	3.382	5.316	3.602	3.941	3.266
		(0.0001)		(0.0030)	(0.0005)	(0.000)

Table 3.6: Singlet excited states (eV) and corresponding oscillator strengths for $Mn(CO)_4NO$.

State	Character	CIS	CIS(D)	EOM-CCSD	B3LYP	CAM-B3LYP	CASPT2 [62]	CASSCF/CCI [62]
1^1B_1	MLCT	3.717	5.762	5.199	4.668	4.677	4.800	4.776
		(0.0015)		(0.0101)	(0.0044)	(0.0049)	(0.327)	(0.327)
1^1B_2	MLCT	3.791	5.866	5.315	4.785	4.762	4.873	4.879
		(0.0068)		(0.0307)	(0.0218)	(0.0231)	(0.013)	(0.013)
1^1A_1	MLCT	5.022	6.520	5.735	4.815	4.881	5.233	5.230
		(0.0010)		(0.0017)	(0.0006)	(0.0008)	(0.275)	(0.275)

Table 3.7: Singlet excited states (eV) and corresponding oscillator strengths for $H_2Fe(CO)_4$.

State	Character	CIS	CIS(D)	EOM-CCSD	B3LYP	CAM-B3LYP
$1^1E'$	Mixed character	1.617	2.631	2.748	2.461	2.369
		(0.0012)		(0.0096)	(0.0070)	(0.0060)
$1^1E''$	Mixed character	2.188	3.386	3.551	3.384	3.325
		(0.000)		(0.000)	(0.000)	(0.000)
$2^1E'$	Mixed character	7.259	8.388	5.044	4.809	5.436
		(0.000)		(0.0041)	(0.0027)	(0.0018)

Table 3.8: Singlet excited states (eV) and corresponding oscillator strengths for $[Ni(CN)_5]^{3-}$.

State	Character	CIS	CIS(D)	EOM-CCSD	B3LYP	CAM-B3LYP
1^1A_{1g}	LMCT	10.167	4.337	7.179	5.675	6.049
		(0.000)		(0.000)	(0.000)	(0.000)
1^1T_{1g}	LMCT	9.667	6.434	7.391	5.692	5.722
		(0.000)		(0.000)	(0.000)	(0.000)
2^1T_{1g}	LMCT	-	-	7.400	5.722	6.132
				(0.000)	(0.000)	(0.000)

Table 3.9: Singlet excited states (eV) and corresponding oscillator strengths for $[TiF_6]^{2-}$.

Table 3.10 describes the degree of multireference character of the studied complexes and gives some insight into the need of using a multireference wavefunction. As described in the article by Lee [61] when a complex has a T_1 value above 0.02 the multireference character is substantial. In 2001, Jiang *et al* analysed the challenges of using T_1 dignostics for 3d transition metals [4]. They concluded that a new criteria, namely $T_1 > 0.05$ is needed to quantify the multireference charater on 3d transition metals. Most of the complexes have a lower than 0.05 value of T_1, except for $H_2Fe(CO)_4$ and $MnCO_4NO$, which have a value of 0.059 and 0.063 respectively. For these complexes it is advisable to use multireference methods.

Transition metal monoxide	**T_1 diag**
$TiCl_4$	0.024
$[VO_4\ ]^{3-}$	0.037
$[Cu(NH_3)_2]^{2+}$	0.020
$[MnCl_5]^{2-}$	0.023
$MnCO_4NO$	0.063
$H_2Fe(CO)_4$	0.059
$[NiCN_5]^{3-}$	0.042
$[TiF_6]^{2-}$	0.019

Table 3.10: T_1 diagnostic results.

In Table 3.11 mean absolute deviations are provided for the discussed complexes, using experimental data or the most robust method (EOM-CCSD). $[Cu(NH_3)_2]^{2+}$ was not included in this error analysis due to the lack of experimental values or reliable theoretical values. The highest error value across the methods is CIS, which does not have correlation energy included. EOM-CCSD mean absolute deviation error value corresponds to its comparison with experiment, when it was available ($TiCl_4$ and $[VO_4\ ]^{3-}$). Some of the studied complexes did not have experimental values to compare with. TD-B3LYP and TD-CAM-B3LYP have much lower error values when compared to CIS and CIS(D) proving to be a valuable tool to calculate inorganic transition metals excitation energies at comparable costs.

Complex	Mean Abs. Dev. (ev)
CIS	1.5
CIS(D)	1.2
EOM-CCSD	0.36
TD-B3LYP	0.60
TD-CAM-B3LYP	0.50

Table 3.11: Mean absolute deviations for the discussed inorganic complexes.

3.3.2 First-row transition metal monoxides

The last part of this chapter focuses on analysing the lowest excited states for first-row transition metal monoxides and the most stable spin states. The low-lying excited states gathered from [56] are based on the most stable geometry from the ground state anion and are going to be compared with values calculated for the ground state neutral complex. In this section TD-DFT from each spin state reference and spin-restricted state-specific calculations were performed for that state and compared to both experiment and previous theory.

Table 3.12 reveals the different bond lengths calculated for the most favourable spin for the transition metal oxides. The metal-oxide bond is important to describe the ground state properties of these complexes. The longest bond length belongs to CuO with 1.750 Å, and the strongest (shortest) is VO 1.560 Å. The variance among the bond lengths is not very large and the maximum difference between the longest and shortest bond length is only 0.19 Å.

	B3LYP/cc-pVTZ	BPW91 [47]	BLYP [47]	B3LYP [47]	CCSD(T) [64]	Expt.
ScO	1.658	1.665	1.679	1.659	1.679	1.668
TiO	1.611	1.618	1.631	1.611	1.628	1.620
VO	1.560	1.586	1.598	1.580	1.602	1.589
CrO	1.613	1.611	1.622	1.615	1.633	1.615
MnO	1.634	1.628	1.642	1.636	1.665	1.646
FeO	1.610	1.608	1.623	1.613	1.609	1.616
CoO	1.590	1.637	1.608	1.629	1.621	1.629
NiO	1.625	1.639	1.650	1.668	1.626	1.627
CuO	1.750	1.734	1.744	1.767	1.711	1.724

Table 3.12: First-row transition metal monoxides bond lengths comparing different methods. The basis set used in reference [47] is 6-311+G*. For reference [64], the basis set used consisted in mixture of different contractions for s, p, d and f orbitals optimised by Wachters [65]. Experimental data was gathered from [66] [67] [68] [69] [70] [71].

For ScO in Table 3.13, the most stable spin state is the $^2\Sigma$. The calculated data agrees with the experimental data performed by Wu *et al.* The $^2\Delta$ state shows a distinct discrepancy from calculated values to the experimental one. The other theoretical values agree with the experiment reasonably well.

In Table 3.14 (TiO), the calculated values and the experimental values predict the same lowest spin state, $^3\Delta$. When looking at $^1\Sigma$, LANL2DZ is further away from the experimental value (0.58 eV) than cc-pVTZ and 6-311G* (0.3 eV). For the $^1\Delta$ state cc-pVTZ underestimates the experimental value around 0.4 eV. Regarding the $^3\Sigma$ spin state, both LANL2DZ and 6-311G* are around 0.3 eV away from the experimental value.

The next metal oxide studied is VO, Table 3.15. The excited states of this monoxide were not studied before, just ground state properties as shown in Table 5.15. The predicted ground state is $^4\Sigma$ state, which agrees with the literature [72].

In Table 3.16, CrO is analysed. The most stable spin state is the $^5\Pi$. For this molecule only two experimental values are available to compare with the calculated results. Theoretical and experimental values agree,

considering the ground state, and are 0.2 eV apart when considering the $^5\Sigma$ state.

The lowest excited states of MnO are described in Table 3.17. $^6\Sigma$ is the most stable spin state for this complex. Theoretical and experimental values agree quite reasonably, except for cc-pVTZ for the $^4\Pi$ state, which is around 0.5 eV higher than the experimental value of 1.08 eV.

Considering FeO in Table 3.18, the most stable spin state is $^5\Delta$. When comparing the experimental and calculated values, there are some discrepancies. For the $^3\Sigma$ state, cc-pVTZ and 6-311G* are about 0.7 eV and 0.6 eV different from the experimental value respectively, while LANL2DZ is almost spot on. The same happens for $^3\Pi$ or $^3\Phi$, where 6-311G* is 0.4 eV higher than the experimental value.

In Table 3.19 CoO is described. Unfortunately, this complex does not have any experimental data to compare to, but the theoretical values calculated in this chapter are compared with other literature data. The ground state is a $^4\Delta$ state. For the $^2\Pi$ state cc-pVTZ is 0.3 eV lower than LANL2DZ and 6-311G*, apart from this discrepancy the other calculated values are in close agreement.

For NiO in Table 3.20, the same $^3\Sigma$ ground state is predicted by theory and experiment. For the excited states, the calculated values are also in close agreement with experiment.

The last studied complex is CuO (Table 3.21). The ground state is a $^2\Pi$ state. Looking at the $^2\Sigma$ state LANL2DZ and 6-311G* are around 0.2 eV higher than the experimental value.

Spin State	Relative energies (eV)			
	cc-pVTZ	LANL2DZ [56]	6-311G* [56]	Expt. [73]
$^2\Sigma$	0.000	0.000	0.000	0.00
$^2\Delta$	1.124	0.712	1.063	1.75
$^2\Pi$	2.028	1.850	1.986	2.05
$^4\Pi$	2.994	-	-	-
$^6\Sigma$	8.303	-	-	-
$^8\Sigma$	17.635	-	-	-

Table 3.13: ScO excitation energies (eV) with B3LYP and different basis sets.

Spin State	Relative energies (eV)			
	cc-pVTZ	LANL2DZ [56]	6-311G* [56]	Expt. [74]
$^1\Sigma$	1.248	0.923	1.293	1.50
$^1\Delta$	0.816	0.623	0.576	0.425
$^3\Delta$	0.000	0.000	0.000	0.00
$^3\Sigma$	1.145	0.926	1.094	0.70
$^3\Pi$ or $^3\Phi$	1.632	1.571	1.587	1.75
$^5\Pi$	3.28	-	-	-
$^7\Pi$	7.18	-	-	-

Table 3.14: TiO excitation energies (eV) with B3LYP and different basis sets.

Spin State	Relative energies (eV) cc-pVTZ
$^2\Sigma$	1.351
$^4\Sigma$	0.00
$^6\Delta$	2.761
$^8\Sigma^+$	6.336

Table 3.15: VO excitation energies (eV) with B3LYP and different basis sets.

Spin State	Relative energies (eV)			
	cc-pVTZ	LANL2DZ [56]	6-311G* [56]	Expt. [75]
$^1\Sigma$	2.222	-	-	-
$^3\Sigma$	0.918	-	-	-
$^5\Pi$	0.000	0.000	0.000	0.00
$^5\Sigma$	0.994	0.725	0.759	0.91
$^5\Delta$	1.408	1.903	1.583	-
$^7\Pi$	1.477	-	-	-

Table 3.16: CrO excitation energies (eV) with B3LYP and different basis sets.

Spin State	Relative energies (eV)			
	cc-pVTZ	LANL2DZ [56]	6-311G* [56]	Expt. [76]
$^2\Pi$	2.201	-	-	-
$^4\Pi$	1.591	1.012	1.184	1.08
$^6\Sigma$	0.000	0.000	0.000	0.000
$^6\Pi$	1.630	1.441	1.505	1.44
$^8\Pi$	1.536	-	-	-

Table 3.17: MnO excitation energies (eV) with B3LYP and different basis sets.

Spin State	Relative energies (eV)			
	cc-pVTZ	LANL2DZ [56]	6-311G* [56]	Expt. [77]
$^1\Sigma$	2.955	-	-	-
$^3\Sigma$	2.059	1.306	1.904	1.228
$^3\Pi$ or $^3\Phi$	1.217	0.879	1.271	0.839
$^5\Delta$	0.000	0.000	0.000	0.000
$^5\Sigma$	0.620	0.640	0.561	0.469
$^5\Pi$	1.171	1.166	1.060	1.129
$^7\Pi$	1.666	-	-	-

Table 3.18: FeO excitation energies (eV) with B3LYP and different basis sets.

Spin State	Relative energies (eV)		
	cc-pVTZ	LANL2DZ [56]	6-311G* [56]
$^2\Pi$	0.827	1.141	1.130
$^4\Sigma$	0.711	0.379	0.360
$^4\Delta$	0.000	0.000	0.000
$^4\Pi$ or $^4\Phi$	0.710	0.648	-
$^6\Delta$	0.571	-	-
$^8\Pi$	6.731	-	-

Table 3.19: CoO excitation energies (eV) with B3LYP and different basis sets.

Spin State	Relative energies (eV)			
	cc-pVTZ	LANL2DZ [56]	6-311G* [56]	Expt. [78]
$^1\Sigma$	1.434	1.451	1.443	-
$^1\Pi$	1.890	1.584	1.561	-
$^3\Sigma$	0.000	0.000	0.000	0.00
$^3\Pi$	0.639	0.678	0.609	0.43-0.55
$^5\Sigma$	1.407	-	-	-
$^7\Pi$	7.217	-	-	-

Table 3.20: NiO excitation energies (eV) with B3LYP and different basis sets.

Spin State	Relative energies (eV)			
	cc-pVTZ	LANL2DZ [56]	6-311G* [56]	Expt. [79]
$^2\Pi$	0.000	0.000	0.000	0.00
$^2\Sigma$	1.258	1.212	1.179	0.97
$^2\Delta$	2.200	2.346	2.290	-
$^4\Sigma$	1.665	-	-	-
$^6\Delta$	7.890	-	-	-
$^8\Delta$	17.110	-	-	-

Table 3.21: CuO excitation energies (eV) with B3LYP and different basis sets.

Table 3.22, shows the mean absolute deviations for the calculated excitation energies concerning the transition metal monoxides. The results are presented using relative energies, so for the most stable spin state, there is no deviation from experiment. Comparing the three basis sets, the mean absolute error value is small, although cc-pVTZ is slightly higher than LANL2DZ and 6-311G*. The ECP basis set has the smallest error (0.23 eV).

Basis set	**Mean Abs. Dev. (eV)**
cc-pVTZ	0.30
LANL2DZ	0.23
6-311G*	0.24

Table 3.22: Absolute mean deviations for each basis set, considering the experimental values as standard.

3.4 Conclusions

Inorganic transition metals are very difficult to investigate creating many problems due to narrow energetic levels or high density of states. These give a broad and featureless spectra that are very hard to analyse and describe. Sometimes, popular methods may not describe the electronic excited states properly like in the case of $TiCl_4$, where TD-B3LYP and TD-CAM-B3LYP are closer to the experimental results. Some care must be taken when choosing the method and the basis set to describe the excited states of any given inorganic transition metal complex accurately.

First-row transition metal monoxides were investigated and the results compared with literature data. For all complexes the same ground state as experimental results was predicted. DFT proves to be very useful for this approach and although the calculated mean absolute deviations are not very large, the effect of using different basis sets can cause some differences.

Bibliography

[1] Curtiss, L. A.; Raghavachari, K.; Redfern, P. C.; Pople, J. A. *J. Chem. Phys.* **1997**, *106*(3), 1063–1079.

[2] Curtiss, L. A.; Raghavachari, K.; Redfern, P. C.; Pople, J. A. *J. Chem. Phys.* **2000**, *112*(17), 7374–7383.

[3] Curtiss, L. A.; Redfern, P. C.; Raghavachari, K. *J. Chem. Phys.* **2005**, *123*(12), 124107.

[4] Jiang, W.; DeYonker, N. J.; Wilson, A. K. *J. Chem. Theory. Comput.* **2012**, *8*(2), 460–468.

[5] Schreiber, M.; Silva-Junior, M. R.; Sauer, S. P. A.; Thiel, W. *J. Chem. Phys.* **2008**, *128*(13), 134110.

[6] Silva-Junior, M. R.; Sauer, S. P.; Schreiber, M.; Thiel, W. *Mol. Phys.* **2010**, *108*(3-4), 453–465.

[7] Paterson, M. J.; Christiansen, O.; Pawłowski, F.; Jørgensen, P.; Hättig, C.; Helgaker, T.; Sałek, P. *J. Chem. Phys.* **2006**, *124*(5), 054322.

[8] Christiansen, O.; Jørgensen, P. *J. Am. Chem. Soc.* **1998**, *120*(14), 3423–3430.

[9] Christiansen, O.; Gauss, J.; Stanton, J. F.; Jørgensen, P. *J. Chem. Phys.* **1999**, *111*(2), 525–537.

[10] de Merás, A. M. S.; Cuesta, I. G.; Koch, H. *Chem. Phys. Lett.* **2001**, *348*(5–6), 469–476.

[11] Amor, N. B.; Villaume, S.; Maynau, D.; Daniel, C. *Chem. Phys. Lett.* **2006**, *421*(4–6), 378–382.

[12] Villaume, S.; Strich, A.; Daniel, C.; Perera, S. A.; Bartlett, R. J. *Phys. Chem. Chem. Phys.* **2007**, *9*, 6115–6122.

[13] Nakatsuji, H.; Ehara, M.; Palmer, M. H.; Guest, M. F. *J. Chem. Phys.* **1992**, *97*(4), 2561–2570.

[14] Wu, H.; Wang, L.-S. *J. Chem. Phys.* **1998**, *108*(13), 5310–5318.

[15] Curelaru, I. M.; Wendin, G. *Physica Scripta* **1980**, *22*(5), 513.

[16] Connor, J.; Hillier, I.; Saunders, V.; Wood, M.; Barber, M. *Mol. Phys.* **1972**, *24*(3), 497–509.

[17] Petit, R.; Briat, B.; Müller, A.; Diemann, E. *Mol. Phys.* **1974**, *27*(5), 1373–1384.

[18] Wu, J.; Wesdemiotis, C. *Chem. Phys. Lett.* **1999**, *303*(1-2), 243–247.

[19] El-Nahas, A. M. *Chem. Phys. Lett.* **2000**, *329*(1-2), 176–178.

[20] Corongiu, G.; Clementi, E. *J. Chem. Phys.* **1978**, *69*(11), 4885–4887.

[21] El-Nahas, A. M.; Tajima, N.; Hirao, K. *Chem. Phys. Lett.* **2000**, *318*(4-5), 333–339.

[22] Bellitto, C.; Tomlinson, A. A. G.; Furlani, C. *J. Chem. Soc. A* **1971**, pages 3267–3271.

[23] Bernal, I.; Elliott, N.; Lalancette, R. *J. Chem. Soc. D* **1971**, pages 803–804.

[24] Whittaker, J. W.; Whittaker, M. M. *J. Am. Chem. Soc.* **1991**, *113*(15), 5528–5540.

[25] Prince, S.; Körber, F.; Cooke, P. R.; Lindsay Smith, J. R.; Mazid, M. A. *Acta Crystallogr., Sect. C: Cryst. Struct.* **1993**, *49*(6), 1158–1160.

[26] Treichel, P. M.; Pitcher, E.; King, R. B.; Stone, F. G. A. *J. Am. Chem. Soc.* **1961**, *83*(11), 2593–2594.

[27] Crichton, O.; Rest, A. J. *J. Chem. Soc., Dalton Trans.* **1978**, (3), 208–215.

[28] Wawersik, H.; Basolo, F. *J. Am. Chem. Soc.* **1967**, *89*(18), 4626–4630.

[29] Bursten, B. E.; Jensen, J. R.; Gordon, D. J.; Treichel, P. M.; Fenske, R. F. *J. Am. Chem. Soc.* **1981**, *103*(17), 5226–5231.

[30] Poletti, A.; Paliani, G.; Cataliotti, R.; Toffani, A.; Santucci, A. *J. Organomet. Chem.* **1972**, *43*(2), 377–383.

[31] Wax, M. J.; Stryker, J. M.; Buchanan, J. M.; Kovac, C. A.; Bergman, R. G. *J. Am. Chem. Soc.* **1984**, *106*(4), 1121–1122.

[32] Wu, J.; Bergman, R. G. *J. Am. Chem. Soc.* **1989**, *111*(19), 7628–7630.

[33] Wenzel, T. T.; Bergman, R. G. *J. Am. Chem. Soc.* **1986**, *108*(16), 4856–4867.

[34] Fisher, B. J.; Eisenberg, R. *Organometallics* **1983**, *2*(6), 764–767.

[35] Janowicz, A. H.; Bergman, R. G. *J. Am. Chem. Soc.* **1982**, *104*(1), 352–354.

[36] Jones, W. D.; Feher, F. J. *J. Am. Chem. Soc.* **1982**, *104*(15), 4240–4242.

[37] Wang, W.; Weitz, E. *J. Phys. Chem. A* **1997**, *101*(12), 2358–2363.

[38] Eyermann, C. J.; Chung-Phillips, A. *J. Chem. Phys.* **1984**, *81*(3), 1517–1518.

[39] Jonas, V.; Thiel, W. *J. Chem. Phys.* **1996**, *105*(9), 3636–3648.

[40] Spiro, T. G.; Terzis, A.; Raymond, K. N. *Inorg. Chem.* **1970**, *9*(11), 2415–2420.

[41] Vinogradov, A.; Dukhnyakov, A. Y.; Ipatov, V.; Onopko, D.; Pavlychev, A.; Titov, S. *Fiz. Teverd. Tela* **1982**, *24*(5), 1417–1422.

[42] Alivov, Y.; Pandikunta, M.; Nikishin, S.; Fan, Z. Y. *Nanotechnology* **2009**, *20*(22), 225602.

[43] Bridgeman, A. J.; Rothery, J. *J. Chem. Soc., Dalton Trans.* **2000**, pages 211–218.

[44] Bridgeman, A. J. *J. Chem. Soc., Dalton Trans.* **1996**, pages 4555–4562.

[45] Xian, H.; Cao, Z.; Xu, X.; Lu, X.; Zhang, Q. *Chem. Phys. Lett.* **2000**, *326*(5-6), 485–493.

[46] Daoudi, A.; Benjelloun, A. T.; Flament, J.; Berthier, G. *J. Mol. Spect.* **1999**, *194*(1), 8–16.

[47] Gennady L. Gutsev, B. K. Rao, P. J. *J. Phys. Chem. A* **2000**, *104*(22), 5374–5379.

[48] Bakalbassis, E. G.; Stiakaki, M.-A. D.; Tsipis, A. C.; Tsipis, C. A. *Chem. Phys.* **1997**, *223*(2-3), 169–182.

[49] Bakalbassis, E. G.; Stiakaki, M.-A. D.; Tsipis, A. C.; Tsipis, C. A. *Chem. Phys.* **1996**, *205*(3), 389–399.

[50] Brocławik, E.; Borowski, T. *Chem. Phys. Lett.* **2001**, *339*(5-6), 433–437.

[51] Dolg, M.; Wedig, U.; Stoll, H.; Preuss, H. *J. Chem. Phys.* **1987**, *86*(4), 2123–2131.

[52] Xu, Z.; Kitchin, J. R. *Catalysis Comm.* **2014**, *52*, 60–64.

[53] Mattheiss, L. F. *Phys. Rev. B* **1972**, *5*, 290–306.

[54] Mattheiss, L. F. *Phys. Rev. B* **1972**, *5*, 306–315.

[55] Terakura, K.; Williams, A. R.; Oguchi, T.; Kübler, J. *Phys. Rev. Lett.* **1984**, *52*, 1830–1833.

[56] Dai, B.; Deng, K.; Yang, J.; Zhu, Q. *J. Chem. Phys.* **2003**, *118*(21), 9608–9613.

[57] Balabanov, N. B.; Peterson, K. A. *J. Chem. Phys.* **2005**, *123*(6), 064107.

[58] Gaussian 09 Revision A.02. Frisch, M. J.; Trucks, G. W.; Schlegel, H. B.; Scuseria, G. E.; Robb, M. A.; Cheeseman, J. R.; Scalmani, G.; Barone, V.; Mennucci, B.; Petersson, G. A.; Nakatsuji, H.; Caricato, M.; Li, X.; Hratchian, H. P.; Izmaylov, A. F.; Bloino, J.; Zheng, G.; Sonnenberg, J. L.; Hada, M.; Ehara, M.; Toyota, K.; Fukuda, R.; Hasegawa, J.; Ishida, M.; Nakajima, T.; Honda, Y.; Kitao, O.; Nakai, H.; Vreven, T.; Montgomery, Jr., J. A.; Peralta, J. E.; Ogliaro, F.; Bearpark, M.; Heyd, J. J.; Brothers, E.; Kudin, K. N.; Staroverov, V. N.; Kobayashi, R.; Normand, J.; Raghavachari, K.; Rendell, A.; Burant, J. C.; Iyengar, S. S.; Tomasi, J.; Cossi, M.; Rega, N.; Millam, J. M.; Klene, M.; Knox, J. E.; Cross, J. B.; Bakken, V.; Adamo, C.; Jaramillo, J.; Gomperts, R.; Stratmann, R. E.; Yazyev, O.; Austin, A. J.; Cammi, R.; Pomelli, C.; Ochterski, J. W.; Martin, R. L.; Morokuma, K.; Zakrzewski, V. G.; Voth, G. A.; Salvador, P.; Dannenberg, J. J.; Dapprich, S.; Daniels, A. D.; Farkas, .; Foresman, J. B.; Ortiz, J. V.; Cioslowski, J.; Fox, D. J.

[59] Almeida, N. M.; McKinlay, R. G.; Paterson, M. J. *Chem. Phys.* **2015**, *446*, 86–91.

[60] McKinlay, R. G.; Almeida, N. M. S.; Coe, J. P.; Paterson, M. J. *J. Phys. Chem. A* **2015**, *119*(39), 10076–10083.

[61] Lee, T. J.; Taylor, P. R. *Int. J. Quantum. Chem.* **1989**, *36*(S23), 199–207.

[62] Heitz, M.-C.; Daniel, C. *J. Am. Chem. Soc.* **1997**, *119*(35), 8269–8275.

[63] Becker, C.; Ballhausen, C.; Trabjerg, I. *Theor. Chim. Acta.* **1969**, *13*(5), 355–364.

[64] Bauschlicher, C. W.; Maitre, P. *Theor. Chim. Acta.* **1994**, *90*(2), 189–203.

[65] Wachters, A. J. H. *J. Chem. Phys.* **1970**, *52*(3), 1033–1036.

[66] Merer, A. J. *Annu. Rev. Phys. Chem.* **1989**, *40*(1), 407–438.

[67] Cheung, A.-C.; Lee, N.; Lyyra, A.; Merer, A.; Taylor, A. *J. Mol. Spectrosc.* **1982**, *95*(1), 213–225.

[68] Ram, R.; Jarman, C.; Bernath, P. *J. Mol. Spectrosc.* **1993**, *160*(2), 574–584.

[69] Srdanov, V. I.; Harris, D. O. *J. Chem. Phys.* **1988**, *89*(5), 2748–2753.

[70] Constants of diatomic molecules, vol. 4, molecular spectra and molecular structure. Huber, K.; Herzberg, G. **1979**.

[71] Green, D. W.; Reedy, G. T.; Kay, J. G. *J. Mol. Spectrosc.* **1979**, *78*(2), 257–266.

[72] Carlson, K. D.; Moser, C. *J. Chem. Phys.* **1966**, *44*(9), 3259–3265.

[73] Wu, H.; Wang, L.-S. *J. Chem. Phys. A* **1998**, *102*(46), 9129–9135.

[74] Wu, H.; Wang, L.-S.; others. *J. Chem. Phys.* **1997**, *107*(20), 8221–8228.

[75] Gutsev, G. L.; Jena, P.; Zhai, H.-J.; Wang, L.-S. *J. Chem. Phys.* **2001**, *115*(17), 7935–7944.

[76] Gutsev, G. L.; Rao, B.; Jena, P.; Li, X.; Wang, L.-S. *J. Chem. Phys.* **2000**, *113*(4), 1473.

[77] Fan, J.; Wang, L.-S. *J. Chem. Phys.* **1995**, *102*(22), 8714–8717.

[78] Wu, H.; Wang, L.-S.; others. *J. Chem. Phys.* **1997**, *107*(1), 16–21.

[79] Wu, H.; Desai, S. R.; Wang, L.-S. *J. Phys. Chem. A* **1997**, *101*(11), 2103–2111.

Chapter 4

Excited electronic states of MnO_4^-: challenges for wavefunction and density functional response theories

The last chapter included a compilation of "well-behaved" inorganic complexes where computational approaches perform as generally expected. The problem with inorganic excited states is that not all the complexes are "well-behaved" and many can create problems. For example, if the ground state is difficult to define or the methods chosen for the excited states do not capture the necessary correlation to characterize them properly. Some of such problems are going to be dealt with in this and subsequent chapters.

The permanganate ion (MnO_4^-) has been one the most studied complexes in transition metal chemistry. It is one of the most prominent oxidation reagents and its violet color is well-known. This complex presents a particular challenge to researchers due to the complex nature of the electronic spectrum. There are many problems that arise, for example a high density of states which are usually very close to each other, leading to overlapping states and broad-featureless experimental spectra [1] [2]. For such systems an array of advanced methodologies may be required to describe the electronic structure for ground and excited states [3, 4, 5, 6, 7, 8, 9, 10].

Research on this d^0 complex dates back to the beginning of the 20^{th} century, more precisely, the 1930s when Teltow started investigating it as being a curious molecule with many interesting properties [11] [12]. Since then, a wide number of studies have been published trying to establish both the ground and excited state properties of MnO_4^-. There are studies involving Hartree-Fock [13], post Hartree-Fock [14], DFT [15] and for excited states, TD-DFT [16, 17, 18, 19] and EOM-CCSD calculations [20]. One of the main reasons for these comprehensive studies are uncertainties that previous researchers found, for example how well can Hartree-Fock describe the electronic ground state of MnO_4^- or the ordering of the orbitals for this method. Previous studies for similar inorganic oxide complexes like TiO_2 clusters [21] showed that Hartree-Fock method was not a good starting point for excited state calculations at all as many unexpected errors could arise.

In 2012 Jose *et al* [22] performed one of the most extensive studies so far. Using a DFT restricted approach they calculated the low-lying excited states, oscillator strengths and analysed the optimised geometries and their vibrational modes for excited states. They found that the first three excited states were distorted from the original tetrahedral geometry, generating C_{3v}, C_{2v} and D_{2d} geometries. These came from Jahn-Teller distortions from the higher symmetry T_d. This behaviour generates a very rich photochemistry [23, 24, 25, 26].

In this chapter, hierarchal methods like coupled-cluster response theory and CASSCF were used to describe this complex. Methods such as CCS, CIS(D), CCSD, CC2 and CC3 were assessed to create a systematic series that can inform on excited states computation for complex cases. This kind of response series has been used for organic molecules, proving to be very good at accurately describing in a convergent manner, the excited electronic states [27] [28].

This chapter further aims to diagnose any intrinsic ground state prob-

lems that MnO_4^- gives to such response methods, and to be able to define the optimal orbitals to describe them. Methods such as EOM-CCSD or LR-CCSD are able to describe the excited states adequately for this complex, although the starting point (HF orbitals) are often far from ideal. Popular methods such as CIS, CIS(D), CC2 and CC3 can fail drastically in their description of the electronic excited states (see Table 4.2). The purpose of this chapter is to understand the effect the ground state reference has on any excited state calculated via response theory. Multiconfigurational methods used in this chapter are useful to understand the orbital relaxation, and RASSCF was chosen for this purpose. As discussed below in the results section the purpose of RASSCF calculations was not to calculate explicitly excited state wavefunctions. The computational cost of such calculations (multiroot eigenvalue calculations) would be very expensive and is beyond the scope of this work. Rather the RAS informs us to the intrinsic problems response approaches may face based on the electronic structure of the ground state.

The next part of this introduction focuses on reviewing some important studies on the MnO_4^- photochemistry. In 1987, Lee *et al* showed that a long lived intermediate plays a very important role in the photodecomposition of the permanganate ion. This intermediate was found to be a peroxo isomer of the anion, see Figure 4.1.

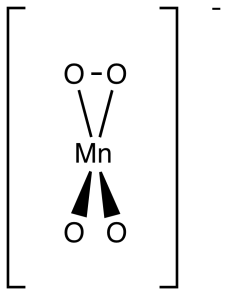

Figure 4.1: MnO_4^- peroxo isomer

After this important discovery, Nakai *et al* [29] studied the photodecomposition using the intermediate referred before. They used symmetry-adapted cluster configuration interaction (SAC-CI) for the calculations.

The following MnO_4^- photodecomposition takes place:

$$MnO_4^- + h\nu \rightarrow [MnO_4^-(\text{peroxo})] + h\nu \rightarrow MnO_2^- + O_2 \qquad (4.1)$$

This was then concluded to be the primary channel for MnO_4^- fragmentation. However, the decomposition of MnO_4^- was observed experimentally at different photon wavelengths, namely, of 311 nm and 578 nm.

A later study by Gutsev *et al* [30] shows that the photofragmentation of MnO_4^- in Equation 4.1 requires extra energy (5 eV). They performed an extensive study in the neutral and negatively charged permanganate, finding ten different isomers for the different charges and spins (neutral $2S+1$=2, 4, 6 and anion $2S+1$=1, 3, 5). The most stable neutral permanganate ($^2B_2$) sits 5.0 eV from the most stable anion ($^1A_1$) with a T_d geometry. As was mentioned previously, they concluded that the release of O_2 can happen in a variety of pathways and the only one that does not involve intermediates is: $MnO_4^- \rightarrow MnO_2^- + O_2$. They found as well, that MnO_4^- can eject an electron first and dissociate:

$$MnO_4^- + h\nu \rightarrow MnO_4 + e^- \rightarrow MnO_2^- + O_2 \qquad (4.2)$$

the same can happen for MnO_3 and MnO_3^-.

The most recent study was performed on the photoabsorption by permanganate ions in vacuum [31]. It was concluded that after submitting the dominant fragment ions of MnO_4^- to irradiation at 540 nm, the products are MnO_3^- and MnO_2^-. Houmøller *et al* performed another interesting study on MnO_4^- comparing an isolated molecule and MnO_4^- with one attached water molecule. They concluded that the permanganate was not affected by the hydration, showing a shift of only about 12 meV. The complete hydration of the complex leads to a blue shift around 0.1 eV. This is a highlight of some of the studies performed on the photodetachment of MnO_4^-. In this chapter a computational approach is used to compare with the best experiment. The results are discussed

in the next sections.

4.1 Computational details

MnO_4^- was optimised using different levels of theory for the ground state. The ground electronic state ($^1A_1$) has a tetrahedral geometry (T_d) and was calculated using a variety of double and triple zeta basis sets, in conjunction with Hartree-Fock, coupled-cluster singles and doubles (CCSD), Bruckner Doubles (BD), and B3LYP. Frequency calculations confirmed a minimum. The optimised structure at the B3LYP/cc-pVTZ level was then used to perform calculations of the lowest electronic singlet excited states. A wide variety of methods was used for excited state calculations: TD-B3LYP, TD-CAM-B3LYP and coupled-cluster response with a range of methods (CIS,CC2, CCSD and CC3) along with the perturbatively corrected method CIS(D). For the TD-DFT calculations the chosen basis set was cc-pVTZ, and for the linear response coupled-cluster an all electron atomic natural orbital (ANO) basis contracted to 6s5p4d3f1g was used on the manganese atom and cc-pVTZ on the oxygen atoms. For EOM-CCSD, cc-pVTZ was also chosen.

EOM-CCSD and LR-CCSD should provide the same result for excited states, because they are different formulations of the same response approach. Transition properties are different though, with LR-CCSD being more accurate. Since using a full point group symmetry is not available in most of the software for excited states, C_{2v} sub group has been chosen in Gaussian 09 [32] and D_2 in Dalton [33]. CC2 and CC3 are widely used in organic chemistry and provide very accurate results [27] [34] so they were tested in transition metal chemistry to understand how they can cope with the difficulties of these systems. For the TD-DFT excited states calculations two different methods were chosen for the calculations, B3LYP and CAM-B3LYP. TD-CAM-B3LYP describes the long range corrections in a better way, allowing more accurate charge transfer calculations. This way it could be evaluated if the considered

cheaper DFT methods would provide a reasonable answer using much less resources than coupled-cluster response, and wether DFT response suffered similar ground state orbital issues as the CC response based on HF orbitals.

At first, CASSCF calculations were planned to study ground state orbital relaxation by obtaining a multiconfigurational wavefunction, but after doing an extensive analysis on the orbitals that needed to be included in the active space it was prohibitive to use this method. The next best option was to use RASSCF (restricted active space self-consistent field), where the orbital space was divided into three parts: RAS1, RAS2 and RAS3 and obtain a balance between static and dynamic correlation. A detailed RASSCF calculation was chosen (40 electrons and 39 orbitals). The RAS1 space consists of occupied orbitals and 17 orbitals were chosen for this. RAS2 is effectively the CAS, where 6 electrons and 9 orbitals were used. For the last part, RAS3, 13 orbitals were chosen. Single particle-holes were considered for RAS1 and RAS3, generating a total of 2,984,730 singlet configurations using Slater determinants. The resulting RAS(40,39,1,1) wavefunction was generated, using a restricted Hartree-Fock (RHF) initial guess, followed by full orbital optimisation. This way it is possible to compare the difference in orbitals from the initial Hartree-Fock picture and to what degree the orbitals from the correlated set compare with this.

4.2 Results and Discussion

MnO_4^- was optimised using various methods and basis sets that are depicted in Table 4.1. For the Hartree-Fock method the Mn-O bond length is significantly smaller than the experimental one, 1.629 Å. Coupled-cluster also underestimates the bond length for Mn-O. Bruckner doubles perform slightly better than CCSD and can be explained by the degree of multireference character existing for the ground state. Looking at DFT, the functional closer to the experimental value is BP86, although

there is a significant variation with functional.

Method	Basis set	Mn-O distance (Å)
HF	cc-pVTZ	1.542
BP86	cc-pVTZ	1.621
M062X	cc-pVTZ	1.573
M06HF	cc-pVTZ	1.554
M06L	cc-pVTZ	1.607
B3LYP	cc-pVTZ	1.601
B3LYP	aug-cc-pVTZ	1.602
CCSD	6-31G(d)	1.594
CCSD	6-311G(d)	1.576
CCSD	cc-pVDZ	1.601
CCSD	cc-pVTZ	1.575
BD	cc-pVTZ	1.590
Experimental [35]	-	1.629

Table 4.1: Mn-O distances with different methods and different basis sets (T_d angles=109.5 °).

4.2.1 Response methods for excited states

In Table 4.2 the results of the lowest energy excited states are given. To compare the different coupled-cluster response methods, it is worth starting with the simplest method CCS and calculate the excited states up to the nominal highest level, CC3. The lowest cost method (CCS), and CIS(D), greatly overestimate the excitation energies of these states by several eV. Clearly the single configuration description of either the ground state, or single particle picture of the excited sates does not describe those excited states well. This creates several issues in methods that use the $\hat{T}_1$ operator to "dress" all response operators via a similarity transformation in reduced cost intermediate methods such as CC2 or CC3. MnO_4^- proves to be a strongly correlated inorganic system, where both CC2 and CC3 methods have some difficulties in dealing with the lowest valence states. CC2 excitation energies are several eV lower than the experimental values, providing negative (non-physical) oscillator strengths. CC3 does not behave better having the same problems dealing with electron correlation, which means it has issues based on the same $\hat{T}_1$ problems as CC2 despite being in principle much more

accurate than CCSD. CCSD provides accurate values, so the problem has to arise from the approximations made on these intermediate methods. The CIS(D) model is related to the CC2 intrinsically, involving a non-iterative doubles correction from perturbation theory to CCS and is therefore sometimes known as CC(2). This has the same approach as CCSDR(3) with non-iterative triples correction to excitation energies relative to the CC3. It is worth mentioning that CCSDR(3) excitation energy is 3.491 eV for the highly non-physical CC3 1^1T_2 state, but caution should be taken given how CC3 and CCR(3) are related.

LR-CCSD or EOM-CCSD have the best performances of all methods, proving to be the most robust ones with less overall errors. From the first two states, 1^1T_1 and 1^1T_2 there are deviations from experimental peaks around 0.2 eV, and 0.4 eV for the third one (2^1T_2). LR-CCSD is more accurate in calculating relaxed density matrices. Figure 4.2 and 4.3 show the dominant transitions in the response eigenvectors for the first three states.

The general consensus regarding the first excited state seems to coincide with the data obtained from previous calculations, t_1 HOMO to the e LUMO (see Figures 4.2 and 4.3). The second and third bands have been proposed with different assignments over the years. The last one reported by DFT calculations [22], proposing a mixing of bands, principally from t_2 HOMO-1 to e LUMO and t_1 HOMO to t_2 LUMO+1 transitions. The former was proved to be dominant for the second band and the latter to the third band. Another aspect worth mentioning is the fact that all transitions have LMCT character (based on EOM-CCSD calculations).

State	Character	CIS	CIS(D)	CC2	LR CCSD	EOM CCSD	CC3	Expt [35]
1^1T_1	LMCT	3.791 (0.00000)	2.730	0.489 (0.00000)	1.9444 (0.00000)	1.926 (0.00000)	1.041	1.71-1.77
1^1T_2	LMCT	3.846 (0.00127)	3.033	0.184 (-0.0342)	2.404 (0.01030)	2.461 (0.01450)	-0.344	2.27 (Srong)
2^1T_2	LMCT	4.588 (0.00224)	3.742	1.861 (-0.02970)	3.871 (0.00253)	3.862 (0.00080)	1.387	3.47 (Weak)

Table 4.2: Excitation energies (eV) and oscillator strengths of the lowest electronic states using a range of many-body wavefunction based response theories. For Mn (6s3p4d3f1g) and cc-pVTZ for O in the response methods, cc-pVTZ for Mn and O with EOM-CCSD.

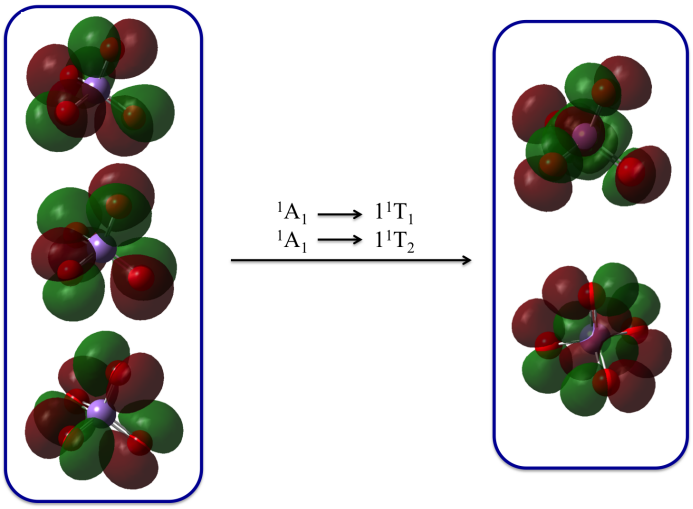

Figure 4.2: Hartree-Fock orbitals involved in the dominant configuration of the first two excited states 1^1T_1 and 1^1T_2.

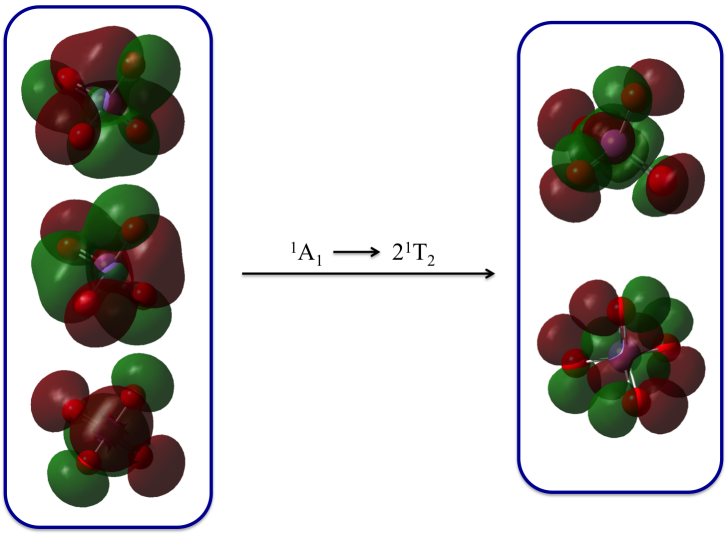

Figure 4.3: Hartree-Fock orbitals involved in the dominant configuration of the third excited state 2^1T_2.

As it was mentioned earlier one may think that the large $\hat{T}_1$ amplitudes can indicate a multireference character [36] in the ground state wavefunction. In Chapter 3 a T_1 diagnostic was used to describe the multireference character of the studied complexes [36]. In this chapter a similar diagnostic is presented in Table 4.3. As it was mentioned before if the value of T_1 is higher than 0.05 for 3d transition metal complexes [37], a multireference wavefunction is important to describe the ground state of a given complex accurately. All the values in Table 4.3 are slightly above this threshold. It seems that for MnO_4^- this diagnostic is basis set invariant.

Basis set	**T_1 value**
6-31G*	0.060
6-311G*	0.056
cc-pVDZ	0.067
cc-pVTZ	0.058
aug-cc-pVTZ	0.060

Table 4.3: T_1 diagnostic results.

4.2.2 RASSCF results

In order to explore and analyse the nature of the electronic ground state in more detail, in particular the effect of orbital relaxation, there is a need for a multiconfigurational method.

Figure 4.4 shows the comparison between Hartree-Fock orbitals and the RAS orbitals and Figure 4.5 shows the comparison between B3LYP orbitals and RAS orbitals. The RHF orbitals are very different from the ones optimised in RAS2 and a significant amount of mixing between the oxygen and manganese centred orbitals takes place. Looking at dominant configurations, RASSCF has one accounting for 73%. Analysing the RAS orbitals it is clear to see that some electron density has been transferred from the oxygens to the 3d and 4s set through orbital relaxation. DFT orbitals allow a much better starting point for the calculation, having a different order from the Hartree-Fock ones and similar

orbitals when compared to the final RAS. The full RAS wavefunction has interesting occupations for the unoccupied orbitals in the RAS2 space of around 0.2 electrons, for RAS1 1.987-1.974 and for RAS3 0.034, see Table 4.4. These occupations show a borderline between strongly/weakly occupied and partially occupied. Orbital relaxation is clearly very important to be able to describe the system properly .

Orbital number	**Occupancies**
RAS1 (orbital 13)	1.974
RAS1 (orbital 16)	1.987
RAS1 (orbital 17)	1.980
RAS1 (orbital 18)	1.858
RAS1 (orbital 19)	1.869
RAS2 (orbital 20)	1.854
RAS2 (orbital 21)	0.199
RAS2 (orbital 23)	0.193
RAS3 (orbital 27)	0.034
RAS3 (orbital 28)	0.033
RAS3 (orbital 29)	0.033

Table 4.4: Most relevant orbital occupancies.

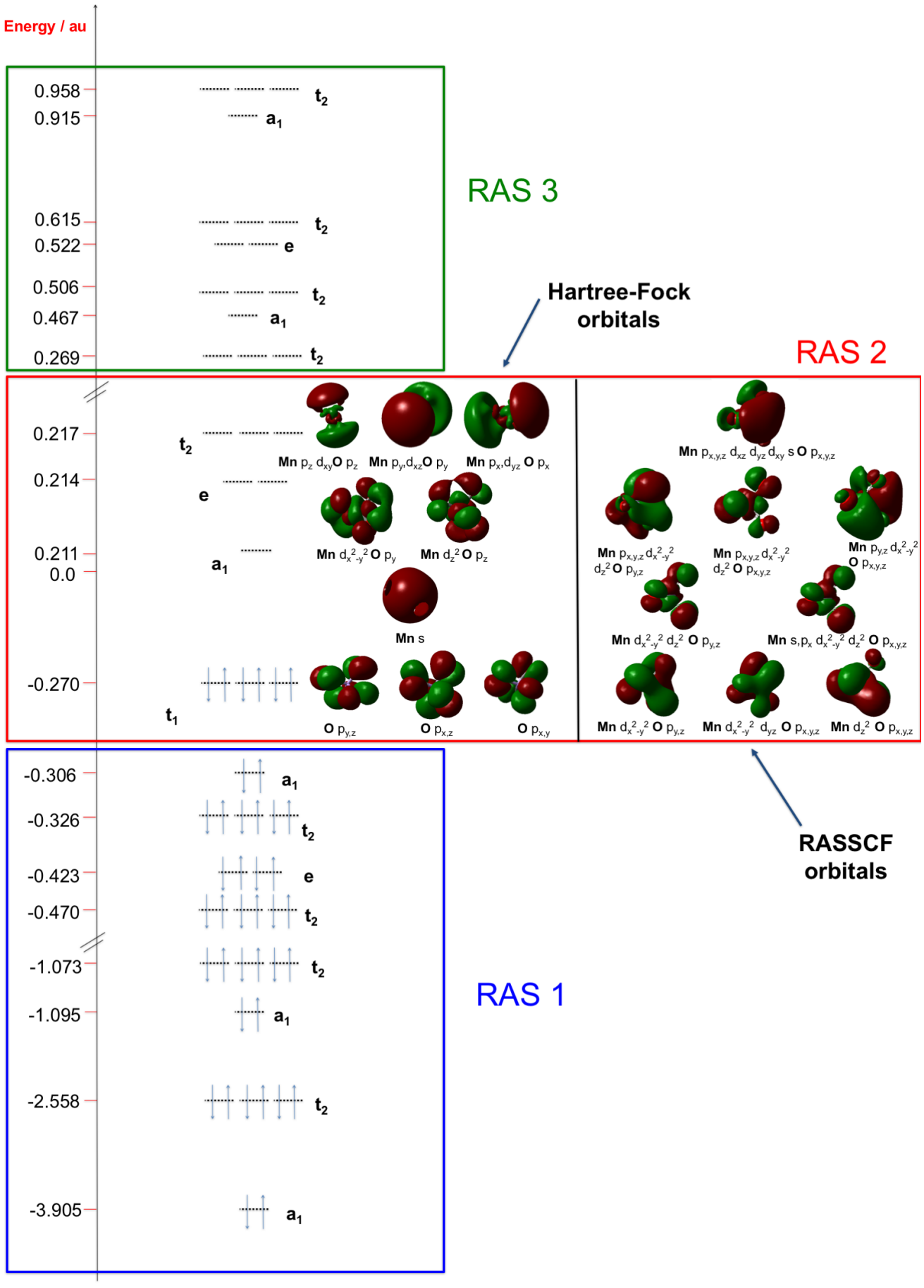

Figure 4.4: Quantitative molecular orbital diagram of MnO_4^- showing canonical Hartree–Fock, together with schematic RASSCF orbital partitioning.

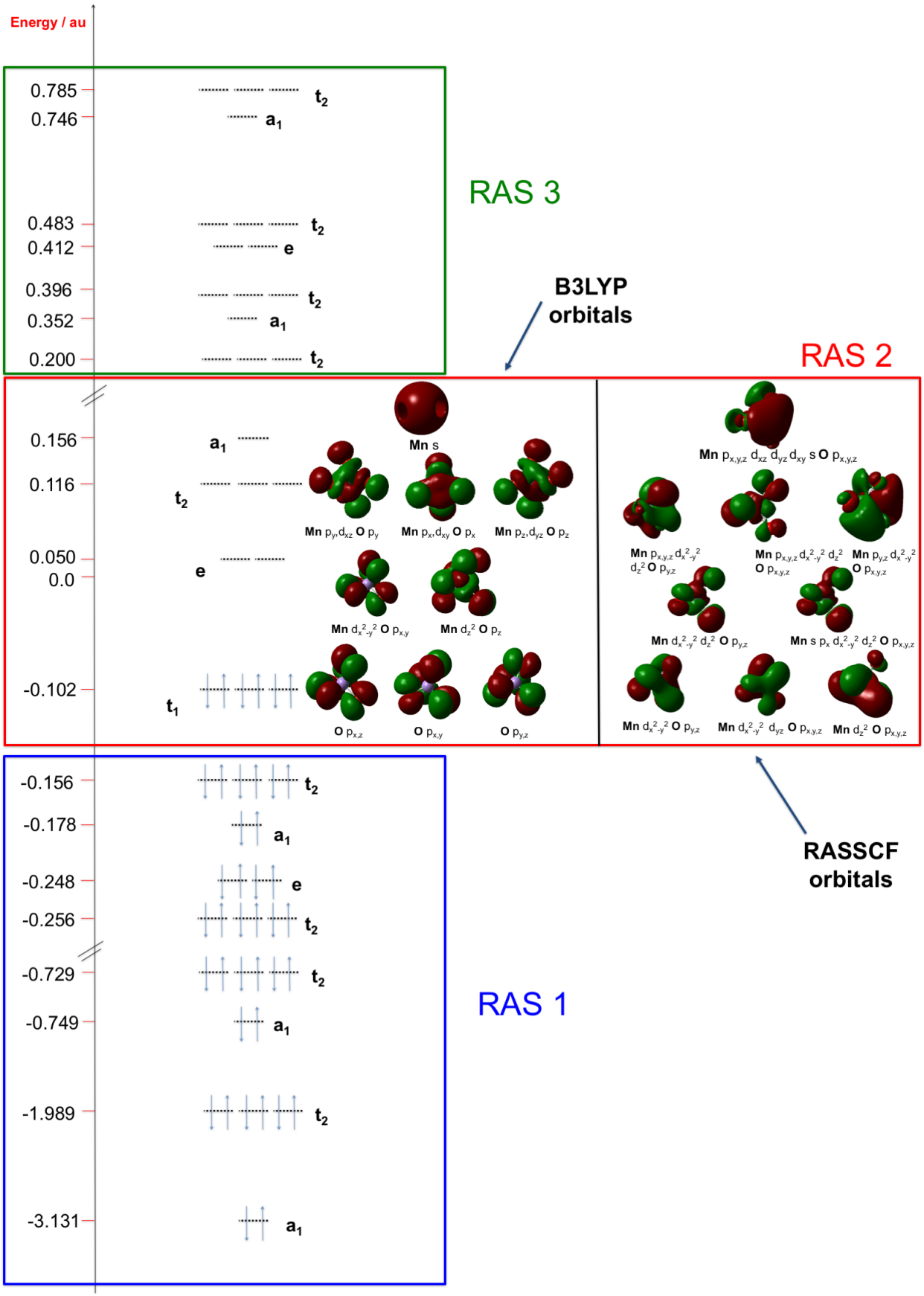

Figure 4.5: Quantitative molecular orbital diagram of MnO_4^- showing B3LYP orbitals, together with schematic RASSCF orbital partitioning.

4.2.3 TD-DFT results

The calculated TD-DFT results are given in Table 4.5. As it was mentioned before two different types of functional were used, TD-B3LYP and the long range corrected TD-CAM-B3LYP. Unlike highly correlated methods like coupled-cluster response TD-DFT has been applied to this system previously. The calculations reveal the same tendency as before, a ligand-to-metal charge transfer for all the calculated electronic states (oxygen to d^0 metal centre). The differences between TD-B3LYP and TD-CAM-B3LYP are very small, so it is possible to conclude that the metal and oxygens are quite mixed and a very small amount of overall charge is transferred over a small distance, so long-range exchange potentials do not affect these states. The absolute mean deviations considering each method are shown in Table 4.6.

State	**Character**	**TD-B3LYP**	**TD-CAM-B3LYP**	**Expt [35]**
1^1T_1	LMCT	2.498	2.393	1.71-1.77
		(0.00000)	(0.00000)	
1^1T_2	LMCT	3.025	2.986	2.27 (Strong)
		(0.00710)	(0.00770)	
2^1T_2	LMCT	4.179	4.194	3.47 (Weak)
		(0.00140)	(0.00070)	
3^1T_2	LMCT	4.716	4.594	3.99 (Strong)
		(0.00800)	(0.00770)	

Table 4.5: Excitation energies (eV) and oscillator strengths of the lowest electronic states using CAM-B3LYP and cc-pVTZ for Mn and O.

4.2.4 Mean absolute deviations

Table 4.6 shows the mean absolute deviations considering every method used assuming the experimental data as the most accurate values. CIS, CC2 and CC3 have the largest absolute mean deviation values. As it was mentioned in Chapter 3, CIS scales as N^4 (where are N the number of electrons in the system), CC2 N^5 and CC3, N^7. CC3 is a computationally more demanding method than CC2 and CIS, but its mean absolute deviation it is the largest for the used methods. However the errors here are much more than quantitative as it was discussed above,

in that the $\hat{T}_1$ amplitudes essentially render these methods useless for this complex, as catastrophic unphysical effects may occur due to the underlying orbital set for the response calculations. EOM-CCSD and LR-CCSD are most accurate methods with the lowest mean absolute deviations. TD-DFT errors are slightly higher, 0.74 eV for TD-B3LYP and 0.67 eV for TD-CAM-B3LYP, but show excellent performance vs cost considering the orbital complexities shown for CC response methods.

State	Abs. Mean Dev. (eV)
CIS	1.6
CIS(D)	0.68
CC2	1.6
EOM-CCSD	0.25
LR-CCSD	0.26
CC3	1.8
TD-B3LYP	0.74
TD-CAM-B3LYP	0.67

Table 4.6: Absolute mean deviations for each method, considering the experimental values as standard.

4.2.5 Photoelectron spectrum

Finally it was considered the use of DFT to understand the photoelectron spectrum of MnO_4^-. The photodetachment spectrum of MnO_4^- is depicted in Figures 4.6(a) and 4.6(b). The first one was calculated computationally, while the second one was performed experimentally by Gutsev *et al.* Figure 4.6 shows transitions from the ground state of MnO_4^- to the ground and excited states of the neutral MnO_4. TD-DFT calculations provided reasonable results for the excited states using B3LYP and CAM-B3LYP, so an evaluation of the photoelectron detachment spectra was performed using DFT. The functional used for these calculations was CAM-B3LYP/cc-pVTZ. To perform a photodetachment calculation, a simulation of the overlap between two vibronic resolved states is considered. The line intensities in a one-photon absorption or emission spectra depend on the square of the dipole moment and the radiation frequency. By calculating these, they allow us to re-

solve the highest probability for any vibronic transition and see what transition corresponds to the highest overlap of the wavefunctions.

When looking at the two different spectra in Figure 4.6, the experimental spectrum, Figure 4.6(b), has two different bands. The first band (X) corresponds to the transition between MnO_4^- $^1A_1$, T_d and the ($^2B_1$, $^2B_2$), C_{2v} neutral ground state of MnO_4. The second band (A) corresponds to the vertical transition between MnO_4^-, ($^1A_1$, T_d) and the $^2A_1$, D_{2d} state of the neutral MnO_4 and has a value of 6.05±0.06 eV. When comparing these results to the ones computationally performed, as shown in Figure 4.6(a); there is a major band around 4.8 eV (38000-39000 cm^{-1}). This can be associated with the first transition and corresponds to the $^1A_1$ to the ($^2B_1$, $^2B_2$) ground state of MnO_4, which is very close to the experimental value (4.80±0.10) eV. The second band (A) was not investigated further here. To conclude, for the studied peak (X), the computational calculations agree reasonably well with experiment.

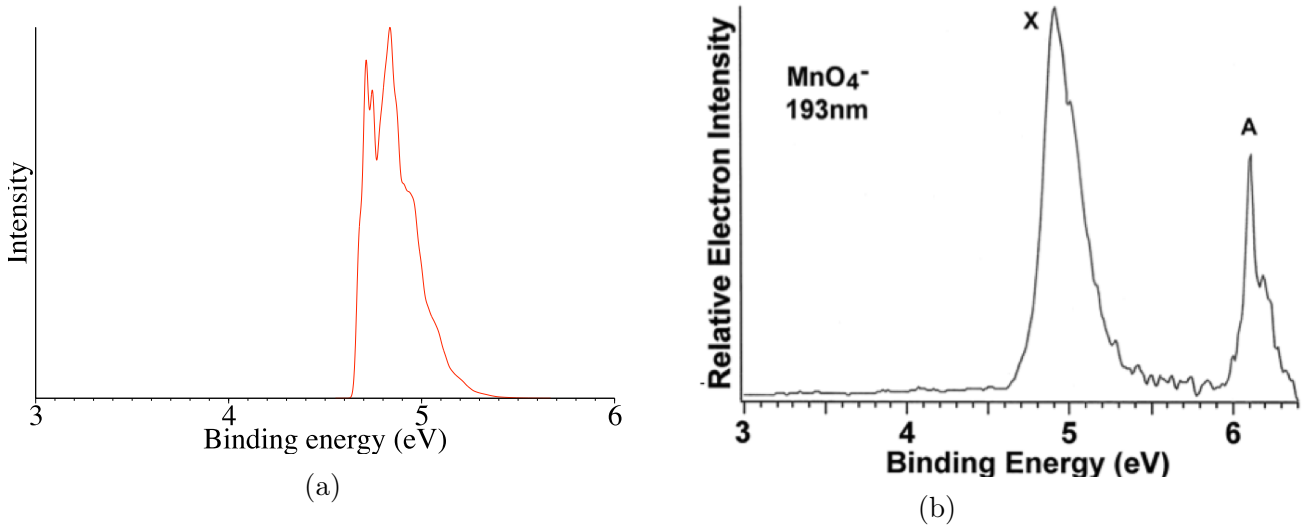

Figure 4.6: a) Computationally calculated, MnO_4^- photoelectron spectrum, b) Experimental photoelectron spectrum of MnO_4^-, performed at 194nm (6.424 eV). Adapted from [30].

4.3 Conclusions

The ground state, excited states and electronic structure of the permanganate anion were examined using a wide variety of electronic structure

methods including RASSCF for the ground state, and linear response coupled cluster for the excited states. These are intrinsic problems associated with the ground state of the system and a fine balance of static and dynamic correlation. MnO_4^- can be described by a single electron configuration, although canonical Hartree-Fock orbitals provide a very bad description of the system. These kind of complexes show that robust methods provide good results in organic systems but can fail in inorganic cases dramatically, where the balance between static and dynamic correlation is not balanced well. In the future other methods can be tested to try and improve the ground state wavefunction, like CASPT2 or NEVPT2 adding the dynamic correlation and explicitly optimising excited states.

Considering the use of less demanding methods like DFT, the low-lying excited states are described relatively accurately with a lower computational cost compared to any other method used. DFT calculations reproduce the essential features of the photoelectron spectrum of MnO_4^-. This widely researched inorganic molecule continues to provide a fascinating test and benchmark of excited state electronic structure methods.

Bibliography

[1] Trushin, S.; Kosma, K.; Fuß, W.; Schmid, W. *Chem. Phys.* **2008**, *347*(1–3), 309–323.

[2] Kotzian, M.; Roesch, N.; Schroeder, H.; Zerner, M. C. *J. Am. Chem. Soc.* **1989**, *111*(20), 7687–7696.

[3] Almeida, N.; McKinlay, R.; Paterson, M. Structure and Bonding; Springer Berlin Heidelberg, 2014; pages 1–32.

[4] Sandroni, M.; Kayanuma, M.; Rebarz, M.; Akdas-Kilig, H.; Pellegrin, Y.; Blart, E.; Le Bozec, H.; Daniel, C.; Odobel, F. *Dalton Trans.* **2013**, *42*, 14628–14638.

[5] Kvapilová, H.; Hoskovcová, I.; Kayanuma, M.; Daniel, C.; Záliš, S. *J. Phys. Chem. A* **2013**, *117*(45), 11456–11463.

[6] Kosma, K.; Trushin, S. A.; Fuß, W.; Schmid, W. E.; Schneider, B. M. R. *Phys. Chem. Chem. Phys.* **2010**, *12*, 13197–13214.

[7] Żurek, J. M.; Paterson, M. J. *J. Chem. Phys.* **2012**, *137*(3), 034308.

[8] Żurek, J. M.; Paterson, M. J. *J. Phys. Chem. A* **2012**, *116*(22), 5375–5382.

[9] Paterson, M. J.; Blancafort, L.; Wilsey, S.; Robb, M. A. *J. Phys. Chem. A* **2002**, *106*(47), 11431–11439.

[10] Greenough, S. E.; Roberts, G. M.; Smith, N. A.; Horbury, M. D.; McKinlay, R. G.; Zurek, J. M.; Paterson, M. J.; Sadler, P. J.; Stavros, V. G. *Phys. Chem. Chem. Phys.* **2014**, *16*, 19141–19155.

[11] Teltow, J. *Z. Phys. Chem. Abt. A* **1938**, *40*, 397–430.

[12] Teltow, J. *Z. Phys. Chem. Abt. A* **1939**, *43*, 198–212.

[13] Hsu, H.-l.; Peterson, C.; Pitzer, R. M. *J. Chem. Phys.* **1976**, *64*(2), 791–795.

[14] Nakai, H.; Ohmori, Y.; Nakatsuji, H. *J. Chem Phys.* **1991**, *95*(11), 8287–8291.

[15] Dickson, R. M.; Ziegler, T. *Int. J. Quantum Chem.* **1996**, *58*(6), 681–687.

[16] Neugebauer, J.; Baerends, E. J.; Nooijen, M. *J. Phys. Chem. A* **2005**, *109*(6), 1168–1179.

[17] Boulet, P.; Chermette, H.; Daul, C.; Gilardoni, F.; Rogemond, F.; Weber, J.; Zuber, G. *J. Phys. Chem. A* **2001**, *105*(5), 885–894.

[18] Menconi, G.; Kaltsoyannis, N. *Chem. Phys. Lett.* **2005**, *415*(1–3), 64–68.

[19] van Gisbergen, S. J. A.; Groeneveld, J. A.; Rosa, A.; Snijders, J. G.; Baerends, E. J. *J. Phys. Chem. A* **1999**, *103*(34), 6835–6844.

[20] Nooijen, M. *J. Chem. Phys.* **1999**, *111*(24), 10815–10826.

[21] Taylor, D. J.; Paterson, M. J. *J. Chem. Phys.* **2010**, *133*(20), 204302.

[22] Jose, L.; Seth, M.; Ziegler, T. *J. Phys. Chem. A* **2012**, *116*(7), 1864–1876.

[23] McKinlay, R.; Paterson, M. *The Jahn-Teller Effect: Fundamentals and Implications for Physics and Chemistry*, Vol. 97; Springer Science & Business Media, 2009.

[24] Mckinlay, R. G.; Żurek, J. M.; Paterson, M. J. In *Theoretical and Computational Inorganic Chemistry*; van Eldik, R., Harvey, J., Eds., Vol. 62 of *Advances in Inorganic Chemistry;* Academic Press, 2010; pages 351–390.

[25] Daniel, C. *Transition Metal and Rare Earth Compounds III;* Springer-Verlag, Berlin, 2004.

[26] Daniel, C. *Coord. Chem. Rev.* **2003**, *238-239*(0), 143–166.

[27] Schreiber, M.; Silva-Junior, M. R.; Sauer, S. P. A.; Thiel, W. *J. Chem. Phys.* **2008**, *128*(13), 134110.

[28] Silva-Junior, M. R.; Sauer, S. P.; Schreiber, M.; Thiel, W. *Mol. Phys.* **2010**, *108*(3-4), 453–465.

[29] Nakai, H.; Ohmori, Y.; Nakatsuji, H. *J. Phys. Chem.* **1995**, *99*(21), 8550–8555.

[30] Gutsev, G. L.; Rao, B. K.; Jena, P. *J. Phys. Chem. A* **1999**, *103*(50), 10819–10824.

[31] Houmøller, J.; Kaufman, S. H.; Støchkel, K.; Tribedi, L. C.; Brøndsted Nielsen, S.; Weber, J. M. *Chem. Phys. Chem.* **2013**, *14*(6), 1133–1137.

[32] Gaussian 09 Revision A.02. Frisch, M. J.; Trucks, G. W.; Schlegel, H. B.; Scuseria, G. E.; Robb, M. A.; Cheeseman, J. R.; Scalmani, G.; Barone, V.; Mennucci, B.; Petersson, G. A.; Nakatsuji, H.; Caricato, M.; Li, X.; Hratchian, H. P.; Izmaylov, A. F.; Bloino, J.; Zheng, G.; Sonnenberg, J. L.; Hada, M.; Ehara, M.; Toyota, K.; Fukuda, R.; Hasegawa, J.; Ishida, M.; Nakajima, T.; Honda, Y.; Kitao, O.; Nakai, H.; Vreven, T.; Montgomery, Jr., J. A.; Peralta, J. E.; Ogliaro, F.; Bearpark, M.; Heyd, J. J.; Brothers, E.; Kudin, K. N.; Staroverov, V. N.; Kobayashi, R.; Normand, J.; Raghavachari, K.; Rendell, A.; Burant, J. C.; Iyengar, S. S.; Tomasi, J.; Cossi, M.; Rega, N.; Millam, J. M.; Klene, M.; Knox, J. E.; Cross, J. B.; Bakken, V.; Adamo, C.; Jaramillo, J.; Gomperts, R.; Stratmann, R. E.; Yazyev, O.; Austin, A. J.; Cammi, R.; Pomelli, C.; Ochterski, J. W.; Martin, R. L.; Morokuma, K.; Zakrzewski, V. G.; Voth, G. A.; Salvador, P.; Dannenberg, J. J.; Dapprich, S.; Daniels, A. D.; Farkas, .; Foresman, J. B.; Ortiz, J. V.; Cioslowski, J.; Fox, D. J.

[33] Aidas, K.; Angeli, C.; Bak, K. L.; Bakken, V.; Bast, R.; Boman, L.; Christiansen, O.; Cimiraglia, R.; Coriani, S.; Dahle, P.; Dalskov, E. K.; Ekström, U.; Enevoldsen, T.; Eriksen, J. J.; Ettenhuber, P.; Fernández, B.; Ferrighi, L.; Fliegl, H.; Frediani, L.; Hald, K.; Halkier, A.; Hättig, C.; Heiberg, H.; Helgaker, T.; Hennum, A. C.; Hettema, H.; Hjertenæs, E.; Høst, S.; Høyvik, I.-M.; Iozzi, M. F.; Jansík, B.; Jensen, H. J. Aa.; Jonsson, D.; Jørgensen, P.; Kauczor, J.; Kirpekar, S.; Kjærgaard, T.; Klopper, W.; Knecht, S.; Kobayashi, R.; Koch, H.; Kongsted, J.; Krapp, A.; Kristensen, K.; Ligabue, A.; Lutnæs, O. B.; Melo, J. I.; Mikkelsen, K. V.; Myhre, R. H.; Neiss, C.; Nielsen, C. B.; Norman, P.; Olsen, J.; Olsen, J. M. H.; Osted, A.; Packer, M. J.; Pawlowski, F.; Pedersen, T. B.; Provasi, P. F.; Reine, S.; Rinkevicius, Z.; Ruden, T. A.; Ruud, K.; Rybkin, V. V.; Sałek, P.; Samson, C. C. M.; de Merás, A. S.; Saue, T.; Sauer, S. P. A.; Schimmelpfennig, B.; Sneskov, K.; Steindal,

A. H.; Sylvester-Hvid, K. O.; Taylor, P. R.; Teale, A. M.; Tellgren, E. I.; Tew, D. P.; Thorvaldsen, A. J.; Thøgersen, L.; Vahtras, O.; Watson, M. A.; Wilson, D. J. D.; Ziolkowski, M.; Ågren, H. *WIREs Comput.Mol.Sci.* **2015**, *4*(3), 269–284.

[34] Silva-Junior, M. R.; Sauer, S. P.; Schreiber, M.; Thiel, W. *Mol. Phys.* **2010**, *108*(3-4), 453–465.

[35] Palenik, G. J. *Inorg. Chem.* **1967**, *6*(3), 507–511.

[36] Lee, T. J.; Taylor, P. R. *Int. J. Quantum Chem.* **1989**, *36*(S23), 199–207.

[37] Jiang, W.; DeYonker, N. J.; Wilson, A. K. *J. Chem. Theory. Comput.* **2012**, *8*(2), 460–468.

Chapter 5

What is the ground state of first row transition metal monocarbonyls? A challenge for quantum chemistry

5.1 Introduction

This chapter aims to characterize the ground state properties of first-row transition metal monocarbonyls using a variety of methods. The main goal is to understand the interactions between the metal and carbonyl group using different computational methods and how each performs in predicting the lowest spin state.

The first experiments on carbon monoxide with metals date back to 19^{th} century when Justus Von Liebig tried to synthesize the first organometallic metal carbonyl. Since then, metal carbonyl bonding has been one of the most extensive studied systems in chemistry. These compounds are very interesting for catalytic properties and are of industrial importance. They play an important role in photodecomposition of organometallics (see chapter 7, where photochemical processes are described). Carbon monoxide is considered to be one of the most important π-acceptor ligand. It can stabilize metals with zero oxidation state in very different carbonyl complexes.

During the 70s and 80s, a lot of research was performed on first-row

transition metal monocarbonyls. A lot of papers were written to try and predict the spectroscopy and structural properties of these [1, 2, 3, 4, 5, 6, 7, 8, 9, 10, 11, 12, 13, 14, 15].

In 1990 Barnes *et al* performed an extensive study in the first and second-row mono and dicarbonyl positive ions [16]. Using *ab initio* calculations they discussed the bonding of these systems in detail, in order to understand the trends these molecules follow. The electropositive metals tend to react, for example with aldehydes or ketones [17]. In 1993 a study performed by René Fournier compiled an extensive study about the high and low-spin states of mono metal carbonyls [18]. A few years later, the same group performed calculations to evaluate geometrical parameters using density functional theory of Ni(CO), Cr(CO) and Cu(CO). For the last two studies it was found that the linear structures are not as stable as bent ones, the difference around 12.6 kJ/mol. This was an interesting result as it had previously been assumed that all the geometries for first-row transition metal monocarbonyls were linear [19]. Another breakthrough was the evaluation of the performance of DFT methods in 1995 by Carlo Adamo *et al* using such systems [20]. They chose the most stable configurations for the ground state calculations based on experiment. In the same year, the same group treated the first excited electronic states using DFT to try and highlight problems with methodology, especially those related to the discrepancy between experimental and theoretical results [21]. In 2001 Zhou *et al* compiled an extensive review that summarized experimental and theoretical studies performed on unsaturated metal monocarbonyls [22]. In 2003 Julien *et al* studied the structure and stability of first-row transition metals using DFT [23]. In the same year an extensive study performed by Gutsev *et al* on M(CO) on 3d monocarbonyls characterized the electronic structure, MC-O bond strength, structure and thermodynamics of these complexes [24].

Performing ground or excited state calculations on the first-row mono-

carbonyls is not an easy task. The proximity of multiple energy states and the multireference character of many of the complexes, lead to multiple sources of error and difficulties in the calculations [25]. To extend previous studies, the paramount issue of calculating the spin states for transition metal monocarbonyls using highly correlated methods, and providing a robust treatment of multireference effects, was undertaken here.

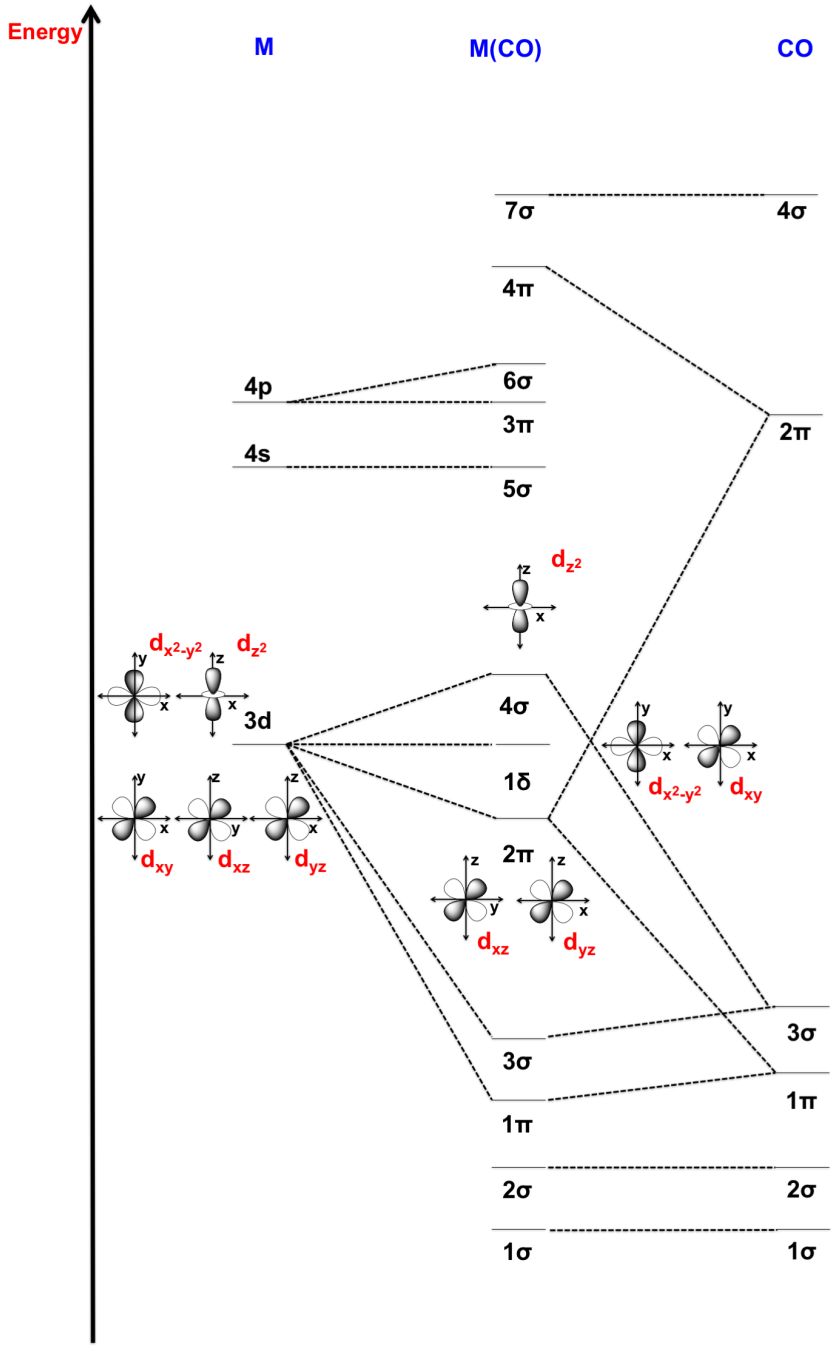

Figure 5.1: Molecular orbital diagram for a linear transition metal monocarbonyl.

5.2 Computational details

In this chapter, Hartree-Fock and coupled-cluster theory were chosen for geometry optimisation purposes. As shown before, CCSD, proves to be very reliable for solving similar ground state geometrical problems. For coupled-cluster, two different basis sets were selected in order to compare the outcome of the calculations and to find out how it would affect the most stable spin state for a given complex. For Hartree-Fock and CCSD a correlation-consistent basis set was chosen, cc-pVDZ. A further single-point was performed for CCSD with cc-pVTZ and a larger basis set chosen for comparison purposes, cc-pwCVTZ [26] [27]. The later basis set allows us to calculate core correlation on ground state properties for first-row transition metal carbonyls as it includes tightly optimised basis functions. The program used for these calculations was Gaussian09 [28]. Analytical frequency calculations were performed in all the geometrically optimised structures to guarantee a minimum.

The second part of this chapter focuses on applying NEVPT2 on the most stable spin state at the CCSD/cc-pVDZ optimised geometry. Dalton2015 [29] was chosen for NEVPT2 calculations which does not use the full point group symmetry, $C_{\infty v}$, but rather C_{2v}. Tracing back to assign the full point group to these states is a challenging task, since $C_{\infty v}$ is a non-abelian point group. The reference space for the monocarbonyls was constructed by having the lowest (1-5) a_1, (1-3) b_1, (1-3) b_2 orbitals and $1a_2$. These correspond to the 1π, 3σ, 2π, 1δ, 4σ, 5σ, 3π and 6σ shown in Figure 5.1 (M(CO)). For Ti(CO) 6 electrons were chosen for the active space. For V(CO) 7 electrons, Cr(CO) 8 electrons, Mn(CO) 9 electrons and Fe(CO) 10 electrons.

To complete this study, MCCI was performed on all the metal monocarbonyls. The same geometry chosen for NEVPT2 was used here (CCSD/cc-pVDZ). The cmin (convergence threshold) used for the MCCI calculations was $3*10^{-4}$.

5.3 Results and discussion

5.3.1 Geometry discussion

In this section the geometrical properties of the studied transition metal monocarbonyls are discussed. As is shown in Table 5.1 for Ti(CO), the bond lengths of the different monocarbonyls are similar among spin states and method (HF and CCSD). The main discrepancy in this table is the difference in bond length between coupled-cluster with cc-pVTZ and cc-pwCVTZ. The core correlated basis set predicts an elongated Ti-C bond of around 0.2 Å. Since both calculations are minima in the potential energy surface, it seems that the core correlation basis functions, influence this result largely.

When looking at V(CO) in Table 5.2, Hartree-Fock overestimates the metal-carbonyl bond for the doublet, quartet and sextet spin states relative to CCSD. For CCSD the bond lengths are very close to each other, considering all the different basis sets. For the sextet, the two DFT functionals from previous work underestimate the bond length compared to coupled-cluster.

For Cr(CO), in Table 5.3 it is intriguing to look at the bond lengths for the quintet. Using CCSD/cc-pVTZ, there is a 0.2 Å difference when comparing it to cc-pVDZ and cc-pwCTVZ for the Cr-C bond length. For the triplet CCSD/cc-pVTZ underestimates the Cr-C bond length in comparison to CCSD/cc-pwcVTZ. For the singlet and septet spin state calculation, Hartree-Fock dissociated the molecule, i.e. was unbound. From previous calculations, BP/VWN and BPW91/6-311+G* predicted a bent structure for the septet.

By looking at Mn(CO) in Table 5.4 for the quartet, it is possible to notice that there are a few discrepancies between the different methods. CCSD/cc-pVTZ and CCSD/cc-pwCVTZ have a difference of 0.2 Å for the Mn-C bond and 0.02 Å for the C-O bond. The literature results

(BP/VWN and BPW91/6-311G*) are 0.2 Å apart, considering the Mn-C bond. BP/VWN predicts a bent structure for the quartet.

The last metal carbonyl considered is Fe(CO) (Table 5.5). The Fe-C bond is one of the shortest bonds considered from the calculations performed, especially for the triplet spin state. From previous literature calculations, BP/VWN predicts a bent geometry for the complex again. Hartree-Fock dissociated the molecule for the singlet spin state.

Ti(CO)

	Method	r Ti-C(Å)	r C-O(Å)	α Ti-C-O (°)
Singlet	HF/cc-pVDZ	1.921	1.154	180.0
	CCSD/cc-pVDZ	1.891	1.196	180.0
	CCSD/cc-pVTZ	1.871	1.190	180.0
	CCSD/cc-pwCVTZ	2.082	1.156	180.0
Triplet	HF/cc-pVDZ	2.084	1.127	180.0
	CCSD/cc-pVDZ	2.009	1.170	180.0
	CCSD/cc-pVTZ	1.997	1.162	180.0
	CCSD/cc-pwCVTZ	2.092	1.160	180.0
Quintet	HF/cc-pVDZ	2.298	1.112	180.0
	CCSD/cc-pVDZ	2.092	1.157	180.0
	CCSD/cc-pVTZ	2.067	1.151	180.0
	CCSD/cc-pwCVTZ	2.055	1.144	180.0
	BP/VWN [18]	1.969	1.175	180.0
	BPW91/6-311+G* [24]	2.016	1.172	180.0
Septet	HF/cc-pVDZ	2.105	1.390	180.0
	CCSD/cc-pVDZ	2.092	1.157	180.0
	CCSD/cc-pVTZ	2.187	1.244	180.0
	CCSD/cc-pwCVTZ	2.152	1.236	180.0

Table 5.1: Ti(CO) bond lengths and angles using different methods for spin states.

V(CO)

	Method	r V-C(Å)	r C-O(Å)	α V-C-O (°)
Doublet	HF/cc-pVDZ	2.004	1.122	180.0
	CCSD/cc-pVDZ	1.856	1.168	180.0
	CCSD/cc-pVTZ	1.834	1.163	180.0
	CCSD/cc-pwCVTZ	1.817	1.158	180.0
Quartet	HF/cc-pVDZ	2.086	1.120	180.0
	CCSD/cc-pVDZ	1.856	1.169	180.0
	CCSD/cc-pVTZ	1.930	1.163	180.0
	CCSD/cc-pwCVTZ	1.913	1.157	180.0
Sextet	HF/cc-pVDZ	2.575	1.106	180.0
	CCSD/cc-pVDZ	2.086	1.146	180.0
	CCSD/cc-pVTZ	2.048	1.140	180.0
	CCSD/cc-pwCVTZ	2.044	1.134	180.0
	BP/VWN [18]	1.925	1.169	180.0
	BPW91/6-311+G* [24]	1.969	1.167	180.0
Octet	HF/cc-pVDZ	2.004	1.122	180.0
	CCSD/cc-pVDZ	2.048	1.404	146.3
	CCSD/cc-pVTZ	2.044	1.398	146.3
	CCSD/cc-pwCVTZ	2.026	1.393	140.7

Table 5.2: V(CO) bond lengths and angles using different methods for spin states.

Cr(CO)

	Method	r Cr-C(Å)	r C-O(Å)	α Cr-C-O (°)
Singlet	HF/cc-pVDZ	∞	∞	∞
	CCSD/cc-pVDZ	1.844	1.150	180.0
	CCSD/cc-pVTZ	1.810	1.144	180.0
	CCSD/cc-pwCVTZ	1.784	1.142	180.0
Triplet	HF/cc-pVDZ	1.947	1.126	180.0
	CCSD/cc-pVDZ	1.803	1.173	180.0
	CCSD/cc-pVTZ	1.788	1.165	180.0
	CCSD/cc-pwCVTZ	1.930	1.156	180.0
Quintet	HF/cc-pVDZ	2.060	1.156	180.0
	CCSD/cc-pVDZ	2.199	1.135	180.0
	CCSD/cc-pVTZ	1.934	1.172	180.0
	CCSD/cc-pwCVTZ	2.131	1.122	180.0
Septet	HF/cc-pVDZ	∞	∞	∞
	CCSD/cc-pVDZ	2.044	1.160	180.0
	CCSD/cc-pVTZ	2.026	1.154	180.0
	CCSD/cc-pwCVTZ	2.031	1.151	180.0
	BP/VWN [18]	2.070	1.162	141.9
	BPW91/6-311+G* [24]	2.156	1.161	139.5

Table 5.3: Cr(CO) bond lengths and angles using different methods for spin states.

Mn(CO)

	Method	r Mn-C(Å)	r C-O(Å)	α Mn-C-O (°)
Doublet	HF/cc-pVDZ	1.852	1.134	180.0
	CCSD/cc-pVDZ	1.758	1.181	180.0
	CCSD/cc-pVTZ	1.740	1.174	180.0
	CCSD/cc-pwCVTZ	1.741	1.166	180.0
Quartet	HF/cc-pVDZ	1.799	1.143	180.0
	CCSD/cc-pVDZ	1.744	1.186	180.0
	CCSD/cc-pVTZ	1.730	1.178	180.0
	CCSD/cc-pwCVTZ	1.961	1.153	180.0
	BP/VWN [18]	1.910	1.170	155.5
	BPW91/6-311+G* [24]	1.727	1.188	180.0
Sextet	HF/cc-pVDZ	2.113	1.152	180.0
	CCSD/cc-pVDZ	2.043	1.168	180.0
	CCSD/cc-pVTZ	2.030	1.160	180.0
	CCSD/cc-pwCVTZ	2.024	1.154	180.0
Octet	HF/cc-pVDZ	1.852	1.134	180.0
	CCSD/cc-pVDZ	2.194	1.156	180.0
	CCSD/cc-pVTZ	2.169	1.152	180.0
	CCSD/cc-pwCVTZ	2.161	1.148	180.0

Table 5.4: Mn(CO) bond lengths and angles using different methods for spin states.

Fe(CO)

	Method	r Fe-C(Å)	r C-O(Å)	α Fe-C-O (°)
Singlet	HF/cc-pVDZ	∞	∞	∞
	CCSD/cc-pVDZ	1.733	1.171	180.0
	CCSD/cc-pVTZ	1.715	1.164	180.0
	CCSD/cc-pwCVTZ	1.718	1.157	180.0
Triplet	HF/cc-pVDZ	1.794	1.134	180.0
	CCSD/cc-pVDZ	1.723	1.174	180.0
	CCSD/cc-pVTZ	1.708	1.166	180.0
	CCSD/cc-pwCVTZ	1.710	1.159	180.0
	BP/VWN [18]	1.803	1.169	158.1
	BPW91/6-311+G* [24]	1.707	1.171	180.0
Quintet	HF/cc-pVDZ	2.005	1.118	180.0
	CCSD/cc-pVDZ	1.892	1.154	180.0
	CCSD/cc-pVTZ	1.876	1.146	180.0
	CCSD/cc-pwCVTZ	1.880	1.140	180.0
Septet	HF/cc-pVDZ	2.236	1.117	180.0
	CCSD/cc-pVDZ	2.090	1.159	180.0
	CCSD/cc-pVTZ	2.068	1.151	180.0
	CCSD/cc-pwCVTZ	2.064	1.147	180.0

Table 5.5: Fe(CO) bond lengths and angles using different methods for spin states

5.3.2 Spin state discussion

In this subsection the energetic analysis of different methods for different spin states is discussed. Table 5.6 shows the postulated ground states for the monocarbonyls assigned experimentally.

The first studied transition metal monocarbonyl was Ti(CO). Looking at Table 5.7, HF, CCSD, NEVP2 and MCCI predict the same spin state, the quintet. The triplet state sits very close in energy, especially for MCCI and NEVPT2 methods. There is an interesting result when comparing CCSD/cc-pVTZ and CCSD/cc-pwCVTZ on Table 5.8. For the singlet state, using a core correlated basis set, the energy gap between spin states decreases substantially.

For V(CO) in Table 5.9, all the methods predict the same state as being the most stable, the sextet. NEVPT2 predicts the quartet to sit 0.28 eV higher in energy than the sextet, although other methods predict a larger energy gap. In Table 5.10, the energetic values of CCSD/cc-pVTZ and CCSD/cc-pwcVTZ predict the same spin state.

The next studied complex was Cr(CO) (Table 5.11). MCCI predicts the septet as the most stable spin state, while CCSD and NEVPT2 predict the quintet. Hartree-Fock dissociated the molecule for the singlet and septet. In Table 5.12 cc-pVTZ and cc-pwcVTZ predict the quintet as the most stable spin state, and the latter considers the septet only 0.12 eV higher in energy, while the former sits higher, 0.50 eV.

For MnCO, coupled-cluster and MCCI predict the sextet as the most stable spin state, while NEVPT2 and HF predict the octet (Table 5.13). It seems that for this complex the extrapolation of the experimental results is not a correct assumption, and MCCI, which is the most robust method predicts the sextet and not the quartet as the most stable spin state [30]. When looking at Table 5.14, cc-pVTZ and cc-pwCVTZ pre-

dict the sextet as the lowest spin state, although the octet sits 0.16 eV and 0.21 eV higher in energy respectively.

Iron monocarbonyl (Table 5.15) does not follow the same trend as the last two metal monocarbonyls and the chosen methods do not give the most stable spin state as $^3\Sigma^-$ from previous work. MCCI, NEVPT2 and CCSD predict the quintet as the most stable spin state. Using different basis sets, as shown in Table 5.16, the quintet is considered the lowest spin state, although the triplet and septet sit close in energy to the quintet (around 1 eV).

Metal	**State**
Ti(CO)	$^5\Delta$
V(CO)	$^6\Sigma^+$
Cr(CO)	$^7A'$
Mn(CO)	$^4\Sigma^-$
Fe(CO)	$^3\Sigma^-$

Table 5.6: Ground states previously postulated [30].

Ti(CO)

Spin State ($2S+1$)	**HF**	**CCSD**	**NEVPT2**	**MCCI**
1	4.47	2.46	2.35	1.43
3	1.89	1.62	0.24	0.64
5	0.00	0.00	0.00	0.00
7	4.25	5.87	7.04	7.32

Table 5.7: Ti(CO) relative energies (eV) calculated with different levels of theory and cc-pVDZ.

Spin State ($2S+1$)	**cc-pVTZ**	**cc-pwCVTZ**
1	2.20	0.98
3	0.92	0.78
5	0.00	0.00
7	6.79	6.78

Table 5.8: Ti(CO) relative energies (eV) calculated with CCSD and valence and core correlated basis sets.

V(CO)

Spin State ($2S+1$)	HF	CCSD	NEVPT2	MCCI
2	4.04	2.26	1.65	1.88
4	2.14	0.87	0.28	0.59
6	0.00	0.00	0.00	0.00
8	3.95	5.77	7.34	7.33

Table 5.9: V(CO) relative energies (eV) calculated with different levels of theory and cc-pVDZ.

Spin State ($2S+1$)	cc-pVTZ	cc-pwCVTZ
2	2.02	2.12
4	0.74	0.87
6	0.00	0.00
8	6.63	5.81

Table 5.10: V(CO) relative energies (eV) calculated with CCSD and valence and core correlated basis sets.

Cr(CO)

Spin State ($2S+1$)	HF	CCSD	NEVPT2	MCCI
1	∞	4.26	2.72	3.15
3	3.63	2.57	1.59	2.87
5	0.00	0.00	0.00	0.92
7	∞	0.65	0.74	0.00

Table 5.11: Cr(CO) relative energies (eV) calculated with different levels of theory and cc-pVDZ.

Spin State ($2S+1$)	cc-pVTZ	cc-pwCVTZ
1	3.51	3.96
3	1.77	1.32
5	0.00	0.00
7	0.12	0.50

Table 5.12: Cr(CO) relative energies (eV) calculated with CCSD and valence and core correlated basis sets.

Mn(CO)

Spin State ($2S+1$)	HF	CCSD	NEVPT2	MCCI
2	8.84	4.23	2.91	3.61
4	6.37	1.82	2.55	1.47
6	0.32	0.00	4.02	0.00
8	0.00	0.08	0.00	0.09

Table 5.13: Mn(CO) relative energies (eV) calculated with different levels of theory and cc-pVDZ.

Spin State ($2S+1$)	cc-pVTZ	cc-pwCVTZ
2	3.93	3.82
4	1.63	0.46
6	0.00	0.00
8	0.16	0.21

Table 5.14: Mn(CO) relative energies (eV) calculated with CCSD and valence and core correlated basis sets.

Fe(CO)

Spin State ($2S+1$)	HF	CCSD	NEVPT2	MCCI
1	∞	3.74	2.40	3.73
3	4.79	1.26	0.94	0.51
5	0.92	0.00	0.00	0.00
7	0.00	1.07	3.98	2.08

Table 5.15: Fe(CO) relative energies (eV) calculated with different levels of theory and cc-pVDZ.

Spin State ($2S+1$)	cc-pVTZ	cc-pwCVTZ
1	3.52	3.42
3	1.10	1.02
5	0.00	0.00
7	0.93	0.98

Table 5.16: Fe(CO) relative energies (eV) calculated with CCSD and valence and core correlated basis sets.

5.3.3 Mean absolute deviations

The last part of the discussion focuses on the error analysis for the energetic calculations regarding spin states. Mean absolute deviations are provided in Table 5.17 and MCCI is considered the most robust method. Hartree-Fock has the highest mean absolute value when compared to MCCI (1.7 eV). Although NEVPT2 is in theory a more robust method than EOM-CCSD, it has a mean absolute deviation value of 0.75 eV, while EOM-CCSD has a mean absolute deviation of 0.57 eV.

Note that the effects of core correlation are not insignificant for these systems with a mean difference between cc-pVTZ and cc-pwCVTZ of 0.26 eV, with no frozen core for the latter basis.

Complex	**Mean Abs. Dev. (eV)**
HF	1.7
CCSD	0.57
NEVPT2	0.75

Table 5.17: Mean absolute deviations in spin analysis for CCSD/cc-pVDZ basis set considering MCCI the best theory.

5.4 Conclusions

Transition metal complexes prove to be one of the most challenging fields for computational inorganic chemists. The calibration performed on the first-row transition metal monocarbonyls is able to establish very important ground state properties. Some of the chosen methods for this study have never been used before in these systems. Methods such as CCSD, NEVPT2 or MCCI can provide a clear picture, exploring gaps that were found in other methods, helping to describe the ground state properties properly. The multireference methods MCCI and NEVPT2 are a valuable tool for these systems. Using MCCI is fundamental to recover balanced static correlation and assign the spin states accurately. It is considered the most robust theoretical method to be applied to these systems.

Clearly electron correlation affects the ground spin state of monocarbonyls. Discrepancy from assigned spin states is explained by the wrong extrapolation of the experimental results calculated for the isolated metals. The studies performed in the past to calculate the atomic energy for isolated transition metals should not necessarily be extrapolated to complexes.

This chapter shows that some care must be taken when analysing the balance between static and dynamic correlation. Inorganic transition metals have a very large dependence on how correlation is defined that can lead to large errors if it is not addressed properly.

Bibliography

[1] Mortola, A. P.; Goddard, W. A. *J. Am. Chem. Soc.* **1974**, *96*(1), 1–10.

[2] Hanlan, L. A.; Huber, H.; Kuendig, E. P.; McGarvey, B. R.; Ozin, G. A. *J. Am. Chem. Soc.* **1975**, *97*(24), 7054–7068.

[3] Hanlan, L.; Huber, H.; Ozin, G. A. *Inorg. Chem.* **1976**, *15*(11), 2592–2597.

[4] Engelking, P. C.; Lineberger, W. C. *J. Am. Chem. Soc.* **1979**, *101*(19), 5569–5573.

[5] Garrison, B. J.; Winograd, N.; Harrison, D. E. *J. Vac. Sci. Technol.* **1979**, *16*(2), 789–792.

[6] A. Rosen, P. G.; Morovic, T. *Surf. Sci.* **1980**, *95*(2–3), 477–495.

[7] Bursten, B. E.; Freier, D. G.; Fenske, R. F. *Inorg. Chem.* **1980**, *19*(6), 1810–1811.

[8] Freund, H.-J.; Dick, B.; Hohlneicher, G. *Theor. Chim. Acta* **1980**, *57*(3), 181–207.

[9] McIntosh, D. F.; Ozin, G. A.; Messmer, R. P. *Inorg. Chem.* **1981**, *20*(11), 3640–3650.

[10] Peden, C. H. F.; Parker, S. F.; Barrett, P. H.; Pearson, R. G. *J. Phys. Chem.* **1983**, *87*(13), 2329–2336.

[11] Guenzburger, D.; Baggio-Saitovitch, E.; De Paoli, M. A.; Manela, H. *J. Chem. Phys.* **1984**, *80*(2), 735–744.

[12] Halle, L. F.; Crowe, W. E.; Armentrout, P. B.; Beauchamp, J. L. *Organometallics* **1984**, *3*(11), 1694–1706.

[13] Huzinaga, S.; Klobukowski, M.; Sakai, Y. *J. Phys. Chem.* **1984**, *88*(21), 4880–4886.

[14] Bauschlicher, C. W. *J. Chem. Phys.* **1986**, *84*(1), 260–267.

[15] Sawaryn, A.; Aldridge, L. P.; Blas, R.; Marathe, V. R.; Trautwein, A. X. *Hyperfine Interact.* **1986**, *29*, 1303–1306.

[16] Barnes, L. A. Ros M. Bauschlicher, C. W. *J. Chem. Phys.* **1990**, *93 (1)*, 609–624.

[17] Halle, L.; Crowe, W.; Armentrout, P.; Beauchamp, J. *Organometallics* **1984**, *3*(11), 1694–1706.

[18] Fournier, R. *J. Chem. Phys.* **1993**, *99*(3), 1801–1815.

[19] Fournier, R. *J. Chem. Phys.* **1993**, *98*(10), 8041–8050.

[20] Adamo, C.; Lelj, F. *J. Chem. Phys.* **1995**, *103*(24), 10605–10613.

[21] Adamo, C.; Lelj, F. *Chem. Phys. Lett.* **1995**, *246*(4–5), 463–468.

[22] Zhou, M.; Andrews, L.; Bauschlicher, C. W. *Chem. Rev.* **2001**, *101*(7), 1931–1962.

[23] Pilme, J.; Silvi, B.; Alikhani, M. E. *J. Phys. Chem. A* **2003**, *107*(22), 4506–4514.

[24] Gutsev, G. L.; Andrews, L.; Jr., C. W. B. *Chem. Phys.* **2003**, *290*(1), 47–58.

[25] Almeida, N.; McKinlay, R.; Paterson, M. Structure and Bonding; Springer Berlin Heidelberg, 2014; pages 1–32.

[26] Balabanov, N. B.; Peterson, K. A. *J. Chem. Phys.* **2005**, *123*(6), 064107.

[27] Balabanov, N. B.; Peterson, K. A. *J. Chem. Phys.* **2006**, *125*(7), 074110.

[28] Gaussian 09 Revision A.02. Frisch, M. J.; Trucks, G. W.; Schlegel, H. B.; Scuseria, G. E.; Robb, M. A.; Cheeseman, J. R.; Scalmani, G.; Barone, V.; Mennucci, B.; Petersson, G. A.; Nakatsuji, H.; Caricato, M.; Li, X.; Hratchian, H. P.; Izmaylov, A. F.; Bloino, J.; Zheng, G.; Sonnenberg, J. L.; Hada, M.; Ehara, M.; Toyota, K.; Fukuda, R.; Hasegawa, J.; Ishida, M.; Nakajima, T.; Honda, Y.; Kitao, O.; Nakai, H.; Vreven, T.; Montgomery, Jr., J. A.; Peralta, J. E.; Ogliaro, F.; Bearpark, M.; Heyd, J. J.; Brothers, E.; Kudin, K. N.; Staroverov, V. N.; Kobayashi, R.; Normand, J.; Raghavachari, K.; Rendell, A.; Burant, J. C.; Iyengar, S. S.; Tomasi, J.; Cossi, M.; Rega, N.; Millam, J. M.; Klene, M.; Knox, J. E.; Cross, J. B.; Bakken, V.; Adamo, C.; Jaramillo, J.; Gomperts, R.; Stratmann, R. E.; Yazyev, O.; Austin, A. J.; Cammi, R.; Pomelli, C.; Ochterski, J. W.; Martin, R. L.; Morokuma, K.; Zakrzewski, V. G.; Voth, G. A.; Salvador, P.; Dannenberg, J. J.; Dapprich, S.; Daniels, A. D.; Farkas, .; Foresman, J. B.; Ortiz, J. V.; Cioslowski, J.; Fox, D. J.

[29] Aidas, K.; Angeli, C.; Bak, K. L.; Bakken, V.; Bast, R.; Boman, L.; Christiansen, O.; Cimiraglia, R.; Coriani, S.; Dahle, P.; Dalskov, E. K.; Ekström, U.; Enevoldsen, T.; Eriksen, J. J.; Ettenhuber, P.; Fernández, B.; Ferrighi, L.; Fliegl, H.; Frediani, L.; Hald, K.; Halkier, A.; Hättig, C.; Heiberg, H.; Helgaker, T.; Hennum, A. C.; Hettema, H.; Hjertenæs, E.; Høst, S.; Høyvik, I.-M.; Iozzi, M. F.; Jansík, B.; Jensen, H. J. Aa.; Jonsson, D.; Jørgensen, P.; Kauczor, J.; Kirpekar, S.; Kjærgaard, T.; Klopper, W.; Knecht, S.;

Kobayashi, R.; Koch, H.; Kongsted, J.; Krapp, A.; Kristensen, K.; Ligabue, A.; Lutnæs, O. B.; Melo, J. I.; Mikkelsen, K. V.; Myhre, R. H.; Neiss, C.; Nielsen, C. B.; Norman, P.; Olsen, J.; Olsen, J. M. H.; Osted, A.; Packer, M. J.; Pawlowski, F.; Pedersen, T. B.; Provasi, P. F.; Reine, S.; Rinkevicius, Z.; Ruden, T. A.; Ruud, K.; Rybkin, V. V.; Sałek, P.; Samson, C. C. M.; de Merás, A. S.; Saue, T.; Sauer, S. P. A.; Schimmelpfennig, B.; Sneskov, K.; Steindal, A. H.; Sylvester-Hvid, K. O.; Taylor, P. R.; Teale, A. M.; Tellgren, E. I.; Tew, D. P.; Thorvaldsen, A. J.; Thøgersen, L.; Vahtras, O.; Watson, M. A.; Wilson, D. J. D.; Ziolkowski, M.; Ågren, H. *WIREs Comput. Mol. Sci.* **2015**, *4*(3), 269–284.

[30] Sugar, J.; Corliss, C. *J. Phys. Chem. Ref. Data Suppl. No. 2* **1985**.

Chapter 6

On the excited states of the nickel carbonyls Ni(CO) and $Ni(CO)_4$: challenging molecules for electronic structure theory

6.1 Introduction

The last chapter dealt with stern challenges describing the ground state of first-row transition metal monocarbonyls. Chapter 6 focuses on an extensive study of the ground and excited states of Ni(CO) and $Ni(CO)_4$.

A wide range of correlated electronic structure approaches were applied to the excited states of these two complexes in order to understand the performance of each method, in addition to set benchmark data for these important metal carbonyls. These complexes are models for unsaturated (NiCO) and saturated transition metal carbonyls ($Ni(CO)_4$) and can tell us more about the behaviour of more complex systems. Methods such as coupled-cluster linear response hierarchy, complete-active-space self-consistent field theory, N-electron valence state multireference perturbation theory, Monte-Carlo , and time-dependent density functional theory with a range of functionals and basis sets were chosen to describe these systems.

Early experimental work on these complexes shows very poor resolution

spectra, with broad and featureless spectra. With the evolution of technology, modern time-resolved pump-probe spectroscopy provided enormous breakthroughs in the area of the photochemistry of saturated metal carbonyls. A few examples are $Cr(CO)_6$, $Mn_2(CO)_{10}$ and $Fe(CO)_5$. All of them undergo extremely fast dissociation events, where a carbonyl group is lost. This is followed by rapid radiationless decay to the ground electronic state of the unsaturated complex. Then they display highly mode-specific vibrational coherences in this 'hot' product [1, 2, 3, 4, 5]. In the past, a lot of studies emerged on the photochemistry of such complexes: CASPT2 for $Cr(CO)_6$ [6][7], EOM-CCSD on $Cr(CO)_6$ [8] and LR-CCSD on $Fe(CO)_5$ [9]. There have also been several time-dependent density functional theory (TD-DFT) studies [7, 6, 8, 10]. TD-DFT offers the possibility of a very low cost, yet accurate treatment of many excited states in such systems, although agreement with *ab initio* methods is far from perfect.

6.1.1 $Ni(CO)_4$

$Ni(CO)_4$ has different properties when compared to complexes that follow rapid radiationless decay. It displays a red luminescence upon excitation on a much longer time scale [11]. The photochemistry of this complex has been studied over the years, using high level methods to describe the ground and excited states accurately. Various theoretical attempts have been made to study the excited states of $Ni(CO)_4$. A few examples are INDO/S [12], CASSCF and CASPT2 [6] and as it was mentioned before TD-DFT [10]. The results were generally poor, for example it was found that CASSCF overestimated excitation energies by around 1 eV compared to experiment.

The electronic absorption spectra of $Ni(CO)_4$ were obtained in previous calculation studies [12] [13]. These were performed both in the gas phase using UV light and in solution. The spectra are poorly resolved and lacking spectral detail. Both gas and solution phase spectra contain

one broad band at 6.0 eV with shoulders lower in energy at 5.5 eV and 5.2 eV in solution, and 5.4 eV and 4.6 eV in the gas phase. Previously all these transitions were assigned as $^1A_1 \rightarrow {}^1T_2$ and considered MLCT states.

6.1.2 Ni(CO)

This unsaturated transition metal carbonyl is important in many areas of catalysis, where it has been assumed to offer a simple model of chemisorption [14, 15, 16, 17] and in catalytic activation processes [18]. As for $Ni(CO)_4$ the σ bonding and the π-back-bonding to the nickel atom are the pillars of the formation of these kind of complexes. Several studies of Ni(CO) were performed in the past focusing on the nature of ground electronic state, see previous chapters. Initially predicted to be an open-shell triplet state [19], more recent calculations have in fact shown that the ground state is a closed-shell singlet (Σ^+) [20] [21] [22]. Based on this several different theoretical studies were performed in order to assess the different properties of the ground and excited states of Ni(CO). Different computational methods have been used to describe both the ground state electronic structure and the respective minimum geometry. High-resolution spectroscopic characterization gives a linear structure with a Ni-C distance of 1.669 Å and C-O distance of 1.153 Å [23].

Other extensive studies focused on analysing the degree of multireference character present in Ni(CO) [21] [24]. Madhavan *et al* after analysing a CI wavefunction proposed a mixture of configurations for the ground state, with $3d^{10}$ accounting for around 60% and the other configuration $3d^94s^1$ accounting for 40% [24]. Another study performed by Blomberg *et al* argued that nickel is better described only by $3d^94s^1$, since its d population is closer to 9 than 10 [21].

In 1994 Persson *et al* analysed and estimated the properties of ground state metal carbonyls (MCO), including Ni(CO) with a range of different transition metals [25]. One of the main concerns was the calculation of the binding energies and bond lengths using different degrees of correlated computational approaches and one-electron basis sets. Using coupled-cluster (CCSD(T)) and a large basis set, the closest value to the experimental binding energy was 142 kJ mol^{-1}, in comparison to 171±6 kJ mol^{-1} (experimental value from [26]). The closest binding energy to experimental data was obtained with CASSCF (170 kJ mol^{-1}), recovering the necessary static correlation to describe the system accurately.

Madhavan *et al* using CI theory characterized the lowest excited states of Ni(CO) [24]. More recently, CCSD, CCSD(T) and EOM-CCSD were chosen to study the geometrical properties and harmonic vibrational frequencies of the low-lying excited electronic states of Ni(CO) using a range of large basis sets [27]. This extensive study revealed the properties of the first excited states of the molecule, where seven different electronic states were computed ($^3\Delta$, $1^3\Sigma$,$1^3\Phi$, $1^3\Pi$, $2^3\Pi$, $1^1\Delta$ and $1^1\Pi$). The chosen method was CCSD(T) due to not only its robustness to describe difficult states but also being able to find accurate bond lengths and harmonic frequencies for the lowest states of each symmetry. It is shown that the π-back-donation from the nickel 3dπ to the carbonyl $2\pi^*$, as well as the σ-polarization, reduces the repulsion between the 4s nickel orbital and CO 5σ. It was also found, that the σ-donation for the CO is much less important than the π-back-donation from the metal in terms of the stability of the complex.

6.2 Computational details

All TD-DFT, EOM-CCSD and CASSCF calculations were performed with Gaussian 09 [28], while Dalton2015 [29] was chosen for the LR-CC and NEVPT2 calculations. Ni(CO)4 and Ni(CO) were initially optimised in their $^1A_1$ and $^1\Sigma^+$ electronic ground states, in T_d and $C_{\infty v}$

point groups respectively, at the CCSD and B3LYP level of theory, with a triple zeta basis set (cc-pVTZ). Frequency calculations confirmed that a minimum was obtained for both complexes.

For the CASSCF calculations different active spaces were chosen. Firstly a (10,11) active space was used comprising ten electrons distributed among five 3d orbitals plus an additional set of d orbitals representing the 4d antibonding equivalents of the 3d orbitals. This process of "orbital doubling" of the d orbitals was introduced in literature by Persson *et al* [25]. This way it is possible to introduce further correlation into the active space to describe dative electron pair bonding and the associated dynamic correlation, which is achieved through the extra node in the internuclear metal-ligand region. The final orbital included in the active space is a 4s nickel orbital. This active space is expected to describe the ground and low-lying excited states of Ni(CO)4 and Ni(CO) qualitatively based on previous CASSCF studies of other first row transition metal carbonyls [9, 30, 31, 32, 33, 34, 35].

Regarding $Ni(CO)_4$ multiconfigurational methods were not used to perform excited state calculations. It is known that these calculations would have a very high computational cost due to their requirement of state averaging associated with the number of states that need to be considered. Concerning Ni(CO), NEVPT2 was considered and the first low-lying excited states were calculated.

For quantitative excitation energies a balanced treatment of dynamical correlation is required and can be obtained through appropriate multireference perturbation theories. NEVPT2 was chosen to perform calculations on low-lying states of Ni(CO). This variant multireference perturbation theory is very powerful and offers a variety of approaches, based on different approximations to the perturbed system. Another important property is the fact that it avoids any problems of intruder states in the perturbation series. The reference space for Ni(CO) was

constructed by having the lowest (1-9) a_1, (1-3) b_1, and (1-3) b_2 orbitals doubly occupied in all configurations, with 12 electrons distributed across the next (10-14) a_1, (4-6) b_1, (4-6) b_2, and $1a_2$ orbitals. NEVPT2 wavefunctions were then evaluated using symmetry for the lowest singlet and triplet states of each irrep with the cc-pVTZ basis.

Finally Monte-Carlo configuration interaction (MCCI) was performed on Ni(CO), to confirm the correct ground state and to examine the first excited states as well. The cut-off chosen was cmin=3x10^{-4} based on previous experience with the MCCI algorithm, and there were 11 frozen orbitals from the core. The multireference character (MR) defined as MR= $\sum_i$ $|c_i|^2$ - $|c_i|^4$, was analysed as well. It has limiting values of zero for a single-configuration and one finds the value of MR around 0.3 for a weekly correlated system (e.g., ground state of hydrogen fluoride at equilibrium), whereas a strongly correlated system (e.g., Cr dimer ground state) has MR around 0.9 [36]. The MCCI calculations were performed using the optimised geometry with B3LYP/cc-pVTZ. cc-pVDZ and cc-pVTZ(D) were chosen for the calculations, due to difficulties in convergence for the full cc-pVTZ basis set. For the latter, the f angular momentum set is removed from the carbons and oxygens, while the g angular momentum functions are removed from the nickel. The difference in values between the two basis sets is compared in the result sections below and, the mean absolute deviations evaluated.

6.3 Results and discussion

6.3.1 Ground state - $Ni(CO)_4$

The most stable ground state geometry for nickel tetracarbonyl is T_d. From the literature $Ni(CO)_4$ was documented as being a closed shell system ($^1A_1$) [6] [10] [37]. Table 6.1 shows the results for $Ni(CO)_4$ where DFT, CCSD and CASPT2 are close to each other and experiment. Even though there is a considerable mixing between the metal and ligand orbitals, the ground state picture can still be depicted as being $3d^{10}$.

The electronic structure can be understood qualitatively in terms of the well-known molecular orbital diagram for tetrahedral π-bonded complexes. This MO picture has been discussed extensively by Bauschlicher *et al* [38]. It is noted that the CCSD T_1 diagnostic is 0.0316. This is large enough to indicate some multireference character when using Hartree-Fock orbitals. However, the system appears well-described, at least qualitatively, by a single configuration. A molecular orbital diagram is shown in Figure 6.1 describing the bonding in $Ni(CO)_4$.

Method	**Ni-C (Å)**	**C-O (Å)**
CCSD/cc-pVTZ	1.831	1.147
B3LYP/cc-pVTZ	1.846	1.136
MN12L/cc-pVTZ	1.819	1.136
MN12SX/cc-pVTZ	1.823	1.131
CASPT2[25] - Ni 5s4p3d1f; C,O 3s2p1d	1.83	1.16
Experimental [37]	1.838	1.142

Table 6.1: $Ni(CO)_4$ optimised geometrical parameters.

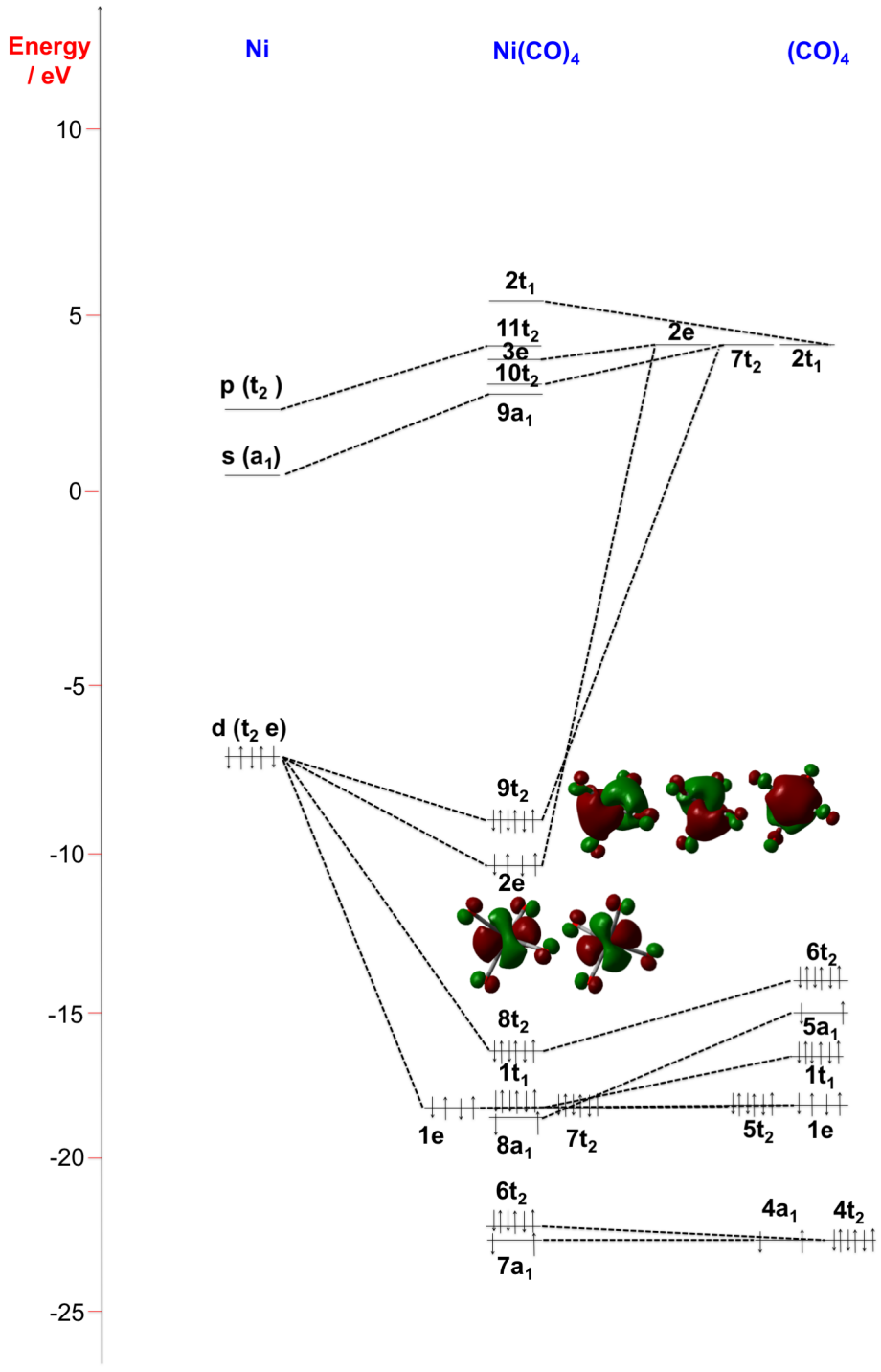

Figure 6.1: $Ni(CO)_4$ HF/cc-pVTZ molecular orbital diagram.

6.3.2 Ground state - Ni(CO)

The unsaturated Ni(CO) molecule presents a much sterner challenge in terms of the ground electronic state. As it was discussed before Ni(CO) was originally believed to be a triplet but the most recent calculations show that is indeed a closed-shell singlet ($^1\Sigma^+$). As before, a HF/cc-pVTZ molecular orbital diagram is depicted in Figure 6.2. The opti-

mised linear singlet geometries are shown in Table 6.2. Electron correlation causes a contraction in N-C bond length, although the C-O distance is very insensitive to this. The CCSD/cc-pVTZ T_1 diagnostic is 0.0459 indicating caution with regard to trusting the results due to a (partially) multireference wavefunction. Similar to its saturated counterpart the electronic structure appears to contain a dominant component with Ni $3d^{10}$ character. Multiconfigurational approaches confirm this with, for example, CAS(10,11) indicating that this dominant configuration accounts for around 86% of the wavefunction. CASSCF further confirms the ground state as a singlet, as does MCCI (vide infra) and NEVPT2 (Table 6.4). The state energies are expressed in terms of irreps of $C_{\infty v}$ point group, e.g. NEVPT2 (partially contracted approach), Table 6.4.

As shown in Table 6.3 the singlet-triplet gap reflects how important electronic correlation is to describe the ground state of Ni(CO). In particular, for DFT one finds that hybrid functionals tend to predict an incorrect triplet geometry and/or spin-state ordering. The degree of (exact) Hartree-Fock exchange appears to be the crucial quantity to describe the singlet spin-state correctly, even with modern meta-GGA functionals such as the Minnesota family. Interestingly CAM-B3LYP describes the triplet geometry and state ordering correctly. As it was noticed from the previous calculations electronic correlation is fundamental to describe this complex. In Table 6.4 the results for NEVPT2 state energies are shown, with a reference space built as described above, for each irrep of C_{2v} symmetry, for the lowest singlet and triplet states.

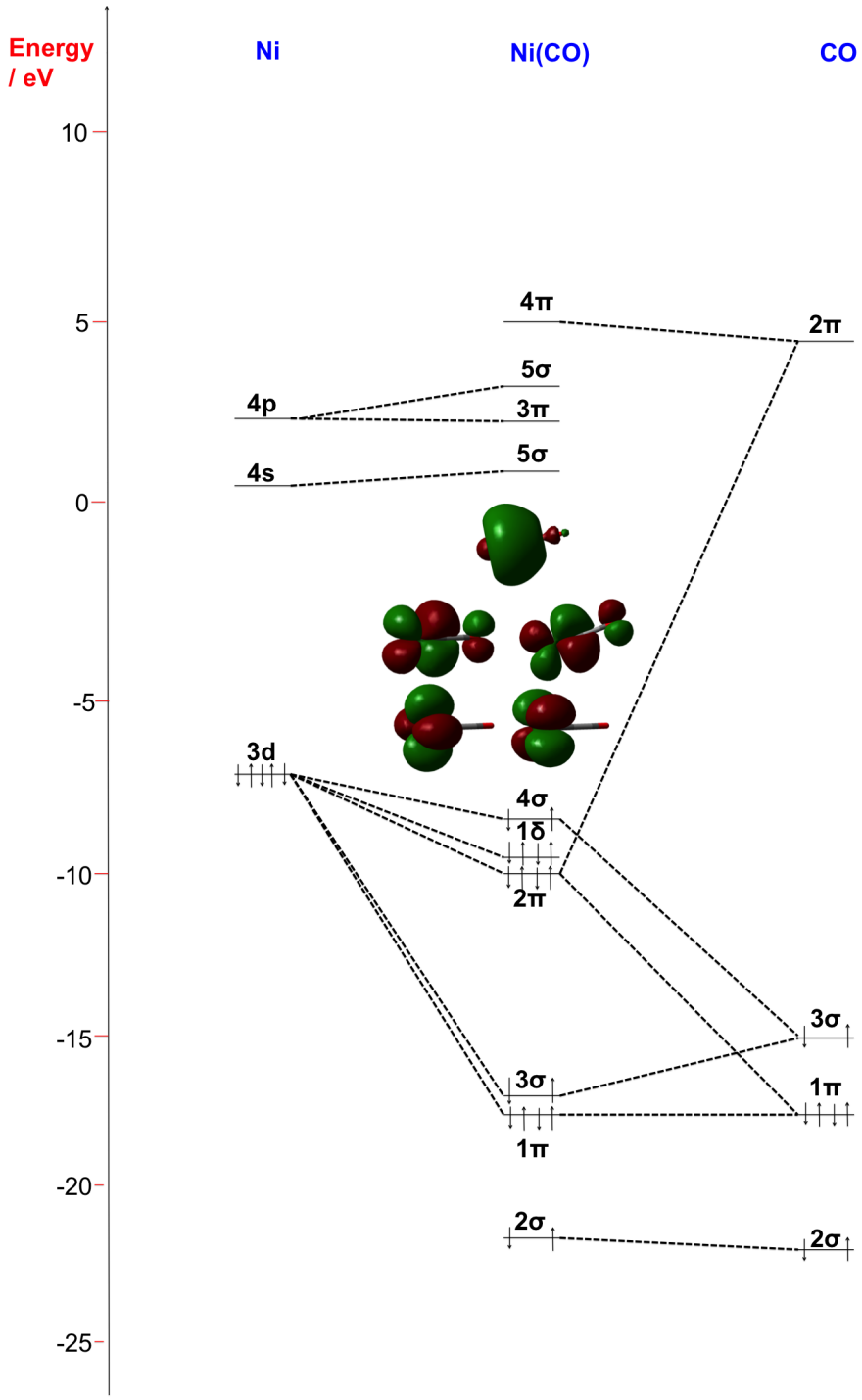

Figure 6.2: Ni(CO) HF/cc-pVTZ molecular orbital diagram.

Method	r Ni-C (Å)	r C-O (Å)	α Ni-C-O(°)
HF/cc-pvTZ	1.756	1.112	180.0
B3LYP/cc-pvTZ	1.683	1.149	180.0
BP86/cc-pvTZ	1.672	1.165	180.0
BP86/6-311+G* [39]	1.675	1.167	-
BPW91/6-311+G*[40]	1.675	1.166	-
B2PLYP/cc-pvTZ	1.682	1.161	180.0
mPW2PLYP/cc-pvTZ	1.682	1.156	180.0
B2PLYPD3/cc-pvTZ	1.682	1.161	180.0
M06/cc-pvTZ	1.685	1.142	174.6
M06L/cc-pvTZ	1.667	1.155	174.9
M06-2X/cc-pvTZ	1.718	1.138	173.5
M06-HF/cc-pvTZ	1.765	1.122	172.3
MN12SX/cc-pvTZ	1.680	1.144	180.0
MP2/cc-pvTZ	1.640	1.174	180.0
CCSD/cc-pvTZ	1.670	1.145	180.0
CCSD(T)/cc-pvTZ[41]	1.687	1.166	-
BD/cc-pvTZ	1.667	1.139	180.0
CASSCF [42] - Ni 8s6p4d; C,O 4s3p	1.683	1.161	-
CASPT2[25] - Ni 5s4p3dlf; C,O 3s2p1d	1.680	1.170 -	
Experimental [23]	1.669	1.153	-

Table 6.2: Ni(CO) singlet geometries.

Method	Single points (eV)	Geometry optimization (eV)
HF/cc-pVTZ	-1.08	-1.59
B3LYP/cc-pVTZ	1.37	0.84
BP86//cc-pVTZ	1.87	1.50
B2PLYP/cc-pVTZ	0.16	-0.43
mPW2PLYP/cc-pVTZ	0.12	-0.49
B2PLYPD3/cc-pVTZ	0.16	-0.43
M06/cc-pVTZ	1.73	1.14
M06L/cc-pVTZ	1.63	1.08
M06-2X/cc-pVTZ	0.45	-0.31
M06-HF/cc-pVTZ	-0.59	-1.62
MN12SX/cc-pVTZ	1.91	-7.70
MP2/cc-pVTZ	4.59	3.44
CCSD/cc-pVTZ	1.63	1.40
BD/cc-pVTZ	1.56	1.37

Table 6.3: Ni(CO) singlet/triplet gaps for various methods. Single-points at CCSD/cc-pVTZ geometry.

State	Energy (eV)
$1\ ^1\Sigma^+$	0.00
$1\ ^1\Delta$	1.14
$1\ ^1\Pi$	2.54
$1\ ^3\Delta$	0.80
$1\ ^3\Pi$	2.38

Table 6.4: Ni(CO) NEVPT2/cc-pVTZ singlet and triplet state energies (B3LYP/cc-pVTZ singlet geometry).

6.3.3 Excited States - $Ni(CO)_4$

The low-lying excited states of $Ni(CO)_4$ are shown in Table 6.5. The complex spectroscopy is a challenging case for computational/inorganic chemists since it has a high density of states (>20, below 6 eV) and it is not easy to classify them. In its ground state $Ni(CO)_4$ has T_d symmetry, so only T_2 symmetry transitions are dipole allowed. This means that apart from these transitions all others do not have an associated oscillator strength. All the low-lying states, and in particular the two bright states observed experimentally, have MLCT character, i.e., from the filled 3d orbitals to those that are predominately of π^* character with largest amplitudes on the carbonyls. The second bright state, 2^1T_2, involves mainly transitions from the same highest filled t-symmetry LF d orbitals to the next lowest empty e-symmetry π^* orbitals. There is a 4.5 eV shoulder in the gas phase spectrum, that is 0.5 eV lower in energy than EOM-CCSD. The highest allowed states for these methods correlate well with the other shoulder that sits around 5.2-5.4 eV.

Similarly to Chapter 4 the most striking results come from the linear response coupled-cluster methods. CC2 produces qualitatively wrong results: for the first T_2 state, the error is around 3.6 eV. CCR(3) also behaves in a unusual way with excitation energies higher than EOM-CCSD or LR-CCSD. Concerning the computational cost of CAM-B3LYP, the performance of this DFT method is very good when compared to more expensive methods. As it was mentioned in Chapter 2 this method was developed to give a long range charge transfer correction of B3LYP. The results obtained with TD-CAM-B3LYP are in very close agreement

with the results obtained with EOM-CCSD and LR-CCSD. The bright states calculated for $Ni(CO)_4$ are in reasonable agreement with experimental values. The TD-CAM-B3LYP excitation energies are close to the two band maxima, although it must be noted that direct comparison between these values and the experimental data is not ideal since the spectrum is very broad. One should include vibronic coupling effects, as well as use a larger one-electron basis set.

As it was shown in the previous chapter the performance of lower cost methods (CIS, CIS(D) or CC2) is interesting and shows that some caution must be taken when applying them to transition metal complexes. There is clearly no smooth convergence of excitation energy for any state with quite large oscillatory behaviour across the LR-CC series. When comparing the CCSD excitation energies with the CIS/CCS the values are quite close, although when comparing the transition strengths, the two brightest states are ordered incorrectly. The low cost doubles fail spectacularly in comparison to complete CCSD. CIS(D) and CC2 significantly underestimate the excitation energies, often by several electron volts. For some of the CC2 excitation energies the higher excited states failed to converge. The poor performance of these models is further discussed below in terms of $\hat{T}_1$ amplitudes. The problems that arise from these intermediate methods are much more severe for the unsaturated metal carbonyl Ni(CO) as well. Including the CCR(3) non-iterative model, this also shows large effects but in the opposite direction, i.e., larger excitation energies consistent with an overall oscillatory pattern in the LR-CC series. The deviations from LR-CCSD are again quite severe , although they are smaller than those of CIS(D), showing that there is a problem in the oscillatory convergence in the LR-CC series. The only discrepancy with LR-CCSD is between the bright 2^1T_2 and dark 3^1T_1 states in which the ordering is inverted.

State	Character	CIS	CIS(D)	CC2	LR CCSD	EOM CCSD	CCR(3)	CAM B3LYP
1^1T_1	MLCT	4.628 (0.0000)	3.282	2.047 (0.0000)	4.715 (0.0000)	4.715 (0.0000)	6.011	4.472 (0.0000)
1^1E	MLCT	4.831 (0.0000)	3.218	1.932 (0.0000)	4.752 (0.0000)	4.752 (0.0000)	6.031	4.665 (0.0000)
1^1T_2	MLCT	5.138 (0.1035)	3.284	1.361 (0.490)	5.051 (0.0550)	5.051 (0.0542)	6.036	4.976 (0.0360)
2^1T_1	MLCT	5.548 (0.0000)	2.847	-	5.132 (0.0000)	5.132 (0.0000)	6.298	4.896 (0.0000)
3^1T_1	MLCT	5.822 (0.0000)	2.944	-	5.374 (0.0000)	5.374 (0.0000)	6.640	5.427 (0.0000)
1^1T_2	MLCT	6.121 (0.0819)	2.841	1.979 (0.0150)	5.564 (0.0780)	5.564 (0.0805)	6.611	5.266 (0.0656)

Table 6.5: Singlet electronic excitation energies (eV) of $Ni(CO)_4$ with cc-pVDZ. Oscillator strengths are given in parentheses. Direct comparison between these values and the experimental data is not ideal since the spectrum is very broad.

6.3.4 Excited States - Ni(CO)

The calculated excited states for Ni(CO) are shown in Tables 6.6 and 6.7 for two different basis sets cc-pVDZ and cc-pVTZ. Considering first LR-CCSD, the first excited electronic state is the dark $1^1\Delta$ state corresponding to transitions from off-axis-δ-symmetry pure Ni d-orbitals to a dσ Ni-carbonyl antibonding orbital. Going from the double zeta basis to the triple zeta the excitation energy increases by around 0.2 eV. The next considered state is the bright state, $1^1\Pi$, which has a very small oscillator strength. This state has a different character than before and involves transitions from Ni-carbonyl π^* orbitals, similar to $Ni(CO)_4$ to the same dσ Ni-carbonyl antibonding orbital. Again, there is an increase of the excitation energy from 1.319 eV to 1.447 eV upon increasing the basis set from cc-pVDZ to cc-pVTZ. The next excited state $2^1\Sigma^+$ has the largest oscillator strength of the low-lying excited states considered, showing a small difference between the double and triple zeta basis set. This state corresponds to a transition from the dσ Ni-carbonyl bonding orbital to its antibonding counterpart. The transition strengths for the bright states are of the same orders of magnitude between CCS and CCSD. The CCS excitation energies show less variation with basis set than CCSD. As discussed in Chapter 4, the low cost doubles fail

spectacularly for Ni(CO) calculating a negative excitation for the lowest $1^1\Delta$ state. Regarding CC2 it also calculates negative excitation energies for both states, while CIS(D) gives spuriously small excitation energies for those. As for $Ni(CO)_4$, CCR(3) shows an overestimation of excitation energies, although it is much less severe (maximum 0.6 eV). The CCR(3) excitation energies show less sensitivity to basis than CCSD. In both bases considered, however, the order of the $1^1\Pi^+$ and $2^1\Sigma^+$ states is inverted, although for both, the states are within < 0.2 eV of each other. Once again, TD-CAM-B3LYP performs very well. There is no noticeable sensitivity to the basis set. The oscillator strengths were calculated to have the correct relative orders of magnitude, although for the $2^1\Sigma^+$ state it is too large compared to LR-CCSD.

It is necessary to understand why these intermediate CCn methods fail, so it is important to rely on CASSCF calculations to assess the nature of the ground states as they are crucial in obtaining excited state data and their responses. Although a (10,11) active space was picked for $Ni(CO)_4$ and Ni(CO) ground state calculations it was found that the ground state on both complexes was dominated by the $3d^{10}4s^0$ on the nickel atom. Even though this is the preferred configuration, it never accounted for more than 90% for Ni(CO). The other large contribution comes from the $3d^84s^2$. There is a small but significant amount of multireference character that has consequences for the lower cost CC response methods. The large $\hat{T}_1$ amplitudes indicate a significant amount of orbital relaxation. One solution for this problem would be to use a better set of underlying orbitals. In the presence of an external field the orbital relaxation here is very large and the $\hat{T}_1$ similarity transformed operators in CCn theory start to cause problems.

It is important to compare the LR-CCSD results with those from NEVPT2 (Table 6.4). Both methods provide close results, for example, for the first dark $1^1\Delta$ state, but agree less well for the next, bright, $1^1\Pi$ state 1.447 eV vs 2.540 eV. In fact, the NEVPT2 excitation energy for this

state is much closer to CCSDR(3) at 2.26 eV. MCCI (Tables 6.8 and 6.9), also shows this state around 2.5 eV. The last part of this investigation focuses on the electronic structure of the electronic excited states of Ni(CO) using MCCI and as well quantifying their multireference character [36] [43]. The cut-off (cmin) for configurations determines the accuracy of a MCCI calculation. The cmin value used was $3x10^{-4}$ for both cc-pVDZ and cc-pVTZ(D) basis sets with 11 frozen orbitals. These represent the core orbitals, that do not have a strong role in the bonding of the complex. The CI spaces are of the order of 10^{21} and 10^{23} Slater determinants for each basis, respectively. The number of spin-adapted configuration state functions (CSFs) in the converged MCCI wavefunctions that approximate those full CI wavefunctions for each separate state are also given in Tables 6.8 and 6.9. MCCI also confirms that the ground state is a singlet, the lowest triplet being 1.4 eV above (in both cases). The increasing size of the basis set has only a very small effect on excitation energies (0.1 eV). The MCCI excited states energies are always larger than those of LR-CCSD. This agrees as well with the CCR(3) excitation energies being larger and the oscillatory convergence across the LR-CC series. The ordering of MCCI excited states agrees with both LR-CCSD and NEVPT2. By looking at the measure of multireference (MR) one may notice that it shows that all the singlet states, even the ground state, are of significant multireference character when expanded in Hartree-Fock orbitals.

State	**Character**	**CIS**	**CIS(D)**	**CC2**	**LR CCSD**	**EOM CCSD**	**CCR(3)**	**CAM B3LYP**
$1^1\Delta$	$d\sigma^*$	1.572	-1.352	-3.121	0.765	0.765	1.367	0.991
		(0.0000)		(0.0000)	(0.0000)	(0.0000)		(0.0000)
$1^1\Pi$	$d\sigma^*$	1.610	0.143	-5.603	1.319	1.319	2.260	1.594
		(0.0003)		(-0.2202)	(0.0004)	(0.0001)		(0.0003)
$2^1\Sigma^+$	$\sigma\sigma^*$	1.169	0.308	-2.504	1.495	1.495	2.135	1.564
		(0.0121)		(0.0000)	(0.0316)	(0.0368)		(0.0149)

Table 6.6: Lowest singlet electronic excited states (eV) of Ni(CO) with cc-pVDZ. Oscillator strengths are given in parentheses.

State	Character	CIS	CIS(D)	CC2	LR CCSD	EOM CCSD	CCR(3)	CAM B3LYP
$1^1\Delta$	dσ^*	1.667	-1.352	-2.681	0.917	0.917	1.508	1.087
		(0.0000)		(0.0000)	(0.0000)	(0.0000)		(0.0000)
$1^1\Pi$	dσ^*	1.646	0.143	-5.194	1.447	1.447	2.378	1.668
		(0.0002)		(-0.610)	(0.0001)	(0.0001)		(0.0003)
$2^1\Sigma^+$	$\sigma\sigma^*$	1.217	0.308	-2.336	1.507	1.507	2.153	1.596
		(0.0119)		(0.2228)	(0.0322)	(0.0322)		(0.0149)

Table 6.7: Lowest singlet electronic excited states (eV) of Ni(CO) with cc-pVTZ. Oscillator strengths are given in parentheses.

State	Energy/eV	Multireference (MR)	CSFs
$1^1\Sigma^+$	0.00	0.65	26320
$1^1\Delta^+$	1.65	0.60	53309
$1^1\Pi^+$	2.44	0.73	46962
$2^1\Sigma^+$	2.54	0.68	56593
$1^3\Delta$	1.41	0.43	45345
$1^3\Pi$	2.10	0.54	50303

Table 6.8: Ni(CO) MCCI (C_{min}=3*10^{-4}/cc-pVDZ energies relative to the lowest totally symmetric singlet State, multireference MCCI diagnostic MR, and number of CSFs in converged CI solution.

State	Energy/eV	Multireference (MR)	CSFs
$1^1\Sigma^+$	0.00	0.65	32489
$1^1\Delta^+$	1.65	0.58	66207
$1^1\Pi^+$	2.56	0.71	55764
$2^1\Sigma^+$	2.69	0.67	67533
$1^3\Delta$	1.45	0.43	60145
$1^3\Pi$	2.56	0.71	55764

Table 6.9: Ni(CO) MCCI (C_{min}=3*10^{-4}/cc-pVTZ(D) energies relative to the lowest totally symmetric singlet State, multireference MCCI diagnostic MR, and number of CSFs in converged CI solution.

6.3.5 Mean absolute deviations

Table 6.10 shows the mean absolute deviations for $Ni(CO)_4$ considering each method used relative to EOM-CCSD. The highest mean absolute deviation is 3.4 eV for CC2. This method once again shows that its description of electron correlation is not ideal for inorganic systems such as this. TD-CAM-B3LYP has a very small error (0.17 eV), proving its reliability, with a lower computational cost than EOM-CCSD/LR-CCSD or CCR(3). Although CCR(3) is normally considered a very ro-

bust method, its mean absolute deviation value (1.2 eV) proves it is not as reliable for these kind of inorganic systems, and its computational cost is very high.

In Tables 6.11 and 6.12 a description of the mean absolute deviations for Ni(CO) with cc-pVDZ and cc-pVTZ is shown. For both tables CC2 is the method showing the highest mean absolute deviation 4.94 eV and 4.69 eV respectively. This proves once again that some care must be taken when using CC2 for computational studies in inorganic systems. CCR(3) which is from the same family as CC2 has an error value of 0.73 eV for cc-pVDZ and 0.72 considering cc-pVTZ. CIS has surprisingly small error values (bellow 0.50 eV), considering its lack of correlation.

$Ni(CO)_4$	**Mean Abs. Dev. (eV)**
CIS	0.28
CIS(D)	2.0
CC2	3.4
CCR(3)	1.2
TD-CAM-B3LYP	0.17

Table 6.10: Mean absolute deviations for the low-lying excited states of $Ni(CO)_4$ with cc-pVDZ considering LR-CCSD/EOM-CCSD the best theory.

Ni(CO)	**Mean Abs. Dev. (eV)**
CIS	0.47
CIS(D)	1.49
CC2	4.94
CCR(3)	0.73
CAM-B3LYP	0.19

Table 6.11: Mean absolute deviations for the low-lying excited states of Ni(CO) with cc-pVDZ considering EOM-CCSD/LR-CCSD the best theory.

Ni(CO)	**Mean Abs. Dev. (eV)**
CIS	0.41
CIS(D)	1.59
CC2	4.69
CCR(3)	0.72
CAM-B3LYP	0.16

Table 6.12: Mean absolute deviations for the low-lying excited states of Ni(CO) with cc-PVTZ considering EOM-CCSD/LR-CCSD the best theory.

6.4 Conclusions

A wide range of correlated methods were applied to the excited electronic states of the saturated and unsaturated binary metal carbonyls $Ni(CO)_4$ and Ni(CO). For Ni(CO) it was found that a correlated treatment is necessary to predict a closed-shell singlet ground state. Both are described qualitatively by a simple single configuration ($3d^{10}$) wavefunction. There are some multireference effects associated with the $3d^84s^2$ metal configuration that have very strong indirect effects on the performance of correlated excited state methodologies. CCn models fail due to the large $\hat{T}_1$ amplitudes, although the full CC response (or equivalent EOM) approaches are very accurate in describing the excited states of these systems. MCCI further quantifies the significant multireference character of the ground and excited electronic singlet states using a recently introduced metric. TD-CAM-B3LYP has an exceptional cost/performance for these very challenging electronic states. These metal carbonyls are simple, yet display richness in their electronic structure that makes them excellent test cases for excited state quantum chemical methodologies.

Bibliography

[1] McKinlay, R.; Paterson, M. In *The Jahn-Teller Effect*; Köppel, H., Yarkony, D. R., Barentzen, H., Eds., Vol. 97 of *Springer Series in Chemical Physics;* Springer Berlin Heidelberg, 2009; pages 311–344.

[2] Trushin, S. A.; Fuss, W.; Kompa, K. L.; Schmid, W. E. *J. Phys. Chem. A* **2000**, *104*(10), 1997–2006.

[3] Trushin, S.; Fuß, W.; Schmid, W. *Chem. Phys.* **2000**, *259*(2–3), 313–330.

[4] Trushin, S.; Kosma, K.; Fuß, W.; Schmid, W. *Chem. Phys.* **2008**, *347*(1–3), 309–323.

[5] Fuß, W.; Trushin, S.; Schmid, W. *Res. Chem. Intermed.* **2001**, *27*(4-5), 447–457.

[6] Pierloot, K.; Tsokos, E.; Vanquickenborne, L. G. *J. Phys. Chem.* **1996**, *100*(41), 16545–16550.

[7] Daniel, C. *Coord. Chem. Rev.* **2003**, *238-239*(0), 143–166.

[8] Villaume, S.; Strich, A.; Daniel, C.; Perera, S. A.; Bartlett, R. J. *Phys. Chem. Chem. Phys.* **2007**, *9*, 6115–6122.

[9] McKinlay, R.; Paterson, M. *The Jahn-Teller Effect: Fundamentals and Implications for Physics and Chemistry*, Vol. 97; Springer Science & Business Media, 2009.

[10] van Gisbergen, S. J. A.; Groeneveld, J. A.; Rosa, A.; Snijders, J. G.; Baerends, E. J. *J. Phys. Chem. A* **1999**, *103*(34), 6835–6844.

[11] Fuß, W.; Schmid, W. E.; Trushin, S. A. *J. Phys. Chem. A* **2001**, *105*(2), 333–339.

[12] Kotzian, M.; Roesch, N.; Schroeder, H.; Zerner, M. C. *J. Am. Chem. Soc.* **1989**, *111*(20), 7687–7696.

[13] Schreiner, A. F.; Brown, T. L. *J. Am. Chem. Soc.* **1968**, *90*(13), 3366–3374.

[14] Kao, C. M.; Messmer, R. P. *Phys. Rev. B* **1985**, *31*, 4835–4847.

[15] Cederbaum, L. S.; Domcke, W.; von Niessen, W.; Brenig, W. *Z. Phys. B Con. Mat.* **1975**, *21*(4), 381–388.

[16] Rosén, A.; Grundevik, P.; Morović, T. *Surf. Sci.* **1980**, *95*(2), 477–495.

[17] Fleisch, T.; Ott, G.; Delgass, W.; Winograd, N. *Surf. Sci.* **1979**, *81*(1), 1–12.

[18] Meriwether, L. S.; Leto, M. F.; Colthup, E. C.; Kennerly, G. W. *J. Org. Chem.* **1962**, *27*(11), 3930–3941.

[19] Walch, S. P.; III, W. A. G. *J. Am. Chem. Soc.* **1976**, *98*(25), 7908–7917.

[20] Rives, A. B.; Fenske, R. F. *J. Chem. Phys.* **1981**, *75*(3), 1293–1302.

[21] Blomberg, M. R. A.; Brandemark, U. B.; Siegbahn, P. E. M.; Mathisen, K. B.; Karlstroem, G. *J. Phys. Chem.* **1985**, *89*(11), 2171–2180.

[22] Daoudi, A.; Benjelloun, A. T.; Flament, J.; Berthier, G. *Journal of Molecular Spectroscopy* **1999**, *194*(1), 8–16.

[23] Yamazaki, E.; Okabayashi, T.; Tanimoto, M. *J. Am. Chem. Soc.* **2004**, *126*(4), 1028–1029.

[24] Madhavan, P.; Whitten, J. *Chem. Phys. Lett.* **1986**, *127*(4), 354–359.

[25] Persson, B. J.; Roos, B. O.; Pierloot, K. *J. Chem. Phys.* **1994**, *101*(8), 6810–6821.

[26] Sunderlin, L. S.; Wang, D.; Squires, R. R. *J. Am. Chem. Soc.* **1992**, *114*(8), 2788–2796.

[27] Horný, L.; Paul, A.; Yamaguchi, Y.; Schaefer, H. F. *J. Chem. Phys.* **2004**, *121*(3), 1412–1418.

[28] Gaussian 09 Revision A.02. Frisch, M. J.; Trucks, G. W.; Schlegel, H. B.; Scuseria, G. E.; Robb, M. A.; Cheeseman, J. R.; Scalmani, G.; Barone, V.; Mennucci, B.; Petersson, G. A.; Nakatsuji, H.; Caricato, M.; Li, X.; Hratchian, H. P.; Izmaylov, A. F.; Bloino, J.; Zheng, G.; Sonnenberg, J. L.; Hada, M.; Ehara, M.; Toyota, K.; Fukuda, R.; Hasegawa, J.; Ishida, M.; Nakajima, T.; Honda, Y.; Kitao, O.; Nakai, H.; Vreven, T.; Montgomery, Jr., J. A.; Peralta, J. E.; Ogliaro, F.; Bearpark, M.; Heyd, J. J.; Brothers, E.; Kudin, K. N.; Staroverov, V. N.; Kobayashi, R.; Normand, J.; Raghavachari, K.; Rendell, A.; Burant, J. C.; Iyengar, S. S.; Tomasi, J.; Cossi, M.; Rega, N.; Millam, J. M.; Klene, M.; Knox,

J. E.; Cross, J. B.; Bakken, V.; Adamo, C.; Jaramillo, J.; Gomperts, R.; Stratmann, R. E.; Yazyev, O.; Austin, A. J.; Cammi, R.; Pomelli, C.; Ochterski, J. W.; Martin, R. L.; Morokuma, K.; Zakrzewski, V. G.; Voth, G. A.; Salvador, P.; Dannenberg, J. J.; Dapprich, S.; Daniels, A. D.; Farkas, .; Foresman, J. B.; Ortiz, J. V.; Cioslowski, J.; Fox, D. J.

[29] Aidas, K.; Angeli, C.; Bak, K. L.; Bakken, V.; Bast, R.; Boman, L.; Christiansen, O.; Cimiraglia, R.; Coriani, S.; Dahle, P.; Dalskov, E. K.; Ekström, U.; Enevoldsen, T.; Eriksen, J. J.; Ettenhuber, P.; Fernández, B.; Ferrighi, L.; Fliegl, H.; Frediani, L.; Hald, K.; Halkier, A.; Hättig, C.; Heiberg, H.; Helgaker, T.; Hennum, A. C.; Hettema, H.; Hjertenæs, E.; Høst, S.; Høyvik, I.-M.; Iozzi, M. F.; Jansík, B.; Jensen, H. J. Aa.; Jonsson, D.; Jørgensen, P.; Kauczor, J.; Kirpekar, S.; Kjærgaard, T.; Klopper, W.; Knecht, S.; Kobayashi, R.; Koch, H.; Kongsted, J.; Krapp, A.; Kristensen, K.; Ligabue, A.; Lutnæs, O. B.; Melo, J. I.; Mikkelsen, K. V.; Myhre, R. H.; Neiss, C.; Nielsen, C. B.; Norman, P.; Olsen, J.; Olsen, J. M. H.; Osted, A.; Packer, M. J.; Pawlowski, F.; Pedersen, T. B.; Provasi, P. F.; Reine, S.; Rinkevicius, Z.; Ruden, T. A.; Ruud, K.; Rybkin, V. V.; Sałek, P.; Samson, C. C. M.; de Merás, A. S.; Saue, T.; Sauer, S. P. A.; Schimmelpfennig, B.; Sneskov, K.; Steindal, A. H.; Sylvester-Hvid, K. O.; Taylor, P. R.; Teale, A. M.; Tellgren, E. I.; Tew, D. P.; Thorvaldsen, A. J.; Thøgersen, L.; Vahtras, O.; Watson, M. A.; Wilson, D. J. D.; Ziolkowski, M.; Ågren, H. *WIREs Comput. Mol. Sci.* **2015**, *4*(3), 269–284.

[30] Paterson, M. J.; Hunt, P. A.; Robb, M. A.; Takahashi, O. *J. Phys. Chem. A* **2002**, *106*(44), 10494–10504.

[31] Worth, G. A.; Welch, G.; Paterson, M. J. *Mol. Phys.* **2006**, *104*(5-7), 1095–1105.

[32] Mckinlay, R. G.; Żurek, J. M.; Paterson, M. J. In *Theoretical and Computational Inorganic Chemistry*; van Eldik, R., Harvey,

J., Eds., Vol. 62 of *Advances in Inorganic Chemistry;* Academic Press, 2010; pages 351–390.

[33] Żurek, J. M.; Paterson, M. J. *J. Phys. Chem. Lett.* **2010**, *1*(9), 1301–1306.

[34] Żurek, J. M.; Paterson, M. J. *J. Chem. Phys.* **2012**, *137*(3), 034308.

[35] Żurek, J. M.; Paterson, M. J. *J. Phys. Chem. A* **2012**, *116*(22), 5375–5382.

[36] Coe, J. P.; Paterson, M. J. *J. Chem. Theory Comput.* **2015**, *11*(9), 4189–4196.

[37] Hedberg, L.; Iijima, T.; Hedberg, K. *J. Chem. Phys.* **1979**, *70*(7), 3224–3229.

[38] Bauschlicher, C. W.; Bagus, P. S. *J. Chem. Phys.* **1984**, *81*(12), 5889–5898.

[39] Zhou, M.; Andrews, L. *J. Am. Chem. Soc.* **1998**, *120*(44), 11499–11503.

[40] Gutsev, G. L.; Andrews, L.; Jr., C. W. B. *Chem. Phys.* **2003**, *290*(1), 47–58.

[41] Sodupe, M.; Jr., C. W. B.; Lee, T. J. *Chem. Phys. Lett.* **1992**, *189*(3), 266–272.

[42] Xu, X.; Lü, X.; Wang, N.; Zhang, Q.; Ehara, M.; Nakatsuji, H. *Int. J. Quantum Chem.* **1999**, *72*(3), 221–231.

[43] Coe, J.; Murphy, P.; Paterson, M. *Chem. Phys. Lett.* **2014**, *604*(0), 46–52.

Chapter 7

On the photodissociation of $Mn_2(CO)_{10}$ and $Cr(CO)_6$ to their corresponding photoproducts: relaxation of excited $Mn(CO)_5$ and $Cr(CO)_5$

7.1 Introduction

Chapter 7 focuses on the photochemistry of $Mn(CO)_5$ and $Cr(CO)_5$ showing the pathway these molecules undergo after the photodissociation of their parent molecules $Mn_2(CO)_{10}$ and $Cr(CO)_6$. The photodissociations, and subsequent non-adiabatic relaxations, as well as Jahn-Teller effects are going to be discussed. As reviewed in Chapter 1 there are different types of conical intersections connecting potential energy surfaces. These depend on the type of molecules studied, two examples are tilted and circular conical intersections (see description in Chapter 1), and these are vital features here.

Rosa *et al* applied DFT and TD-DFT to a wide range of transition metal systems to study their ground and excited states. One such system is $Mn_2(CO)_{10}$ [1]. The ability these smaller complexes have to mimic bigger complexes with more "exotic" ligands is a great advantage. Binary transition metal carbonyls are perhaps one the most studied classes of

complexes in this area. The aim of this study by Rosa *et al* was to understand better the photochemistry resulting from both Mn-Mn and Mn-CO bond dissociation channels. Although it is considered a small complex it is still very demanding. Early versions of density functional theory mentioned in Chapter 2, such as LDA were chosen with a mixture of double and triple zeta STO basis sets. They found that low energy excitations were due to $\sigma \rightarrow \sigma^*$ and $d\pi \rightarrow \sigma^*$ transitions, with ligand field (LF) $d \rightarrow d$ transitions occurring at higher energy. The metal 4p orbitals were also found to mix in with metal 3d orbitals in these σ and σ^* orbitals. Originally, the Mn-Mn dissociation was thought to occur from the $\sigma \rightarrow \sigma^*$ transition and the Mn-CO dissociation from ligand field transitions. The same authors performed another study to look at the potential energy curves for Mn-Mn and Mn-CO bond dissociation channels. LDA was used with different corrections to the exchange and correlation energy. It was concluded that Mn-Mn bond dissociation occurs from the low energy $\sigma \rightarrow \sigma^*$ transition. This transition can also lead to axial or equatorial CO loss as the responsible states for this dissociation are near degenerate to the low energy $\sigma \rightarrow \sigma^*$ transition at the equilibrium geometry. The most important conclusion is that upon the photoexcitation of $Mn_2(CO)_{10}$ above 266 nm is the ejection of a single carbonyl ligand.

$Cr(CO)_6$ has been the subject of much theoretical and experimental studies, for example to resolve its spectra and determine the nature of its excited states. A few theoretical methods were applied to this complex that include for example the INDO/S method [2], SAC-CI (symmetry adapted configuration interaction), CASSCF and CASPT2, TD-DFT [3] [4] and the most recent study involved methods such as EOM-CCSD and STEOM-CCSD [5]. The paper by Villaume *et al* shows a shoulder at 3.92 eV for the absorption spectra, which the authors assigned to the $^1A_{1g} \rightarrow ^1T_{2u}$ MLCT transition, which showed a low oscillator strength. There were two other absorption bands reported at 4.37 eV and 5.20 eV which represent the $^1A_{1g} \rightarrow ^1T_{2u}$ MLCT transitions. These two transi-

tions are the most dominant ones (stronger) in the spectrum. $Cr(CO)_6$ also undergoes ultrafast photochemistry, that causes the loss of one carbonyl ligand. The loss of the carbonyl ligand for both complexes leads to a Jahn-Teller type conical intersection and the formation of photoproducts, $Mn(CO)_5$ and $Cr(CO)_5$. These are going to be discussed in the next sections. The pathways that $Mn_2(CO)_{10}$ and $Cr(CO)_6$ undergo upon irradiation with light to form $Mn(CO)_5$ and $Cr(CO)_5$ are portrayed in Figure 7.2. An example of a $Cr(CO)_6$ molecular orbital diagram is portrayed in Fig 7.1.

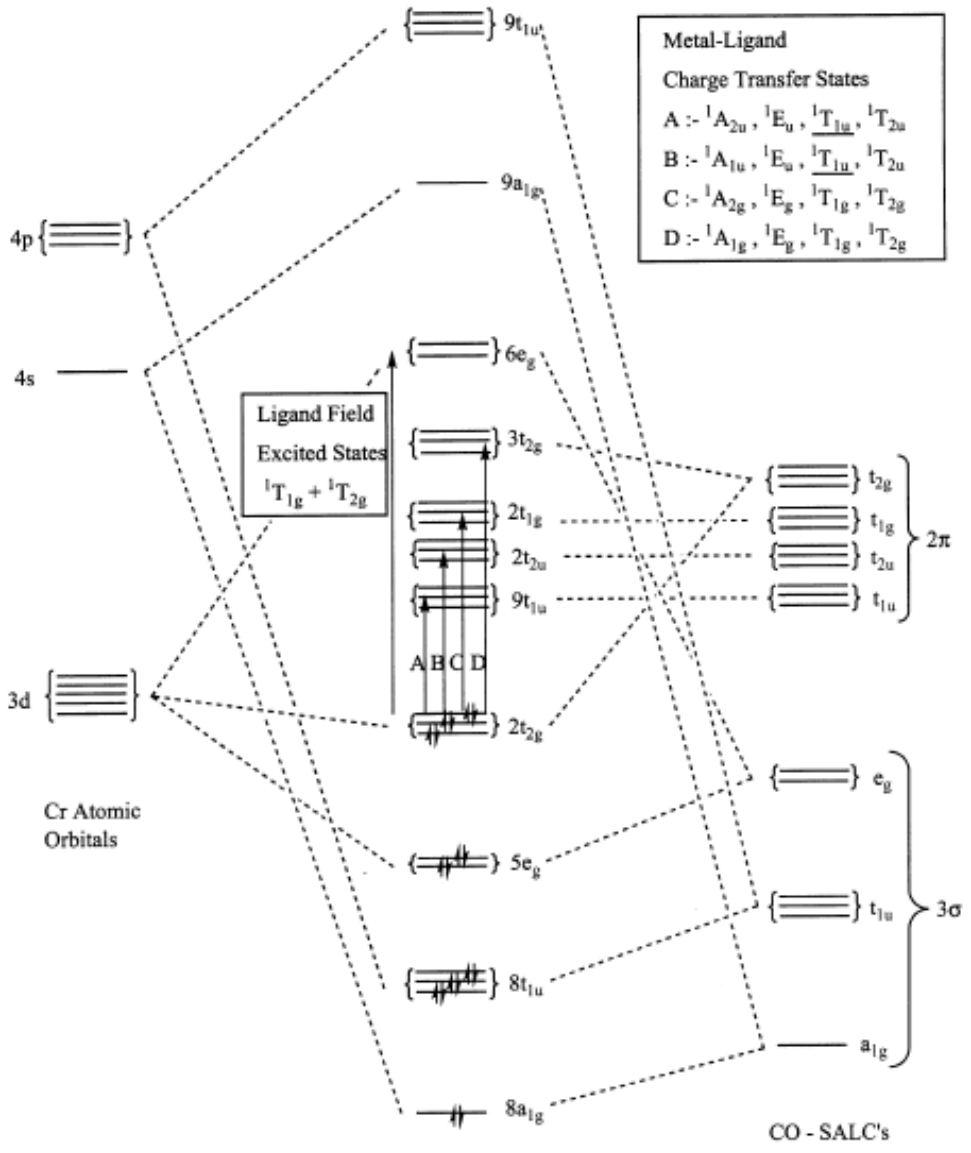

Figure 7.1: Qualitative MO diagram for $Cr(CO)_6$. The only two orbitally and spin allowed transitions are MLCT ($d\pi^*$) $^1A_{1g} \rightarrow a^1T_{1u}$ ($2t_{2g}^6 \rightarrow 2t_{2g}^5\ 9t_{1u}^1$ and b^1T_{1u} ($2t_{2g}^6 \rightarrow 2t_{2g}^5\ 2t_{2u}^1$). The ligand field excited states ($^1T_{1g}$ and $^1T_{2g}$) lie higher in energy Adapted from: "Non-Adiabatic direct dynamics study of chromium hexacarbonyl photodissociation", *The Journal of Physical Chemistry A* **2002**, *106*, 10494-10504.

The most recent work that predicted the formation of hot photoproducts was Fuß *et al*, who performed several experimental studies. They used pump probe laser techniques with transient ionisation spectroscopy to describe these femtosecond phenomena [6, 7, 8, 9, 10, 11]. These experiments work in such a way: the system is "pumped" by initial excitation energy, then the nuclei respond, and this effect is probed with a second time-delayed laser pulse. A important finding from these experiments was a coherent oscillation observed for the various unsaturated ion fragments for the dissociation process of several different metal carbonyls. It was found that the transitions were dominated by one large peak which relates to one specific molecular vibration, usually a bending. The first photoproduct of these reactions is formed in a femtosecond timescale and there are no indications of fluorescence [12] [13].

7.1.1 $Mn(CO)_5$ and $Cr(CO)_5$

Mapping the topology of the ground and excited state potentials is fundamental to describe phenomena that take part on a femtosecond timescale. One of these phenomena is the geometrical rearrangement of resulting photoproducts after CO loss or metal-metal bond cleavage in $Mn_2(CO)_{10}$ and $Cr(CO)_6$. These areas of the potential energy surfaces include strong non-adiabatic coupling, for example the seam of conical intersection, which details the connection between the excited state and ground state. Electronic structure methods are pushed to their limit here and multireference methods are fundamental to describe these areas of the potential energy surface. CASSCF and CASPT2 are obvious choices. CASSCF is a suitable method to study and detail these structures, but chemical intuition is needed to decide which active space to choose. Previous CASSCF calculations [12], found Jahn-Teller geometries present in the photodissociation pathways for these systems, with a trigonal bipyramidal geometry (D_{3h}). The topology on the lower surface around the point of intersection has a number of symmetry equiv-

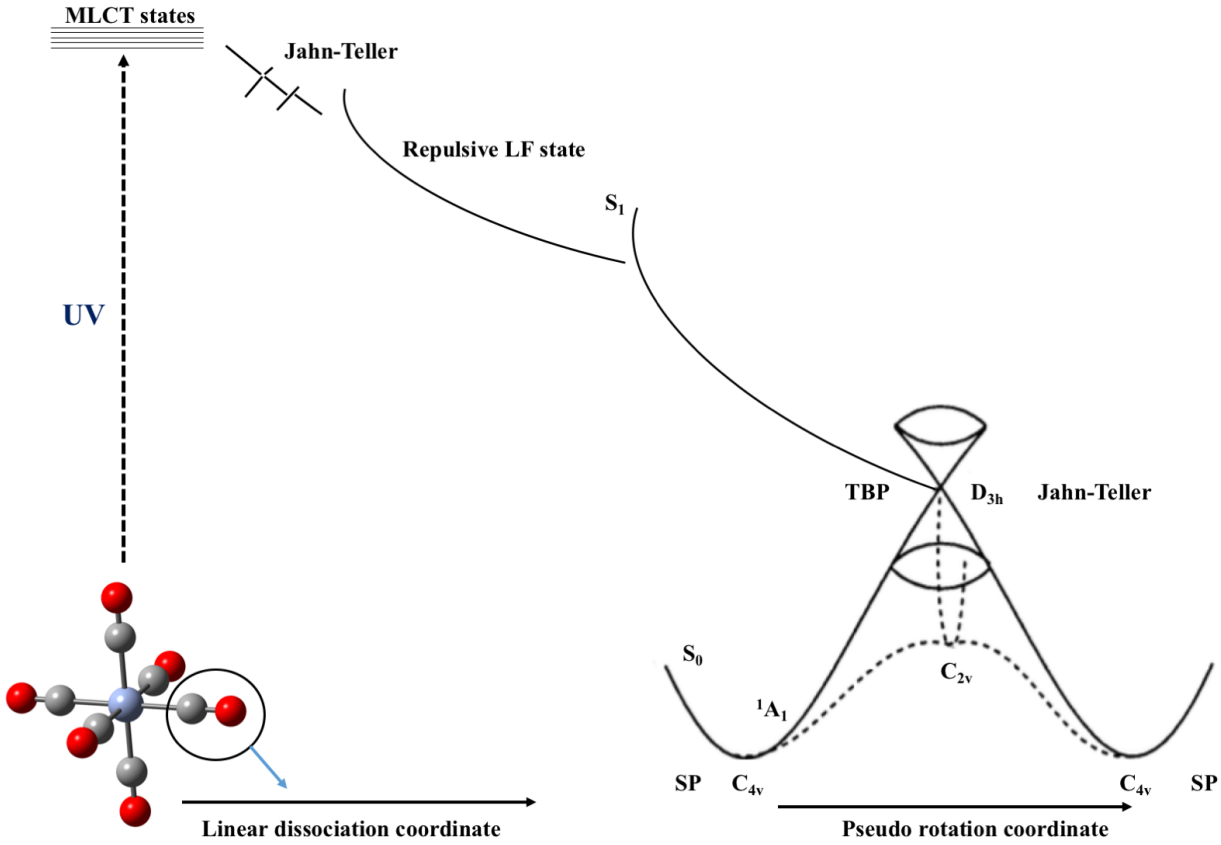

Figure 7.2: General schematic potential energy surface of linear photodissociation coordinate which leads to $M(CO)_5$ (M=Mn,Cr) in the excited state using $Cr(CO)_6$ as an example. Subsequent decay to the ground state occurs via a Jahn-Teller conical intersection with D_{3h} symmetry at trigonal bipyramidal geometry. The molecule can then pseudorotate in the moat of the conical intersection. The pseudorotational coordinate is an antisymmetric bend of the three in-plane ligands. Adapted from: "Non-Adiabatic direct dynamics study of chromium hexacarbonyl photodissociation", *The Journal of Physical Chemistry A* **2002**, *106*, 10494-10504.

alent minima separated by equivalent transition states. For $Mn(CO)_5$ and $Cr(CO)_5$ the surfaces are very similar and involve the following: C_{4v} square pyramidal (minimum) and three C_{2v} transition states. The calculated barrier heights for $Mn(CO)_5$ are very small, which indicate effectively free pseudorotation in the vibrational hot photoproducts. A pseudorotation corresponds to a stereoisomerization of a molecule by its internal rotation. One such case is the Berry pseudorotation mechanism [14] [15]. For $Cr(CO)_5$ there is a more substantial barrier, around 44 kJ mol^{-1} that indicates a pseudorotation may become trapped around one single minima (Figure 7.2). This is consistent with previous results from experimental observation.

In this chapter CASPT2 is used to validate other studies performed using multiconfigurational methods [12] [16]. The effect of dynamic correlation using an accurate method such as CASPT2 is a valuable tool to understand the reaction pathway these photoproducts undergo.

7.2 Computational details

The initial approach to investigate $Mn(CO)_5$ and $Cr(CO)_5$ using multireference methods was to choose all the 3d metal orbitals for the active space. For $Mn(CO)_5$ (7,5) and for $Cr(CO)_5$ (6,5) active spaces were the initial choice. This active space, proves to be problematic to converge, so was extended by adding the 4d equivalent counterpart of each 3d orbital already in the active space, but adding an extra node in the internuclear M-L bonding region (antibonding node). This effectively allows the effect of the dative bonding in an M-CO bond, since it variationally introduces dynamic electron correlation into the wavefunction allowing the donor pair of electrons to be further apart. A (7,8) active space for $Mn(CO)_5$ and (6,8) for $Cr(CO)_5$ were more adequate to treat electron correlation and to converge the wavefunction. There is one d orbital and corresponding antibonding orbital which were removed from the active space. They are not required to describe the ground and excited states of these two complexes correctly [12]. Considering C_{2v}, there is a $d_{x^2-y^2}$ mixed with d_{z^2} in the orbital stack which is clearly antibonding between the metal and the carbon. For C_{4v} and D_{3h} there is a $d_{x^2-y^2}$ and d_{z^2} respectively, higher in the orbital stack which were not included in the calculations as they are unoccupied in all states discussed.

A pesudopotential basis set was chosen (LANL2DZ). The calculations consisted of an initial Hartree-Fock calculation in the designated symmetry. The second step consisted in a CASSCF geometry optimisation with the optimised orbitals, followed by a single point CASPT2 cal-

culation. For the conical intersection point, the CASSCF optimisation step was performed using Gaussian09 [17]. After this step a single point calculation using CASPT2 was performed in MOLPRO [18]. Frequency calculations were performed on all the geometry points on the potential energy surface to guarantee that they were minima (C_{4v}) or transition states (C_{2v}).

7.3 Results and discussion

7.3.1 $Mn(CO)_5$

The set of orbitals shown at each geometry (Figures 7.3, 7.4, 7.5, 7.6, 7.7 and 7.8) correspond to notional "bonding" and "antibonding" pairs. For C_{2v} geometry, the bonding orbitals are almost pure 3d with small contributions from the ligands. The antibonding pair of the C_{2v} orbitals is shown in Figure 7.4 and corresponds physically to the 4d orbitals. For C_{4v}, the set of bonding orbitals is an almost pure 3d (Figure 7.5), with low molecular orbital coefficients on the ligands. The antibonding set is more mixed than for C_{2v} (Figure 7.6, especially b). For the point of conical intersection, D_{3h} the stack of bonding orbitals (Figure 7.7) is a pure one as well. For this symmetry, the molecular orbital coefficients are small for the ligands. The orbital occupancy for C_{2v} and C_{4v} geometries is: $(d_{xy})^2$ $((d_{yz})(d_{xz}))^4$ $(d_{z^2})^1$ and for D_{3h} $((d_{xz})(d_{yz}))^4$ $((d_{xy})(d_{x^2-y^2}))^3$.

$\mathbf{C}_{2v}$

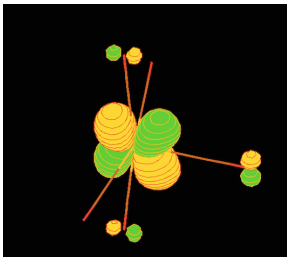

(a) Orbital occupancy = 1.910

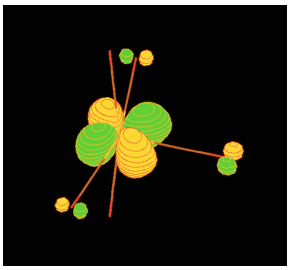

(b) Orbital occupancy = 1.910

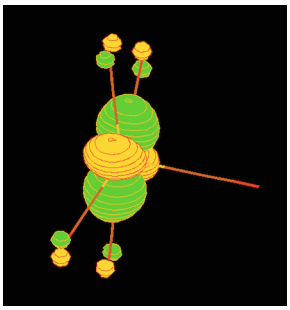

(c) Orbital occupancy = 1.908

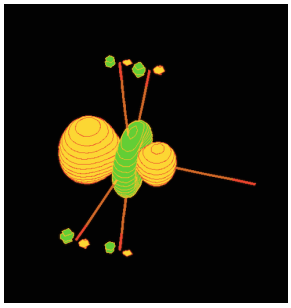

(d) Orbital occupancy = 0.961

Figure 7.3: $Mn(CO)_5$ (7,8) - 3d set of optimised CASSCF orbitals for CASPT2/LANL2DZ

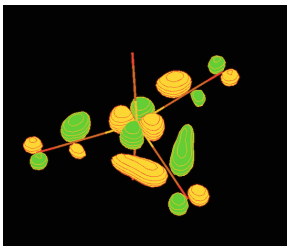

(a) Orbital occupancy = 0.089

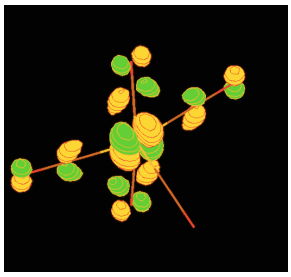

(b) Orbital occupancy = 0.088

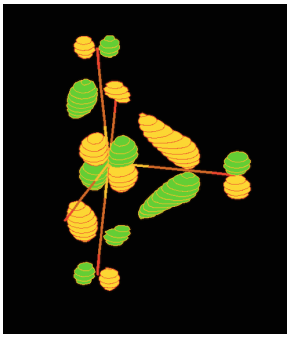

(c) Orbital occupancy = 0.088

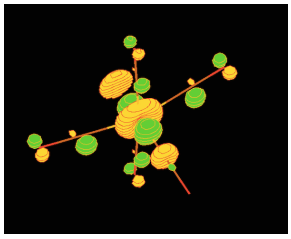

(d) Orbital occupancy = 0.044

Figure 7.4: $Mn(CO)_5$ (7,8) - 4d set of optimised CASSCF orbitals for CASPT2/LANL2DZ

$\mathbf{C}_{4v}$

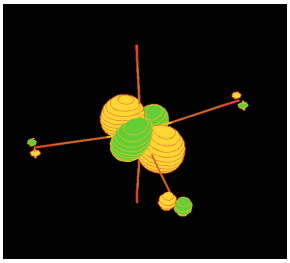

(a) Orbital occupancy = 1.982

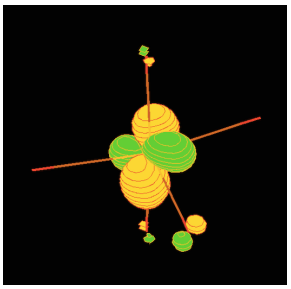

(b) Orbital occupancy = 1.898

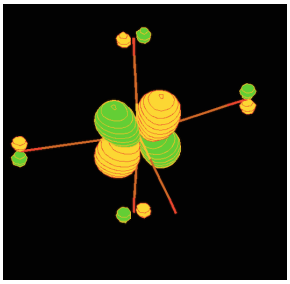

(c) Orbital occupancy = 1.892

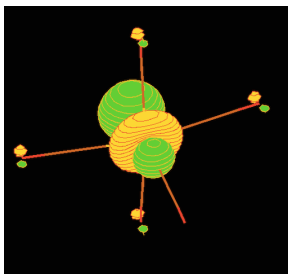

(d) Orbital occupancy = 0.961

Figure 7.5: $Mn(CO)_5$ (7,8) - 3d set of optimised CASSCF orbitals for CASPT2/LANL2DZ

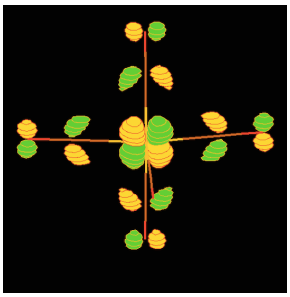

(a) Orbital occupancy = 0.107

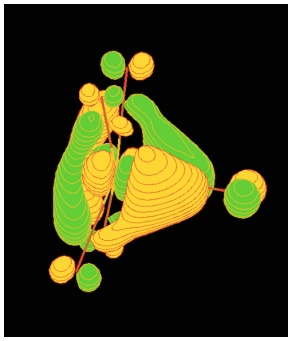

(b) Orbital occupancy = 0.100

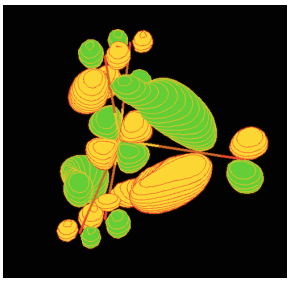

(c) Orbital occupancy = 0.054

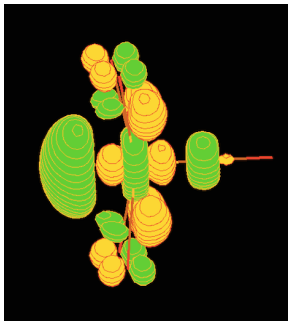

(d) Orbital occupancy = 0.006

Figure 7.6: $Mn(CO)_5$ (7,8) - 4d set of optimised CASSCF orbitals for CASPT2/LANL2DZ

$\mathbf{D}_{3h}$

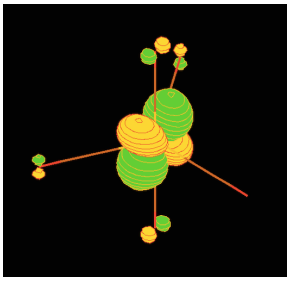

(a) Orbital occupancy = 1.907

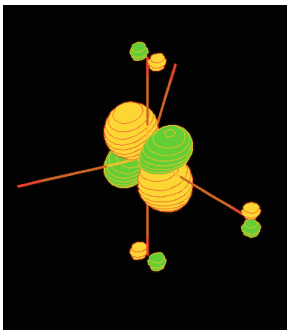

(b) Orbital occupancy = 1.907

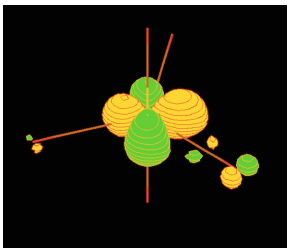

(c) Orbital occupancy = 1.430

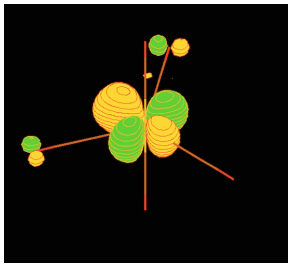

(d) Orbital occupancy = 1.430

Figure 7.7: $Mn(CO)_5$ (7,8) - 3d set of optimised CASSCF orbitals for CASPT2/LANL2DZ

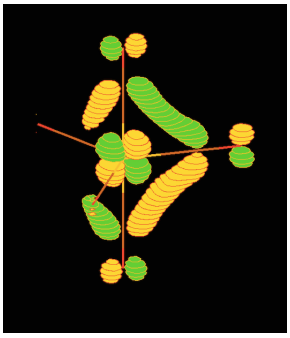

(a) Orbital occupancy = 0.090

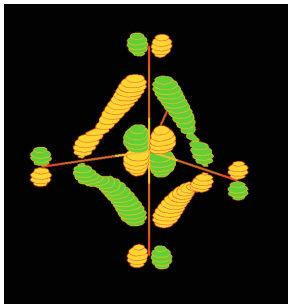

(b) Orbital occupancy = 0.090

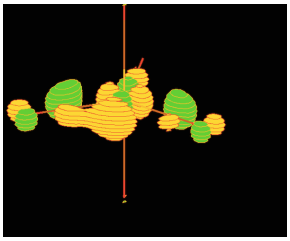

(c) Orbital occupancy = 0.073

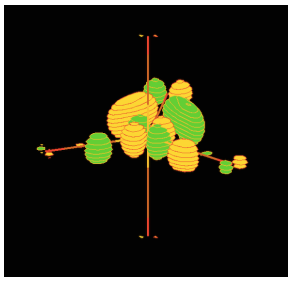

(d) Orbital occupancy = 0.073

Figure 7.8: $Mn(CO)_5$ (7,8) - 4d set of optimised CASSCF orbitals for CASPT2/LANL2DZ

7.3.2 $Cr(CO)_5$ orbitals used

In Figures 7.9, 7.10, 7.11, 7.12, 7.13 and 7.14 the different set of orbitals are depicted. They were used for $Cr(CO)_5$ CASPT2 calculations. There is more mixing in the orbitals, especially for C_{2v} and C_{4v}. For this complex, the choice of orbitals is the same as $Mn(CO)_5$, so one of the d orbitals for each symmetry calculation was left out (see computation details).

For C_{2v} in Figure 7.9 there is some orbital mixing especially for d), which is not a pure d orbital. The antibonding set of orbitals is shown in Figure 7.10. The four orbitals selected are of mixed character especially b) and c). For C_{4v}, in Figure 7.11 there is considerable mixing of the metal orbitals, especially c). On the contrary, for this geometry, the "antibonding" set of orbitals depicted (Figure 7.12) are pure 4d with very small mixing from the ligands. The orbital occupancy for these two geometries is: $(d_{xy})^2\ ((d_{yz})(d_{xz}))^4$.

The point of conical intersection D_{3h} shown in Figure 7.13 exhibit pure 3d bonding orbitals with small molecular orbital coefficients on the ligands. The antibonding orbitals (Figure 7.14) were chosen carefully, so the optimisation step for CASSCF and the single point CASPT2 would converge. The D_{3h} orbital occupancy is: $((d_{xz})(d_{yz}))^4\ (d_{xy})^1(d_{x^2-y^2})^1$.

$\mathbf{C}_{2v}$

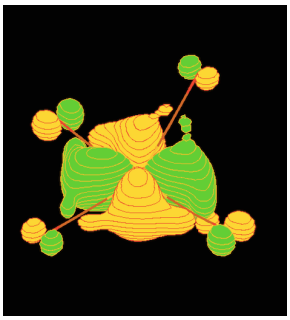

(a) Orbital occupancy = 1.896

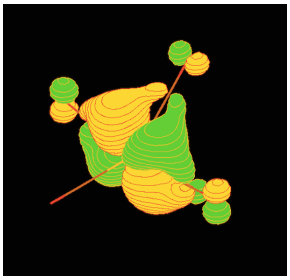

(b) Orbital occupancy = 1.893

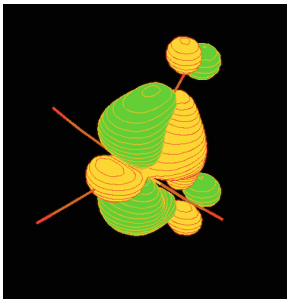

(c) Orbital occupancy = 1.876

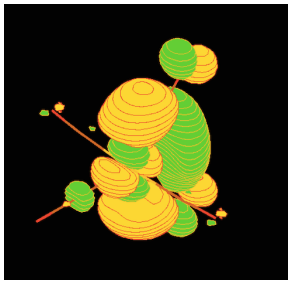

(d) Orbital occupancy = 0.102

Figure 7.9: $Cr(CO)_5$ (6,8) - 3d set of optimised CASSCF orbitals for CASPT2/LANL2DZ.

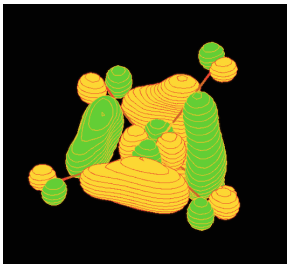

(a) Orbital occupancy =0.097

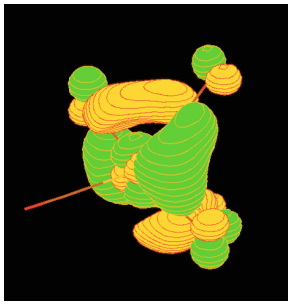

(b) Orbital occupancy =0.092

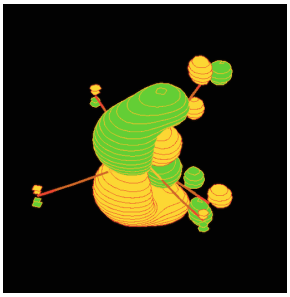

(c) Orbital occupancy = 0.036

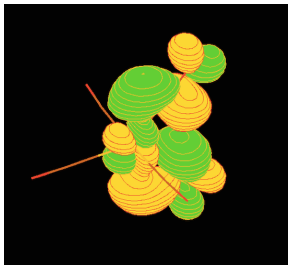

(d) Orbital occupancy = 0.007

Figure 7.10: $Cr(CO)_5$ (6,8) - 4d set of optimised CASSCF orbitals for CASPT2/LANL2DZ.

$\mathbf{C}_{4v}$

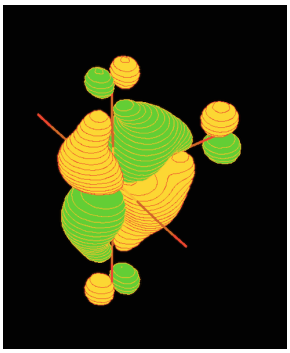

(a) Orbital occupancy = 1.899

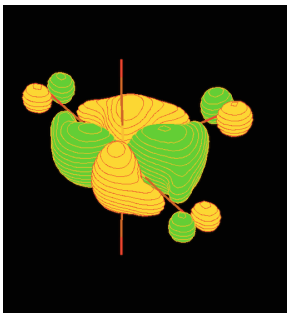

(b) Orbital occupancy = 1.899

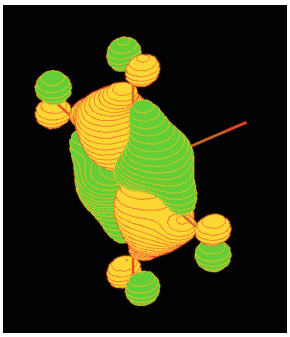

(c) Orbital occupancy = 1.898

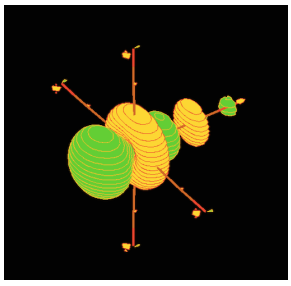

(d) Orbital occupancy = 0.096

Figure 7.11: $Cr(CO)_5$ (6,8) - 3d set of optimised CASSCF orbitals for CASPT2/LANL2DZ.

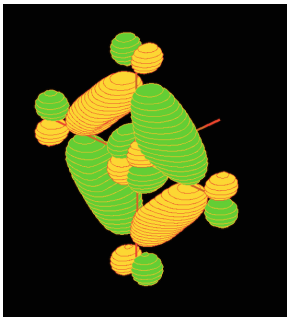

(a) Orbital occupancy = 0.092

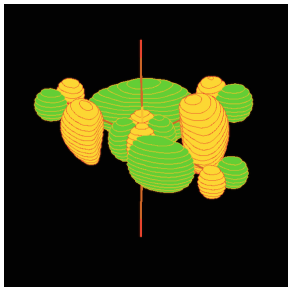

(b) Orbital occupancy = 0.092

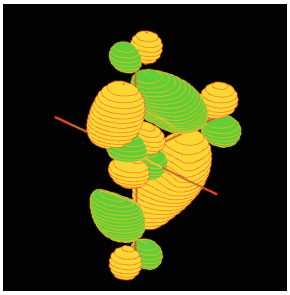

(c) Orbital occupancy = 0.015

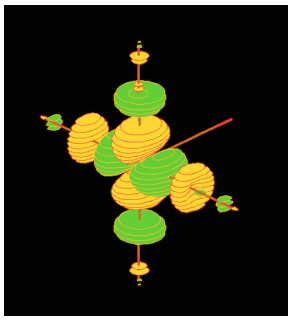

(d) Orbital occupancy = 0.008

Figure 7.12: $Cr(CO)_5$ (6,8) - 4d set of optimised CASSCF orbitals for CASPT2/LANL2DZ.

$\mathbf{D}_{3h}$

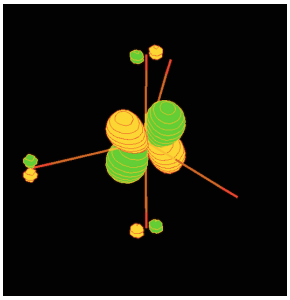

(a) Orbital occupancy = 1.894

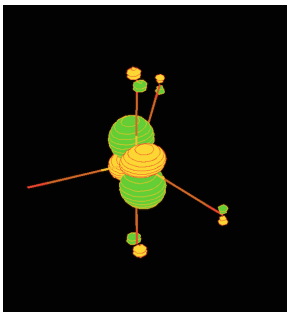

(b) Orbital occupancy = 1.894

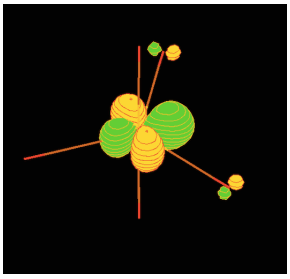

(c) Orbital occupancy = 0.978

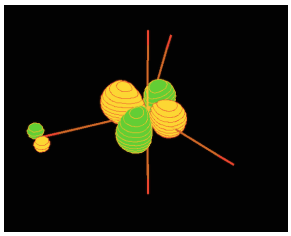

(d) Orbital occupancy = 0.933

Figure 7.13: $Cr(CO)_5$ (6,8) - 3d set of optimised CASSCF orbitals for CASPT2/LANL2DZ.

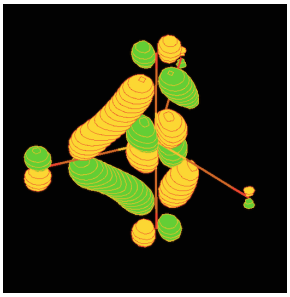

(a) Orbital occupancy = 0.099

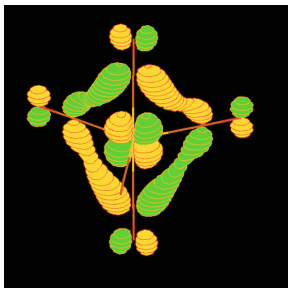

(b) Orbital occupancy = 0.099

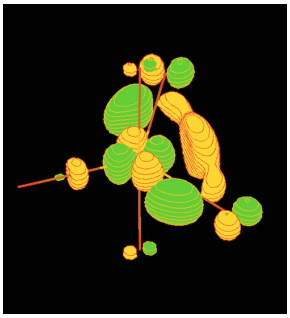

(c) Orbital occupancy = 0.052

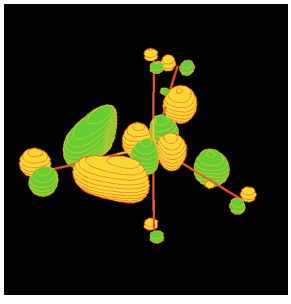

(d) Orbital occupancy = 0.050

Figure 7.14: $Cr(CO)_5$ (6,8) - 4d set of optimised CASSCF orbitals for CASPT2/LANL2DZ.

7.3.3 Comparison of the potential energy surface of the photoproducts: $Mn(CO)_5$ and $Cr(CO)_5$

$Mn(CO)_5$

Optimised geom. point	CASSCF (kJ mol^{-1})	CASPT2 (kJ mol^{-1})
$\mathbf{C_{4v}}$	0.00	0.00
$\mathbf{C_{2v}}$	0.12	0.067
$\mathbf{D_{3h}}$	32.59	31.84

Table 7.1: $Mn(CO)_5$ energetics relative to C_{4v} (minimum).

$Cr(CO)_5$

Optimised geom. point	CASSCF (kJ mol^{-1})	CASSCF [12] (kJ mol^{-1})	CASPT2 (kJ mol^{-1})
$\mathbf{C_{4v}}$	0.00	0.00	0.00
$\mathbf{C_{2v}}$	46.94	44.21	53.56
$\mathbf{D_{3h}}$	96.51	86.85	78.06

Table 7.2: $Cr(CO)_5$ energetics relative to C_{4v} (minimum).

Tables 7.1 and 7.2 compare the effects of additional dynamic correlation on these kind of complexes. The objective was to compare whether there was any quantitative differences between CASSCF and CASPT2 results. For example, if there are any affects in the activation energy between C_{4v}, minima on the potential energy surface, and the C_{2v} the transition states. For $Mn(CO)_5$, the gap in energy between the C_{2v} structure and D_{3h} is 32.47 kJ mol^{-1} and 31.77 kJ mol^{-1} using CASSCF and CASPT2 respectively (D_{3h} - C_{2v}). The perturbation included in the multireference wavefunction did not affect this gap substantially. The activation energy (C_{2v} - C_{4v}) shown in Table 7.1 confirms the free pseudorotation for $Mn(CO)_5$. The values calculated are very small: 0.12 kJ mol^{-1} for CASSCF and 0.067 kJ mol^{-1} for CASPT2, again further dynamic correlation having only a negligible effect.

The relative energies of $Cr(CO)_5$ are quantatively different to $Mn(CO)_5$. A comparison for this was also added from previous results (Table 7.2)

[12] of CASSCF calculations on this system on a similar level to here. The basis set used was slightly different. The gap between the conical intersection point (D_{3h}) and C_{2v} is 49.57 kJ mol^{-1} for CASSCF and 24.50 kJ mol^{-1} for CASPT2. The stabilization energy from D_{3h} to C_{4v} is much larger than the previous complex, for CASSCF, 96.51 kJ mol^{-1} and for CASPT2, 78.06 kJ mol^{-1}. Comparing the two CASSCF values, there is around 10 kJ mol^{-1} difference between the two values and the activation energy (C_{2v} - C_{4v}) is 46.94 kJ mol^{-1} for CASSCF and 53.56 kJ mol^{-1} considering CASPT2.

An important conclusion that can be drawn from all the data is that explicit dynamic correlation may be included, but it does not have such an important effect if orbital doubling is used as well. When performing calculations on these systems without using orbital doubling the occupation of the 3d orbitals is around 1.99. When including 4d orbitals, the occupation changes to 1.8-1.9 for the 3d orbitals and 0.1-0.2 for the 4d. The numbers obtained with the CASPT2 calculations provide validation of this approach since it proves that dynamic correlation does not have a large influence in the results. The Jahn-Teller stabilization energy appears to be slightly more sensitive to additional dynamic correlation than the barrier to pseudorotate. Both complexes have similar geometry with just one electron different, but the activation energy of $Mn(CO)_5$ is almost zero, while $Cr(CO)_5$ is 53.56 kJ mol^{-1} (CASPT2). Below, in Figures 7.15(a) and 7.15(b) there are pictorial descriptions of the potential energy surfaces from these two complexes along a linear cut including two minima. The radial distance between the conical intersection and the transition state is not allowed to vary.

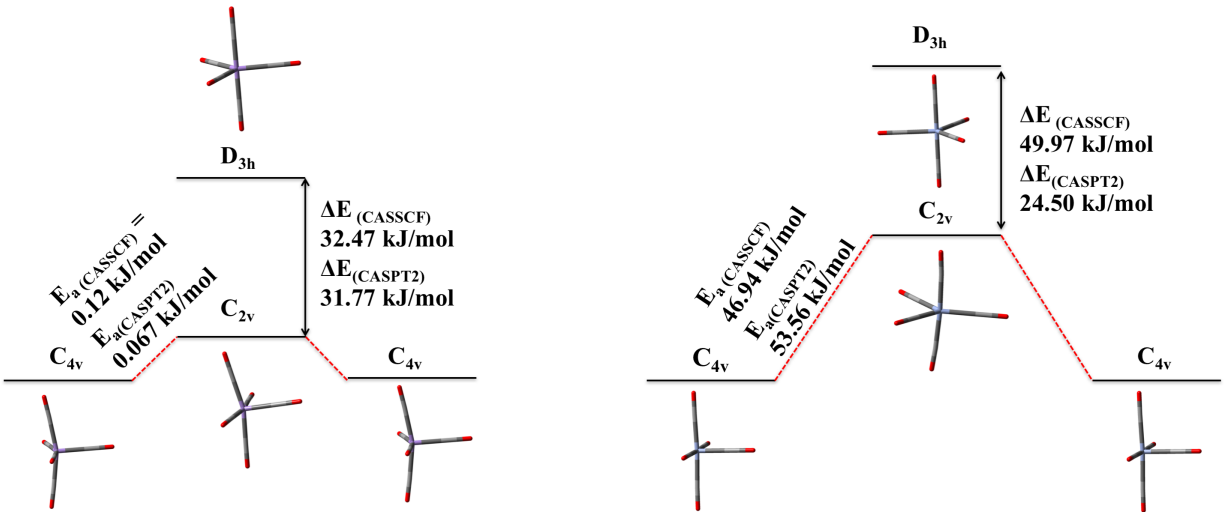

(a) $Mn(CO)_5$ (b) $Cr(CO)_5$

Figure 7.15: Pictorial potential energy surfaces for the discussed photoproducts.

7.4 Conclusions

Transition metal carbonyls have very interesting photochemistry and many can undergo, Jahn-Teller distortions through conical intersections when chemically excited. It is very demanding to study these systems, because the choice of the active space is very difficult, and convergence issues are common. This study aimed at analysing the effects of dynamic correlation on $Mn(CO)_5$ and $Cr(CO)_5$. The effect of perturbation theory on a multireference wavefunction was more noticeable in the closed-shell complex ($Cr(CO)_5$) than for the open-shell case ($Mn(CO)_5$). For $Cr(CO)_5$ there was a quantitative difference with a larger barrier of pseudorotation compared to $Mn(CO)_5$. The results obtained validate the previous approaches to these kind of transition metal complexes using orbital doubling. In the future, multistate dynamical simulations would allow us to analyse in further detail how the system evolves, and these results validate CASSCF wavefunctions for such simulations.

Bibliography

[1] Rosa, A.; Ricciardi, G.; Baerends, E. J.; Stufkens, D. J. *Inorg. Chem.* **1995**, *34*(13), 3425–3432.

[2] Kotzian, M.; Roesch, N.; Schroeder, H.; Zerner, M. C. *J. Am. Chem. Soc.* **1989**, *111*(20), 7687–7696.

[3] van Gisbergen, S. J. A.; Groeneveld, J. A.; Rosa, A.; Snijders, J. G.; Baerends, E. J. *J. Phys. Chem. A* **1999**, *103*(34), 6835–6844.

[4] Amor, N. B.; Villaume, S.; Maynau, D.; Daniel, C. *Chem. Phys. Lett.* **2006**, *421*(4-6), 378–382.

[5] Villaume, S.; Strich, A.; Daniel, C.; Perera, S. A.; Bartlett, R. J. *Phys. Chem. Chem. Phys.* **2007**, *9*, 6115–6122.

[6] Trushin, S. A.; Fuss, W.; Schmid, W. E.; .; Kompa, K. L. *J. Phys. Chem. A* **1998**, *102*(23), 4129–4137.

[7] Trushin, S.; Fuß, W.; Schmid, W. *Chem. Phys.* **2000**, *259*(2–3), 313–330.

[8] Fuß, W. W.; SA, T.; WE, S. *Res. Chem. Intermed.* **2001**, *27*(4-5), 447–457.

[9] Trushin, S.; Kosma, K.; Fuß, W.; Schmid, W. *Chem. Phys.* **2008**, *347*(1-3), 309–323.

[10] Fuß, W.; Schmid, W. E.; Trushin, S. A. *J. Phys. Chem. A* **2001**, *105*(2), 333–339.

[11] Trushin, S. A.; Fuss, W.; Kompa, K. L.; Schmid, W. E. *J. Phys. Chem. A* **2000**, *104*(10), 1997–2006.

[12] Paterson, M. J.; Hunt, P. A.; .; Robb, M. A.; Takahashi, O. *J. Phys. Chem. A* **2002**, *106*(44), 10494–10504.

[13] Worth, G. A.; Welch, G.; Paterson, M. J. *Mol. Phys.* **2006**, *104*(5-7), 1095–1105.

[14] Ugi, I.; Marquarding, D.; Klusacek, H.; Gillespie, P.; Ramirez, F. *Accounts. Chem. Res.* **1971**, *4*(8), 288–296.

[15] Gillespie, P.; Hoffman, P.; Klusacek, H.; Marquarding, D.; Pfohl, S.; Ramirez, F.; Tsolis, E. A.; Ugi, I. *Angew. Chem. Int. Edit.* **1971**, *10*(10), 687–715.

[16] Mckinlay, R. G.; Jurek, J. M.; Paterson, M. J. In *Theoretical and Computational Inorganic Chemistry*; van Eldik, R., Harvey, J., Eds., Vol. 62 of *Advances in Inorganic Chemistry;* Academic Press, 2010; pages 351 – 390.

[17] Gaussian 09 Revision A.02. Frisch, M. J.; Trucks, G. W.; Schlegel, H. B.; Scuseria, G. E.; Robb, M. A.; Cheeseman, J. R.; Scalmani, G.; Barone, V.; Mennucci, B.; Petersson, G. A.; Nakatsuji, H.; Caricato, M.; Li, X.; Hratchian, H. P.; Izmaylov, A. F.; Bloino, J.; Zheng, G.; Sonnenberg, J. L.; Hada, M.; Ehara, M.; Toyota, K.; Fukuda, R.; Hasegawa, J.; Ishida, M.; Nakajima, T.; Honda, Y.; Kitao, O.; Nakai, H.; Vreven, T.; Montgomery, Jr., J. A.; Peralta, J. E.; Ogliaro, F.; Bearpark, M.; Heyd, J. J.; Brothers, E.; Kudin, K. N.; Staroverov, V. N.; Kobayashi, R.; Normand, J.; Raghavachari, K.; Rendell, A.; Burant, J. C.; Iyengar, S. S.; Tomasi, J.; Cossi, M.; Rega, N.; Millam, J. M.; Klene, M.; Knox, J. E.; Cross, J. B.; Bakken, V.; Adamo, C.; Jaramillo, J.; Gomperts, R.; Stratmann, R. E.; Yazyev, O.; Austin, A. J.; Cammi, R.; Pomelli, C.; Ochterski, J. W.; Martin, R. L.; Morokuma, K.; Zakrzewski, V. G.; Voth, G. A.; Salvador, P.; Dannenberg, J. J.; Dapprich, S.; Daniels, A. D.; Farkas, .; Foresman, J. B.; Ortiz, J. V.; Cioslowski, J.; Fox, D. J.

[18] Molpro, version 2012.1, a package of ab initio programs. Werner, H.; Knowles, P. J.; Knizia, G.; Manby, F. R.; Schütz, M.; others. **2012**.

Chapter 8

Bottom-up approach for the formation of supramolecular chromophores from first principles

8.1 Introduction

The last chapter of this thesis focuses on intermolecular aggregates. These systems are not as difficult to study from the electronic structure point of view as the ones analysed in the previous chapters, but their size imposes many challenges. The first part of this chapter discusses theoretical calculations of a bottom-up approach to create a hydrogel from scratch and all the steps involved in the formation of its supramolecular structure (p-[4,6-Bis(p-carboxybenzoylamino)-1,3,5-triazin-2-ylamin] carbonyl benzoic acid). The second part focuses on collaborative work on gelation landscape engineering using a similar multi-reaction supramolecular hydrogelator system.

For the first part of this chapter, it is necessary to describe the main features of this chromophore, which are its gel formation ability, giving supramolecular structures with very interesting properties. Using DFT (density functional theory) it is possible to describe the self-assembly of this gel structure with a good level of accuracy, starting with the monomer up to the tetramer. Using a bottom-up approach it helps to characterize the multichromophoric self-assembly of these type of gels

which are often pH dependent. Starting with smaller units it is easier to tune them finely to get a larger hierarchical supramolecular chromophore. Self-assembly is a very attractive approach since it allows the development of very complex supermolecular structures, using simple and small molecules. The interest in these kind of structures grew in the last few years, when it became possible to use them as sensing or binding agents [1, 2, 3, 4, 5, 6, 7]. One of the main advantages working with these kind of systems is to avoid using biological or synthetic polymers. Some of them have been used for drug delivery, microelectronics and even cell growth [8] [9]. There are different forces that can hold the structures together, for example strong π-π interactions, or hydrogen bonds. Another property of these gels is that they are often organogelators, which usually have a low molecular weight and can incorporate and immobilize large numbers of solvent molecules, allowing the formation of fibrous aggregations (gels), using non-covalent bonding. The intermolecular distance among the structures can be adjusted, tuning the π-π interactions. This type of bottom-up approach allows the formation of nanostructures, which are very packed together and can create very complex and organized assembles [10].

A particular structure has been developed showing interesting properties as a self-assembled gel which is based on derivatives of benzene-1,3,5-tricarboxamide (BTA) [11] [12]. Some properties characterizing this family of derivatives have been described, showing how to synthesize them and how the pH can be changed for the formation of a gel network [13] [14]. These kinds of BTA structures can be self-assembled and form supramolecular columns that can be either in solid state or in solution [15] [16]. These can develop well-defined nanostructures as well as liquid crystalline phases [17] [18] [19]. Some structural changes can be made to side chains used to construct different, but very interesting structures. This fine-tuning requires small changes in the molecular structure and can lead to very desirable structures that have various potential applications. Bernet *et al* found a very promising structure

with regards to a gel formation, being pH dependent and performed spectroscopic and theoretical calculations for a particular 1,3,5-benzene tricarboxamide base structure [20]. They recognized that the pH affects the supramolecular formation and creates a photoluminescence display. So far, few computational studies on BTA derivatives have been performed [12, 11, 21, 22]. Most of the experimental works have been performed using organic solvents or polymer melts, but water was never used. This structure created a particular interest since it is pH reversible and exhibits a blue light emission upon UV irradiation. Some care must be taken with the formation of the luminescent supramolecular hydrogel since the pH must be decreased slowly, providing a gradual change of colour, which can be used for many applications especially as a sensor.

Examining all these possibilities in detail, it was decided to try and create another structure but with the same properties. The BTA assembly was changed and instead of using benzene-1,3,5-triazine, the ring was bonded to the side chains through a nitrogen. These changes lead to significant modifications in the behaviour of the chromophores.

The second part of this chapter focuses on gelation landscape engineering using a multi-reaction supramolecular hydrogelator system. Hydrogelating molecules can be controlled by kinetic and thermodynamic processes. A pathway selectivity can be used to form a complex chemical network. This kind of procedure allows a range of different materials to be formed, using a bottom-up approach to create a desirable structure. Using the reaction of trialdehyde and the tuberculosis drug isoniazid, the formation of hydrazone products leads to the creation of different gelation pathways. The resulting keto or enol tautomers form very different materials. Depending on the choice of self-assembly path, different materials can be created [23, 24, 25, 26, 27, 28, 29, 30, 31, 32].

In this chapter low molecular weight gelators (LMWGs) are investigated. Recently a new approach arose: the use of chemical reactivity to ei-

ther form or deform gelatinous materials and this way to sample the pathway complexity, although until today no chemical reactions have been used to control selectivity. This work is based on single step reactivity and has not been used for multi-step reactions yet. Recently, some experimental work has been performed in order not only to control chemical reactivity using catalytical methods but also to control the assembly processes and spatial distribution. The reaction pathway of 1,3,5-triformylphoroglucinol and isoniazid, tuberculosis drug generates three hydrazone species, products A, B and C, Figure 8.1. Product C is observed in two tautomeric forms, C_e and C_k, that correspond to the enol and keto forms. For A and B only the enol form is observed. Another important characteristic of these gels is the setting, which is reversible, meaning that the tautomerisation is also reversible. This is the first example in the literature of a keto-enol tautomerisation reversibility of these kind of compounds in water.

Computational calculations were performed to back up the bottom-up approach for the formation of these gelators for species B and C. Geometry optimisation calculations were performed (details provided in the next section) and reaction pathways calculated as well as absorption spectra for these two species. Figure 8.1 shows the different species studied and how they interchange between each other.

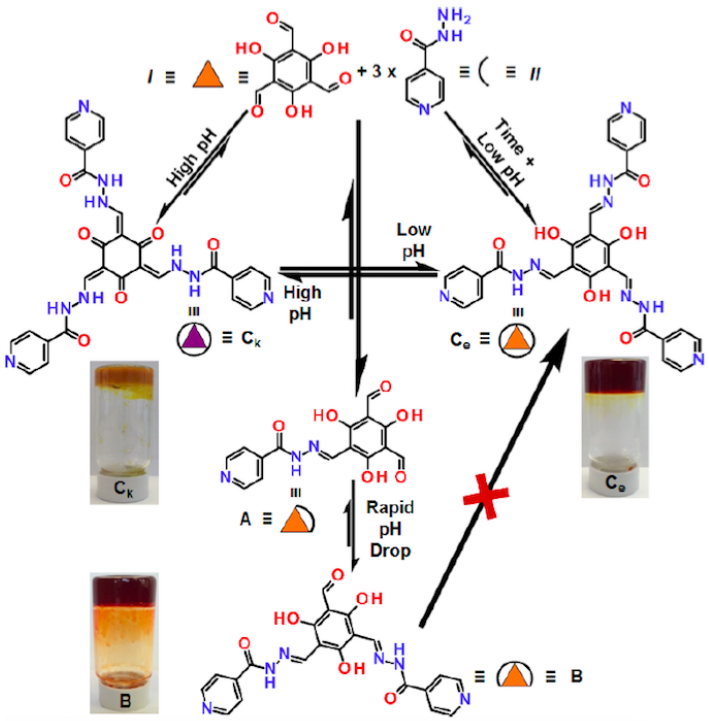

Figure 8.1: Formation of the different forms of gel formation: $\mathbf{C_e}$, $\mathbf{C_k}$, **B** and **A** - Adapted from: "Gelation landscape engineering using a multi-reaction supramolecular hydrogelator system", *The Journal of the American Chemical Society* **2015**, *137*(45), 14236-14239.

One of the ways of analysing in detail the gel formation is to inspect the samples under a microscope. Scanning electron microscopy (SEM) is a powerful technique that allows scientists to inspect samples at a high level of detail. The pictures of the fibrous nature of these structures can be visualized in Figures 8.2 and 8.3. In the result section the stacking up of the different species (B, C_e and C_k) will be portrayed, using a bottom-up approach, showing how the π-stacking and hydrogen bonding keeps these structures together, backing up the gel formation theory.

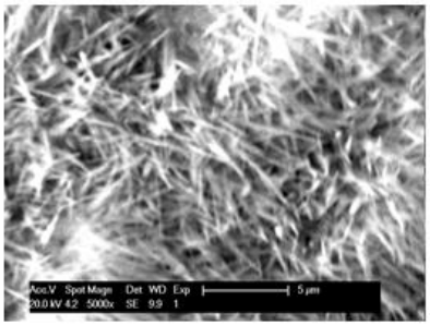

Figure 8.2: SEM images showing the fibrous nature of the gel B - Adapted from: "Gelation landscape engineering using a multi-reaction supramolecular hydrogelator system", *The Journal of the American Chemical Society* **2015**, *137*(45), 14236-14239.

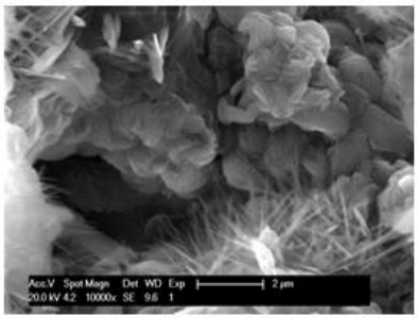

(a) Ce

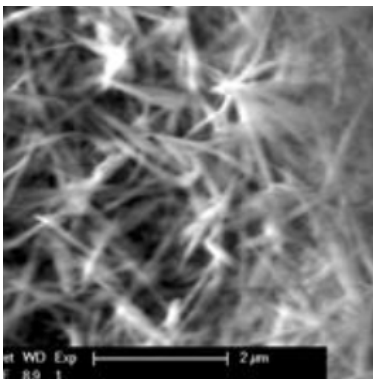

(b) Ck

Figure 8.3: SEM images showing the fibrous nature of the gels C_e and C_k - Adapted from: "Gelation landscape engineering using a multi-reaction supramolecular hydrogelator system", *The Journal of the American Chemical Society* **2015**, *137*(45), 14236-14239.

8.2 Computational Details

For the first part of the study presented in this chapter a variety of methods were chosen for the different parts of the investigation. All chromophores structures (1-8, see below) were optimized using the B3LYP and B97D density functionals with the all-electron basis set 6-311+G(d). All excited states reported here were calculated from an optimized geometry (structures 1 to 4, see below) using the long range corrected functional CAM-B3LYP and the all-electron basis set 6-311+G(d). Frequency calculations were performed to make sure that all the structures calculated were a minimum on the potential energy surface.

The second part of this Chapter uses B97D/6-311G(d) for the geometry optimisation calculation, because the dispersion effects included in this functional allow a more realistic approach to these kind of gelators. For the absorption spectra the SMD solvation model was used [33]. This model is denoted as "continuum" since the solvent is not represented explicitly. It is a universal model so it can be used for any kind of solvent. For the TD-DFT calculations B97D3 [34] [35] functional was chosen with a Pople basis set, 6-311G(d). The choice of this functional was based on a test on functional dependence on the spectroscopic properties. It was observed that the functional that produced results in the closest agreement with experiment is the dispersion corrected B97D3 functional. All theoretical calculations were performed using Gaussian 09 [36].

8.3 Results and discussion

8.3.1 Part I

In structures 1 to 8 (Figure 8.4 to Figure 8.11), there is a similar effect for the stacking of triazine rings, driven by π-π interactions and the amine hydrogen bonding among the layers. There is a difference in how both DFT methods calculate the interactions between the triazine rings. B97D uses Grimme's dispersion, which brings the different monomers together with a dispersion component added to the method. Comparing the tetramer (structure 4 and structure 8), the latter packs the different layers closer than when using B3LYP. Looking at the Tables 8.1 and 8.2, it is shown that the rings stack at closer distances, around 0.3 Å difference on average. More information about bond lengths and trends are discussed in the following section.

Structure 1

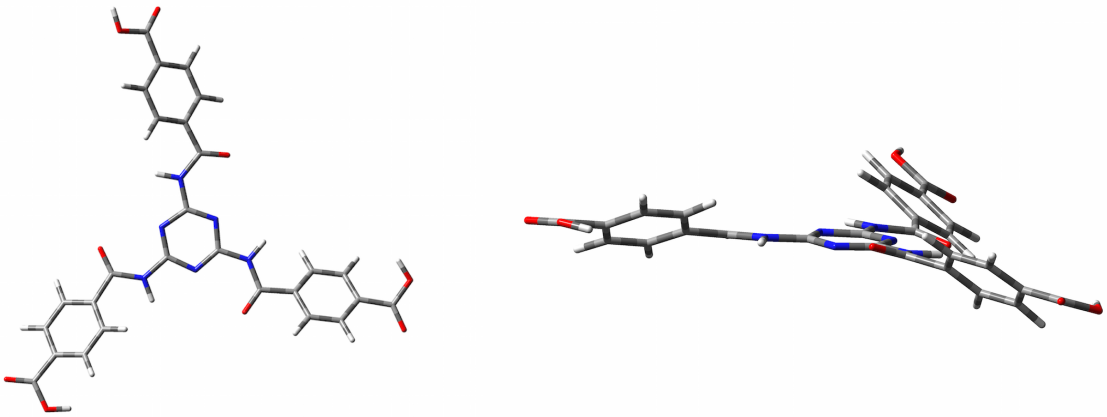

(a) Top view (b) Side view

Figure 8.4: Monomer of p-[4,6-Bis(p-carboxybenzoylamino)-1,3,5-triazin-2-ylamin] carbonyl benzoic acid optimised using B3LYP/6-311G(d).

Structure 2

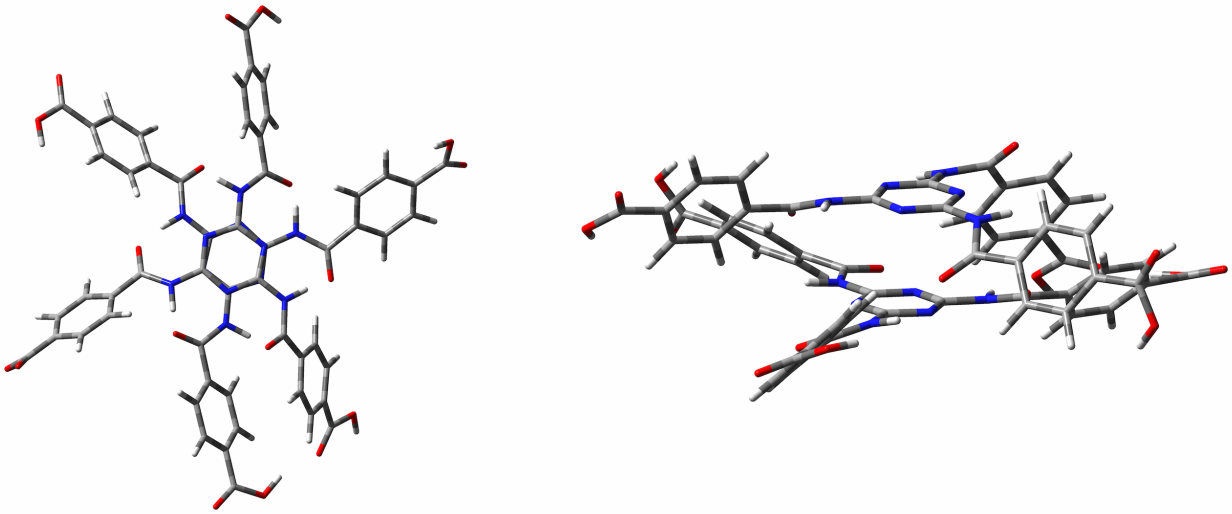

(a) Top view (b) Side view

Figure 8.5: Dimer of p-[4,6-Bis(p-carboxybenzoylamino)-1,3,5-triazin-2-ylamin] carbonyl benzoic acid optimised using B3LYP/6-311G(d).

Structure 3

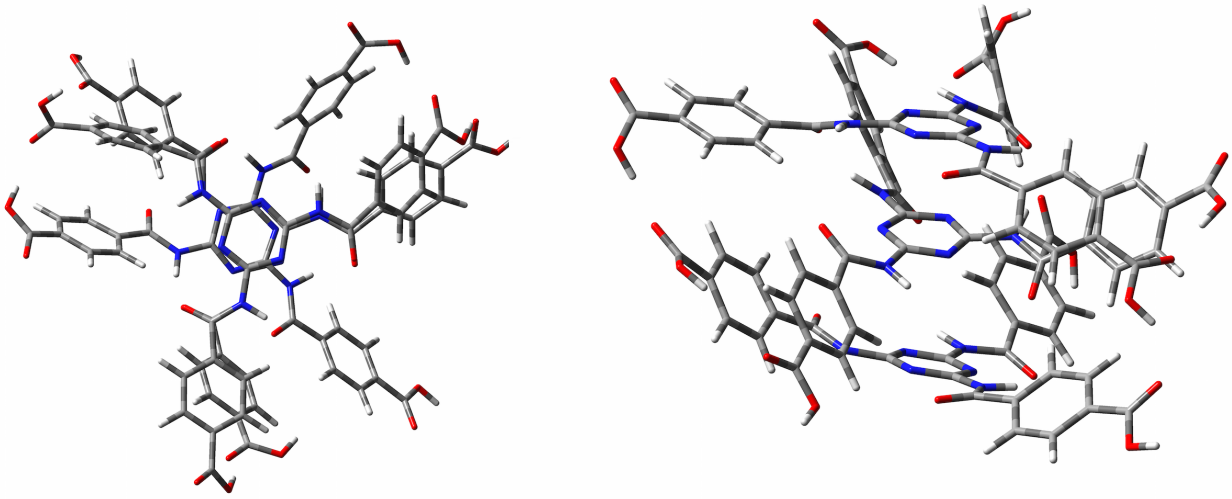

(a) Top view (b) Side view

Figure 8.6: Trimer of p-[4,6-Bis(p-carboxybenzoylamino)-1,3,5-triazin-2-ylamin] carbonyl benzoic acid optimised using B3LYP/6-311G(d).

Structure 4

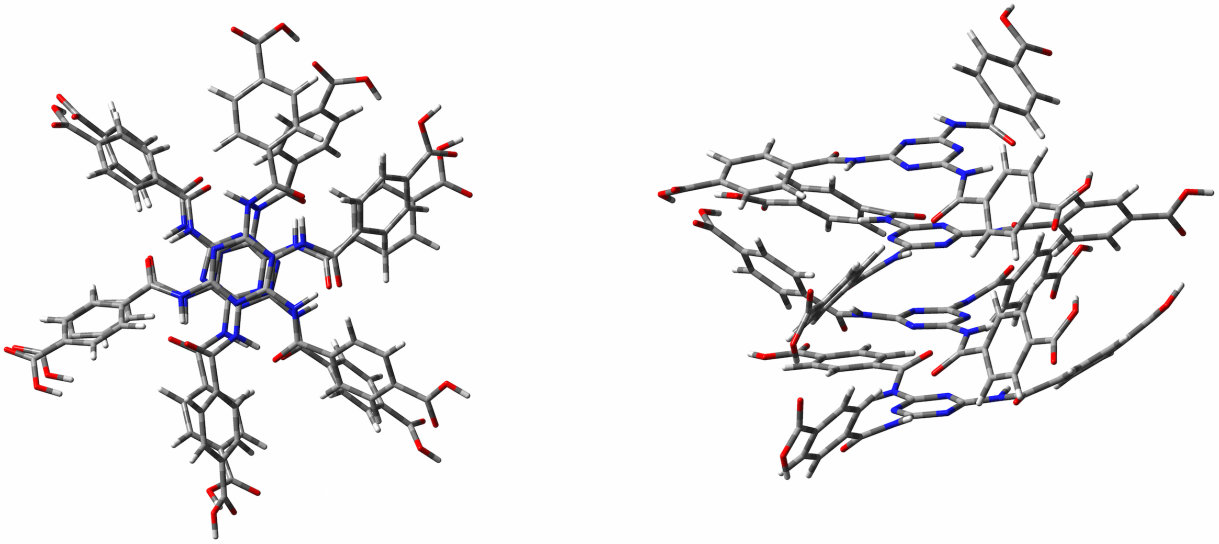

(a) Top view (b) Side view

Figure 8.7: Tetramer of p-[4,6-Bis(p-carboxybenzoylamino)-1,3,5-triazin-2-ylamin] carbonyl benzoic acid optimised using B3LYP/6-311G(d).

Structure 5

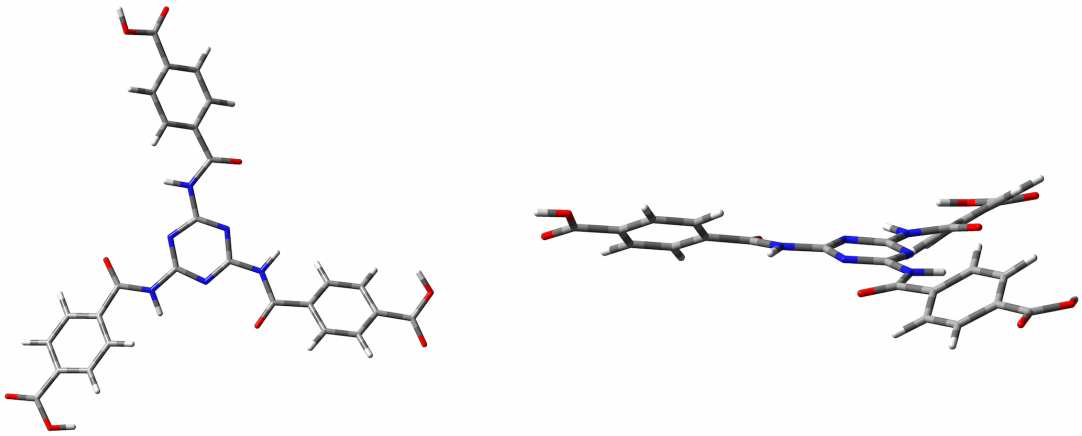

(a) Top view (b) Side view

Figure 8.8: Monomer of p-[4,6-Bis(p-carboxybenzoylamino)-1,3,5-triazin-2-ylamin] carbonyl benzoic acid optimised using B97D/6-311G(d).

Structure 6

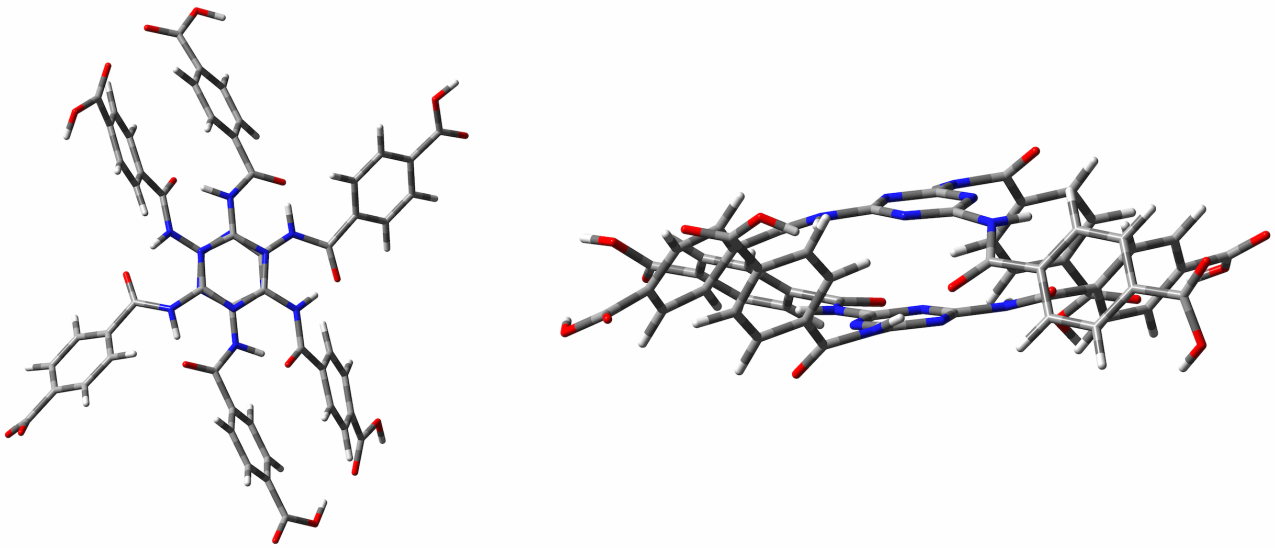

(a) Top view (b) Side view

Figure 8.9: Dimer of p-[4,6-Bis(p-carboxybenzoylamino)-1,3,5-triazin-2-ylamin] carbonyl benzoic acid optimised using B97D/6-311G(d).

Structure 7

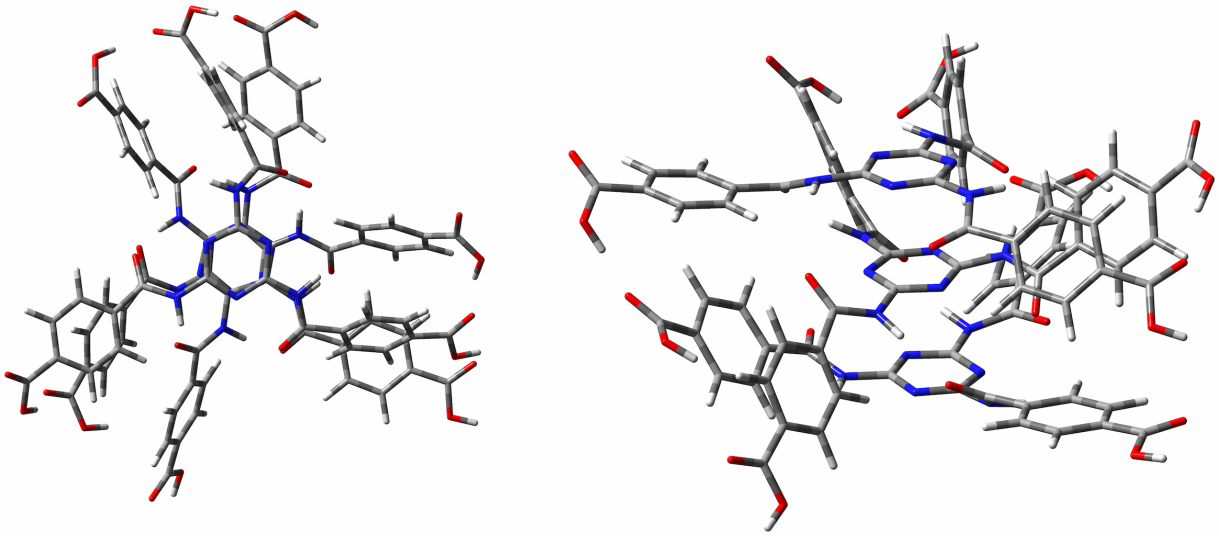

(a) Top view (b) Side view

Figure 8.10: Trimer of p-[4,6-Bis(p-carboxybenzoylamino)-1,3,5-triazin-2-ylamin] carbonyl benzoic acid optimised using B97D/6-311G(d).

Structure 8

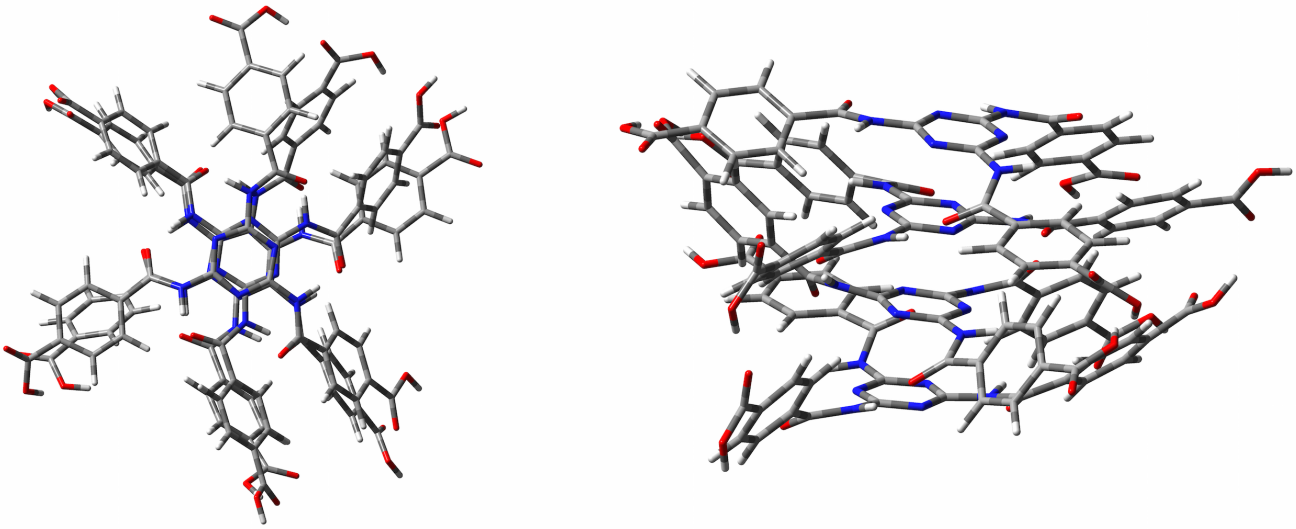

(a) Top view (b) Side view

Figure 8.11: Tetramer of p-[4,6-Bis(p-carboxybenzoylamino)-1,3,5-triazin-2-ylamin] carbonyl benzoic acid optimised using B97D/6-311G(d).

Bond lengths, angles and dihedrals comparison

Focusing on the distances, angles and dihedrals among the different layers; the optimised structures of the tetramer were chosen, structure 4 (using B3LYP) and structure 8 (using B97D). Figure 8.12 shows how the measurements between the different layers were analysed and how the two different theoretical methods affect the calculations. α corresponds to the distances between atoms of different rings and β to the angles between them. γ and δ correspond to dihedrals. With this information it is possible to compare how the different methods affect the distances among layers/atoms, the angles and dihedrals. Comparing the distances between the rings, B97D shows an average stacking of 0.3 Å closer between the layers. Considering the angles and dihedrals, as it was mentioned previously, B97D includes a dispersion effect which makes the rings pack closer together, affecting the angles and dihedrals. When looking at the angles, for B3LYP between 6(1)-6(2)-5(2) is 87.97° and for B97D 80.68°. There is a substantial difference for 3(1)-3(2)-(2), B3LYP predicts the angle to be 89.98° while B97D, 98.20°. The other angles are not very different, the maximum deviation is 2.0°. For the dihedrals, when considering 6(1)-1(1)-6(2)-1(2), B3LYP predicts 174.02° and B97D 170.93°. This is the largest difference for the dihedrals.

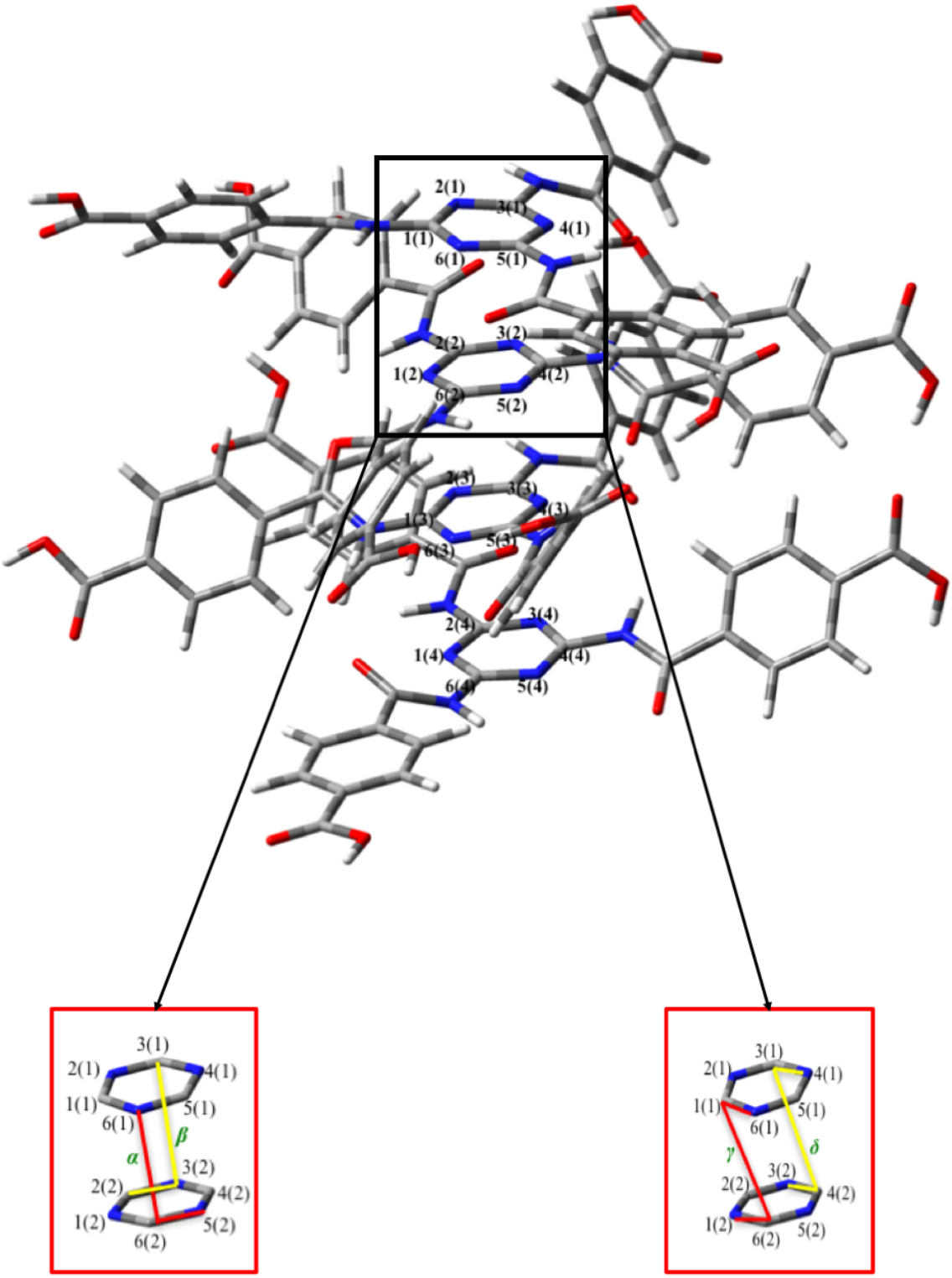

Figure 8.12: Numbering and measurement of bond lengths, angles and dihedrals for B3LYP.

Table 8.1: Bond lengths, angles and dihedrals.

Bond lengths (α) (Å)		**Angles** (β) (°)		**Dihedrals** (γ) **and** (δ) (°)	
1(1)—1(2)	3.424	**6(1)—6(2)—5(2)**	87.97	**6(1)—1(1)—6(2)—1(2)**	174.02
2(1)—2(2)	3.573	**3(1)—3(2)—2(2)**	89.98	**4(1)—3(1)—4(2)—3(2)**	-173.53
3(1)—3(2)	3.647	**6(2)—6(3)—5(4)**	91.54	**6(2)—1(2)—6(3)—1(3)**	-171.56
4(1)—4(2)	3.553	**3(2)—3(3)—2(3)**	89.46	**4(2)—3(2)—4(3)—3(3)**	-176.09
5(1)—5(2)	3.374	**6(3)—6(4)—5(4)**	82.93	**6(3)—1(3)—6(4)—1(4)**	174.82
6(1)—6(2)	3.355	**3(3)—3(4)—2(4)**	96.09	**4(3)—3(3)—4(4)—3(4)**	-172.59
1(2)—1(3)	3.436				
2(2)—2(3)	3.549				
3(2)—3(3)	3.523				
4(2)—4(3)	3.482				
5(2)—5(3)	3.435				
6(2)—6(3)	3.359				
1(3)—1(4)	3.631				
2(3)—2(4)	3.471				
3(3)—3(4)	3.394				
4(3)—4(4)	3.384				
5(3)—5(4)	3.418				
6(3)—6(4)	3.550				

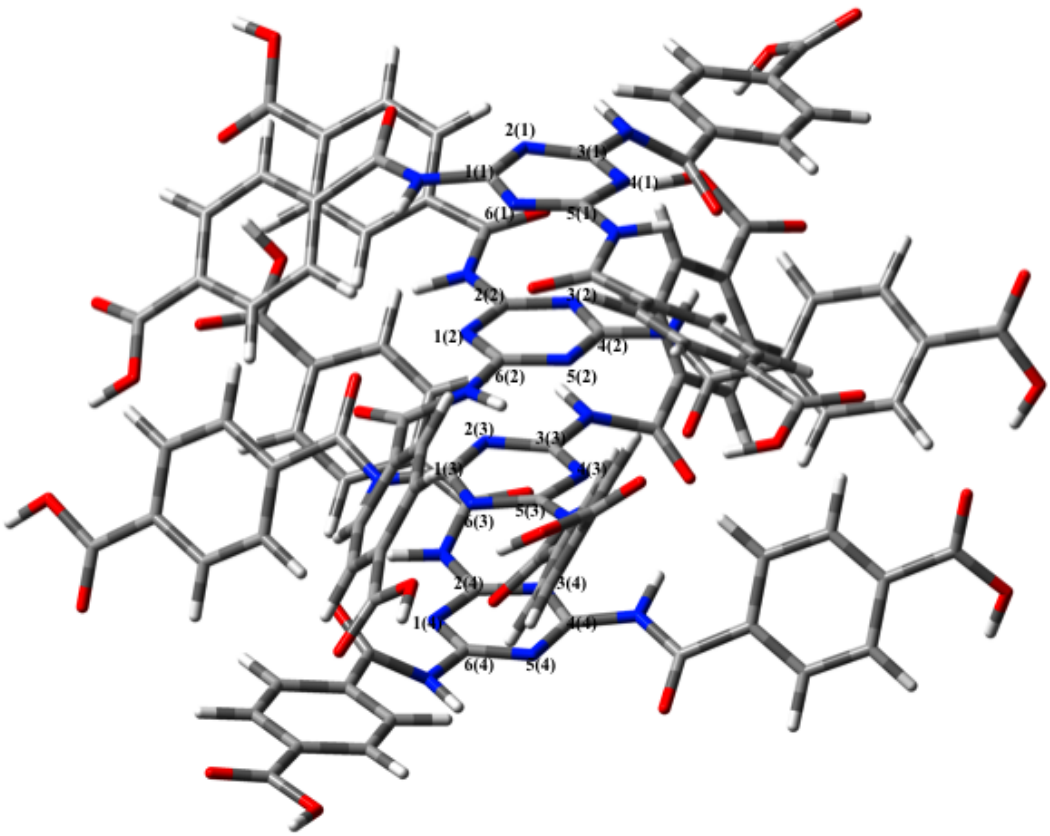

Figure 8.13: Numbering and measurement of bond lengths, angles and dihedrals for B97D.

Table 8.2: Bond lengths, angles and dihedrals.

Bond lengths (α) (Å)		**Angles** (β) (°)		**Dihedrals** (γ) **and** (δ) (°)	
1(1)—1(2)	3.167	**1(1)—6(2)—5(2)**	80.68	**1(1)—1(1)—6(2)—1(2)**	170.93
2(1)—2(2)	3.202	**3(1)—3(2)—2(2)**	98.20	**4(1)—3(1)—4(2)—3(2)**	-176.39
3(1)—3(2)	3.256	**6(2)—6(3)—5(4)**	89.54	**6(2)—1(2)—6(3)—1(3)**	-169.15
4(1)—4(2)	3.208	**3(2)—3(3)—2(3)**	89.49	**4(2)—3(2)—4(3)—3(3)**	177.58
5(1)—5(2)	3.055	**6(3)—6(4)—5(4)**	81.53	**6(3)—1(3)—6(4)—1(4)**	172.88
6(1)—6(2)	3.131	**3(3)—3(4)—2(4)**	96.33	**4(3)—3(3)—4(4)—3(4)**	-174.00
2(2)—2(3)	3.202				
3(2)—3(3)	3.139				
4(2)—4(3)	3.088				
5(2)—5(3)	3.126				
6(2)—6(3)	3.083				
1(3)—1(4)	3.255				
2(3)—2(4)	3.104				
3(3)—3(4)	3.103				
4(3)—4(4)	3.100				
5(3)—5(4)	3.028				
6(3)—6(4)	3.141				

Absorption spectra

Only on structure 1 to 4 TD-DFT calculations were performed (due to convergence issues) and were used to compare the trends from the previous results obtained by Bernet *et al* [20]. There are experimental spectra to compare the results obtained. The trends found by previous researchers in similar structures are compared to the results obtained in this chapter. Analysing the spectral data gathered from structures 1 to 4, it is possible to conclude that there are two clear peaks, one at 190 nm and another at 235 nm. Two clear bands are shown for the monomer, with the second one having a much larger oscillator strength. Looking at structure 2 (dimer), the major peak occurs around 235 nm. In this structure, for the two clear bands shown before, there is only one with an oscillator strength similar to the highest peak in structure 1. For structure 3 (trimer) and structure 4 (tetramer) a major band is found around 260 nm. By analysing these results it is possible to observe a small red shift from structures 1 to 4. This provides a clear picture of the major peaks and transitions for the monomer up to tetramer (structures 1 to 4). From the 1,3,5-benzene tricarboxamide structure mentioned before [20], it has been found a strong charge transfer from the peripheral side

groups to the central aromatic cores. To analyse this specific property another calculation was performed to further characterise the states (see the following subsection).

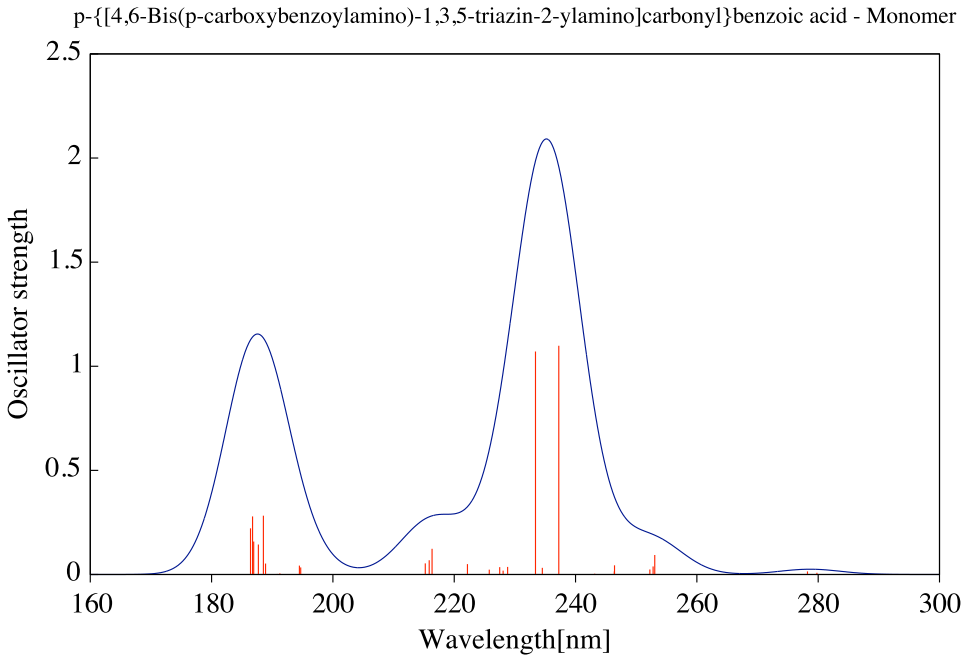

Figure 8.14: Mononer/structure 1 - TD-CAM-B3LYP.

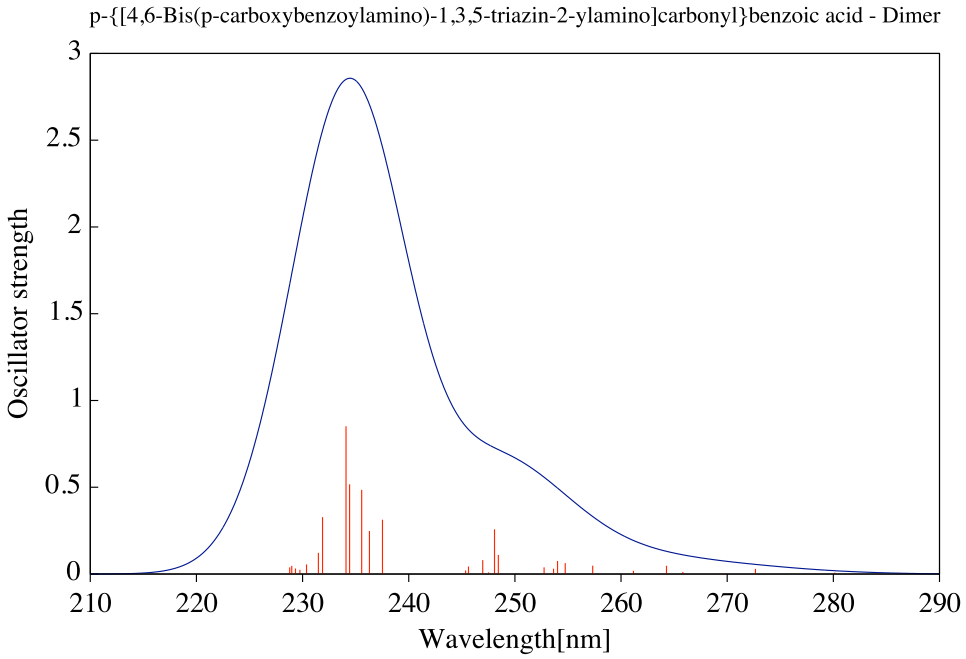

Figure 8.15: Dimer/structure 2 - TD-CAM-B3LYP.

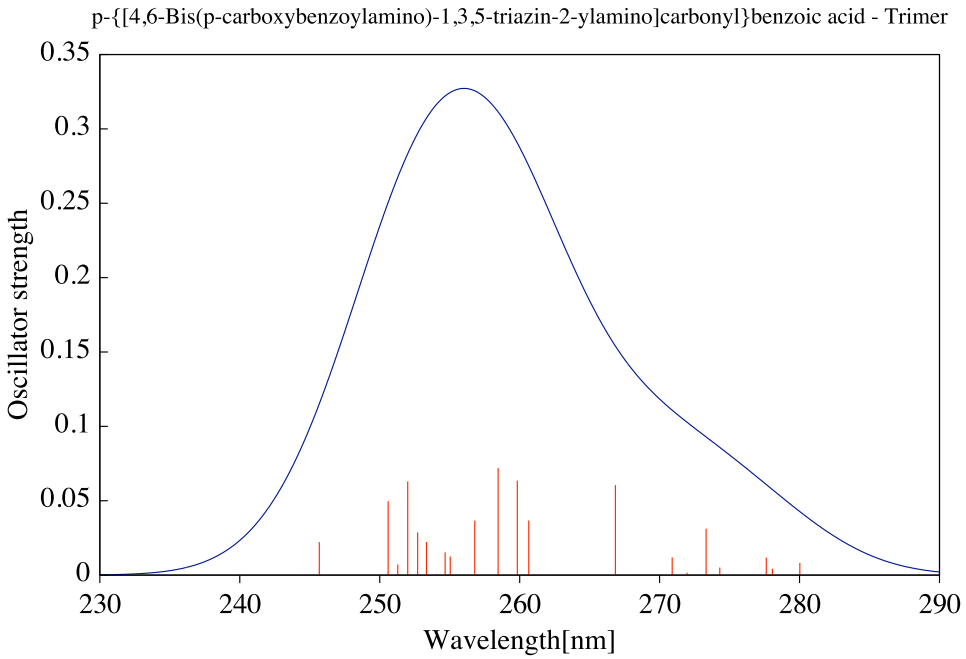

Figure 8.16: Trimer/structure 3 - TD-CAM-B3LYP.

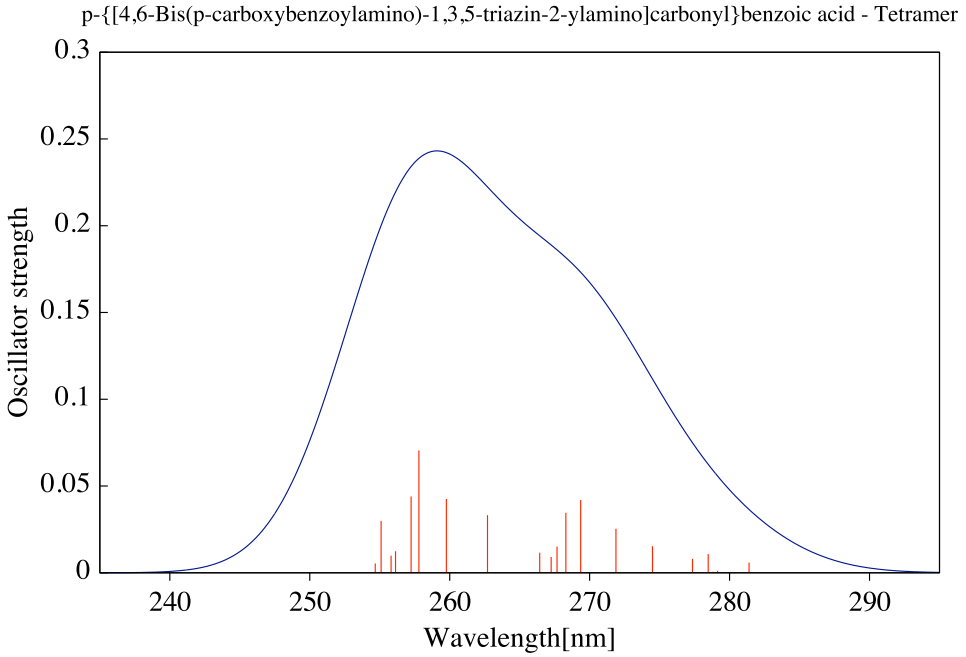

Figure 8.17: Tetramer/structure 4 - TD-CAM-B3LYP.

Natural transition orbitals

To perform a more in depth analysis, natural transition orbitals (NTOs) [37] were chosen. For the monomer, the major transition corresponds to 233 nm (f=1.071), for structure 2, 234 nm (f=0.852), for structure 3, 258 nm (f=0.072) and for structure 4 to 260 nm (f=0.042). Comparing

these results to the ones mentioned before, one may notice that only the trimer shows the same trends, having charge transfers from the peripheral side groups to the central aromatic cores. Looking at monomer, dimer and tetramer, one may verify that their transfers are different, showing ligand-to-ligand charge transfers, mainly $\pi \rightarrow \pi^*$ transitions, corresponding to the peaks seen before.

Monomer

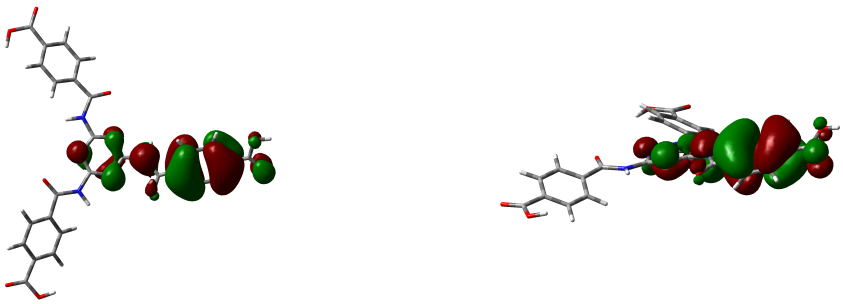

(a) Top view (b) Side view

Figure 8.18: Natural bond orbitals - Hole.

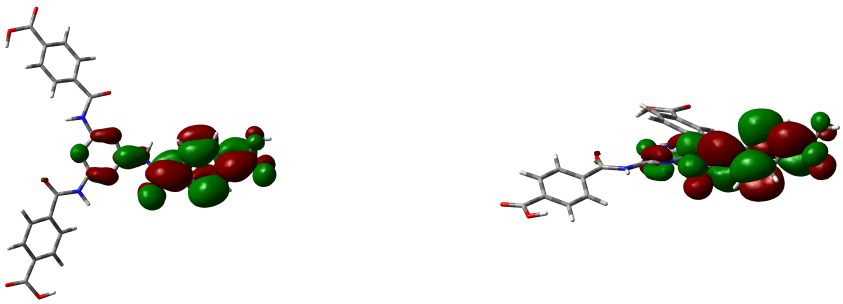

(a) Top view (b) Side view

Figure 8.19: Natural bond orbitals - Particle.

Dimer

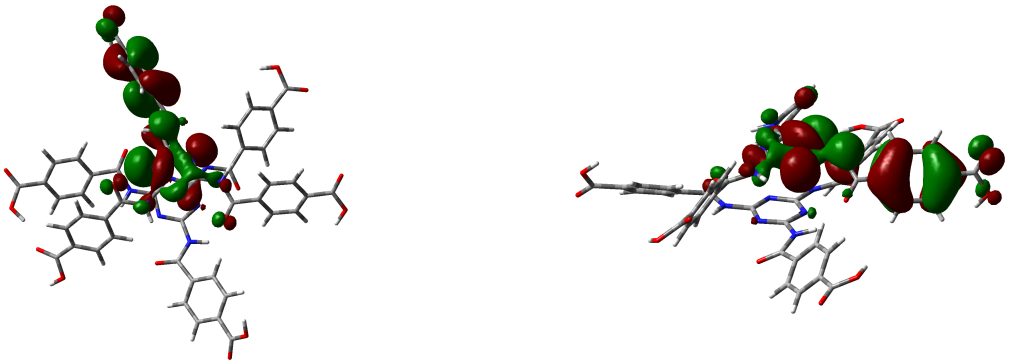

(a) Top view (b) Side view

Figure 8.20: Natural bond orbitals - Hole.

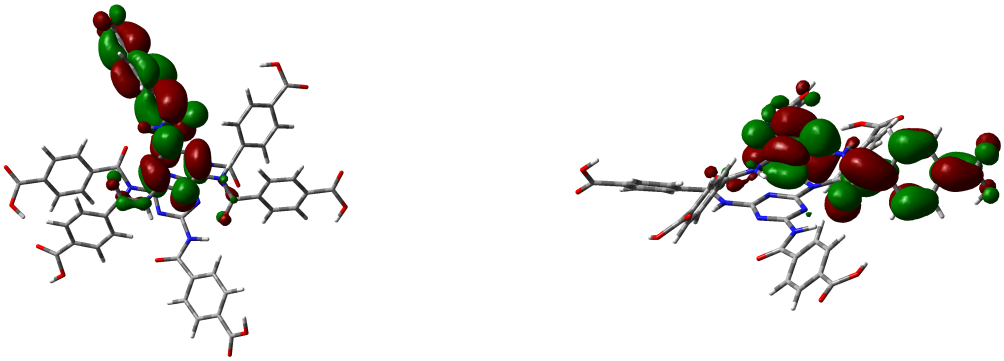

(a) Top view (b) Side view

Figure 8.21: Natural bond orbitals - Particle.

Trimer

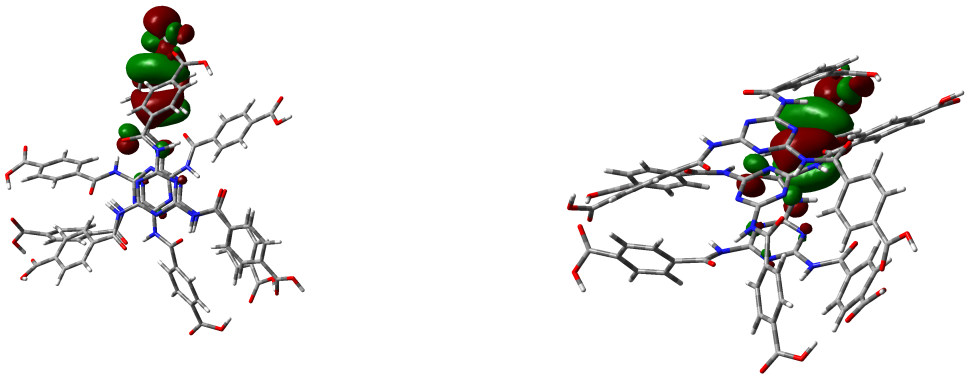

(a) Top view (b) Side view

Figure 8.22: Natural bond orbitals - Hole.

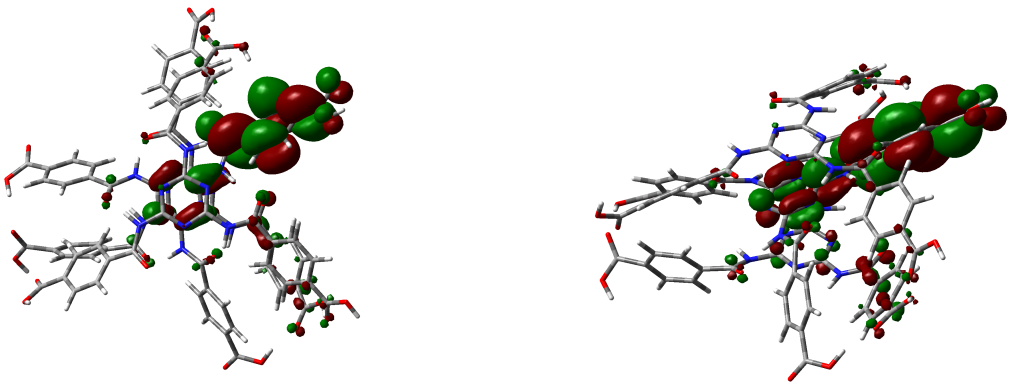

(a) Top view (b) Side view

Figure 8.23: Natural bond orbitals - Particle.

Tetramer

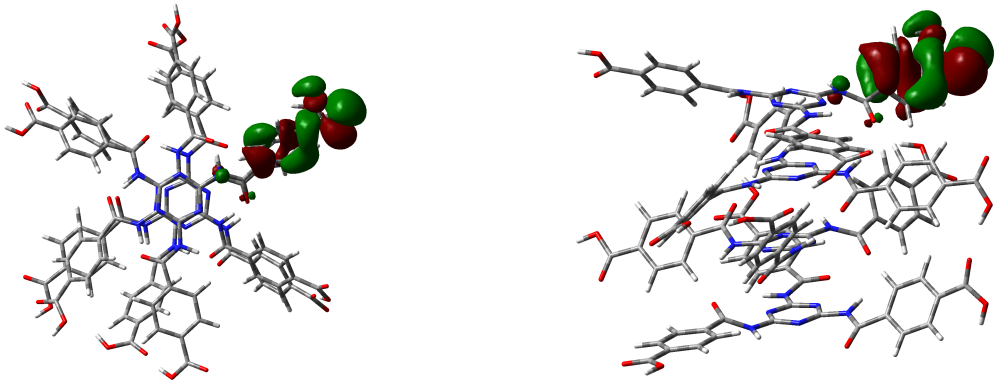

(a) Top view (b) Side view

Figure 8.24: Natural bond orbitals - Hole.

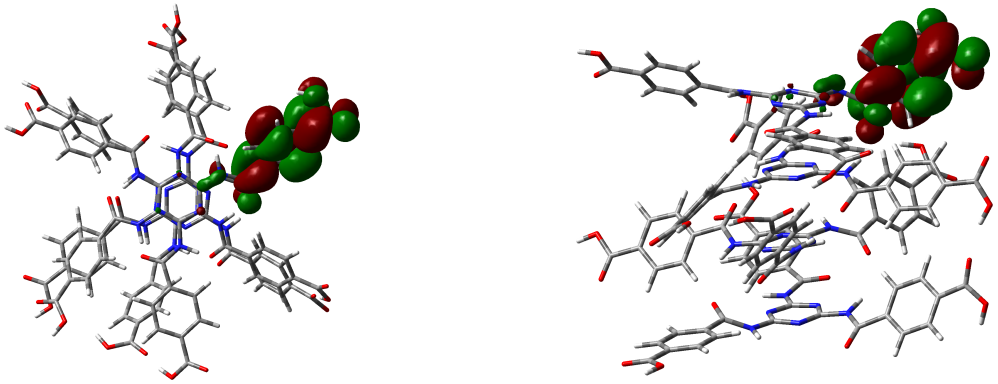

(a) Top view (b) Side view

Figure 8.25: Natural bond orbitals - Particle.

8.3.2 Part II

Geometry Optimisation - Trimer

For the B structure geometry optimisation, it is possible to see how the rings stack on each other to form a supramolecular structure. The π-π stacking is fundamental for stabilizing the structure and the hydrogen bonds help to keep it together and form the LGWs. The same phenomena happen when looking at C_e and C_k, both of which form a very structured gel network. It is very interesting to look at the C_e enol and C_k species, where the tautomer C adopts the initially pH dependent structure. The enol form is observed in low pH solutions, around 8 or less and the keto form is found in high pH solutions, around 9.5 and 12. The formation of both species is pH reversible and can be interchanged.

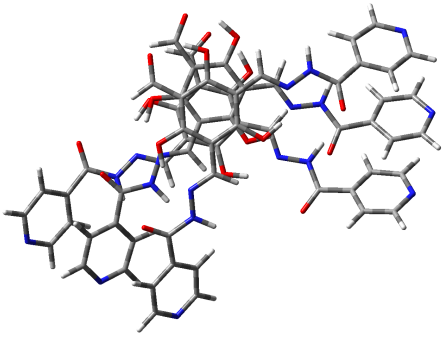

Figure 8.26: B top view

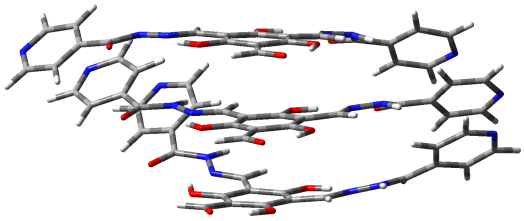

Figure 8.27: B side view

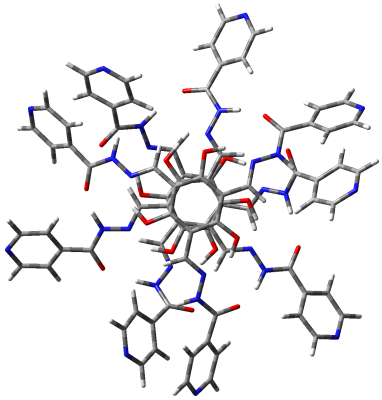

Figure 8.28: C_e top view

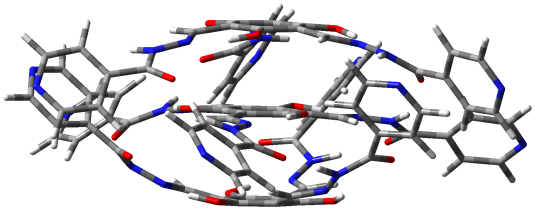

Figure 8.29: C_e side view

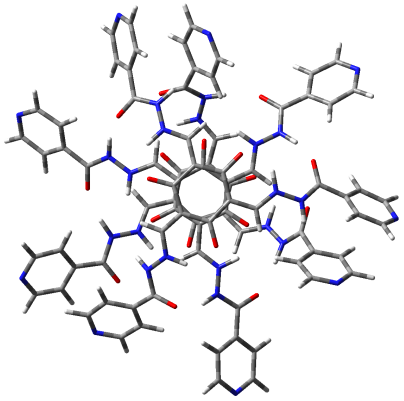

Figure 8.30: C_k top view

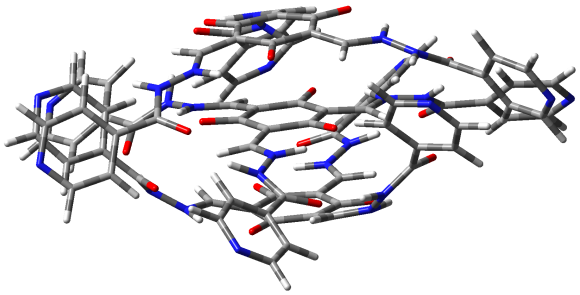

Figure 8.31: C_k side view

Reaction pathways

Computational studies on the reaction pathways have been performed for the B, C form. As it was discussed in the introduction previously, B only exists in one tautomeric form, shown in Figures 8.26 and 8.27. This reaction pathway illustrates the calculated profile it would take from enol to keto, Figures 8.32 and 8.33. The reaction ΔE is 6.3 kJ/mol and the activation barriers are large going from min1 to min4.

For the C structure the activation energy from min1 to min2 is quite large (26.4 kJ/mol), but from min2 to min3 or min3 to min4 the energetic barrier smaller, Figures 8.34 and 8.35. The activation barriers are smaller than the B form, showing evidence why these species exist in two stable tautomeric forms but the B species does not.

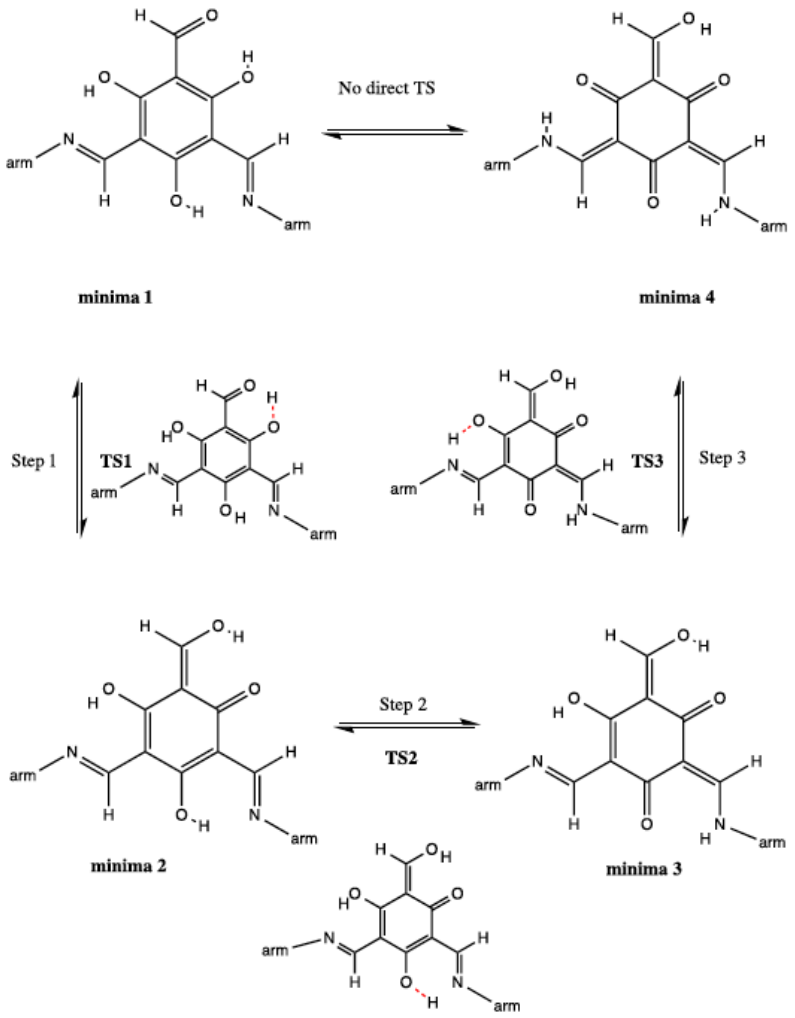

Figure 8.32: Reaction pathway diagram of the B enol to the B keto tautomerisation.

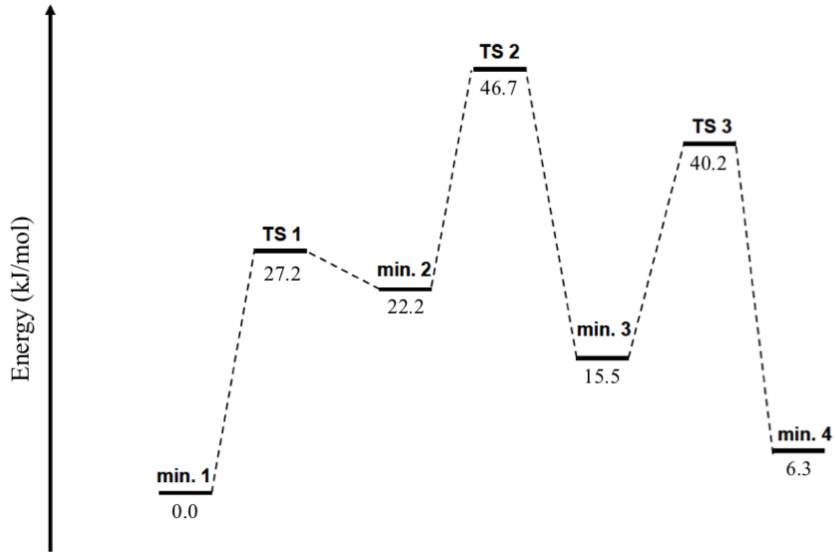

Figure 8.33: Reaction pathway diagram B enol to B keto form showing energy differences among the tautomers and the barrier size among them. The structures were optimised with B3LYP/6-311G(d).

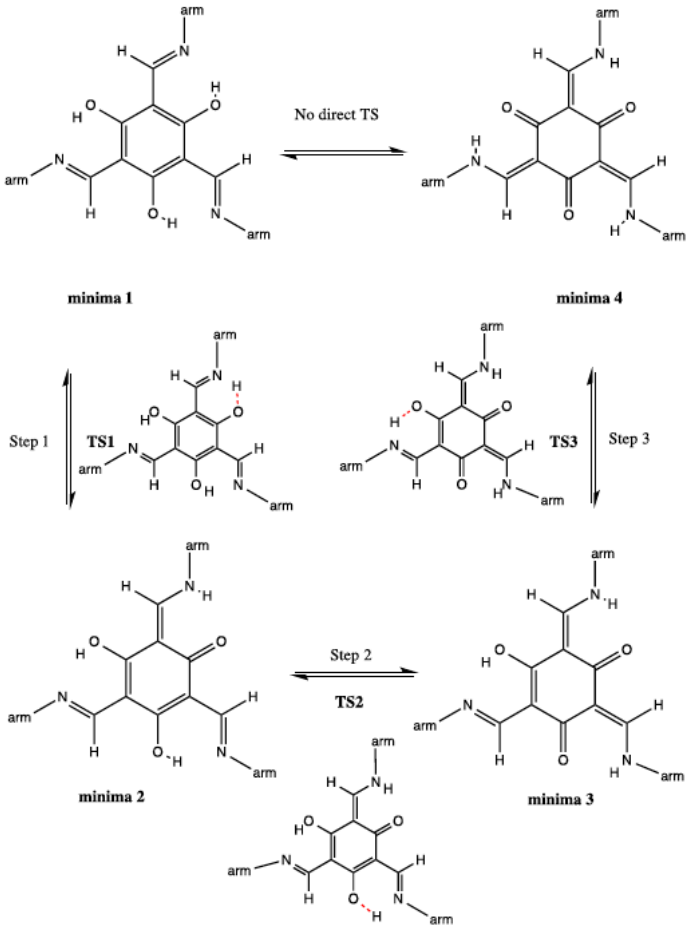

Figure 8.34: Reaction pathway diagram of the C enol to the C keto tautomerisation (C_{3h}) symmetry). Arm corresponds to $NHCOC_5H_4N$.

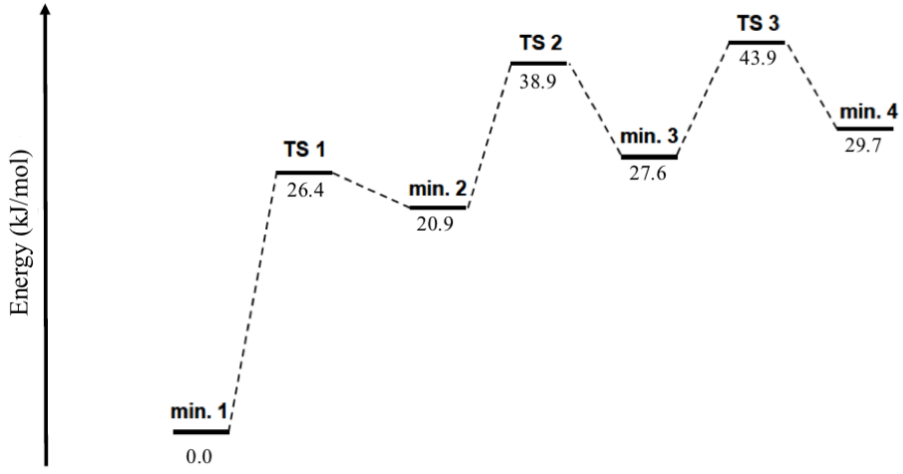

Figure 8.35: Reaction pathway diagram C enol to C keto form showing energy differences among the tautomers and the barrier size among them (C_{3h}) symmetry). The structures were optimised with B3LYP/6-311G(d).

Absorption spectra

When looking at the absorption spectra for B structure, two major peaks are relevant: one at 300 nm and another around 465 nm. Concerning the tautomeric species, their spectra are similar although C_e has a major peek around 360 nm, C_k is blue shifted by around 20 nm. There are two smaller absorption peeks around 600 nm for C_e and 530 nm for C_k, again 70 nm blue shifted. When comparing this data to the experimental UV/VIS absorption spectra performed by the experimentalists, some conclusions can be drawn. There is a small difference of results when comparing it to the experimental data since it has been performed in a slightly basic environment, although the solvent used was the same (water). The two major peaks mentioned before, concerning the species B show up around 300 nm and 410 nm. The second peak is blue shifted compared to the computational spectra. For C_e a major peak arises around 410 nm, but for C_k two peaks are present, one around 275 nm and another 350 nm, both fairly broadened. For C_e the major peak is red shifted in the experimental spectrum and for C_k is blue shifted when compared to the theoretical calculations. The experimental UV/VIS absorption spectra were added below for a comparison to the TD-DFT calculations.

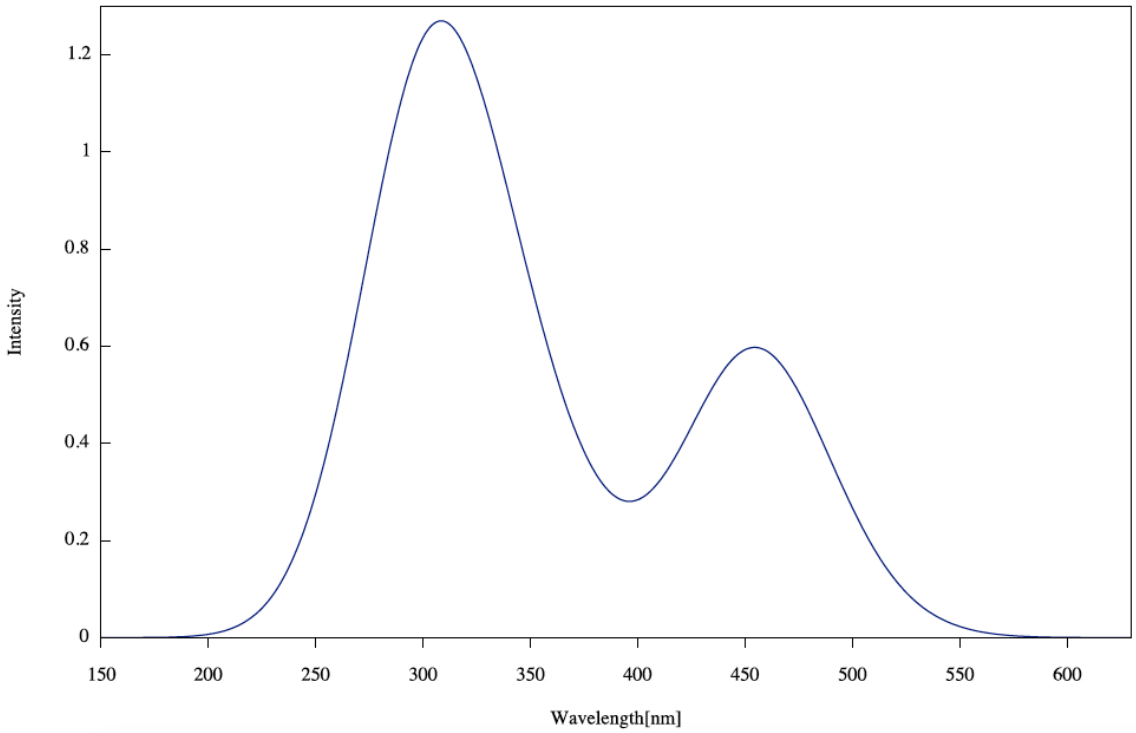

Figure 8.36: Deprotoanted - Monomer - B structure - TD-B97D3 – SMD with 6-31G(d) basis set with water as a solvent – 50 states included.

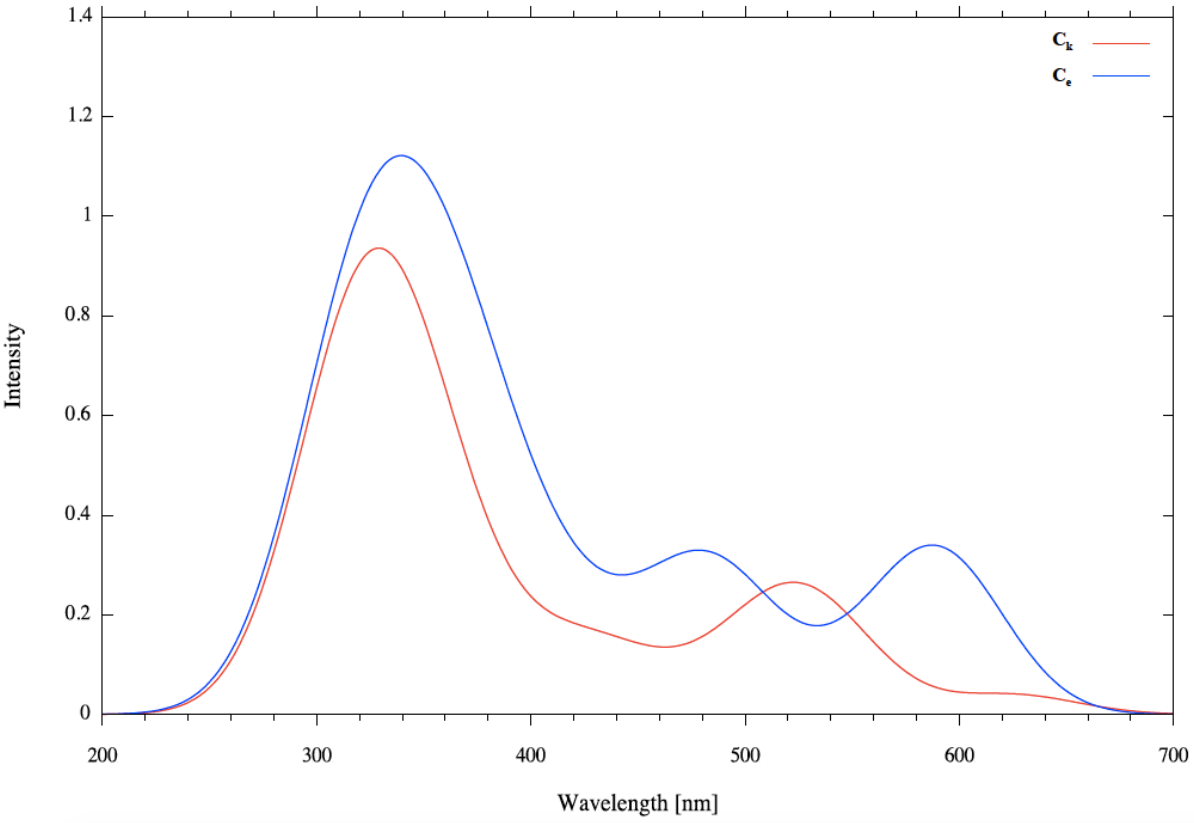

Figure 8.37: Deprotoanted - Monomer - C_e and C_k structures - TD-B97D3 – SMD with 6-31G(d) basis set with water as a solvent – 50 states included.

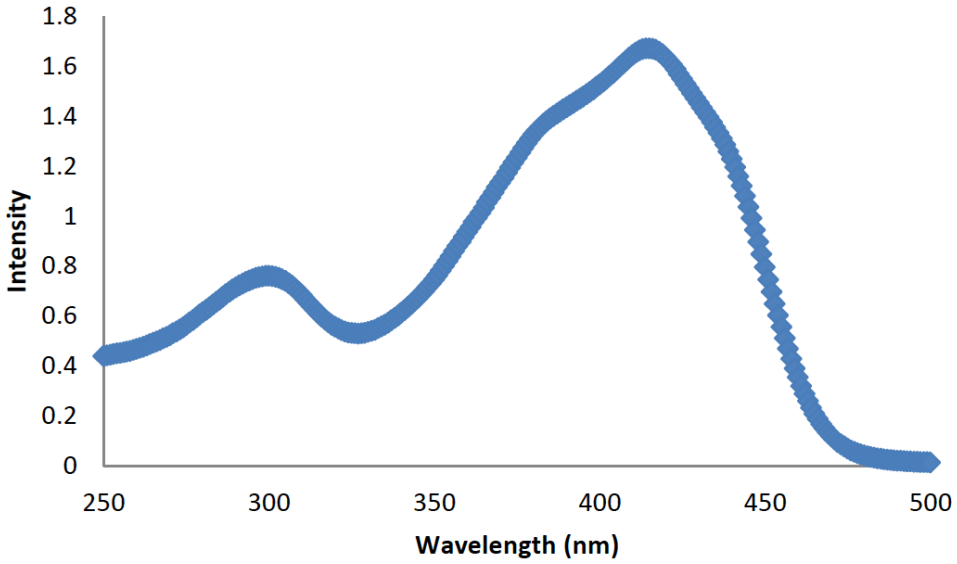

Figure 8.38: Experimental **B** UV/VIS absorption spectra in slightly basic water - Adapted from: "Gelation landscape engineering using a multi-reaction supramolecular hydrogelator system", *The Journal of the American Chemical Society* **2015**, *137*(45), 14236-14239.

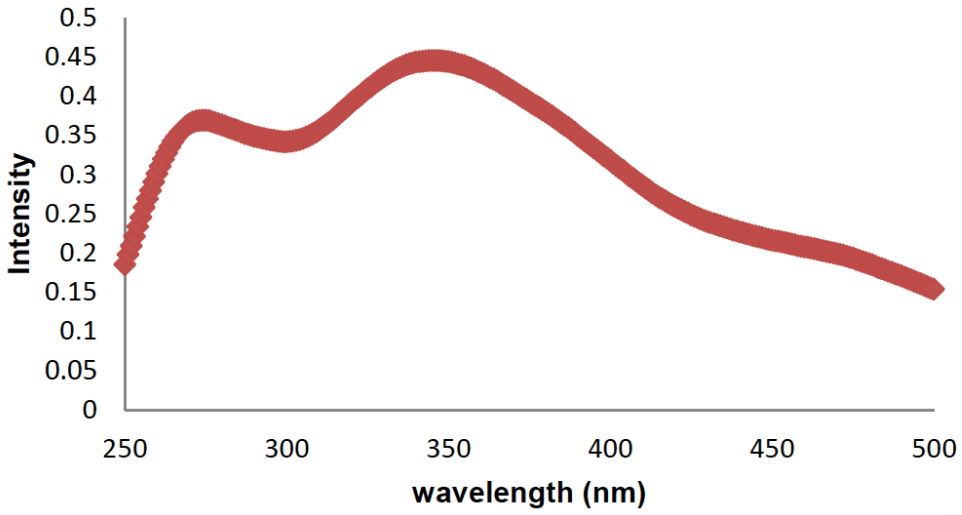

Figure 8.39: Experimental $\mathbf{C_k}$ UV/VIS absorption spectra in slightly basic water - Adapted from: "Gelation landscape engineering using a multi-reaction supramolecular hydrogelator system", *The Journal of the American Chemical Society* **2015**, *137*(45), 14236-14239.

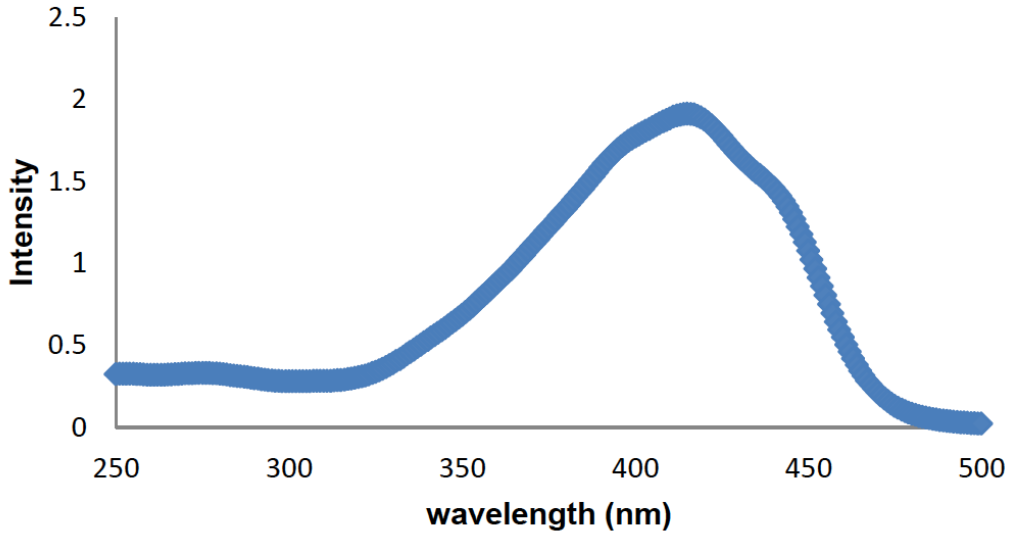

Figure 8.40: Experimental $\mathbf{C_e}$ UV/VIS absorption spectra in slightly basic water - Adapted from: "Gelation landscape engineering using a multi-reaction supramolecular hydrogelator system", *The Journal of the American Chemical Society* **2015**, *137*(45), 14236-14239.

8.4 Conclusions

A bottom-up approach is fundamental in supramolecular chemistry as it helps build very interesting structures, that can be predicted from a theoretical point of view. Another aspect is to back-up experimental data and help define properties that experimentalists might have some difficulty in measuring. For the first part of this work, all the data generated is currently undergoing laboratory work, in an attempt to synthesize the gel and form the hydrogel supramolecular structure. A lot of different properties were calculated and can be matched to experimental work in the coming months, and will complement the results obtained.

For the second part of this work, it is shown that the self-assembly of supramolecular structures with engineered reaction pathways are possible and can be generated by a bottom-up approach from first principles. The spectra generated though possess some differences from experimental ones, but have the same qualitative trends, which is encouraging for

such large complex systems.

Bibliography

[1] Swinburne, A. N.; Paterson, M. J.; Beeby, A.; Steed, J. W. *Org. Biomol. Chem.* **2010**, *8*, 1010–1016.

[2] Dickson, S. J.; Paterson, M. J.; Willans, C. E.; Anderson, K. M.; Steed, J. W. *Chem-Eur J.* **2008**, *14*(24), 7296–7305.

[3] Dickson, S. J.; Wallace, E. V. B.; Swinburne, A. N.; Paterson, M. J.; Lloyd, G. O.; Beeby, A.; Belcher, W. J.; Steed, J. W. *New J. Chem.* **2008**, *32*, 786–789.

[4] Filby, M. H.; Dickson, S. J.; Zaccheroni, N.; Prodi, L.; Bonacchi, S.; Montalti, M.; Paterson, M. J.; Humphries, T. D.; Chiorboli, C.; Steed, J. W. *J. Am. Chem. Soc.* **2008**, *130*(12), 4105–4113.

[5] Barnard, A.; Dickson, S. J.; Paterson, M. J.; Todd, A. M.; Steed, J. W. *Org. Biomol. Chem.* **2009**, *7*, 1554–1561.

[6] Swinburne, A.; Paterson, M.; Beeby, A.; Steed, J. *Chem-Eur J.* **2010**, *16*(9), 2714–2718.

[7] Swinburne, A.; Paterson, M.; Fischer, K.; Dickson, S.; Wallace, E.; Belcher, W.; Beeby, A.; Steed, J. *Chem-Eur J.* **2010**, *16*(5), 1480–1492.

[8] Estroff, L. A.; Hamilton, A. D. *Chem. Rev.* **2004**, *104*(3), 1201–1218.

[9] Terech, P.; Weiss, R. G. *Chem. Rev.* **1997**, *97*(8), 3133–3160.

[10] Brunsveld, L.; Folmer, B. J. B.; Meijer, E. W.; Sijbesma, R. P. *Chem. Rev.* **2001**, *101*(12), 4071–4098.

[11] Stals, P. J. M.; Smulders, M. M. J.; Martín-Rapún, R.; Palmans, A. R.; Meijer, E. *Chem-Eur J.* **2009**, *15*(9), 2071–2080.

[12] P. Lightfoot, M.; S. Mair, F.; G. Pritchard, R.; E. Warren, J. *Chem. Commun.* **1999**, pages 1945–1946.

[13] Howe, R. C. T.; Smalley, A. P.; Guttenplan, A. P. M.; Doggett, M. W. R.; Eddleston, M. D.; Tan, J. C.; Lloyd, G. O. *Chem. Commun.* **2013**, *49*, 4268–4270.

[14] Patrick J. M. Stals, Jan F. Haveman, A. R. A. P.; Schenning, A. P. H. J. *J. Chem. Educ.* **2009**, *86*(2), 230.

[15] Stals, P. J.; Everts, J. C.; de Bruijn, R.; Filot, I. A.; Smulders, M. M.; Martín-Rapún, R.; Pidko, E. A.; de Greef, T. F.; Palmans, A. R.; Meijer, E. *Chem-Eur J.* **2010**, *16*(3), 810–821.

[16] Nguyen, T.-Q.; Martel, R.; Avouris, P.; Bushey, M. L.; Brus, L.; Nuckolls, C. *J. Am. Chem. Soc.* **2004**, *126*(16), 5234–5242.

[17] Matsunaga, Y.; Miyajima, N.; Nakayasu, Y.; Sakai, S.; Yonenaga, M. *Bull. Chem. Soc. Jpn.* **1988**, *61*(1), 207–210.

[18] Xue, C.; Ilhan, F.; Jin, S.; Cheng, S.; Meador, M.; Eby, R. In *Abstracts of papers of the american chemical society*, Vol. 227, pages U361–U361. Amer Chemical Soc 1155 16th St, NW, Washington, Dc 200036 USA, 2004.

[19] Stals, P. J. M.; Haveman, J. F.; Martin-Rapun, R.; Fitie, C. F. C.; Palmans, A. R. A.; Meijer, E. W. *J. Mater. Chem.* **2009**, *19*, 124–130.

[20] Bernet, A.; Albuquerque, R. Q.; Behr, M.; Hoffmann, S. T.; Schmidt, H.-W. *Soft Matter* **2012**, *8*, 66–69.

[21] Rochefort, A.; Bayard, É.; Hadj-Messaoud, S. *Adv. Mater.* **2007**, *19*(15), 1992–1995.

[22] Lewis, F. D.; Long, T. M.; Stern, C. L.; .; Liu, W. *J. Phys. Chem. A* **2003**, *107*(18), 3254–3262.

[23] Korevaar, P.; George, S.; Markvoort, A.; Smulders, M.; Hilbers, P.; Schenning, A.; De Greef, T.; Meijer, E. W. *Nature* **2012**, *481*, 492–496.

[24] Korevaar, P. A.; Newcomb, C. J.; Meijer, E. W.; Stupp, S. I. *J. Am. Chem. Soc.* **2014**, *136*(24), 8540–8543.

[25] Raeburn, J.; Zamith Cardoso, A.; Adams, D. J. *Chem. Soc. Rev.* **2013**, *42*, 5143–5156.

[26] Cardoso, A. Z.; Alvarez Alvarez, A. E.; Cattoz, B. N.; Griffiths, P. C.; King, S. M.; Frith, W. J.; Adams, D. J. *Faraday Discuss.* **2013**, *166*, 101–116.

[27] Aggeli, A.; Nyrkova, I.; Bell, M.; Harding, R.; Carrick, L.; McLeish, T.; Semenov, A.; Boden, N. *Proc. Natl. Acad. Sci. U. S. A.* **2001**, *98*(21), 11857–11862.

[28] Friggeri, A. *J. Org. Biomol. Chem* **2005**, *3*, 2917–2920.

[29] Korevaar, P. A.; de Greef, T. F. A.; Meijer, E. W. *Chem. Mater.* **2014**, *26*(1), 576–586.

[30] Baskakov, I. V.; Legname, G.; Baldwin, M. A.; Prusiner, S. B.; Cohen, F. E. *Journal of Biological Chemistry* **2002**, *277*(24), 21140–21148.

[31] Misra, N.; Lees, D.; Zhang, T.; Schwartz, R. *Comput. Math. Methods Med.* **2008**, *9*(3-4), 277–293.

[32] Kumar, M.; Brocorens, P.; Tonnelé, C.; Beljonne, D.; Surin, M.; George, S. J. *Nature comm.* **2014**, *5*.

[33] Marenich, A. V.; Cramer, C. J.; Truhlar, D. G. *J. Phys. Chem. B* **2009**, *113*(18), 6378–6396.

[34] Grimme, S.; Ehrlich, S.; Goerigk, L. *J. Comput. Chem.* **2011**, *32*(7), 1456–1465.

[35] Grimme, S. *J. Comp. Chem.* **2006**, *27*(15), 1787–1799.

[36] Gaussian 09 Revision A.02. Frisch, M. J.; Trucks, G. W.; Schlegel, H. B.; Scuseria, G. E.; Robb, M. A.; Cheeseman, J. R.; Scalmani, G.; Barone, V.; Mennucci, B.; Petersson, G. A.; Nakatsuji, H.; Caricato, M.; Li, X.; Hratchian, H. P.; Izmaylov, A. F.; Bloino, J.; Zheng, G.; Sonnenberg, J. L.; Hada, M.; Ehara, M.; Toyota, K.; Fukuda, R.; Hasegawa, J.; Ishida, M.; Nakajima, T.; Honda, Y.; Kitao, O.; Nakai, H.; Vreven, T.; Montgomery, Jr., J. A.; Peralta, J. E.; Ogliaro, F.; Bearpark, M.; Heyd, J. J.; Brothers, E.; Kudin, K. N.; Staroverov, V. N.; Kobayashi, R.; Normand, J.; Raghavachari, K.; Rendell, A.; Burant, J. C.; Iyengar, S. S.; Tomasi, J.; Cossi, M.; Rega, N.; Millam, J. M.; Klene, M.; Knox, J. E.; Cross, J. B.; Bakken, V.; Adamo, C.; Jaramillo, J.; Gomperts, R.; Stratmann, R. E.; Yazyev, O.; Austin, A. J.; Cammi, R.; Pomelli, C.; Ochterski, J. W.; Martin, R. L.; Morokuma, K.; Zakrzewski, V. G.; Voth, G. A.; Salvador, P.; Dannenberg, J. J.; Dapprich, S.; Daniels, A. D.; Farkas, .; Foresman, J. B.; Ortiz, J. V.; Cioslowski, J.; Fox, D. J.

[37] Martin, R. L. *J. Chem. Phys.* **2003**, *118*(11), 4775–4777.

Summary/Conclusions

This thesis covers a wide range of problems using computational chemistry. Particular focus is on inorganic excited states and the challenges they present to an accurate treatment.

Chapter 3 provided an essential computational study for very commonly used complexes in inorganic chemistry. A rational approach to these complexes is fundamental to explore the rich electronic spectra of first-row transition metal complexes. DFT proves to be very useful for this approach and sometimes calculates results closer to the experimental values than more computationally expensive approaches.

Chapter 4 focused on the permanganate ion. This small molecule showed that methods that perform very well for organic systems such as CC2 and CC3 can fail and provide spurious results in inorganic systems where the balance between static and dynamic correlation is not appropriate. RASSCF calculations showed the importance of orbital relaxation in the ground state. It is the primary reason for the failure of CC2 and CC3 methods in response theory.

Chapter 5 used a range of methods on transition metal monocarbonyls. Multireference methods are a valuable tool to study these systems. This chapter demonstrates that methods like CCSD, NEVPT2 or MCCI can provide a clear picture, exploring gaps that were found in earlier studies, helping to give a picture of ground spins states.

In Chapter 6 two inorganic complexes were studied ($Ni(CO)_4$ and Ni(CO)) where similar problems to Chapter 4 arise. There are some multireference effects associated with the $3d^8 4s^2$ metal configuration that have very strong indirect effects in the performance of correlated excited state methodologies for both complexes. CCn models fail due to the large $\hat{T}_1$

amplitudes associated with the poor canonical Hartree-Fock orbitals.

Chapter 7 contrasted the energetical differences for the photoproducts of the non-adiabatic radiotionless decay of $Mn_2(CO)_{10}$ and $Cr(CO)_6$. It was also analysed the effect of perturbation theory on the multireference wavefunctions. The effect of perturbation was more noticeable in the closed-shell complex ($Cr(CO)_5$) than it was for the open-shell case ($Mn(CO)_5$). For $Cr(CO)_5$ there was a larger barrier of pseudorotation compared to $Mn(CO)_5$, which is free to pseudorotate.

The final chapter focuses on a slightly different topic, namely intermolecular aggregates. It is shown that understanding the self-assembly of supramolecular structures with engineered reaction pathways is possible.